rijksuniversiteit
groningen

AGN relics in the radio sky

A LOFAR look into spectral ageing and AGN duty cycles

Proefschrift

ter verkrijging van de graad van doctor aan de
Rijksuniversiteit Groningen
op gezag van de
rector magnificus prof. dr. E. Sterken
en volgens besluit van het College voor Promoties.

De openbare verdediging zal plaatsvinden op

vrijdag 6 februari 2015 om 12.45 uur

door

Aleksandar Shulevski

geboren op 11 december 1978
te Bitola, Macedonië

Promotor:	Prof. dr. R. Morganti
Copromotor:	Prof. dr. P. D. Barthel
Beoordelingscommissie:	Prof. dr. M. A. Garrett
	Prof. dr. A. G. de Bruyn
	Prof. dr. G. Giovannini

ISBN 978-90-367-7632-5
ISBN 978-90-367-7631-8 (electronic version)

To my families

Front cover: The AGN radio relic B2 0924+30 and the surrounding radio sky as imaged by LOFAR at a frequency of 140 MHz. The relic rises over one of the stone runs on the slopes of Baba mountain located in the vicinity of the town of Bitola in Macedonia. Not to scale.
Back cover: A spectral index map of the giant radio galaxy NGC 6251 superposed on the radio sky as seen by LOFAR.

Cover design: Aleksandar Shulevski

Printed by: Ipskamp Drukkers BV, Enschede

Contents

1 Introduction **1**
- 1.1 Extragalactic radio sources . . . 1
- 1.2 AGNs as the engines of relic creation . . . 3
  - 1.2.1 AGN radio relics in detail . . . 5
- 1.3 AGN radio relic taxonomy . . . 6
  - 1.3.1 Relics associated with restarted AGN . . . 6
  - 1.3.2 Relics of switched off AGN - faders . . . 8
- 1.4 LOFAR . . . 10
- 1.5 This thesis . . . 13

2 Recurrent radio emission and gas supply: the radio galaxy B2 0258+35 **15**
- 2.1 Introduction . . . 17
- 2.2 Observations and data reduction . . . 19
- 2.3 Low surface-brightness, extended structure: a radio relic? . . . 20
- 2.4 Recurrent activity and supply of gas . . . 23
- 2.5 Conclusion and future studies . . . 25

3 The peculiar radio galaxy 4C 35.06: a case for recurrent AGN activity? **27**
- 3.1 Introduction . . . 29
- 3.2 Data available, new observations and data reduction . . . 31
  - 3.2.1 LOFAR . . . 31
  - 3.2.2 H I - 21cm and continuum from the WSRT . . . 33
- 3.3 Results . . . 33
  - 3.3.1 The radio continuum structure from WSRT and LOFAR . . . 33
  - 3.3.2 The H I gas . . . 34
  - 3.3.3 Spectral analysis . . . 35
- 3.4 Discussion . . . 40
  - 3.4.1 The presence of cold gas . . . 42
- 3.5 Conclusions . . . 43

4 AGN duty cycle estimates for the ultra-steep spectrum radio relic VLSS J1431.8+1331 45
4.1 Introduction . . . 47
4.2 Observations and data reduction . . . 49
4.3 Results . . . 50
4.3.1 Radio morphology . . . 50
4.3.2 Spectral analysis and radiative ages . . . 51
4.4 Discussion . . . 60
4.5 Conclusions . . . 62
Appendix 4.A Relic discovery in the field . . . 62
Appendix 4.B Synchrotron emission models . . . 62

5 Age mapping of the AGN relic B2 0924+30: the LOFAR perspective 65
5.1 Introduction . . . 67
5.2 Observations and data reduction . . . 67
5.3 Results . . . 70
5.3.1 Spectral analysis . . . 70
5.4 Discussion . . . 77
5.5 Conclusions . . . 78
Appendix 5.A Spectra of some field sources . . . 78
Appendix 5.B LOFAR Double-Double radio galaxy discovery . . . 78
Appendix 5.C Abell 781 . . . 79

6 A LOFAR search for AGN radio relics around young radio sources 83
6.1 Introduction . . . 85
6.2 MSSS data . . . 85
6.3 Results and conclusions . . . 88

7 LOFAR first look at the giant radio galaxies NGC 6251 and 3C 236 91
7.1 Introduction . . . 93
7.2 Data . . . 94
7.3 Results . . . 95
7.3.1 NGC 6251 . . . 95
7.3.2 3C 236 . . . 99
7.4 Discussion . . . 99
7.4.1 NGC 6251 . . . 99
7.4.2 3C 236 . . . 102
7.5 Conclusion . . . 104

8 Summary and future prospects 107
8.1 The AGN - relic connection . . . 107
8.2 Results and future work . . . 111

Appendices 115

A Radio sources in the LOFAR field centered on B2 0258+35 **117**
A.1 Motivation . . . 117
A.2 Results . . . 117
A.2.1 Source extraction . . . 118
A.2.2 Position accuracy . . . 119
A.2.3 Spectra . . . 119
A.2.4 NVSS Dropouts . . . 122
A.3 Diffuse extended sources . . . 123

B Clock/TEC fit on an interleaved LOFAR HBA observation **127**
B.1 Introduction . . . 127
B.2 Clock - TEC fitting . . . 128
B.3 Solution stability . . . 129
B.4 Conclusions and outlook . . . 132

C The ghostly outer lobes of 4C 34.47 **133**
C.1 Introduction . . . 133
C.2 Discussion . . . 133

Bibliography **137**

Resume **147**

Samenvatting **155**

Резиме 163

Acknowledgements **171**

Chapter 1

Introduction

A beginning is the time for
taking the most delicate care that
the balances are correct.

– from the "Manual of Muad'Dib" by
Princess Irulan

1.1 Extragalactic radio sources

EXTRATERRESTRIAL sources of radio emission were known since the discovery of Karl Jansky (Jansky 1933) that the center of the Galaxy emits radio waves. He made the discovery while searching for sources of cosmic interference to terrestrial radio communications. Later, Grote Reber (Reber 1944) imaged radio sources on the sky with a backyard radio telescope he had built and radio astronomy was born. It has opened a new window on the universe and has exposed to us physical processes operating on vastly different energy scales than the ones we had hitherto observed.

The first surveys of the radio sky have uncovered strong discrete sources of radiation which were identified with supernova remnants. The most famous example is the Crab nebula, the strongest radio source in the constellation of Taurus (the Bull), or as it is known to radio astronomers TauA[1]. Another one of these remnants is located in the constellation of Cassiopea and designated CasA. As radio surveys became more precise, an altogether different class of radio sources was discerned (ForA, HerA, PerA, CygA). In the mid 1950s using interferometric radio telescopes it was inferred that they are double

[1] The traditional naming convention is that one assigns capital letters starting at the beginning of the alphabet taking the brightest radio source in the constellation first and continuing towards the fainter. This applies only to the brightest sources. Standard radio surveys use the sky coordinates of a given source to construct its name

sources, symmetric regions of radio emission, usually located on opposite sides of a large elliptical galaxy (Baade & Minkowski 1954). The source in the constellation of Cygnus, CygA, represents one of the most famous examples. In the 1970s it was discovered that their twin lobes of radio emission were energized by thin jets originating from the cores of the galaxies hosting them. These galaxies were named radio galaxies, due to their brightness in the radio domain.

The energy contained in the radio emissions of these sources is very tiny when it reaches us on Earth. The flux density[2] (or specific flux) of one of the strongest ones (CygA) is around $10^{-22}\mathrm{Wm}^{-2}\mathrm{Hz}^{-1}$ measured at a frequency of 150 MHz. The SI derived unit for the flux density used in radio astronomy which is adapted to these low energy scales is the Jansky (Jy). CygA has a flux density of around 10 000 Jy at 150 MHz. However, taking into account the enormous distances to these objects and the dimensions of the radio emitting regions, the energy stored in them is enormous, as is their specific luminosity (or power density, expressed in units of WHz^{-1}) of their power source.

The nature of the ultimate power source in these galaxies has puzzled astronomers for quite some time. No physical process was known to be capable of releasing that much energy over time while being confined in a small region of space in the core of a galaxy. The tiny size of the power source region could be estimated because the source regions at the base of the jets in some of these galaxies varied on the timescale of several hours, and as a consequence the emission region was on the same spatial scale as the extent of our solar system (Burbidge et al. 1963).

At about the same time when these discoveries were being made, Lynden-Bell & Rees (1971) proposed that the energy source could be gravitational in its essence; gravitational (potential) energy of in-falling matter converted to radiation of photons over a large extent of the EM spectrum as well as relativistic particles and magnetic fields expelled in a jet far away from the host galaxy. The cause for the gravity well was a Super Massive Black Hole (SMBH), weighing several million solar masses. The phenomenon was called an Active Galactic Nucleus (AGN).

It is now known that the SMBHs assembled relatively quickly in the early universe. The accretion rates then must have been larger than what is observed in the local universe; it is believed that the SMBH accretion proceeded as galaxies evolved. The assembly process of bulges in disk galaxies proceeded in concert with the growth of the SMBHs which they hosted. This notion is based on the famous M-σ relation of BH mass vs. the velocity dispersion of the bulge (e.g., Ferrarese & Merritt 2000).

When there is available fuel supply nearby the SMBH accretes and a AGN is formed, which may interact with the Inter Stellar Medium (ISM) of the host galaxy and even regions beyond, in the Intergalactic Medium (IGM). Radiative and mechanical energy (as well as momentum) is transferred out and can affect galaxy evolution processes. AGN activity represents a relatively short phenomenon when compared to the lifetime of its host galaxy. However, AGN activity is a recurring process, which can influence the host galaxy intermittently over cosmic time.

Not all AGN are (strong) radio sources, as is evident in many Seyfert galaxies (which have very bright AGN powered nuclei, but show no or very low levels of radio emission). Whether this is an intrinsic property, and why it is the case is an open question at this time. The interplay between BH spin (relative to the accretion disk if it is present), magnetic field, and the accretion flow can possibly be a decisive factor whether a particle

[2] Power spread over a unit surface area per unit frequency

jet is launched and consequently whether the AGN generates large scale radio emission.

In this thesis, we are concerned with the radio-loud AGN, which are prodigious radio emitters. The AGN radio activity results in various radio source morphologies. This simplified picture reflects the broad outlines of our understanding of AGNs as well as their role in the processes concerning galaxy evolution. Some details are still unclear; the exact mechanisms of AGN fueling are not so clear, especially when taking into account the spatial scales of the problem. How does the gas from the ISM get to the gravitational sphere of influence of the SMBH is a mystery, even though some clues are slowly emerging (Hardcastle et al. 2007; Best & Heckman 2012; Gaspari et al. 2013). The feedback details are also problematic. How does the energy and momentum transfer proceed? To what extent are radio jets responsible for the energy transfer and what are the mechanisms of the interaction between them and the ISM? Tracers of this interaction have been found observing cold H I outflows in galaxies (Morganti et al. 2013; Gereb et al. 2014) and beyond (McNamara et al. 2000).

We also need to quantify the total energy output by AGN in the IGM over cosmic time to get a handle of the AGN energy input into the total heating energy budget influencing galaxy formation / evolution. We know that AGN radio activity is episodic (e.g., Schoenmakers et al. 2000), but the activity duty cycle is not yet tightly constrained. Knowing the AGN duty cycle becomes important in any such estimates. For example, for their sample of sources Parma et al. (2007) report an active timescale of 10^7 to 10^8 years and a switched-off timescale an order of magnitude shorter. We need better constraints on the details of the AGN duty cycle for various types of radio sources. The only observational tracer of past AGN activity is seen in the radio domain - the topic of this thesis research. We derive constraints on the AGN duty cycle by studying radio emissions created by (past) activity outbursts. In some cases, when the AGN is not active, the radio source represents an AGN radio relic; aged plasma expelled by the AGN in the corresponding accretion event or events. Most of this thesis focuses on studies of such objects.

1.2 AGNs as the engines of relic creation

Once a radio-loud AGN shuts down, the ejected plasma can be still observed, at progresively lower radio frequencies as it ages and loses energy through synchrotron radiation and expansion (Figure 1.1).

This process gives rise to radio source morphologies which are distinct w.r.t the morphologies encountered in cases of active sources (ex. jets, hotspots), and have characteristic steeply rising spectra towards lower frequencies. Classification of these radio relics is not straightforward, as there are various complications involved in the processes at hand. Below, we give an overview of the observed relics and make an inventory of their properties. We can classify the radio relic sources in two broad groups: restarted and fading. The difference between these being that in the restarted cases the AGN is active at the moment (at low levels of activity or restarted) while the fading sources show no observational evidence of an active AGN and all of the radio emission comes from the aging plasma ejected by the AGN before its shutdown. Complicating things is the fact that if we do not observe an AGN signature (radio core) that does not mean that it is not present. It can be too weak to be detected or it can be that our observations do not have sufficient resolution to resolve it. We should have this in mind when interpreting

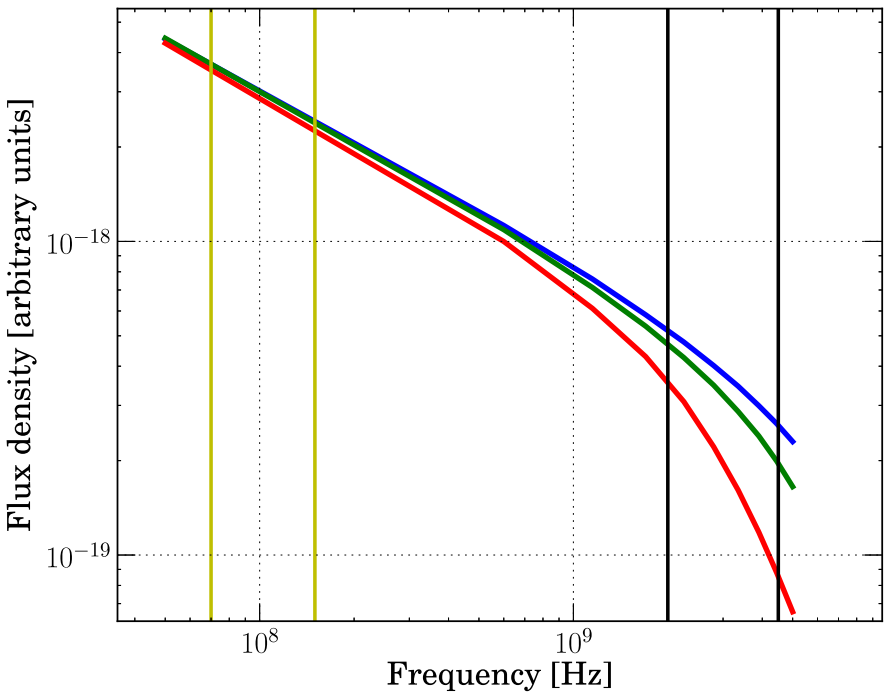

Figure 1.1: Jaffe-Perola (JP) synchrotron emission model for plasma aged 50 Myr (blue), 60 Myr (green) and 80 Myr (red) assuming an infinitesimally short duration of the AGN activity episode. The black vertical lines mark hypothetical mid and high frequency radio bands, while the yellow vertical lines mark lower frequency radio bands (the low and high frequency bands of the LOFAR telescope).

our observations.

High dynamic range radio surveys sensitive to low surface brightness diffuse radio emission are needed to discover new AGN radio relics and to constrain their properties. Due to their spectral properties, radio relics are brightest in low frequency radio maps, so ongoing and future surveys with novel instruments such as the LOw Frequency ARray (discussed below) offer unique contribution towards these goals.

We should also keep in mind that processes other than AGN activity can produce (steep spectrum) radio sources, for example radio relics created by merging galaxy clusters as well as radio halos connected to clusters of galaxies. In these cases, merger shocks can (re)accelerate relativistic electrons, or amplify magnetic fields and thus (re)generate radio emission. High resolution LOFAR observations are crucial to distinguish between radio sources of different origin.

1.2.1 AGN radio relics in detail

The radio relic emission from radio-loud AGN represents the best observable to trace recurrent activity. Morphology and spectral index analysis are the main tools to assess the duty cycle of the recurrent activity. Already by looking at the variety of sources found, it is clear that the astrophysics of a start-stop-restart episode are far from being clear. The following aspects play an important role.

Origins and evolution

During their active stage, which may last up to 10^8 years, the strong radio sources associated with elliptical galaxies are supplied with energy from the AGN via plasma beams or jets. Owing to the continuous accumulation of new relativistic particles, the total spectra of active radio sources are usually well approximated by a power law over a wide range of frequencies. The injection of energy also sustains the growth of these radio sources that is governed by the balance between the internal plasma pressure in the radio lobes and the pressure in the hot X-ray emitting gas in the medium into which they must expand (Scheuer 1974).

At some point however, the AGN activity stops or falls to such a low level that the plasma outflow can no longer be sustained, the radio emitting lobes are no longer supplied with relativistic particles and the radio source is expected to undergo a period of fading before it disappears completely. In the fading phase, the radio core, well-defined jets, and compact hot- spots will disappear because they are the structures produced by more or less ongoing activity. On the other hand, the radio lobes may still remain detectable for a long time if they are subject only to radiative losses of the relativistic electrons (see the case of B2 0924+30 (Cordey 1987; Jamrozy et al. 2004) for a discussion of a rare case of an FRII (Fanaroff & Riley 1974) fader, also analyzed in Chapter 5 of this thesis).

A possible explanation for the observational scarcity of fading radio galaxies may be their relatively fast spectral evolution during the fading phase of their life cycle. Radiative synchrotron losses and the inverse Compton (IC) scattering off of the cosmic microwave background (CMB) photons preferentially deplete the high-energy electrons. The fading lobes are expected to have very steep ($\alpha < -1.5$)[3] convex radio spectra characteristic of an electron population that has radiated away much of its original energy (Komissarov & Gubanov 1994). In the absence of fresh particle injection, the high-frequency radio spectrum develops an exponential cutoff. At this point, the adiabatic expansion of the radio lobes shifts this spectral break to lower frequencies and the source quickly disappears. On the other hand, if the source expansion is somehow reduced, or even stopped, the fossil radio lobes may still be detected for a period of time, at least at low frequency.

Fueling mechanisms

An AGN needs to accrete gas in order to stay active. One of the biggest unknowns of the AGN fueling mechanism is how to get the gas down to the "last parsec" scale where the gravitational influence of the SMBH starts to be dominant over the general gravitational potential of its host galaxy. It is clear that whatever the mechanism to do this is, it has to involve loss of (a significant amount of) angular momentum. Major mergers were

[3] $S \propto \nu^{\alpha}$ is the spectral index notation convention accepted throughout this thesis

thought to be the main way to do it, but it turns out that the evidence to support this is scant at best. Optical major merger morphology studies find that there is no difference between post major merger remnants which host an active AGN and those that do not (Cisternas et al. 2013).

Fueling by stellar winds is another mechanism of interest (Ciotti et al. 2010). This mechanism gains importance when we realize that the typical amount of accreting gas for an active AGN is not that large - about 0.1 $M_{\odot}yr^{-1}$. Metals have been discovered in gas outflows driven by AGN (Veilleux et al. 2014), but the exact mechanism of transporting the gas close to the SMBH is again an issue.

This problem has been given significant attention recently, and encouraging results (Gaspari et al. 2013) suggest that we can at least see the outlines of an answer. Their idea is that the gas of the ISM generates thermal instabilities through chaotic interactions and cools; the cooled gas decouples from the hot phase and "rains" onto the SMBH. The AGN feedback interrupts this process and the accretion stops, turning off the AGN. We see that this scheme leads to a natural explanation of the AGN duty cycle. However, this fueling scheme may not work in gas-poor galaxies.

Cooling of hot gas from the galactic halo is an alternative explanation. Marasco et al. (2012) propose that a concentrated starburst region (or supernova explosions) in the host galaxy drives hot gas in its halo which cools down, subsequently acting as a seed and entraining more gas from the halo which "rains" onto the galaxy. The problem with this proposition is that the timescale of parcels of gas hitting the center of the host galaxy may not be enough to explain the AGN duty cycle. Also, the fueling has to be sustained on timescales of at least 10^7 - 10^8 years.

1.3 AGN radio relic taxonomy

The number of known AGN radio relics is very small when compared to the observed population of radio sources related to AGN activity. This fact becomes even more apparent for some sub-types of relics. In Table 1.1 we give an overview of AGN radio relics corresponding to the properties given below.

1.3.1 Relics associated with restarted AGN

A variety of morphologies observed in radio sources suggest that their AGN has gone through multiple phases of radio-loud activity. The type of resulting morphology likely depends on the power of the source, the duty-cycle of the activity, the cause of the interruption of the activity and the surrounding environment properties. A common characteristic is the presence of a central radio source that is currently active.

Radio relics around young radio sources

Compact Steep Spectrum / Gigahertz Steep Spectrum (CSS/GPS) sources are thought to be young radio sources based on their linear dimensions combined with their spectral properties. Lifetimes in the range of 10^5 - 10^6 years or less have been inferred from spectral index studies and kinematics/advance of the hotspots (ex. Conway 2002). The turnover frequency in their spectra correlates with their relatively young age - see Fanti (2009) for one of the latest (short) review on CSS/GPS sources.

It has been known for a while that far too many compact radio sources are observed compared to the number of large radio sources (see e.g. O'Dea & Baum 1997). Reasons for this could be selection effects due to the boosting of their radio emission when confined by a dense medium (Morganti et al. 2011). However, other effects are likely to play a role as well, such as:

- The same mechanism that makes the BH activity intermittent (e.g. starvation).
- Mechanisms disrupting the jet flow like radiation pressure instability in the accretion disk (Czerny et al. 2009) or even mergers (Saxton et al. 2001) or
- Jets growing in length beyond their scale length and developing a re-confinement shock (Kaiser 2009).

Thus, we likely have a situation in which some radio sources may switch off soon after the onset and produce very small-scale radio relics (Kaiser 2009; Kunert-Bajraszewska et al. 2006, 2010a). The size of these relics can reach 10's of kpc and they are coexistent with the restarted CSS/GPS source.

Alternatively, we can observe the previous phase of AGN activity which has generated radio lobes out to a larger distance (few 100's kpc, as for example in the case of B2 0258+35, studied in detail in Chapter 2). The radio emission of the compact source can be connected to the relic emission or not. Re-supply of the relic might be happening, but it may be undetectable. The radio spectrum of the relic is steep ($-2 < \alpha < -1$). We can select these sources using targeted observations, or by picking out steep spectrum sources from catalog comparison studies at different observing frequencies (see Table 1.1 for examples).

Radio galaxies with restarted compact cores

These sources have the large scale appearance of radio galaxies (RGs), having jets and active radio lobes (of both FRI and FRII type), and a prominent core which shows substructure reminiscent of a CSS source. Representative of the former is 4C 35.06 (discussed in Chapter 2 of this thesis), while we can take 3C 236 as the FRII example of this class (it is also a giant radio galaxy). The extended radio morphology of these galaxies may show characteristics of aging (no jets, no hotspots), or in some cases, the large scale radio lobes may still be replenished through jets expelled by the AGN before the shutdown. The AGN has restarted once more and produced the compact source we observe at the present epoch.

Radio galaxies with double-double morphology

The so called "double-double" radio galaxies (DDRGs) are an example of radio sources whose morphology suggests coexistence of an earlier radio activity episode with a current re-start of AGN activity. These are usually of the FR II type, relatively large in extent (100 - 3000 kpc), but with an additional pair(s) of radio lobes at a greater distance from the host galaxy indicating an earlier phase of AGN activity. Their morphology is symmetric, and jets(s) or a core may or may not be visible. Their AGN could have turned off, or had an interruption (modulation) of activity (lasting for a few 10^7 years). Depending

on the duration of this "off" episode, the outer lobes can be still replenished by jet material (visible or not) which is still traveling through the IGM after the AGN shutdown and before the restart (or the increase in its activity). The observed radio spectral index is usually indicative of a currently active source ($-1 < \alpha < -0.8$), unless there is no replenishing (outer lobes) in which case the spectral index is steeper. Eventually the outer lobes will disappear if not replenished.

They should be at least as common as radio-loud sources are throughout the universe, but we can detect them only before the outer lobes have completely disappeared. We can detect the inner lobes morphologically as normal radio-loud galaxies, or observe at low frequencies for signatures of the outer lobes (to do this we need imaging with high dynamic range). Examples are listed in Table 1.1.

Relics associated with radio galaxies

Morphologically equivalent to RGs (with or without core or visible jets), these objects also show signs of relic emission alongside their radio lobes. In some cases the relic regions are too well delineated in terms of the spectral index properties to be explained as being backflows from the shock regions associated with the hotspots. It is possible that these objects represent the final stage in the rejuvenation process of DDRGs, as the inner lobes overtake and fill in the older outer lobes. In this scenario, the older lobe remnants are the relic regions we observe, especially if there is a slight misalignment between the subsequent episodes of activity.

1.3.2 Relics of switched off AGN - faders

These are sources in which the extended radio emission is not replenished and show no evidence of a core, jets or active hotspots. The radio lobes are aging and have very steep spectra ($\alpha \sim -2$). There might be some slight core activity, but most of the flux is coming from the extended radio lobes. Their sizes can vary from radio galaxy-like down to CSS scale. Detecting them is easier at low frequencies. The best known example of a fader is B2 0924+30 (mentioned previously) which is also the only known fader among radio sources located outside of a galaxy cluster environment. Their relative scarcity may point to the fact that the fading timescale of AGN relics is short compared to the duration of the active phase.

Table 1.1: Taxonomy of known AGN radio relics.

ID	α_{J2000} [h m s]	δ_{J2000} [d m s]	z	S_{1400} [Jy]	Ref.
Restarted AGN					
Relics associated with CSS and GPS sources					
B0108+388	01 11 37.3	39 06 28	0.669	0.4	(1)
B0941-080	09 43 36.9	-08 19 31	0.228	2.7	(1)
B2 0258+35	03 01 42.4	35 12 21	0.016	1.8	Chapter 2
Radio galaxies with restarted (compact) cores					
3C 317	15 16 44.5	07 01 18	0.034	1.8	(5)
4C 29.30	08 40 02.3	29 49 03	0.065	0.7	(7)
J1247+6723	12 47 30	67 23 16	0.017	0.26	(9)
3C 315	15 13 40.1	26 07 31	0.108	21	(10)

Table 1.1: Continued

ID	α_{J2000} [h m s]	δ_{J2000} [d m s]	z	S_{1400} [Jy]	Ref.
4C 35.06	03 01 51.5	35 50 30	0.047	0.6	Chapter 3
3C 236	10 06 01.7	34 54 10	0.100	3.2	(17)
3C 338	16 28 38.5	39 33 06	0.03	3.7	(18)
		DDRGs			
B0925+42	09 29 15.5	41 47 55.7	0.365	0.1	(3)
B1240+38	12 42 33.9	38 36 52.1	0.3	0.02	(3)
B1450+33	14 53 02.5	33 08 10.5	0.249	0.4	(3)
B1834+62	18 35 1 0.5	62 04 01.5	0.519	0.6	(3)
3C 219	09 21 08.6	45 38 57	0.174	8	(3)
3C 455	22 55 03.9	13 13 34	0.543	5.2	(3)
4C 26.35	11 58 20.1	26 21 12	0.112	0.96	(3)
B2 0039+32	00 41 46.6	32 25 10	0.45	0.9	(4)
4C 02.27	09 35 18.2	02 04 16	0.649	0.9	(11)
B0818+214	08 21 07.5	21 17 03	-	0.19	(14)
J0927+29	09 27 43.8	29 32 32	-	-	Chapter 5
3C 293	13 52 17.8	31 26 46	0.045	4.85	(6)
		Relics associated with radio galaxies			
3C 388	18 44 02.4	45 33 30	0.09	5.8	(8)
4C 12.03	00 09 52.6	12 44 05	0.156	2.01	(11)
3C 16	00 37 44.6	13 19 55	0.405	1.8 (12)	
4C 23.56	21 07 14.8	23 31 45	2.483	0.68	(13)
		Faders			
J0128-2538	01 28 34.5	-25 38 22.9	-	0.005	(2)
J0128-2539	01 28 24.7	-25 39 11.1	0.207	0.03	(2)
J0128-2540	01 28 31.1	-25 40 31.8	-	0.00	(2)
J0439+5304	04 39 53.9	53 04 12	-	0.008	(2)
J1114+1519	11 14 13.2	15 19 44.1	-	0.002	(2)
J1133+2325	11 33 45	23 25 14	-	0.02	(2)
J1152+3732	11 52 36.1	37 32 46.6	0.229	0.02	(2)
J2216-1725	22 16 58	-17 25 08	0.136	0.01	(2)
J2313+3842	23 13 46.8	38 42 16.1	-	0.03	(2)
J2345+2157	23 45 15.4	21 57 39.8	0.15	0.01	(2)
J1431.8+1331	14 31 50.1	13 32 05	0.16	0.02	Chapter 4
B2 0924+30	09 27 23.5	29 55 30	0.025	0.4	Chapter 5
WNB 0951+60	09 55 29.9	60 23 17	0.199	-	(15)
WNB 1127+49	11 30 18.3	49 11 16	0.260	-	(15)
B2 1150+37	11 52 36.4	37 32 44	0.229	0.01	(15)
WNB 2317+42	23 19 47.2	42 51 10	0.017	0.04	(15)
WNB 1734+6407	17 35 04.6	64 06 07.7	0.141	-	(16)
WNB 1829+6911	18 29 05.6	69 14 06.0	0.204	-	(16)
WNB 1851+5707a	18 52 08.5	57 11 42.3	0.107	-	(16)
WNB 1851+5707b	18 52 09.7	57 11 56.6	0.107	-	(16)
B2 0120+33	01 23 39.9	33 15 22.1	0.016	-	(16)
B2 1610+29	16 12 35.5	29 29 05.3	0.032	-	(16)

Table 1.1: Continued

ID	α_{J2000} [h m s]	δ_{J2000} [d m s]	z	S_{1400} [Jy]	Ref.
J0035.1-6748	00 35 07.9	-67 48 40.7	1.82	0.001	(19)
J0102.1-6552	01 02 12.1	-65 52 19.6	1.1	0.01	(19)

References: (1) Stanghellini et al. (2005) (2) Dwarakanath & Kale (2009) (3) Schoenmakers et al. (2000) (4) Konar et al. (2013) (5) Venturi et al. (2004) (6) Joshi et al. (2011) (7) Chandola et al. (2010) (8) Roettiger et al. (1994) (9) Marecki et al. (2003) (10) Cheung et al. (2009) (11) Jamrozy et al. (2009) (12) Leahy & Perley (1991) (13) Blundell & Fabian (2011) (14) Marecki & Szablewski (2009) (15) Parma et al. (2007) (16) Murgia et al. (2011) (17) Barthel et al. (1985) (18) Ge & Owen (1994) (19) Saripalli et al. (2012)

1.4 LOFAR

The LOw Frequency ARray (LOFAR) telescope (van Haarlem et al. 2013) is a radio telescope which uses the aperture synthesis technique to image the radio sky. It has a novel design in that it does not use classical parabolic dishes or receiving elements, but simple dipoles. The dipoles are concentrated in groups, called stations all connected to the central correlator in Groningen, the Netherlands.

LOFAR covers two frequency bands in the low radio frequencies: 15 - 80 MHz (LBA) and 110 - 240 MHz (HBA). The two frequency bands are covered with different dipole antennas. The Low band antennas (LBA) are positioned in the station in a circular area roughly 90 meters across. The high band antennas (HBA) are arranged in tiles.

LOFAR has six stations concentrated in an area with diameter of 300 meters (the so called super terp) located near the village of Exloo in the Netherlands, and additional stations extend further out. The stations in the area around the super terp make up the core of LOFAR. A core station configuration is shown in Figure 1.3. At intermediate distances from the core (up to 80 km) the station configuration changes to a remote station layout which has a single HBA dipole field. Outside of the Netherlands, the station layout changes again to the international station layout. The international stations are built in several European countries (UK, Germany, France, Sweden, Poland) which participate in the LOFAR effort.

LOFAR is a software telecsope. It uses digital beam forming to observe and track the sky (Figure 1.4). The LOFAR beam is variable, unlike the beam of a parabolic reflector and has to be treated as such in the calibration procedures. There is a possibility of forming multiple beams to track several objects simultaneously, as well as observing in a "fly's eye" mode with multiple beamlets covering the station FoV to search for pulsars. Different setups are possible trading the number of beams for observing bandwidth.

The instrument has very large fractional bandwidth. For example, in the HBA band, it has a bandwidth of 64 MHz for an observing frequency of 150 MHz. The observing band is subdivided into sub-bands. Each covers 200 kHz and is composed of 64 frequency channels, providing very fine frequency resolution needed for pulsar and transient studies as well as SETI.

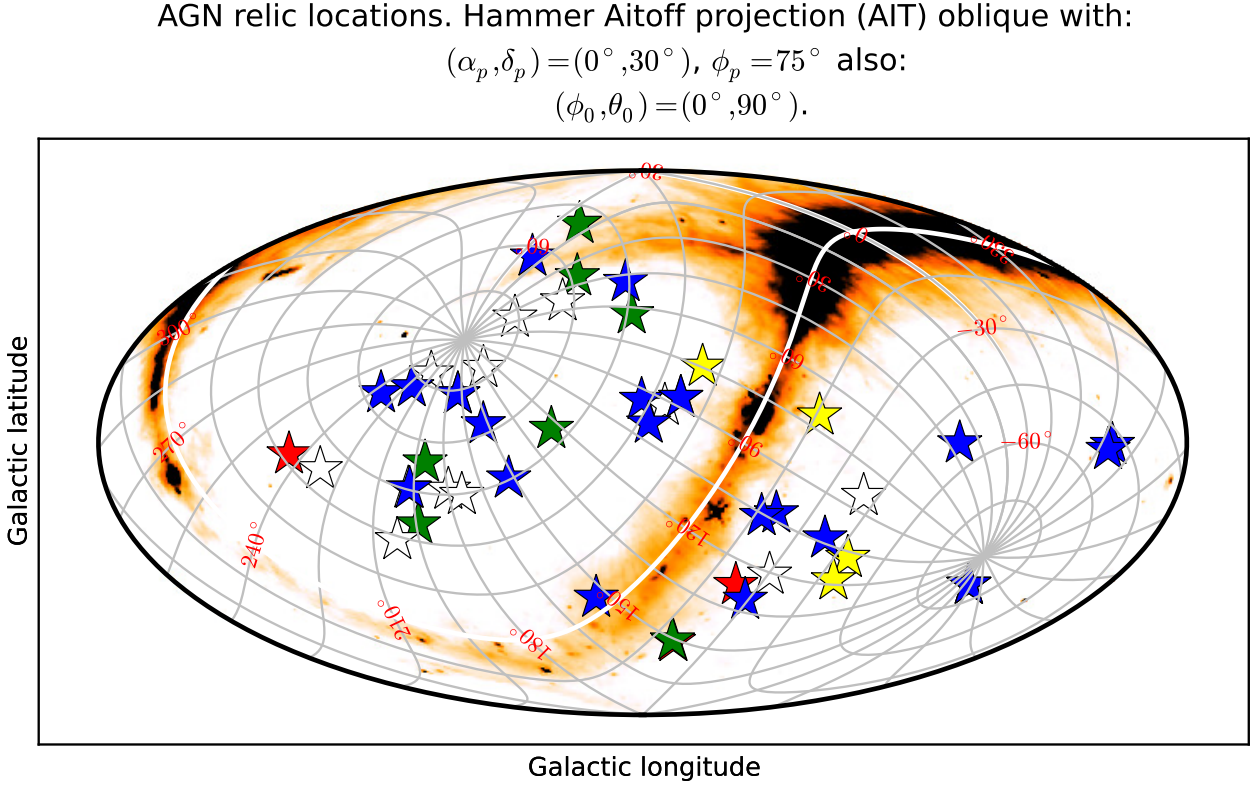

Figure 1.2: Distribution across the sky for some of the relics. Marker colors correspond to groups in Table 1.1: compacts - red, RGs - yellow, RGs with compact cores - green, DDRGs - white and faders - blue.

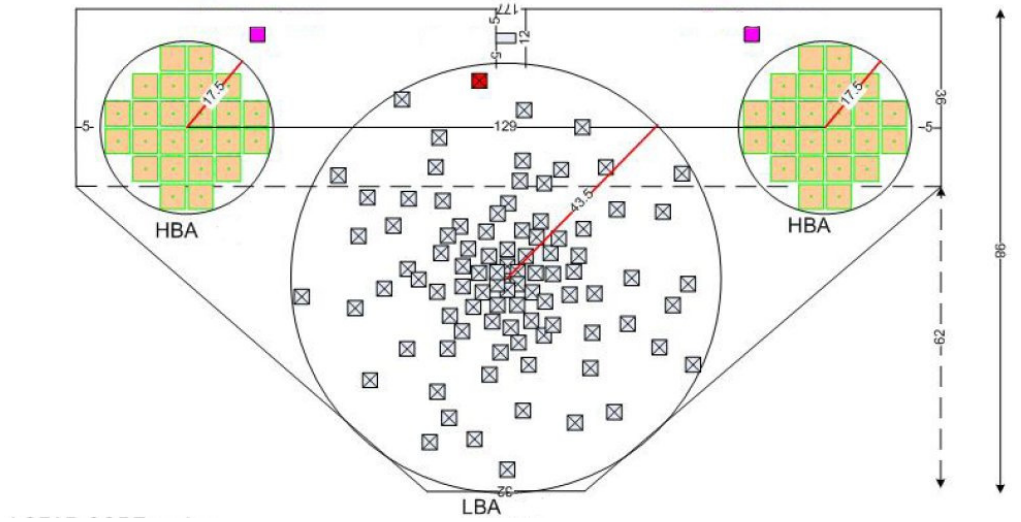

Figure 1.3: LOFAR core station setup, including the LBA dipole field (center) and the two HBA dipole tile groups.

The dipoles of the stations in the very center of the array (in the so-called super-terp) are used for ultra high energy (UHE) cosmic ray studies (triggered by particle detectors dispersed between the stations).

Depending on the science case, different observing configurations can be used. The longest Dutch baselines have lengths of around 80 km, which enables LOFAR to reach the imaging resolution of the FIRST[4] radio survey of 5″.

The international baselines form a mini VLBI network at low frequencies, making LOFAR the most versatile instrument on the planet in its frequency range and a testbed precursor for the Square Kilometre Array (SKA) telescope.

Novel techniques are being used to calibrate the observations and correct for the beam effects as well as mitigate the ionospheric phase distortions. This includes careful radio frequency interference (RFI) excision, solving the full measurement equation during the calibration of the observations, and imaging the full bandwidth over a large FoV. The LOFAR LBA station beam is around 8 degrees wide at Full Width Half Maximum (FWHM), and the HBA band station beam has a FWHM of 5 degrees. This makes LOFAR a very efficient survey telescope, but it also means that during the imaging one can no longer approximate the image as being flat; one has to account for the curvature of the celestial coordinate system over the large FoV. LOFAR uses its own custom developed imager to do a 3D inversion from UVW visibility space to the image plane while deconvolving and taking into account the variable station beams.

[4] FIRST is the Faint Images of the Radio Sky at Twenty centimeters radio survey performed by the VLA.

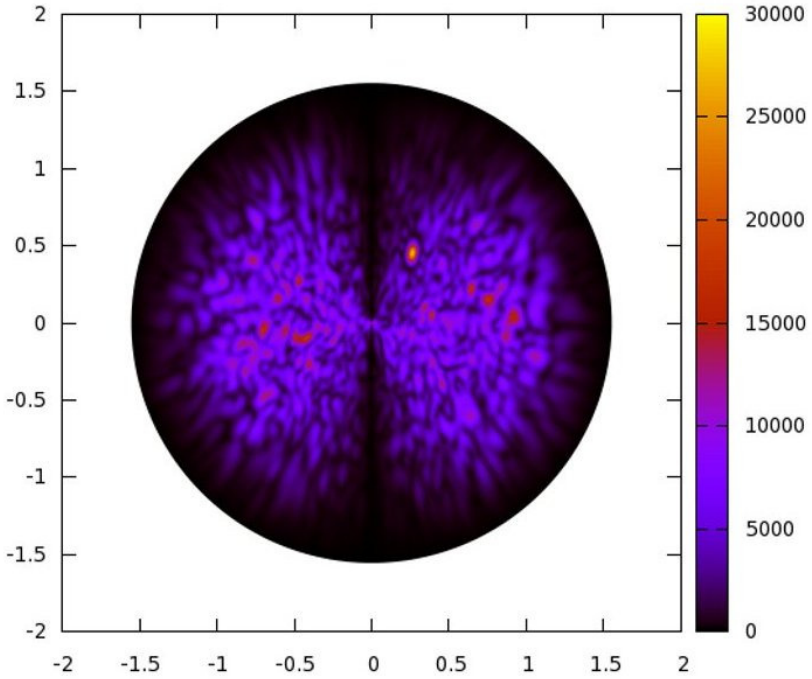

Figure 1.4: Plot of one LOFAR core station LBA beam pattern analytic model (Yatawatta 2007). Elevation is measured in the radial direction with the zenith being at the center of the plot. Zero azimuth is at 15:00 hrs. position and increases counter-clockwise. The map color indicates the norm of the Jones E matrix. This caption was produced for an observing frequency of 80 MHz with the beam pointing in the direction of 60 degrees elevation and 60 degrees azimuth.

1.5 This thesis

In this thesis, we are tracing the recurrent activity of several restarted radio AGN. The goal is to put constraints on the duty cycle of AGN activity and to extend our knowledge of the sources in our study down to the lowest radio frequencies, by using LOFAR. LOFAR provides us with the advantage of having sufficient spatial resolution at the lowest frequencies.

In **Chapter 2** we study the CSS source B2 0258+35, elaborating on the discovery of a very faint surface brightness radio relic around it. Using previous studies, we place limits on the age of the relic emission and estimate the AGN accretion rate.

We continue on studying the duty cycle of AGN in a radio source located in the center of the galaxy cluster Abell 407. Using LOFAR, in **Chapter 3** we confirm the previous tentative detection of an AGN radio relic located around 200 kpc away from the AGN which has a morphology indicative of a restarted source. We study in detail the spectral index properties of different spatial scales of 4C 35.06.

Chapter 4 and **Chapter 5** deal with a study of two fading radio sources, J1431.8+1331 and B2 0924+30. The former has a curious radio morphology which shows a fading AGN activity with a possible plasma bubble being expelled from the host galaxy in which a reacceleration episode might have happened sometime in the past. B2 0924+30 is an interesting example of the only FR-II fader known so far. We have imaged the sources using LOFAR and fit aging models to our data as well as literature data to extract source ages of resolved source regions. We show that the shutdown of the AGN has happened around 10^8years ago and trace the relic hotspots and core in our age maps. We report the discovery of a small scale DDRG in the LOFAR FoV of B2 0924+30.

In **Chapter 6** we perform a low frequency search using LOFAR of relic radio emission around CSS and GPS sources. We use data from the initial release of the Multifrequency Snapshot Sky Survey (MSSS).

Chapter 7 details the study of two giant radio galaxies: 3C 236 and NGC 6251. We map the lowest energy particles at around 140 MHz and we use spectral index studies to shed light on the detailed particle population distribution in the radio lobes of our targets.

Chapter 2

Recurrent radio emission and gas supply: the radio galaxy B2 0258+35

A process cannot be understood by stopping it.

– from the first Mentat law

Abstract

Outlined is the discovery of a very faint, diffuse, low surface-brightness (0.5 mJy beam^{-1}, 1.4 mJy arcmin^{-2} on average) structure around the radio source B2 0258+35 hosted by an HI-rich early-type galaxy (NGC 1167). Because B2 0258+35 is a young compact steep spectrum (CSS) source, the newly discovered structure could represent a remnant from an earlier stage of activity of an active galactic nucleus (AGN). We explain in detail all possibilities for triggering the radio activity in B2 0258+35 regarding gas accretion in a recurrent AGN activity framework. NGC 1167 hosts a very regular, extended and massive H I disk that has been studied in great detail. It has regular kinematics on large scales, which, together with stellar population studies of NGC 1167, exclude the possibility of a recent merger as the trigger for the current AGN activity that is responsible for the CSS source. Previous studies of the H I closer to the core seem to preclude the assumption of a circum-nuclear disk of H I as the source of the accreting gas. We consider the cooling of gas from the hot X-ray halo as a possible alternative option for the fueling of the AGN, as suggested for other sources of similar radio power as B2 0258+35. This would provide a more likely explanation for the recurrent activity. Furthermore, if the previously made suggestion in the literature that the inner CSS may not be able to grow to large scales is correct, this implies that different cycles of activity may have different characteristics (e.g. radio power of the emission). Estimates are given for the age of the faint diffuse emission as well as for the current accretion rate, which agree well with literature values. If our assumptions about the accretion mechanism are correct, similar large-scale, relic-like structures should be more commonly found around early-type galaxies, which will hopefully be confirmed by the next generation of sensitive, low-frequency radio surveys.

A. Shulevski, R. Morganti, T. Oosterloo and C. Struve
Astronomy & Astrophysics, **545**. A91, 2012

2.1 Introduction

Active Galactic Nuclei (AGN) have been recognized in recent years to have a profound influence on their surrounding interstellar medium (ISM) and, in consequence, also on the evolution of the host galaxy (see Kauffmann & Haehnelt 2000; Matteo et al. 2005; Bower et al. 2006). Radio-loud AGN can exert this influence not only through their collimated radio jets but also through the cocoon of shocked medium around them (Wagner & Bicknell 2011; Wagner et al. 2012). Therefore, they can influence a large volume in (and outside) the host galaxy. Although this type of AGN is relatively rare and shortlived, the radio phase can be recurrent during the life of the galaxy (see Saikia & Jamrozy 2009; Randall et al. 2011; Best et al. 2005, for some examples). This may substantially increase the impact that radio-loud AGN have on the ISM and their role in galaxy evolution. However, the life-cycle of a radio source still poses many open questions (e.g. if radio activity is occurring in every galaxy and what are the details of the "duty cycle" of the recurrent activity), which limit our understanding of the impact of this type of nuclear activity.

What do we know about the life-cycle of a radio source? The first phase of a radio source has been identified with compact sources with a steep or peaked spectrum (so called compact steep spectrum (CSS) and gigahertz peaked spectrum (GPS) sources), see Fanti et al. (1990), O'Dea (1998) and Fanti (2009) for a recent overview. These sources already have the morphology of grown-up sources but their size is comparable to galactic scales, i.e. the inner few kpc of the host galaxy. Most of them are expected to grow to large radio galaxies (Fanti 2009) although some may actually never reach this phase, either because the fueling of the AGN "engine" stops or because of a hostile ISM (Kunert-Bajraszewska et al. 2006). See also de Vries et al. (2009) and de Vries (2009), Chapter 6.

The typical lifetime of a radio source ranges between 10^7 and 10^8 yrs (Parma et al. 1999, 2007) and after that the nucleus switches off. This may result in the formation of a relic source that will slowly fade away. The relic structures (with no nuclear activity present) are very rare, with only a handful known (Cordey 1987; Parma et al. 2007). The situation seems to be more common where the radio source is intermittently active; in that case one may find fossil radio plasma left over from an earlier phase of activity, while newly restarted core and radio jets are visible as well. Evidence for a re-start in the activity of radio sources after a period of shut-down of the central engine, or of rejuvenated sources has been found in several cases (Schoenmakers et al. 1999; Murgia et al. 2011; Stanghellini et al. 2005; Saikia & Jamrozy 2009) although proper statistics of the occurrence and characteristics are not available.

The off-phase in most cases appears to be shorter than or at most comparable with the active phase (Parma et al. 2007). However, statistical studies using luminosity functions (Shabala et al. 2008; Best et al. 2005) have shown that the life-cycle of radio-loud AGN depends on the radio power, with powerful (i.e. Fanaroff-Riley type 2 or FRII, Fanaroff & Riley 1974) radio sources becoming active only every one-to-few Gyr, while low-power radio sources (Fanaroff-Riley type 1, FRI) would need to spend more than a quarter of their life in an active phase (Best et al. 2005). This would suggest that signs of past radio-loud activity could be more common in the latter sources. Unfortunately, no systematic search for such signatures has been possible so far and studies of single objects are relatively sparse and limited (Stanghellini et al. 2005; Tremblay et al. 2010). Whether

radio emission from a previous phase of activity is still observable also depends on the external conditions, with the hot X-ray environment particularly suitable for keeping the relic confined and limiting the adiabatic losses (Murgia et al. 2011).

For understanding the origin of the recurrent nuclear activity, it is also important to have comprehensive information about the assembly and evolution of the host galaxy. The commonly considered way to (re-)trigger an AGN is to provide a fresh supply of gas. The presence of gas is often observed in early-type galaxies, typical hosts of radio-loud AGN. Although the presence of this gas does not appear to have a clear connection with the presence of an active nucleus (see Oosterloo et al. 2010), it is interesting to note that the occurence of H I in restarted sources seems to be higher than in other radio sources (Chandola et al. 2010; Saikia & Jamrozy 2009). This could suggest a possible link between the presence or injection of gas and the activity.

Thus, identifying cases of recurrent radio activity and understanding their time scale (as well as the gas content and kinematics close to the AGN) is challenging, but extremely important to fully probe the impact of radio-loud AGN on the host galaxy and their importance for feedback effects. The study of objects for which information at different wavebands is available allows a better understanding of the origin of the activity and to connect the history of the host galaxy with the history of the nuclear activity. This combination has triggered our interest in the object that is the subject of this paper.

We present the discovery of diffuse, low-brightness extended radio emission around the young CSS radio source B2 0258+35. A first hint of this structure was detected in a preliminary continuum image obtained by Struve (2010). This has inspired a more detailed look at the data that we present now in this paper.

B2 0258+35 is hosted by the field early-type galaxy NGC 1167 ($z = 0.0165$)[1].

The central radio source has been studied by Giroletti et al. (2005) and was classified as a CSS source. These authors derived an age for this structure of $9 \cdot 10^5$ yr. The CSS source has a radio luminosity of $L_{408\,\mathrm{MHz}} = 10^{24.37}$ WHz^{-1}. The radio structure of the CSS source has no hot spots (although the structure appears to be the result of a strong interaction with the ISM), so if this is indeed a young radio galaxy, it might evolve into an FR I. This is consistent with the measured radio power. However, Giroletti et al. (2005) have argued that this source might represent an example of a CSS source that will not grow to become a kilo-parsec-scale radio galaxy.

What makes B2 0258+35 notable is the *large, massive disk of H I* that has been studied in detail and can provide additional insight into the formation history of the host galaxy. The disk (with $\mathrm{M}_{HI} = 1.5 \cdot 10^{10}$ $\mathrm{M}_\odot$ and diameter of 160 kpc, see Fig.1 right, Noordermeer, van der Hulst, Sancisi, Swaters, & van Albada 2005 and Struve, Oosterloo, Sancisi, Morganti, & Emonts 2010a) shows *extremely regular kinematics* within the inner $r < 65$ kpc and signs of interaction with several satellite galaxies in the outer regions where the gas appears to be slightly disturbed. The detailed work of Struve et al. (2010a) shows that the disk has grown by accretion of cold gas from satellite galaxies. Furthermore, its regularity implies that the host galaxy has not suffered a major merger in the center in at least the past 1 Gyr. H I has been detected also in absorption - with much higher resolution observations - against the central CSS source. The kinematics of this gas have been studied in Struve (2010), Chapter 7, and appear to be quite regular, consistent with the velocities of the large-scale disc. However, a blueshifted, possibly

[1] The adopted cosmology in this work is: $H_0 = 73$ km s^{-1}Mpc^{-1} , $\Omega_{matter} = 0.27$, $\Omega_{vacuum} = 0.73$. At the redshift of B2 0258+35, $1'' = 0.34$ kpc

outflowing component has being detected both in H I and in CO. Thus, thanks to the H I , we have a clear view of the recent assembly history of the host galaxy. In this paper we explore how this relates (or not) to the radio-loud phase(s) of activity.

The paper is structured in the following way. In Section 2.2 we describe the observations and the data reduction procedure. Section 2.3 presents the results and discusses the origin of the newly found extended radio structure as a possible signature of recurrent activity in this galaxy. In Section 2.4 we combine this with information about the gas supply by using results from (recent) H I studies. Section 2.5 presents some additional implications and discusses future work prospects.

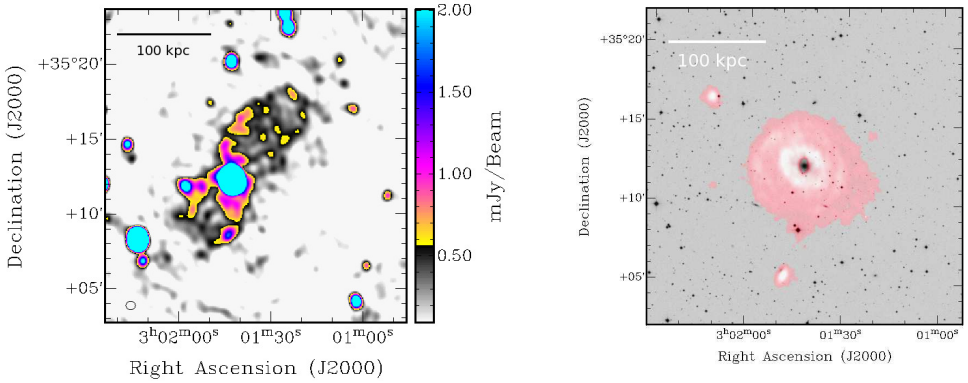

Figure 2.1: Left: continuum image of the diffuse emission around B2 0258+35. The synthesized beam is indicated with the ellipse at bottom left. The intensity ranges from 100 μJy (1σ) to 2 mJy (20σ). Right: 21-cm H I total intensity image taken from Struve (2010) superposed onto a DSS2 optical image. Scale as indicated.

2.2 Observations and data reduction

B2 0258+35 was observed with the Westerbork Synthesis Radio Telescope (WSRT) for 12 x 12h. The data were originally taken for line (H I) observations (analysis and discussion of the results are presented in Struve, Oosterloo, Sancisi, Morganti, & Emonts 2010a; see that paper for more details). Because of this, the observations were centered around the frequency of 1.39 GHz (H I in the rest frame of the source) and used a bandwidth of 20 MHz. The data reduction was performed using the Miriad package (Sault et al. 1995) as described in Struve et al. (2010a). 3C 48 and 3C 147 were used as flux and band-pass calibrators, respectively.

We have extracted from these data the continuum with the line-free channels in the band. The continuum subtraction was performed on the visibilities using the task *uvlin* with a second-order polynomial. Data from eleven of these observing runs were used to

produce continuum maps. One dataset was not included in the final map because of low quality of the data owing to technical problems in that observation.

Each observation was separately imaged and several self-calibration runs were performed (solving, at the beginning, for phase only and for amplitude and phase at the end of the procedure) before obtaining the final image. The images were obtained using uniform weighting, but were subsequently convolved with a Gaussian of $30''$ FWHM to enhance the extended emission. These images were then combined to produce a final image where an extended low surface brightness emission appears very clearly (see Fig. 2.1, left panel). The r.m.s. noise of the final image is 100 μJy beam^{-1}, with a beam size of $39'' \times 33''$ at a position angle of 2°.

2.3 Low surface-brightness, extended structure: a radio relic?

The final radio continuum image is shown in Figure 2.1 in the left panel. In addition to the central (unresolved at our spatial resolution) CSS source, we detect an extended, low surface brightness structure. The average surface brightness is 0.5 mJy beam^{-1} (measured in a region encompassing the northern lobe). This translates into about 1.4 mJy arcmin^{-2} which is on the faint end compared to the source sample published by Saripalli et al. (2012). Accordingly, even after the spatial smoothing, the structure remains very faint, only a few sigma above the noise. The high contrast in the flux levels between the central CSS source and the extended structure additionally complicates imaging this structure. The extended radio emission has a total projected linear size of 240 kpc and a distinctive double-lobed appearance, with relatively bright edges in some locations. The central CSS source has a total flux of 1.8 Jy ($L_{1.4\mathrm{GHz}} = 2.1 \cdot 10^{23}$ WHz^{-1}), while the peak of the extended structure is ~ 2.4 mJy. It has a total flux of 119 mJy (integrated over a region determined by visual inspection of the image encompassing the entire diffuse emission region). This gives a radio luminosity of $L_{1.4\mathrm{GHz}} = 5.5 \cdot 10^{22}$ WHz^{-1} for the diffuse emission.

Because of the extremely low surface brightness and the lack of collimated and/or compact features (such as jets and hot spots), the newly found, extended radio structure can be explained as lobes left over from a previous cycle of nuclear activity. The spatial resolution of our image does not allow us to verify whether a connection exists between the inner CSS source and the extended, low surface brightness lobes. Neither can we derive any value for the spectral index: if some injection of "fresh" electrons is still ongoing, we would not expect these extended structures to have an extremely steep spectral index. Therefore, the question of whether the extended, low surface brightness structure in B2 0258+35 is a relic structure or if the lobes still receive some feeble injection of fresh electrons cannot be answered with the present observations. This will be possible with planned follow-up low-frequency observations.

However, we note that the extended structure shows relatively bright edges, in particular in the northern lobe. This could be the result of the interaction of the radio plasma with the ISM/IGM and may suggest in-situ acceleration of the electrons. Alternatively, the structure is not a relic but radio plasma is still flowing through from the active nucleus, albeit likely at a low rate. The morphology of the extended structure bears some

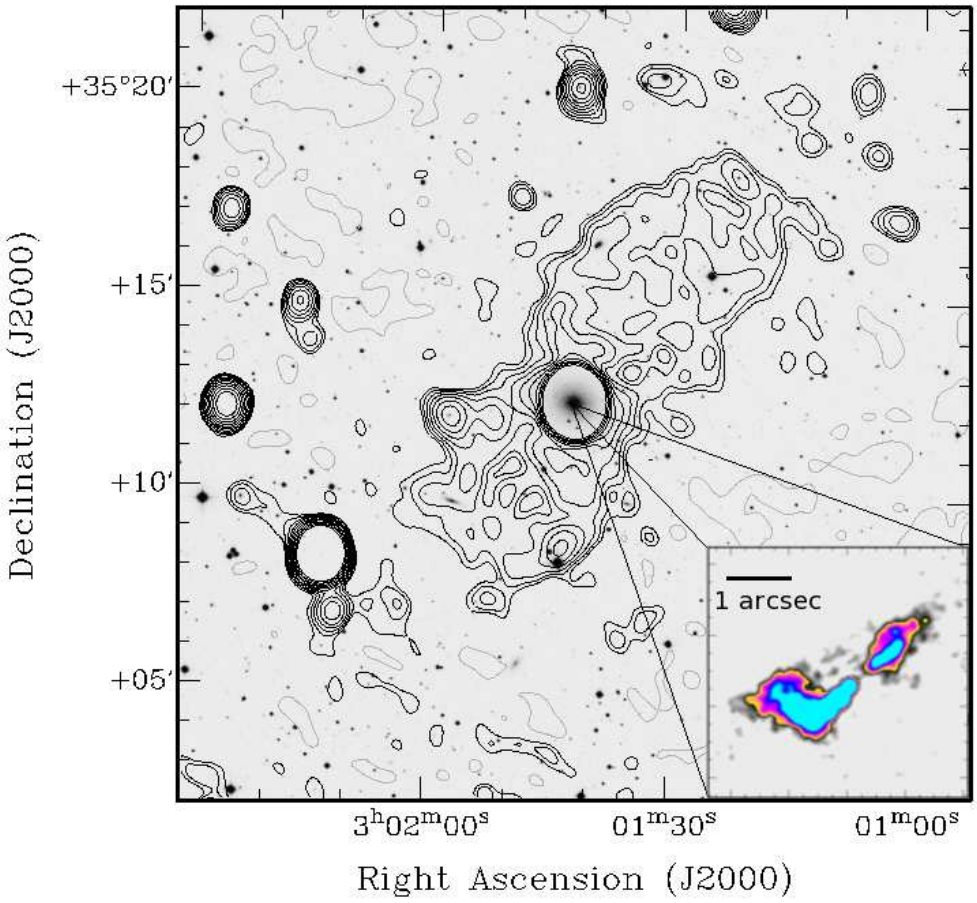

Figure 2.2: Contours of the diffuse radio emission around B2 0258+35 overlaid on a DSS2 image. The contour levels range from 0.2 mJy beam^{-1}to 20 mJy beam^{-1}(2σ to 20σ) increasing by a factor of 1.5 and are marked in black. Negative countours at -0.2 mJy beam^{-1}are gray. The inset at bottom right shows the VLA image of the central CSS source (Giroletti et al. 2005). Note the similarity in the overall orientation between the CSS source and the diffuse emission.

similarities with radio-bubble structures found in low-luminosity radio sources (see Hota & Saikia 2006 for a compilation) and in some radio galaxies, such as Centaurus A (Morganti et al. 1999) and M 87 (Churazov et al. 2001). In both cases, spectral index studies (Hardcastle, Cheung, Feain, & Stawarz 2009 for Centaurus A and the recent study at low frequencies using LOFAR for M 87, de Gasperin et al. 2012, to be submitted) have found no steepening in the spectral index of the diffuse lobes. This suggests that, indeed, some injection of fresh electrons is still ongoing.

In the absence of spectral index data, we attempted to obtain an estimate of the age of the extended radio emission in B2 0258+35 by treating it as buoyant bubbles rising through the IGM away from the host galaxy. The forces considered to act on the bubble are the buoyancy and IGM ram pressure forces. Under these assumptions, we can use an expression for the velocity with which the bubble rises (Ogrean et al. 2011; Churazov et al. 2001):

$$v \sim \sqrt{\frac{r}{R}\frac{8}{3C}} \cdot v_k,$$

where r is the radius of the bubble, R the distance of the bubble center from the host galaxy, $v_k = \sqrt{gR}$ is the Keplerian velocity at the distance of the bubble, g the gravitational acceleration, and C is the drag coefficient. We restricted our attention to the northern lobe and approximated its radius (assuming spherical geometry) by half of its width (as observed in Figure 2.1) for our purposes. This is motivated by the fact that the width would reflect its real size most closely; the height is influenced by the expanding motion, which would yield a poorer size estimate. Consequently, we have $r = 50$ kpc, $R = 50$ kpc and $C = 0.75$. The value for the drag coefficient was adopted following Churazov et al. (2001), who derived it based on hydro-dynamical simulations of buoyant bubbles traveling through a stratified and compressible medium. In contrast, Ogrean et al. (2011) adopted a value of 0.5, which is a value for a solid sphere moving through an incompressible fluid. We assumed the value for the Keplerian velocity from Struve et al. (2010a), who measured the rotational velocity of the H I disk at a distance of $R = 50\,kpc$ from the host galaxy to be $v_k = 325$ km s^{-1}. Using these values for the variables, we obtain for the bubble rising speed a value of ~ 613 km s^{-1}. Treating this bubble as originating from the last burst of AGN emission before shutdown, and assuming a uniform motion, we derive the time elapsed since the activity ceased to be as $\sim 8 \cdot 10^7$ yr. This is a lower limit because of projection effects, and it broadly agrees with estimates from previously cited publications in this paper for relics around CSS sources.

It is interesting to note that the estimated age of the CSS source is very young (the ratio of the timescales is about 0.01) when compared to the estimated time elapsed since cessation of the AGN activity in the previous cycle. Therefore, if we assume that the CSS source marks the beginning of the current newest phase of AGN activity, the time between subsequent phases of activity is about 10^8 yrs, in agreement with current estimates (Parma et al. 2007). All of this holds, of course, if we assume that the observed extended structure is indeed a radio relic.

2.4 Recurrent activity and supply of gas

As was mentioned in the introduction, radio structures that represent signatures of past activity in the host galaxy have been found in several objects. The question for all these objects - including B2 0258+35 - is what causes the activity to stop and restart. Gas and dust are considered the source of fuel for the triggering (or re-triggering) of AGN. Although radio-loud AGN are typically hosted by early-type galaxies, it has been shown that gas is observed in many of them at least on the kpc scale (Oosterloo et al. 2010; Serra et al. 2012; Alatalo et al. 2011; Young et al. 2011). Therefore, the availability of gas, at least on these large scales, is not a problem. However, this gas does not appear to have a clear connection with an active nucleus (Oosterloo et al. 2010).

Perturbations produced by mergers or accretions could provide a mechanism for the gas to loose angular momentum and fall into the super massive black hole (SMBH). B2 0258+35 is a rare case for which the recent merger history of the host galaxy can be reconstructed from the kinematics of the gas. H I has been detected in this object not only in absorption against the radio core, but also in a large-scale ($\sim$ 160 kpc diameter) disk structure (see Fig. 1, right panel). Owing to sensitivity limitations of current radio telescopes, H I emission is quite rarely detected at the typical distance of radio galaxies. Even more rare are cases of large H I disks for which a detailed analysis of the gas kinematics can be performed. The kinematics of the H I over the inner 65 kpc radius are extremely regular (see Fig. 5 in Struve, Oosterloo, Sancisi, Morganti, & Emonts 2010a). Outside this radius, signs of recent or ongoing interaction are seen, although the H I disk remains kinematically regular. This has suggested that, even if part of the gas was brought in by a major merger, this must have been *more than a Gyr ago*. After that, the continuous supply from gas-rich satellite galaxies has been the main mechanism bringing new cold gas. However, this has happened at the outskirts of the disk and without significantly disturbing the kinematics of the gas. No small halo clouds were found in this object.

Therefore, considering this detailed analysis and comparing the time scale with those of the radio structures derived for the "relic" (Section 2.3) and for the inner CSS (Giroletti et al. 2005), we conclude that despite the huge reservoir of H I in this object, we do not find a link between merger or accretion activity and the cycle of radio emission. The data rule out a major merger as trigger of the radio emission. Signatures of minor accretions are observed in the outer regions of the disk and they do not appear to have left any signature that could indicate a clear link between the formation history of the host galaxy and the life-cycle of the radio activity. Even invoking an extreme time-delay between these events (longer than in other studied cases, see Emonts, Morganti, Tadhunter, Holt, Oosterloo, van der Hulst, & Wills 2006), the fact that more than one stage of activity is seen cannot be unambiguously linked to clear events in the process of building of the gas disk. This is reminiscent of what was already found in the case of Centaurus A (Struve et al. 2010b). Therefore, despite the large reservoir of H I in the disk, the actual fuel of the AGN may have a different origin.

Mass loss from stars formed during a star-burst phase (e.g. triggered by a merger) has been suggested as a reservoir for the growth of the black hole and the trigger of its activity (Wild et al. 2010). This way of fueling could also explain a delay (of a few $\times$ 100

Myr) between the star-burst phase and the onset of the radio phase observed in several radio sources (Emonts et al. 2006). However, in B2 0258+35, the optical spectrum does not show signatures of young stars (Emonts 2006, Chapter 4). This would imply a far too long delay (on the order of Gyr) between the stellar evolution and the onset of the radio emission, making this scenario very unlikely (see however Ciotti, Ostriker, & Proga 2010 for further details).

The possibility that warm halo clouds ($10^4 - 10^6$ $M_\odot$) fuel the AGN has been recently proposed by McKernan et al. (2010). The main problem in this scenario is the assumption that the orbits of these warm halo clouds are random. However, there is clear evidence that the halo clouds are likely rotating, and are not in random orbits. Any amount of rotation would cause these clouds never to fall to the center (only the non-rotating clouds on radial orbits will fall to the center) but, instead, to strongly interact with the halo (Marasco, Fraternali, & Binney 2012). The current theory is also that most of these clouds would evaporate before hitting the disk or the center (Heitsch & Putman 2009).

Finally, the possibility that gas cooling from the hot galactic halo supplies fuel to the SMBH via e.g. Bondi accretion, and that it is the dominant mode of accretion in low-power radio galaxies has been suggested by several studies (Croton et al. 2006; Allen et al. 2006; Hardcastle et al. 2007; Balmaverde et al. 2008). This is also supported by the analysis of the optical emission lines in radio galaxies carried out by Buttiglione et al. (2010). In radio galaxies with low-excitation spectra (a group that includes all low-power radio galaxies, i.e. FR I type) the characteristics of the optical lines and the powering of the jets can be explained as proceeding directly from the hot X-ray emitting phase of the ISM/IGM in a manner analogous to Bondi accretion. In addition to this, Binney et al. (2009) have suggested a possible formation mechanism for high-velocity clouds; they can in turn supply the fuel to the SMBH.

Using the information from the radio data, we can infer the accretion rate necessary for fueling the radio AGN following the method presented by Allen et al. (2006), Balmaverde et al. (2008) (see also Morganti et al. 2009). The radio core flux density of B2 0258+35 at 1.6 GHz was measured by Giroletti et al. (2005) - using the VLBA - to be $7.4\,mJy$.

This gives a core luminosity of $L_{core} \approx 3.5 \cdot 10^{21}\,W \cdot Hz^{-1}$, which can be converted into jet power - $P_j \approx 1.2 \cdot 10^{36}\,W$. Balmaverde et al. (2008) found a relation between the Bondi accretion power and the jet power that, if applied to B2 0258+35, gives $P_B \approx 6.5 \cdot 10^{37}\,W$, corresponding (using $P_B = 0.1\dot{M}c^2$) to a mass accretion rate of at most 0.1 $M_\odot\ yr^{-1}$.

Unfortunately, although X-ray observations at 2-10 keV (Akylas & Georgantopoulos 2009) show an X-ray halo that extends beyond $D_{25} \sim 49\,kpc$ (Rasmussen, private communication), the modeling of the density and temperature profile for estimating the Bondi accretion rate is not available. Thus, we limit ourselves to comparing the values obtained with what is found for other radio galaxies. For example, using the same reasoning as outlined above, $\dot{M} \sim 0.1$ $M_\odot\ yr^{-1}$ was found for NGC 315 (Morganti et al. 2009), quite high when compared to e.g. the sample in Allen et al. (2006), but inside the range (although toward the high end) of the distribution for radio galaxies

found by Balmaverde et al. (2008). This seems to support the argument that cooling of hot gas, resulting in a Bondi type of accretion, can be responsible for feeding the AGN.

If the cooling of the hot gas is at the origin of the activity fueling, one may wonder whether, in the process of cooling, the gas would spend enough time in the H I phase, and be observable in H I absorption against the nuclear regions of radio continuum. The advantage of observations of H I in absorption is that the gas can be traced to very small scales (unlike for hot gas observed in X-ray) and can provide the kinematics and the distribution of at least the cold component. In this respect, it is intriguing that the occurrence of H I in the central regions of restarted radio sources appears to be higher than in other radio sources (Chandola et al. 2010; Saikia & Jamrozy 2009; Geréb et al. 2013). If confirmed for more objects, this suggests that the presence/availability of (cold) gas may be connected with the duty-cycle of radio sources. B2 0258+35 confirms this trend with H I absorption detected against the central component (Struve 2010). However, is this H I able to reach the SMBH and fuel the AGN?

For the FR I radio galaxy NGC 315, an in-falling cloud of H I has been observed at a few pc distance from the core (Morganti et al. 2009), corresponding to accretion rates in the range $10^{-4} - 10^{-3}$ $M_\odot$ yr^{-1} (inferred from H I absorption studies using the radio continuum of the core). Although the presence of the H I in-fall is intriguing, the accretion rate is lower than what is required to fuel the AGN. However, it has to be mentioned that this is probably a lower limit, since the H I absorption probes only the gas detected against the continuum. For B2 0258+35, the highest resolution available so far for H I absorption studies does not reach these small linear scales. The H I absorption study (Struve 2010) shows that, down to a linear scale of $\sim$ 300 pc, most of the gas has relatively regular kinematics, in good agreement with the kinematics of the large scale disc. At this resolution, the only deviation from circular motion appears to be the gas associated with a blueshifted, possibly outflowing component that has been detected both in H I and in CO. If the lack of additional deviation from circular motion, and in particular infalling cloud(s), is confirmed by high - resolution VLBI observations, this would imply that the hot gas dominates the accretion and e.g. the cooling gas would spend only a very short time in the H I phase.

If the activity is related to cooling of the X-ray gas, one can imagine, as already described by other authors, a cycle that would explain not only the triggering but also the interruption of the activity.

The radio emission would be responsible for heating the ISM/IGM, thus stopping the accretion, and, as a consequence of this, the radio emission would be interrupted. This would allow the ISM/IGM to cool again, and after a while the radio emission would restart - thus the cycle can go on (McNamara & Nulsen 2007; Randall et al. 2011; Gaspari et al. 2012).

2.5 Conclusion and future studies

We have presented the discovery of an extended and low surface brightness radio emission around the young (CSS) radio source B2 0258+35 hosted in an H I-rich early-type galaxy. The newly found radio emission has a distinct double-lobed appearance and is likely a left-over from a previous cycle of activity of the galaxy. The faint lobes may indeed not

be completely dead relics, but may still be weakly refueled with "fresh" electrons from the nucleus in a similar way as e.g. the middle lobe of Centaurus A (Morganti et al. 1999). This may explain why the large and faint structure is still visible (although the source is not in a cluster environment). Only a study of the spectral index may help in verifying this hypothesis.

It is intriguing to note the speculation from Giroletti et al. (2005) that the inner CSS (with an estimated age of $9 \cdot 10^5$ yr) might not grow to become a large-scale radio galaxy. No final hot spots are observed although the structure appears to be the result of a strong interaction with the ISM. Considering that the previous cycle of activity did manage to expand to hundreds of kpc in size, this would suggest that every cycle of activity can have different characteristics or that the ISM is now particularly rich and can affect the new radio source more drastically.

The huge H I disk found in B2 0258+35 has a very regular kinematics that do not show any obvious connection with the triggering of the radio source. According to the conclusion of Struve et al. (2010a), no major merger has recently occurred in this galaxy and, therefore, a major merger as a trigger of the radio emission is ruled out. Minor accretions are also excluded, because they appear to have perturbed the H I only mildly at large radii. We see no indication in the high-resolution data (Struve 2010) that (some of the) gas in a circum-nuclear disk is indeed fueling the AGN. However, we cannot completely exclude the presence of such a gas until even higher resolution data are available. Future VLBI studies may be able to shed more light on this. The possibility that despite the large reservoir of H I in the disk, the actual fuel of the AGN may originate from the cooling of gas in the hot halo is an interesting alternative and would also help to explain the recurrent activity.

In the future, sensitive low-frequency surveys that cover a large area of the sky will allow finding out how common left-over radio emission from a previous cycle of activity is and tell us about the duty cycle of the radio emission. Sensitive, low-frequency observations are a reliable way to identify these sources, see Dwarakanath & Kale (2009), van Weeren et al. (2009). Increasing the known number of these structures (which is now limited) will allow us (combined with multi-waveband information) to understand under which conditions the radio phase (re-)starts, what the time-scales of this phenomenon are and, as a result, we will learn more about the impact of the radio plasma on the host galaxy and the surrounding IGM. In particular, if the cooling of the hot halo is, indeed, a reservoir for the triggering of the AGN, then we would expect relatively regular cycles of activity and we would expect to observe structures similar to B2 0258+35 in many more objects.

All these requirements are currently being met by LOFAR (and will be met by the SKA in the future). The deep surveys planned with LOFAR (Rottgering 2010) which will cover large areas of the sky, will allow us to find, how common structures like the one detected in B2 0258+35 are. LOFAR 60 MHz observations of B2 0258+35 have been already performed to detect or set a limit to the brightness of the extended structure at lower frequency and learn more about its origin. These data will be presented in a future paper.

Chapter 3

The peculiar radio galaxy 4C 35.06: a case for recurrent AGN activity?

Say not, 'I have found the truth,'
but rather, 'I have found a truth.'

– Khalil Gibran

Abstract

Using observations obtained with the LOw Fequency ARray (LOFAR), the Westerbork Synthesis Radio Telescope (WSRT) and archival Very Large Array (VLA) data, we have traced the radio emission to large scales in the complex source 4C 35.06, located in the core of the galaxy cluster Abell 407. At higher spatial resolution, the source was known to have two inner radio lobes spanning 31 kpc and a diffuse, low brightness extension running parallel to them, offset by about 11 kpc.

At 60 MHz, we detect the radio emission of this structure extending out to 210 kpc. At 1.4 GHz and intermediate spatial resolution, the structure appears to have a helical morphology.

We have derived the characteristics of the radio spectral index across the source. We show that the source morphology is most likely the result of at least two separate episodes of AGN activity hosted by one of the galaxies located in the cluster core of Abell 407, possibly connected with a late switching off of the nucleus and a delay between the two phases of about 35 Myr. The outermost regions of radio emission have a steep spectral index, indicative of old plasma. We connect the spectral index properties of the resolved source structure with the integrated flux density spectral index of 4C 35.06 and suggest an explanation for its unusual integrated flux density spectral shape, possibly providing a proxy for future studies of more distant radio sources through inferring their detailed spectral index properties and activity history from their integrated spectral indices.

We propose that the AGN is intermittently active as it moves in the dense environment in the cluster core. In this scenario, the AGN turned on sometime in the past, and has produced the helical pattern of emission, possibly a sign of jet precession/merger during that episode of activity. Using LOFAR, we can trace the relic plasma from that episode of activity out to greater distances from the core than ever before.

We detect with the WSRT H I in absorption against the center of the radio source. The absorption profile is relatively broad (FWHM of 288 km s^{-1}), similar to what is found in other clusters. The derived column density is $N_{HI} \sim 4 \cdot 10^{20}$ cm^{-2} for a $T_{spin} = 100$ K. This detection supports the connection - already suggested for other restarted radio sources - of a connection between the presence of cold gas and restarting activity. The cold gas appears to be dominated by a blue-shifted component although the broad H I profile could also include gas with different kinematics.

Understanding the duty cycle of the radio emission as well as the triggering mechanism for starting (or restarting) the radio-loud activity can provide key constraints to quantify the impact of AGN feedback on galaxy evolution. The study of these mechanisms at low frequencies using morphological and spectral information promises to bring new important insights in this field.

A. Shulevski, R. Morganti, P. D. Barthel et al.
submitted to *Astronomy & Astrophysics*

3.1 Introduction

For some time now it has been recognized that the active phase of radio-loud Active Galactic Nuclei (AGN) can be recurrent (see Saikia & Jamrozy 2009, for a review). Therefore, this activity can have a repeated impact on the AGN host galaxy and its environment, starting from the initial phase of the radio source's life (O'Dea 2002) on to its later stages (McNamara et al. 2000). The morphology of a (recurrent) radio source can vary significantly (see e.g. Schoenmakers et al. 2000; Murgia et al. 2011). Therefore, only a combination of radio morphology and radio spectral index[1] analyses can reliably tell us whether a radio source had recurring activity, thereby impacting more than once its host galaxy. A typical radio-loud AGN in its active phase (which can last for up to several 10^7 years) is characterized by the presence of a radio core and extended lobes with or without visible jets. When the AGN shuts down, emission from the core disappears for the duration of the "off" phase. The large scale radio lobes might still be replenished with particles if the information of the core shutdown has not had enough time to propagate out. However, once the supply of energetic particles coming from the core stops, the lobe plasma starts to age producing a so-called *relic* structure and the radio source enters a fading phase in its life-cycle. It is possible that during this time the AGN re-activates, in which case we can again observe an active radio core (possibly with new jets / lobes expanding outwards into the ISM / IGM) co-existing with a fading radio relic on larger scales.

The energy loss mechanism for relic radio plasma is mostly through synchrotron radiation (with possible adiabatic expansion related losses). Its observational signature is a steepening of the radio spectrum of the emission regions (synchrotron radiation depletes high energy particles faster compared to low energy ones), making them relatively brighter at low frequencies (Kardashev 1962). Thus, the relic radio emission is typically faint and detecting it requires low frequency observations with high sensitivity.

This work is part of a larger study where we investigate radio sources with restarted activity expanding our studies to low frequencies, using the LOw Frequency ARray (LOFAR, van Haarlem et al. 2013). Our aim is to describe in more detail their activity history (duty cycle). We also benefit from the advantage of having sufficient spatial resolution to be able to study resolved source structure at low frequencies. We relate our results to the integrated flux density spectral properties of these sources in an attempt to extrapolate our results to the high redshift source population (in which case we would have poorer spatial resolution).

In this work, we investigate the complex radio morphology of 4C 35.06 (B2 0258+35B; Bondi et al. 1993). Liuzzo et al. (2010) did a study of UGC 2489 using the Very Large Baseline Array (VLBA) and they detected an extended source on a milli arcsec scale with a core flux density of ~ 2.6 mJy, stating that the VLBA detection coincides with one of the cores of the cD galaxy UGC 2489 (marked with a cross in Figure 3.1). UGC 2489 represents the core of the Abell 407 galaxy cluster (Schneider & Gunn 1982, see Figure 3.1). The radio luminosity of 4C 35.06 is $L_{1.4GHz} = 2.5 \cdot 10^{24}$ WHz^{-1}. This value is consistent according to Best & Heckman (2012) with being a Low Excitation Radio Galaxy (LERG) as confirmed by the low resolution optical spectra of the host galaxy (Schneider & Gunn 1982; Crawford et al. 1999) showing no emission lines.

In the VLA maps we can see two inner radio lobes spanning 31 kpc and a diffuse,

[1] We use the $S \propto \nu^{\alpha}$ definition for the spectral index α throughout this writing.

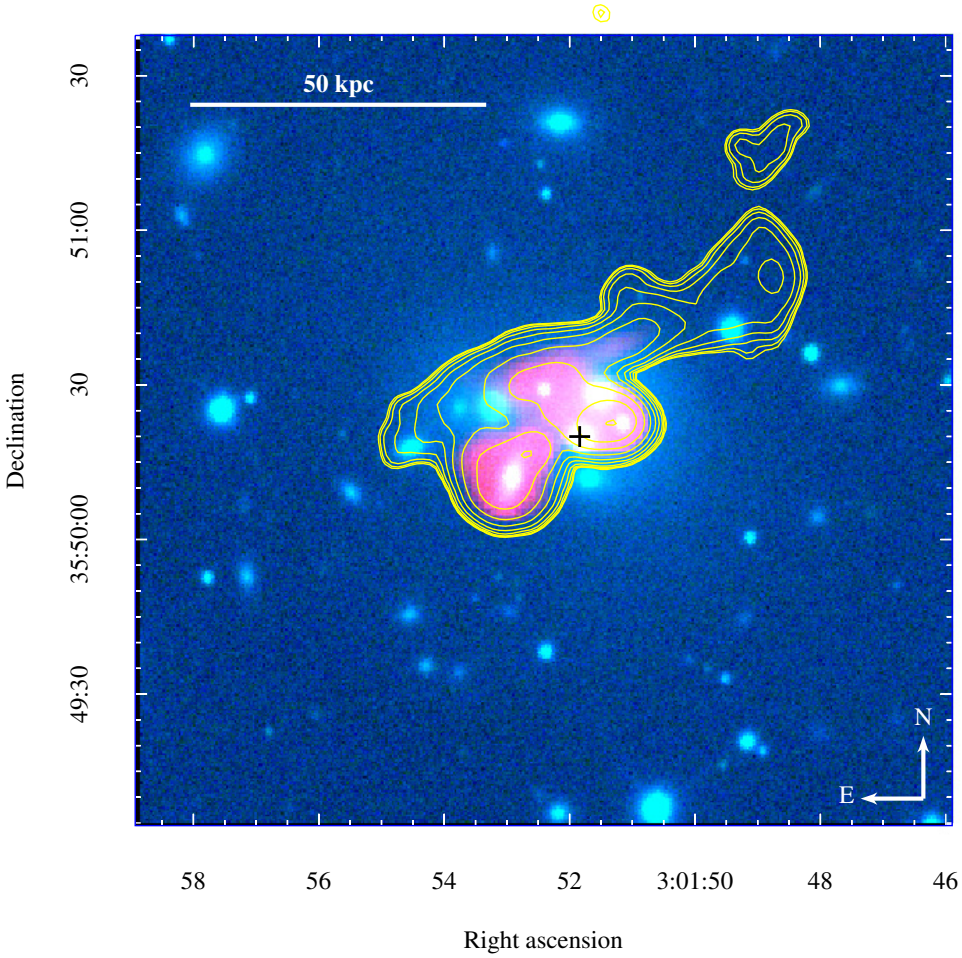

Figure 3.1: Optical image of UGC 2489 taken from the Sloan Digital Sky Survey (SDSS, Aihara et al. 2011) showing its multi-component core structure. The red intensity overlay shows a 4885 MHz VLA archival image. In yellow we over-plot contours from a 1415 MHz VLA archival image. Contours are log scaled, there are 10 contour levels going from 4σ to 500σ. Details about the VLA images can be found in Table 3.1. The stellar halo around the cores is roughly 40 kpc in extent. We mark the position of the core hosting the AGN with a black cross.

low brightness extension running parallel to them, oriented south-east to north-west (see Figure 3.1). The puzzling structure hints at the possibility of multiple AGN activity episodes combined with motion of the host core within the cD galaxy, making this source particularly interesting for studying AGN recurrent activity and the triggering of the active phases.

We made use of images available in the Jansky Very Large Array (VLA) archive. Furthermore, we took advantage of the fact that this source was included in one of the fields observed by the LOFAR during commissioning tests.

In addition, we also present new Westerbork Synthesis Radio Telescope (WSRT) observations obtained to investigate the presence of cold gas (H I) in this object. As mentioned above, one of the open questions is the relation between the gas and the fueling of multiple phases of activity. Atomic neutral hydrogen can, in principle, provide such fuel.

The paper is organized in the following way. Section 3.2 discusses the data reduction procedure, while in Section 3.3 we present the LOFAR image and quantities derived from it. We discuss the implications of our results, in combination with results of previous studies in Section 3.4, and we conclude with a summary in Section 3.5.

Throughout this paper we use a Hubble constant H_o= 73 km s $^{-1}$ Mpc^{-1}, $\Omega_\Lambda = 0.73$ and $\Omega_M = 0.27$. At the distance of 4C 35.06, using $z = 0.046276$ (corrected to the reference frame defined by the CMB), this results in 1 $''$ = 0.872 kpc (Wright 2006).

Table 3.1: Summary of the images of 4C 35.06 used in this work.

Instrument	ν [MHz]	Beam size	Noise [mJy/b]	Ref.
LOFAR	61	$51''$x $43''$	35	(1)
WSRT	1360	$30''$x $13''$	0.18	(1)
VLA (B)	1415	$4.8''$x $4.1''$	0.29	(2)
VLA (C)	4885	$3.8''$	0.04	(3)

References: (1) This work; (2) Gregorini et al. (1988) (VLA archive image); (3) Bondi et al. (1993) (VLA archive image).

3.2 Data available, new observations and data reduction

3.2.1 LOFAR

The observations using LOFAR were carried out in the night of October 8, 2011 using the low band antennas (LBA) at 61 MHz centered on B2 0258+35A observed as part of the LOFAR commissioning efforts. 4C 35.06 is located about half a degree to the north from the phase center. Table 3.2 summarizes the observational configuration.

The data were flagged to remove radio frequency interference (RFI) using the AO flagger package (Offringa et al. 2012) and averaged to a frequency resolution of 192 kHz per channel and a time resolution of 10 seconds per sample. Calibration was performed using the Black Board Selfcal (BBS) package using the complete bandwidth. The set up of the observations did not include observations of a flux calibrator, therefore the initial

Table 3.2: LOFAR observational configuration

No. of sub-bands	29
Central Frequency [MHz]	61.62
Bandwidth [MHz]	5.6
Integration time	1 second
Observation duration	6 hours
Polarization	Full Stokes
No. of LOFAR stations used	32
UV range	$20\lambda - 4000\lambda$

calibration model was derived from a VLSS[2] image following the procedure described in van Weeren et al. (2012b) and de Gasperin et al. (2012). The image from which the initial model was derived had a size of $8^\circ \times 8^\circ$, to encompass the Full Width at Half Maximum (FWHM) of the LOFAR station (primary) beam, as well as ensure that any brighter sources beyond the FWHM are included in the model. The model components were specified as having a spectral index of $\alpha = -0.8$. During the calibration, we have solved for the complex valued station gains and for the differential Total Electron Content (dTEC) over the full bandwidth.

Imaging was done in the Common Astronomy Software Applications package (CASA, McMullin et al. 2007), using multi-scale clean (Cornwell 2008). We imaged by selecting the data in UV distance below 20 km, limiting ourselves to baselines having satisfactory calibration solutions, avoiding as much as possible calibration errors induced by the ionosphere, while retaining enough spatial resolution. We weighted the baselines used for imaging using Briggs weights with the robust parameter set to -0.1 (Briggs 1995). We have used multi frequency synthesis (assuming no frequency dependence) imaging over the entire bandwidth.

After obtaining the initial image, we have performed a correction for the primary (station) beam shape to ensure a correct flux scale over the FoV. The correction was applied by deriving the average LOFAR station beam, using CASA to image (with the same settings as were applied in the imaging) a grid of BBS simulated point sources covering the LOFAR FoV. The recovered flux densities were used to derive the primary beam which we use to correct the image.

Before the final imaging, three self-calibration runs were performed by iterating over the procedure described above. We have reached an image noise of about 35 mJy beam^{-1} measured away from bright sources. The size of the restoring beam is $51''$x $43''$.
We have checked the flux scale across the final image, by comparing the flux densities of sources in our LOFAR image with their values in existing surveys. Compact sources with $S/N > 10$ were extracted using the PyBDSM package (Ramanujam 2007) and their flux at 61 MHz compared with the extrapolation from the VLSS, WENSS[3] and NVSS[4] catalogs. The derived LOFAR flux densities were estimated to be accurate to $\sim 10\%$ level.

[2] VLSS (Cohen et al. 2007) is the VLA Low frequency Sky Survey carried out at a frequency of 74 MHz

[3] WENSS stands for the Westerbork Northern Sky Survey carried out at a frequency of 325 MHz (Rengelink et al. 1997)

[4] NVSS stands for the NRAO VLA Sky Survey carried out at a frequency of 1.4 GHz (Condon et al. 1998)

A check of the positional accuracy of the LOFAR image was performed by plotting the differences between positions of the sources extracted from the LOFAR image and matched sources from the NVSS survey. Again, we used PyBDSM to extract point sources from the LOFAR image. Positional differences for source matches between the WENSS and NVSS catalogs were used as control. On average, the derived position offset for point sources in the vicinity of 4C 35.06 extracted from the LOFAR image and the corresponding NVSS catalog sources is less than $5''$ without any obvious systematics. Thus, for the purpose of this study, we concluded that there is no position offset in the LOFAR image.

3.2.2 H I - 21cm and continuum from the WSRT

WSRT observations to search for H I in 4C 35.06 were performed at three epochs (2013 April 8 and 11, June 12) for 8, 7 and 6 hours respectively. The observing band was centered on 1356.8 MHz, the frequency of H I for z = 0.0464, the redshift of 4C 35.06. The total bandwidth was 20 MHz, corresponding to a velocity range of $\sim$ 4422 km s^{-1} and was covered with 1024 channels (dual polarization). In order to increase the signal-to-noise ratio, four channels were binned resulting in a spectral resolution of 17 km s^{-1} in the output data cube. The data reduction was performed using the MIRIAD package (Sault et al. 1995). After flagging, bandpass and phase calibration were performed. The continuum emission was subtracted, using the task *uvlin*, by making a second order polynomial fit to the line-free channels of each visibility record.

Cubes with different weighting were obtained. For an intermediate weighting (Briggs with the robust parameter set to 0.4), the final r.m.s. noise was 0.2 mJy beam^{-1}chan^{-1} for a velocity resolution of 15 km s^{-1} and spatial resolution of $34''$ x $14''$.
In addition to the line cube, a continuum image was obtained using the line-free channels. The peak of the continuum emission was 221 mJy and the r.m.s. noise was 0.18 mJy beam^{-1}.

3.3 Results

3.3.1 The radio continuum structure from WSRT and LOFAR

Our LOFAR and WSRT images of 4C 35.06, as well as data derived from the archival VLA images are presented in Fig. 3.2. Looking at the morphology traced by the different images at different resolution, we can note several things.

Firstly, Figure 3.2 indicates that the emission parallel to the inner radio lobes is connected to the more distant regions and has a helical structure (best seen in the left panel of Figure 3.2). The WSRT resolution is high enough that we resolve the morphology and can claim that the helicity is real and not an artifact of the elongated WSRT beam. The helicity might indicate precession in the radio jet which has deposited the plasma, triggered by accretion disk instabilities (Kunert-Bajraszewska et al. 2010b) or maybe a possible sign of a past black hole merger of two cores in UGC 2489.

The zoom-in of the central region of 4C 35.06 in the LOFAR image (labeled C) is shown in the right panel of Figure 3.2 along with the same region as observed by the VLA at higher frequencies.

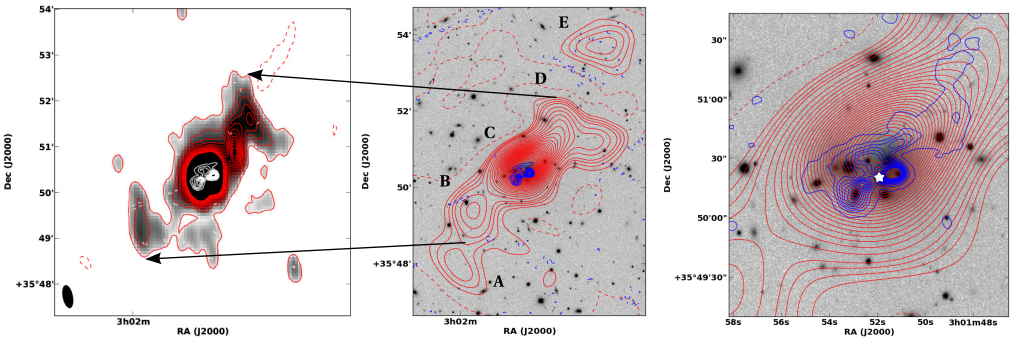

Figure 3.2: Left: WSRT 1360 MHz continuum image of 4C 35.06. Overlaid in red are 15 contours taken from the same image, spanning the range $(-5, 150)\sigma$, while plotted in white are 4885 MHz VLA contours of the central region with 15 contour levels spanning $(-5, 370)\sigma$. The WSRT beam is shown in the lower left corner. **Middle:** The 4C 35.06 radio source as seen by LOFAR, represented by red contours (33 levels spanning $(-3, 183)\sigma$) over an inverted grayscale SDSS image of the central region of the Abell 407 cluster. The peak flux in this map is 9.1 Jy. Regions in the LOFAR map are marked A through E. Overlaid in blue are the VLA 4885 MHz image contours. **Right:** LOFAR 61 MHz (red) and VLA 1415 MHz (blue) contours overlaid over an inverted grayscale SDSS image of the cluster core (UGC 2489). The location of the core hosting the AGN is marked with a white star. Arrows mark the extent and the location of the regions of interest in different images. The relevant beam sizes and noise levels of the images are given in Table 3.1.

The source region labeled E is noticeable as a barely visible surface brightness enhancement in a VLSS image of 4C 35.06, and it is detected at a 2σ level in a VLA image by Gregorini et al. (1988). It is now unambiguously detected in the LOFAR image. Its projected distance from the central region (C) is $\sim$ 210 kpc.

The region labeled A was previously detected by the VLSS (blended with the rest of the source) and partially by the WENSS, however our LOFAR map detects it with better resolution and allows us to clearly morphologically separate it from other regions of 4C 35.06.

The second interesting result is that, as shown in the right panel of Figure 3.2, the peak flux of 4C 35.06 as seen by LOFAR is offset by $10''$ to the north-west w.r.t the radio lobes seen in the VLA maps. This is a sufficiently large value to be considered a real effect and not a systematic offset (see sub-section 3.2.1). We interpret this difference between the peak flux density position and overall source position as intrinsic in the case of the extended source 4C 35.06 and indicative of its (spectral) properties.

3.3.2 The H I gas

Atomic neutral hydrogen is detected against the central region of 4C 35.06. Figure 3.3 shows the H I profile (obtained from the combination of all WSRT data) extracted against the brighter (western) lobe of the central source (Figure 3.1). The profile is obtained after Hanning smoothing and averaged over a region encompassing the western inner

lobe. Given the limited spatial resolution of the WSRT H I observations, we can only say that H I is seen in from of the western lobe which, in fact, includes the radio core of the source.

The profile is complex, with a broader component with FWHM of 288 km s^{-1} centered at 13858 km s^{-1}. The peak absorption is ~ 0.8 mJy which corresponds to a low optical depth of $\tau = 0.0036$. From the parameters of the absorption we can estimate a column density of $N_{HI} \sim 4 \cdot 10^{20}$ cm^{-2} for a $T_{spin} = 100$ K.

The H I profile is relatively broad compared to that typically found in radio galaxies (Geréb et al. 2014), but resembles what is observed in some other clusters; we discuss this in more details in Section 3.4.1. While at uniform weighting the profile is dominated by two relatively narrow components, the broad component becomes more prominent at lower spatial resolution, suggesting that it belongs to a diffuse distribution of gas. However, given the low S/N of the detection this result will need to be verified with deeper observations. Compared to the systemic velocity of the host galaxy (14120 km s^{-1}), the peak of the H I profile appears blueshifted (see Figure 3.3). However, the total width of the profile encompasses the range in velocity of the galaxies in the cluster core.

In addition to the absorption profile, there are at least three detections of H I emission in the WSRT FoV. All three have an optical counterpart in the SDSS. One of these detections is identified with UGC 2493, a (disturbed, possibly merging) galaxy pair having a redshift of z=0.0437, which makes it a member of Abell 407 according to Chen et al. (1998). It is located at a radial distance of 210 kpc from the Abell 407 cluster core (UGC 2489). The other two detections are located at coordinates: J030219+354601 (H I disk associated with a edge on galaxy) and J030217+355533.

3.3.3 Spectral analysis

Following the work of Murgia et al. (2011), we investigate the characteristics or the integrated spectrum of the source and then we turn to the spatially resolved analysis of the spectral index with the aim of getting a detailed handle on the past and present activity history.

We have compiled integrated flux density measurements of 4C 35.06, as shown in Table 3.3. The flux density values are taken from the literature, or measured from archival images, with comparable sensitivity to the extended emission. They are plotted in Figure 3.4 along with our LOFAR flux value.

The best power-law fit to the integrated flux density data points has a spectral index of $\alpha = -1.01 \pm 0.02$. Although this is not an extremely steep spectral index, it is steeper when compared to what is usually seen in the lobes of radio galaxies ($\alpha \sim -0.7 \pm 0.1$). The integrated spectrum does not show a spectral break.

This indicates that we average over regions of different ages having different intrinsic brightness. The sum of those spectra, each having spectral breaks at different frequencies, produces the remarkably straight integrated spectrum.

High redshift radio sources that will be detected in future radio surveys will be (in most cases) unresolved. Therefore, it is important to benchmark the information obtained from the integrated flux density spectral studies against the one for the spatially resolved studies.

To expand on the different phases of radio-loud activity in this object, we used our LOFAR and WSRT observations, as well as archival VLA images to distinguish between

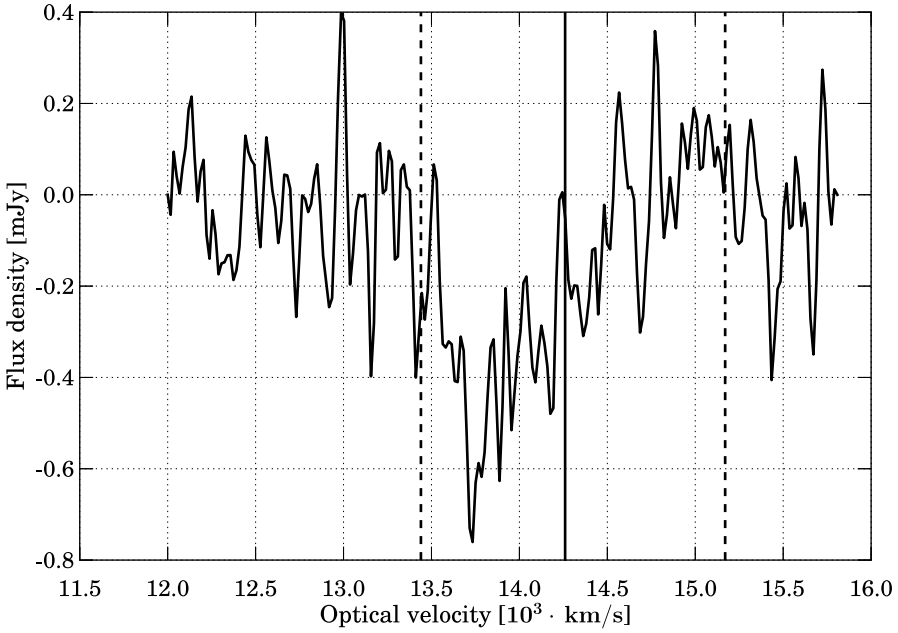

Figure 3.3: H I absorption profile in 4C 35.06 (Hanning smoothing applied). The full vertical line marks the systemic velocity of 4C 35.06 host galaxy, while the two vertical dashed lines mark the highest and lowest velocity of the galaxies in the cluster core.

the spectral index of the inner regions of 4C 35.06, and the outer regions of extended radio emission. We used images with matching resolution at different frequencies. The resulting spectral index images are shown in Figure 3.5.

We see that the inner region where the core and the two brighter lobes are located shows a typical spectral index in the range of $\alpha \sim -0.6$ to $\alpha \sim -0.8$, indicative, as shown by the morphology of the inner double-lobed source, of an active region. However, there is a spectral steepening ($\alpha \sim -1.2$) in the extended emission just to the north-east of the inner lobes (Figure 3.5, left panel). This is the region of the source where we detect the peak flux in our LOFAR map (see Figure 3.2, right panel), in agreement with LOFAR being more sensitive to regions having steeper spectrum. Thus, this region could indeed represent a region of older radio plasma.

We used lower resolution images to derive a spectral index map for the larger scale regions of the source. The steepening seen at higher resolution in the structure running parallel to the inner brighter lobes, is also visible and continues out to larger scales. This can be seen in the right panel of Figure 3.5. Going to the north-west, the spectral index remains at a value of around -1.2 up to ~ 50 kpc from the central region, while on the south-eastern side it steepens already to about -1.4 quite close to the central region. This trend suggests that the outer, extended, regions of the source are composed of aged plasma.

We have fitted a KGJP synchrotron aging model (Komissarov & Gubanov 1994;

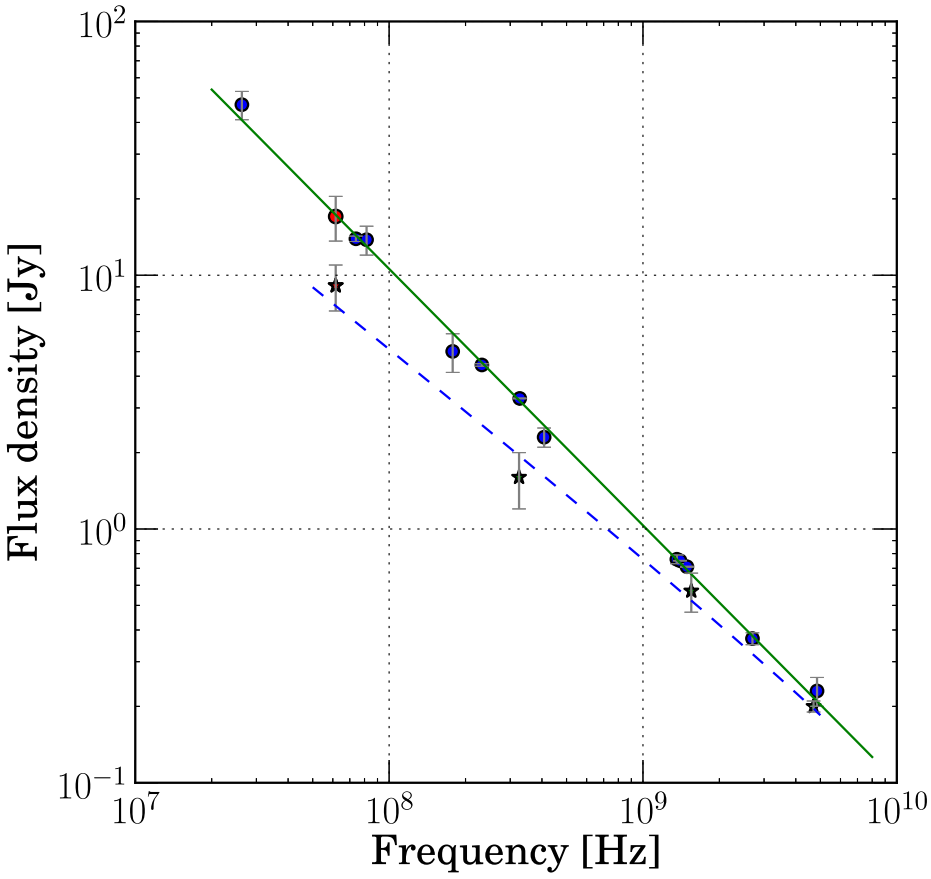

Figure 3.4: Integrated flux values for 4C 35.06 based on the data listed in Table 3.3 (circles) and its central region (stars). We mark the LOFAR data points in red. The green line represents a power law fit, while the blue dashed line gives the synchrotron aging model fit for region C.

Table 3.3: Data used in Figure 3.4.

Source	ν [MHz]	S_ν [Jy]
Clark Lake[1]	26.3	47.0 ± 6.0
LOFAR[2]	61.6	17.04 ± 3.41
VLSS[3]	74.0	13.92 ± 0.34
Cambridge[4]	81.5	13.80 ± 1.8
4C[5]	178.0	5.01 ± 0.87
MIYUN[6]	232.0	4.43 ± 0.05
WENSS[7]	327.0	3.27 ± 0.01
B2[8]	408.0	2.30 ± 0.20
WSRT[9]	1360.0	0.76 ± 0.03
NVSS[10]	1400.0	0.750 ± 0.002
VLA[11]	1490.0	0.710 ± 0.003
BKB77[12]	2700.0	0.37 ± 0.02
GB6[13]	4850.0	0.23 ± 0.03

[1] Verkhodanov et al. (2009); Viner & Erickson (1975)
[2] This work
[3] Cohen et al. (2007), CLEAN bias correction applied (+0.7 Jy)
[4] Verkhodanov et al. (2009); Readhead & Hewish (1974)
[5] Pilkington & Scott (1965), flux set to Baars et al. (1977) x 1.067 (corrected according to Helmboldt et al. 2008)
[6] Verkhodanov et al. (2009); Zhang et al. (1997)
[7] Rengelink et al. (1997)
[8] Colla et al. (1973), flux set to Baars et al. (1977) x 1.091 (corrected according to Helmboldt et al. 2008)
[9] This work
[10] Condon et al. (1998)
[11] C array
[12] Verkhodanov et al. (2009); Bridle et al. (1977)
[13] Verkhodanov et al. (2009); Gregory & Condon (1991)

van Weeren et al. 2009) to the integrated flux density measurements at four different frequencies (images listed in Table 3.1) for the central region of the source (labeled C in Figure 3.6). We have used an injection index of $\alpha_0 = -0.8$. The equi-partition value for the magnetic field was calculated to be $5.34\,\mu$G. The best fit model gives a source age of $t_s = t_{on} + t_{off} = 1.5 + 10$ Myr. The model supports the observation that the central region is the youngest region of the source. We show the fits in Figure 3.4.

We have also determined the spectral index of the outermost source region labeled E, as well as that of region labeled A by measuring the flux density of these regions as seen in the LOFAR image. We have adopted the measurement procedure outlined by Klein & Emerson (1981). The measurements were done by integrating the flux density over measurement areas in the regions A and E where the surface brightness was above the 3 σ level in the LOFAR, VLSS, WENSS and NVSS images, as well as in our continuum WSRT image and thus calculating the spectral index. The derived values are given in Table 3.4.

We plot the data from Table 3.4 in Figure 3.6 and fit a power-law to the data points

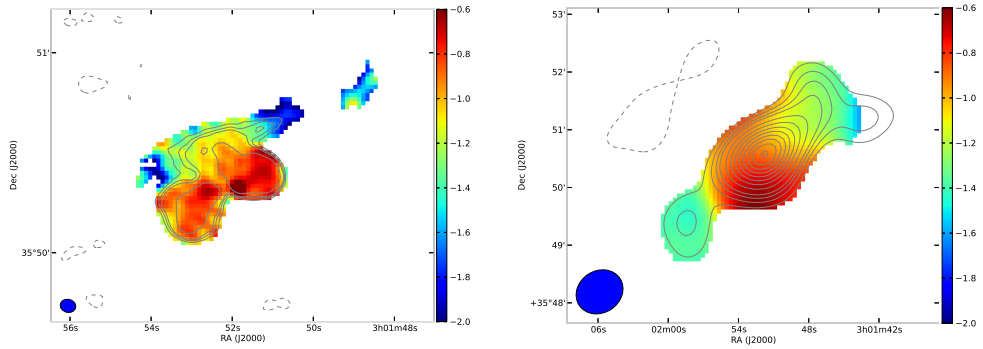

Figure 3.5: Left: α_{1415}^{4885} spectral index map of the inner lobes of 4C 35.06 using the archival VLA images listed in Table 3.1. Overlaid are VLA 4885 MHz contours $(-5, 18, 27, 36, 81)\sigma$. **Right:** α_{61}^{1360} spectral index map of the extended emission of 4C 35.06 using the LOFAR and WSRT images from this work. Overlaid are 33 contour levels from the LOFAR map spanning the range $(-3, 183)\sigma$. The beam sizes are given in the lower left corner.

Table 3.4: Measured flux density values for the regions labeled A and E in the LOFAR image.

ν [MHz]	S_ν [Jy]	
	Region A	α
61.6	0.77 ± 0.16	
74.0	0.51 ± 0.12	-1.36 ± 0.09
325.0	0.075 ± 0.005	
1360.5	< 0.0023	
	Region E	α_{61}^{74}
61.6	0.96 ± 0.20	
74.0	0.32 ± 0.12	< -2[a]
325.0	< 0.022	
1360.5	< 0.0015	

[a] Region E is detected in the LOFAR and VLSS images, and the other measurements are only upper limits. Hence, we show only an illustrative polynomial fit, but do not attempt to derive a spectral index.

for region A. The spectrum of region E is poorly constrained, but we note that it is ultra steep ($\alpha < -2$). Region A also has a somewhat flatter spectrum ($\alpha = -1.36 \pm 0.09$) in line with what we expect from the spectral trend of the inner regions. More sensitive observations at higher frequencies (with sufficient resolution) are needed to determine the exact spectral index of the outermost regions.

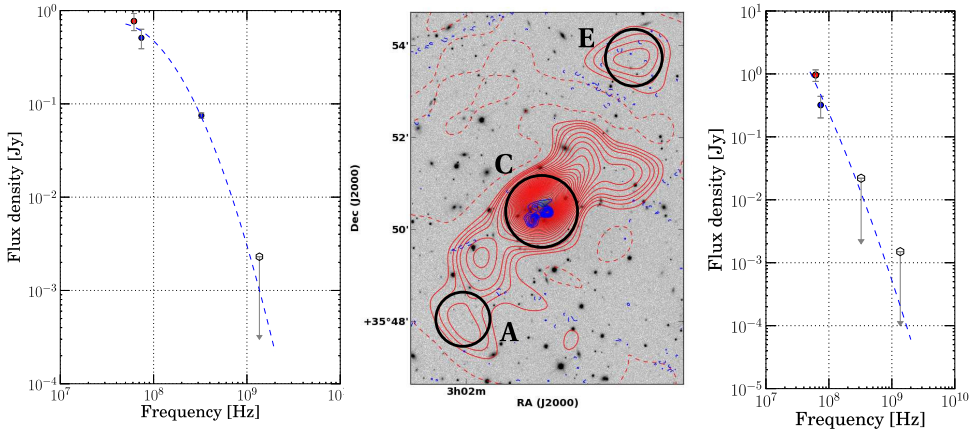

Figure 3.6: Left: The dashed blue line represents a second order polynomial fit to all the data points. The upper limit data point is not taken into consideration. **Middle:** The 4C 35.06 radio source as seen by LOFAR, represented by red contours over an inverted grayscale SDSS image of the central region of the Abell 407 cluster. Overlaid in blue are the VLA 4885 MHz image contours. Black circles mark the measurement areas in regions A, C and E. **Right:** Second order polynomial fit for region E. The data points which are upper limits are represented with empty markers and downward pointing arrows.

3.4 Discussion

Figure 3.1 shows the radio emission around the galaxies comprising the Abell 407 core (cataloged as UGC 2489). We can see that there are two lobes detected by the VLA, and diffuse emission that extends to the north-east. Going further out, this emission extends into a helical extension as seen in the grayscale WSRT image shown in the left panel of Figure 3.2.

The extended emission to the north-west continues out to an even larger distance than previously known, i.e. ~ 210 kpc from the central region of 4C 35.06. It is labeled as region E in the LOFAR image (marked by the red contours in the middle panel of Figure 3.2).

The overall source morphology is suggestive of (at least) two distinct episodes of radio activity in 4C 35.06. The extended emission is a remnant of the previous active phase, whilst the twin lobes detected by the VLA show the current activity cycle.

Using the morphological and spectral results described above, we propose that 4C 35.06 can be interpreted as a source in which we are seeing (at least) two subsequent episodes of AGN activity.

To explain the complex radio morphology as well as the spectral indices we have derived, we propose that the AGN is intermittently active as it moves in the dense environment in the cluster core. In this scenario, the AGN turned on sometime in the past, and has produced the helical pattern of emission visible in the left panel of Figure 3.2, possibly a sign of jet precession / merger during that episode of activity. Using LOFAR, we can trace the relic plasma from that episode of activity out to greater

distances from the core than ever before. The spectral index maps of the source indicate that this phase of activity has resulted in an FRI-type radio galaxy (spectrum steepening from the core towards the edges). Then, the AGN activity has ceased (perhaps gradually), and after a period of time during which the host galaxy moved some distance to the position we observe it at now, it has started again, producing the less steep spectrum inner lobes. These lobes have clear double morphology, they are clearly outlined and both morphologically and spectrally distinct from the surrounding steeper spectrum region. At the present epoch, we observe an aged FRI like large scale structure with an embedded restarted radio source, similar to the objects analyzed for example by Murgia et al. (2011), Giacintucci et al. (2007) and Ge & Owen (1994).

An alternative possibility would be that the different radio components (on small and large scales) belong to activity connected to different cores of UGC 2489 that were active at different times. For example, a core that could have been active in the past is the core labeled E in Schneider & Gunn (1982) based on its position in relation to the extended radio emission. However the radio emission over different spatial scales seems to be part of one coherent structure, centered on the currently active AGN, so we consider this hypothesis a less likely explanation of the observed morphology.

We have been unable to unambiguously determine a spectral break in the integrated source spectrum. The images we have lack the proper frequency coverage at high spatial resolution to allow us to determine a spectral break and in that way derive an age for the different emission regions.

We can estimate the AGN activity timescale by using galaxy kinematics. The cores of UGC 2489 are embedded in a common stellar envelope (probably a remnant of previous mergers). The radial velocity difference of the AGN host galaxy and the stellar envelope (as reported by Schneider & Gunn 1982) is 320 km s^{-1}. Assuming that the radial velocity is equal to the velocity in the plane of the sky, the projection of the section of the orbit traversed can be estimated by measuring the current angular separation between the AGN host galaxy and the "ridge" of steeper spectrum emission to the north-east. This separation is $13''$ or 11.3 kpc at the distance of UGC 2489. Under the assumption that the shutdown and restart were near instantaneous, we get an upper limit for the elapsed time between the two episodes of AGN activity of around 34.5 Myr. It matches the duration of the AGN dormant phase of some of the fading radio sources reported in the sample of Parma et al. (2007), and also is in agreement with the derived duration of the inactive phases for the sample of Murgia et al. (2011). It is larger compared to the off times found for the objects studied by Konar et al. (2013).

We can estimate at what frequency would the spectral break be located for the aged plasma originating from the past activity episode (before the shutdown). Following Murgia et al. (2011), the break frequency $\nu_b[GHz]$ is related to the magnetic field strength in the emission region $B[\mu G]$ and the time elapsed $t_s[Myr]$ since the start of the activity as:

$$\nu_b = \frac{1}{1+z} \cdot \left(1590 \cdot \frac{B^{1/2}}{(B^2 + B_{IC}^2) \cdot t_s} \right)^2$$

where $B_{IC} = 3.25(1+z)^2$ is the inverse Compton equivalent magnetic field. Assuming (for simplicity) that the active and shut down timescales are the same, $t_s = 70$ Myr in our case. Taking Region A as an example, we can estimate the value of the equipartition magnetic field by following the prescription of Miley (1980) to be $B = 2.7\mu$G. For the

spectral break frequency we get a value of $\nu_b = 1.8$ GHz. The spectrum of Region A shown in Figure 3.6 is consistent with a spectral break at that frequency.

Region E has a steeper spectrum. This claim is supported by the preliminary measurement at 150 MHz using LOFAR (Marisa Brienza, private communication), which is in agreement with our earlier estimates. This may mean that region E is older, it is actually the oldest source region that we observe.

Schneider & Gunn (1982) estimate that the UGC 2489 galaxies will merge due to dynamical friction (as evidenced by the stellar envelope surrounding the galaxies, created by stripping) in at most 2 Gyr, leaving us the possibility for the AGN to experience a series of outbursts before the final merger.

An interesting similar example is presented by the radio source 3C 338, hosted by the cD galaxy (NGC 6166) in the core of the galaxy cluster Abell 2199. This is a steep spectrum radio source ($\alpha < -1.5$). The radio morphology (Ge & Owen 1994) is suggestive of a restarted source, with at least two phases of AGN activity, where the oldest radio plasma appears to be offset from an active core. In these respects, this radio source is very similar to 4C 35.06. Burns et al. (1983) give a thorough overview of radio sources hosted by cluster core galaxies and suggest how the motion of the AGN host galaxy can give rise to a radio morphology similar to what we observe. We note that merging of galaxy cores on timescales of 10^7 yrs. can trigger an activity episode, which is in agreement with the derived dormant time for 4C 35.06.

It is worth mentioning that we have considered the possibility that the outer extended emission could be a mini cluster halo. They are found in the centers of relaxed clusters (as is Abell 407) and are associated with peaks in X-ray emission according to the review of Feretti et al. (2012). However, the morphology of 4C 35.06 makes it difficult to make a case for it being so.

In these types of restarted radio sources which are located in galaxy clusters, there is a possibility that the ICM medium is dense enough near the cluster core, thus heightening confinement pressure. It can have an impact on any older outburst of AGN plasma, keeping it confined for longer periods of time, and prolonging the time in which it can be detected by low frequency radio observations such as we are presenting in this work.

3.4.1 The presence of cold gas

The detection of neutral hydrogen adds a new interesting component to the study of this object.

While cold molecular gas is found in many systems (Edge 2001; Salomé & Combes 2003) it is less than would be expected if cooling dominated (McNamara et al. 2004). Recent results from ALMA (McNamara et al. 2014) have shown that the role of the cold gas is even more relevant as it can be used to trace feedback effects and outflows. The potential of using cold gas for tracing these effects has been already extensively shown using H I in the case of field radio galaxies (see e.g. Morganti et al. 2005, 2013, and references therein). Thus, tracing the presence and kinematics of H I in the center of clusters is an important complementary way to study cold molecular gas.

H I in absorption has been detected before in clusters (for example Abell 2597 (PKS 2322-123) O'Dea et al. 1994; Taylor et al. 1999), Abell 1795 (4C 26.42, van Bemmel et al. 2012) in addition to other famous objects in centers of clusters, like Hydra A (Taylor 1996) and Cygnus A (Struve & Conway 2010).

Although a systematic inventory of the occurrence of H I in clusters is not yet available, the statistics seems to be biased toward observing and detecting H I in the center of cooling core clusters. Abell 407 likely does not belong to this group, having a core which is not relaxed, but nevertheless we detect H I.

The fact that 4C 35.06 is a restarted radio source may suggest a connection between the presence of gas and the restarting of the radio-loud phase: indeed such a relation is often seen in non-cluster radio sources. There, restarted radio sources show an incidence of H I detections higher than in other extended sources (Saikia et al. 2007; Chandola et al. 2010, 2011), also Morganti et al. (2005).

The H I profile detected in 4C 35.06 appears to be broader than in typical radio galaxies (Geréb et al. 2014).

However, it resembles some of the profiles found in other clusters (in particular Abell 2597 and Abell 1795 mentioned above) that show relatively broad wings in the H I absorption profile, perhaps a signature of the more disturbed kinematics of the gas due to the cluster environment.

The radial velocity of the AGN host galaxy is 14120 km s^{-1}, according to Schneider & Gunn (1982), while as mentioned above, the H I absorption profile peaks at 13858 km s^{-1}, indicating a dominant blueshifted component that could naively be associated to an outflow. On the other hand, the broad wings of the profile (both blueshifted and redshifted) could suggest that the kinematics of the gas is much more complex. However, it is worth remarking that McNamara et al. (2014) suggested the presence of an outflow of cold (molecular) gas derived from ALMA data in Abell 1835 as a result of the interaction between the gas and the radio source. If this is confirmed, it may suggest that at least part of the gas is associated with outflows of cold gas in clusters; the case of 4C 35.06/Abell 407 could be one example.

In low-luminosity radio sources with low-excitation spectra like 4C 35.06, the possibility of the activity being supported by gas cooling from the hot galactic halo via e.g. Bondi accretion has been suggested by several studies (Croton et al. 2006; Allen et al. 2006; Hardcastle et al. 2007; Balmaverde et al. 2008). Taking the core luminosity measured by Liuzzo et al. (2010) and following the reasoning of Balmaverde et al. (2008), connecting the radio core luminosity to the radio jet power and relating that to the Bondi accretion power ($P_B = 0.1\dot{M}c^2$), we estimate that the accretion rate of 4C 35.06 is on the order of 0.2 $\dot{M}_{\odot} yr^{-1}$.

If part of the detected H I is associated with infalling gas (something possible given the width of the profile that spans also to redshifted velocities) it could provide the required fueling material. The gas could be chaotically losing angular momentum in the ISM of the AGN host and accreting, as suggested by Gaspari et al. (2013).

Thus, although most of the H I profile 4C 35.06 appears to be blueshifted, the width of the profile requires more detailed (and higher spatial resolution) observations in order to pin down the location and the exact kinematics of the gas.

3.5 Conclusions

As part of a commissioning LOFAR observation of the nearby Compact Steep Spectrum radio source B2 0258+35A, we have made a 61 MHz map of 4C 35.06 (B2 0258+35B), a radio source hosted by the core of the galaxy cluster Abell 407. This source has a complex morphology on several spatial scales. We used our LOFAR image in combination with

archival VLA imaging as well as VLSS, WENSS and other survey data to argue that the most extended emission can be interpreted as a remnant of a past episode of AGN activity. The integrated spectral index is moderately steep and shows no signs of spectral curvature. We confirm the existence of an extended emission region and derive spectral index maps of the inner parts of the source closer to the AGN.

We discuss a few possible scenarios regarding the nature of the source and conclude that the best fitting explanation is that we observe two distinct episodes of AGN activity in 4C 35.06.

We also present a discovery of H I in absorption close to the AGN host galaxy. The H I detection has a broad profile, suggestive of a complex gas dynamics and a possible outflow.

A better handle of the timescales involved can be obtained by better spectral coverage at sufficient resolution to disentangle the various source structures. Depending of the relative contributions of the smaller scales, our study shows that it is possible to use the integrated source spectrum as a proxy to learn more about the spectral behavior on smaller scales and the source activity history. This is important in studies of more distant sources which in general would be unresolved in future surveys.

Chapter 4

AGN duty cycle estimates for the ultra-steep spectrum radio relic VLSS J1431.8+1331

The universe seems neither benign nor hostile, merely indifferent.

– Carl Sagan

Abstract

Steep spectrum radio sources associated with Active Galactic Nuclei (AGN) may contain remnants of past AGN activity episodes. Studying these sources gives us insight into the AGN activity history. Novel instruments like the LOw Frequency ARray (LOFAR) are enabling studies of these fascinating structures to be made at tens to hundreds of MHz with sufficient resolution to disentangle their complex morphology.

Our goal is to characterize the integrated and resolved spectral properties of VLSS J1431+1331 and estimate source ages based on synchrotron radio emission models, thus putting constraints on the AGN duty cycle.

Using a broad spectral coverage, we have derived spectral and curvature maps, and used synchrotron ageing models to determine the time elapsed from the last time the source plasma was energized. We have used LOFAR, Giant Metrewave Radio Telescope (GMRT) and Jansky Very Large Array (VLA) data.

We have confirmed the morphology and the spectral index values found in previous studies of this object. Based on our ageing analysis, we infer that the AGN which created this source currently has very low levels of activity, or that it is switched off. The derived ages for the larger source component range from around 60 to 130 Myr, hinting that the AGN activity decreased/stopped around 60 Myr ago. We observe that the area around the faint radio core located in the larger source component is the youngest, while the overall age of the smaller source component shows it to be the oldest part of the source.

Our analysis suggests that VLSS J1431.8+1331 is an intriguing, two-component source. The larger component seems to host a faint radio core, suggesting that the source may be an AGN radio relic. The spectral index we observe from the smaller component is distinctly flatter at lower frequencies than the spectral index of the larger component, suggesting the possibility that the smaller component may be a shocked plasma bubble. Studying the integrated source spectrum, we deduce that its shape and slope can be used as tracers of the activity history of this type of steep spectrum radio sources. We discuss the implications this conclusion has for future studies of radio sources having similar characteristics.

A. Shulevski, R. Morganti, P. D. Barthel et al.
submitted to *Astronomy & Astrophysics*

4.1 Introduction

Active Galactic Nuclei (AGN) are cosmic powerhouses, which produce prodigious amounts of energy and deposit it into the interstellar and the intergalactic medium (ISM, IGM). In order to estimate the total energy output of an AGN over cosmic time, it is necessary to determine its duty cycle; the length of time during which the AGN is active and shut down. This is important, since while we have some knowledge of the energy output of an AGN during the duration of the active phase (Best et al. 2005; Shabala et al. 2008), we have a limited insight into the AGN duty cycle (Murgia et al. 2011; Konar et al. 2013). Evidence for multiple episodes in radio AGN activity has been growing steadily (Schoenmakers et al. 2000; Best 2009; Saikia & Jamrozy 2009; Dwarakanath & Kale 2009). Parma et al. (2007) have shown that in their source sample of several AGN radio relics the period of time that an AGN is active is $10^7 - 10^8$ years, while the time between the active phases is an order of magnitude shorter. The missing pieces of information are important for various reasons. The (total) energy budget is important to the study of galactic evolution as the AGN energy output influences the cooling of gas and galactic assembly. Another important area of astrophysics which is affected is the star formation history in the host galaxy, as AGN "feedback" can potentially quench star formation through influencing the ISM. The AGN fuelling (Ciotti et al. 2010; Gaspari et al. 2013) can potentially be also interrupted.

An observational signature of a "switched off" AGN is the steep spectrum of the associated radio emission at high frequencies ($\alpha < -1.5$)[1], leading to brighter emission at low frequencies. The reason for this is that to first order (neglecting other energy loss mechanisms), the plasma ejected from the AGN during its active phase will mainly lose energy through synchrotron radiation and inverse Compton (IC) scattering of electrons off Cosmic Microwave Background (CMB) photons. As a consequence, high energy particles which radiate the most at high radio frequencies lose their energy fastest. This produces a characteristic synchrotron radio spectrum which over time evolves in such a way that most of the particles which still radiate after the AGN has shut down are low energy particles and the radio emission is strongest at low frequencies. Thus, low frequency radio surveys are the best tool for detecting such sources.

van Weeren et al. (2009, 2011) have studied several steep spectrum sources identified by matching the VLSS and NVSS[2] catalogues. One of these, VLSS J1431.8+1331 was identified as being potentially an AGN relic. It has an ultra steep ($\alpha \simeq -2$) spectrum at high frequencies with a radio morphology pointing towards a complex activity history. It presents two distinct source regions, a larger one and a smaller one (henceforth labeled A and B respectively), connected by a faint bridge of radio emission (Figure 4.1). Region A appears to contain a faint radio core and has a steep spectrum showing little spectral curvature compared to region B whose spectrum flattens out at low frequencies.

The host galaxy of VLSS J1431.8+1331 is the Brightest Cluster Galaxy (BCG) of the galaxy cluster maxBCG J217.95869+13.53470 (Koester et al. 2007), located at a redshift[3] of $z = 0.1599$.

The cluster has been observed in X-rays by Ogrean et al. (2011) using XMM Newton.

---

1 We use the $S \propto \nu^{\alpha}$ definition for the spectral index α throughout this writing.

2 VLSS is the VLA Low frequency Sky Survey carried out at 74 MHz (Cohen et al. 2007). NVSS stands for the NRAO VLA Sky Survey carried out at a frequency of 1.4 GHz (Condon et al. 1998)

3 The adopted cosmology in this work is: $H_0 = 70.5$ km s^{-1}Mpc^{-1}, $\Omega_M = 0.27$, $\Omega_\Lambda = 0.73$. At the red-shift of VLSS J1431+1331.8 $1'' = 2.747$ kpc (Wright 2006).

They have derived temperature excesses to the north and west of the BCG, and a slight increase in entropy coinciding with the south-west component of radio emission. Based on these observations, they propose that maxBCG J217.95869+13.53470 has interacted with a smaller group of galaxies located to the north-east of the BCG. According to the analysis presented, the smaller galaxy group came from the south-east, and we are observing the system a short while after closest approach. Shocks related to this process might have compressed a bubble of plasma expelled by the AGN and revived its synchrotron emission, thus giving rise to the smaller region of radio emission to the south-west.

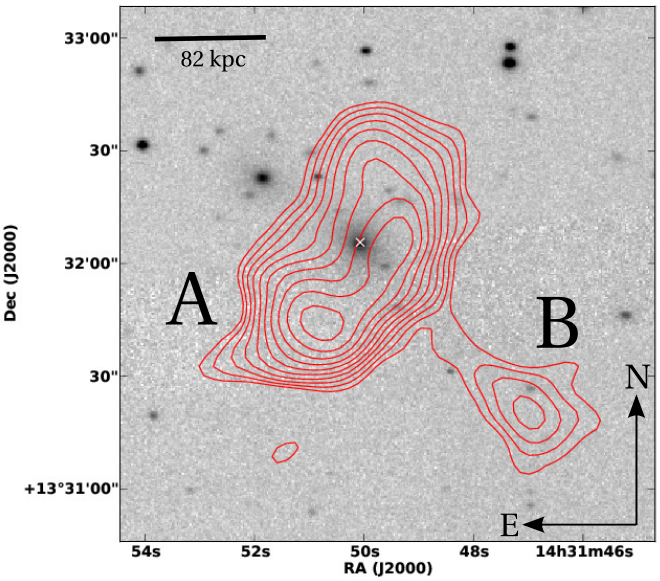

Figure 4.1: LOFAR HBA image contours (red) of VLSS J1431.8+1331 (centered on 148 MHz and with a bandwidth of 48 MHz) superposed on a Sloan Digital Sky Survey (SDSS) grayscale image of the galaxy cluster maxBCG J217.95869+13.53470. Ten log spaced contour levels are shown in red spanning the surface brightness interval between -10 and 100 mJy beam^{-1}, with a beam size of $10.5'' \times 8''$. The white cross marks the position of the Bright Cluster galaxy (BCG) AGN host and labels mark the source components.

In this work, we aim to investigate this hypothesis and to derive more information on the physical nature of the various source components of VLSS J1431.8+1331. Using observations made with the LOFAR telescope's (van Haarlem et al. 2013) high band antennas, we perform spectral index mapping down to around 140 MHz with a resolution comparable to that of the Giant Metrewave Radio Telescope (GMRT) and the Jansky Very Large Array (VLA) study made by van Weeren et al. (2009) at higher frequencies. The resulting broad-band data set has enabled us to study in detail the ageing of the plasma across the source. By doing this, we can put constraints on the timescales involved in the past activity of the AGN responsible for the radio emission, and compare our findings with the results of previous studies. The organization of this paper is as follows. Section 4.2 describes our data set and overviews the data reduction procedures. In

Section 4.4 we present the results of the data analysis, and we discuss our findings in Section 4.4. We finish by presenting our conclusions in Section 4.5.

4.2 Observations and data reduction

The target was observed on the night of February 17, 2013 for a total on source time with LOFAR's high band antennas (HBA) of 5.7 hours. The HBA observation was taken in interleaved mode, i.e. 3C 295 was observed as a calibrator source for two minutes, following by a scan of the target of 11 minute duration with a one minute gap between calibrator and target scans allowing for beam forming and target re-acquisition. 325 sub-bands were recorded covering 64 MHz of bandwidth between 116 MHz and 180 MHz. Each sub-band has 64 frequency channels spanning a bandwidth of 200 kHz. The integration time was set to 2 seconds for both calibrator and target. Four polarizations were recorded. The HBA station field of view (FoV) spans around 4 degrees full width at half maximum (FWHM).

Table 4.1: LOFAR observation configuration

Central Frequency [MHz]	140
Bandwidth [MHz]	64
Integration time	2 seconds
Observation duration	6 hours
Polarization	Full Stokes
UV range	$100\lambda - 20k\lambda$

The data were pre-processed by the observatory pipeline (Heald et al. 2010) as follows. Each sub-band was automatically flagged for RFI using the AOFlagger (Offringa et al. 2012), and averaged in time to 10 seconds per sample and in frequency by a factor of 16, which gives us 4 channels per sub-band in the output data. The calibrator data were used to derive amplitude solutions for each station using the Black Board Self calibration - BBS (Pandey et al. 2009) tool which takes into account the time and frequency varying LOFAR station beams. The calibrator flux density scale was set according to Scaife & Heald (2012). The obtained (complex) station gain solutions were used to fix the target amplitude scale.

Only the Dutch LOFAR stations were used. The amplitude corrected target visibilities were phase (self)calibrated incrementally, using progressively longer baselines to get to the final resolution (Vilchez et al. in prep.). The initial phase calibration model was derived from the VLSS catalog covering the FoV out to the first null of the station beam. It included spectral index information for each source. Before initializing the calibration, we have concatenated the data into 4 MHz (20 SB) groups previously averaging each sub-band to 1 frequency channel. We have chosen this setup to maximize the S/N while maintaining frequency dependent ionospheric phase rotation to a manageable level. We have not performed any directional solving and did not explicitly correct for ionospheric effects.

The station beams are complex valued, time, frequency and direction dependent, and are not the same for all of the stations. Taking this into account, the imaging was done by using the LOFAR imager (Tasse et al. 2013), which incorporates the LOFAR beam

and uses the A-projection (Bhatnagar et al. 2013) algorithm to image the entire FoV. The imager does not (at this stage) implement spectral index correction when it does the multi-frequency imaging. We have used Briggs weights (Briggs 1995) with the robustness parameter set to -2 (uniform weights) and performed a UV plane selection to include all of the baselines to achieve the highest possible resolution. Discarding 8 MHz from either edge of the band, we have imaged the data such as to obtain a final HBA data-set of six images of 8 MHz bandwidth each. We have averaged these images together to obtain one broadband image. Deconvolution artifacts are present around the sources in the image, mostly due to residual calibration errors caused by ionospheric disturbances.

Given the low declination of the target, some uncertainties still exist about the accuracy of the LOFAR in-band spectral index. Thus, we have decided to use only two LOFAR HBA images (given in table 4.2) in our spectral analysis.

In addition to our LOFAR data, we use GMRT and VLA data kindly supplied by RvW to constrain the spectral index and curvature. The properties of the dataset are listed in Table 4.2. For the purposes of our work, we list the properties of the smoothed GMRT and VLA images (adapted to the LOFAR HBA synthesized beam size). The r.m.s. noise values for each of the flux measurements were derived according to Klein & Emerson (1981) taking into consideration the background noise away from bright sources and scaling for the contribution of the size of the measurement region used on the target. To account for the flux uncertainties stemming from the 3C 295 flux scale and the imperfections of the beam model, we have added in quadrature 20% of the measured flux density value to the derived noise in the case of the LOFAR measurements. The same was done for the GMRT measurements, but the flux density value added was 5% (Chandra et al. 2004). The details of the GMRT and VLA data sets and the reduction procedure can be found in van Weeren et al. (2009, 2011).

Table 4.2: Details about the images used in our analysis.

Instrument	ν [MHz]	$\Delta\nu$ [MHz]	σ [mJy beam^{-1}]
LOFAR[a]	144	48	0.5
LOFAR[a]	135	8	2.3
LOFAR[a]	145	8	1.8
GMRT[bd]	325	32	0.1
GMRT[bd]	610	32	0.1
VLA[bd]	1425	100	0.05
VLA[cd]	1425	100	0.02

[a] Beam size: $10.5''$x $8''$
[b] Smoothed to the LOFAR beam size.
[c] Original VLA resolution of $1.6''$x $1.5''$.
[d] Details about the data set and imaging setup can be found in van Weeren et al. (2011).

4.3 Results

4.3.1 Radio morphology

Figure 4.2 shows the LOFAR image of the target spanning the HBA band. We can discern two different source regions (described in detail by van Weeren et al. 2011), the

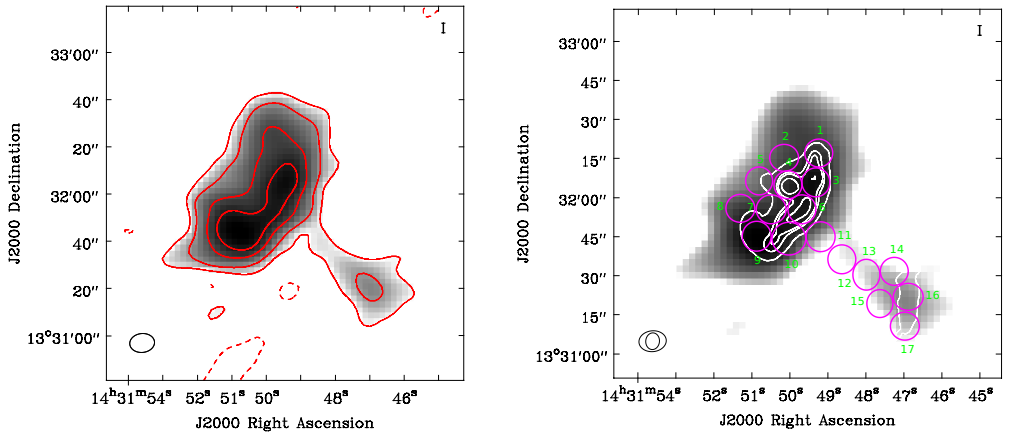

Figure 4.2: Left: LOFAR HBA grayscale image of VLSS J1431.8+1331. Overlaid contours (in red): $[-6, 20, 40, 90, 150] \times \sigma$, $\sigma = 0.5$ mJy beam^{-1}. **Right:** Measurement regions (outlined in magenta) used in the spectral (ageing) analysis. VLA 1425 MHz high resolution contours (van Weeren et al. 2011) are shown in white, outlining a core inside region 4. Contour levels: $[-3, 3, 9, 12, 20] \times 4 \cdot 10^{-2}$ mJy beam^{-1}. The beam sizes are indicated in the lower left corner.

larger and brighter one (A) to the north-east, and a smaller region (B) to the south-west connected by a faint "bridge" of radio emission. Both regions seem to be slightly curved to the north-east; this is more noticeable for region B in the higher resolution image, outlined in contours in the right panel. A hint of a faint radio core is visible in the high resolution VLA image of van Weeren et al. (2011), while the brightest part of the target in the LOFAR image is the south-eastern part of region A.

The right panel in Figure 4.2 shows the flux density measurement regions used in the subsequent analysis. The measurement areas have been chosen to be of similar size to the synthesized LOFAR beam. We have measured the flux density in each area using our maps (LOFAR, GMRT and VLA), thus covering about a factor of 10 in frequency range (144 to 1425 MHz). All of the maps were convolved to the same restoring beam size as that of the HBA beam of $10.5'' \times 8''$.

4.3.2 Spectral analysis and radiative ages

In what follows, we use the LOFAR measurements to extend the spectral index analysis to the lowest frequencies ever for this object. Our goal is to trace the lowest energy particle population to better constrain the radio spectra at low frequencies. We also map the radiative ages over the source surface by fitting synchrotron ageing models to our data.

Spectral index and curvature

We have derived spectral index and spectral curvature (SPC = $\alpha_{\rm low} - \alpha_{\rm high}$) maps of the target. In Figure 4.3 we present the spectral index derived from the LOFAR HBA, GMRT and VLA maps and the corresponding spectral curvature across the source. The spectral indices were derived by least squares fitting of a power law to the data for each pixel of the maps. Pixels which had a value below 15σ for each map were blanked. This was mainly done to avoid the artifacts present around the target in the LOFAR HBA images. The maximum UV distance of the LOFAR data of 20 $k\lambda$ corresponds to the one of the GMRT and VLA of 22 $k\lambda$ ensuring that the structures visible in the maps are not artifacts.

Region A shows a relatively steep low frequency spectral index of $\alpha \sim -1.2$ around the radio core and the western edge. The spectral index steepens to around $\alpha \sim -2$ going towards the edges. The spectral curvature map indicates that for this source component the spectrum is flat around the radio core, with breaks at higher frequencies developing at the western edge and at the south-east.

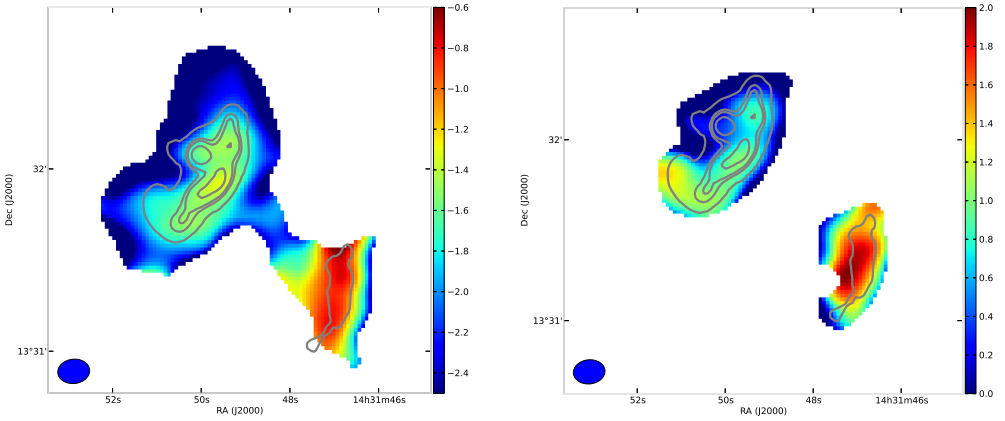

Figure 4.3: Left: α_{144}^{325} spectral index map of VLSS J1431+1331. **Right:** $\alpha_{144}^{610} - \alpha_{610}^{1425}$ spectral curvature map using LOFAR, GMRT and VLA images. Overlaid are 1425 MHz high resolution VLA contours (levels as in Figure 4.2). The beam size is indicated in the lower left corner.

Ages

Synchrotron spectral ageing theory was established by Kardashev (1962). Later, these foundations were expanded by Pacholczyk (1970); Jaffe & Perola (1973) and Tribble (1993); Komissarov & Gubanov (1994); Murgia et al. (1999, 2011) among others. Appendix B gives an overview of the ageing models we have used in this work.

When the AGN is active, it accelerates charged particles resulting in them having a power law energy distribution. The particles lose energy mainly by radiating synchrotron radiation and through IC scattering off of CMB photons. The radio spectrum has a

spectral index α_0 at low frequencies which depends on the energy distribution of the radiating particles and which is commonly known as injection (spectral) index. Typical values for the injection spectral index are $\alpha_0 \in [-0.6, -0.8]$. At high frequencies, due to the preferential cooling of high energy electrons through synchrotron radiation and IC scattering, the radio spectrum steepens, and a spectral break develops. After the AGN shuts down, the active radio regions stop being replenished with energetic particles, and the spectrum exhibits a steep drop-off at high frequencies.

In order to get an estimate on the ages of the different regions, we have fitted synchrotron ageing models to the data. The fitting was performed using the Kapteyn package (Terlouw & Vogelaar 2012) utilizing a Python based code which implements the models (see Appendix B for details). We have used models with a Jaffe-Perola energy loss term assuming instantaneous particle injection and continuous particle injection followed by ageing (JP and KGJP respectively) to estimate the ages. We have also tried a continuous injection only (CI) model for the source area containing the radio core (area 4) and found it to be inconsistent with the data (Figure 4.4).

The determination of the radiative ages requires knowledge about the magnetic field. We calculate it according to Miley (1980) using the assumption of equipartition between the energy contained in the field and relativistic particles, taking for the cutoff frequencies values of 10 MHz and 10 GHz and an electron to proton ratio equal to unity. The calculation was done for regions A and B separately, taking the path length through the regions to equal the average of their major and minor axes as projected on the sky. We set the spectral index to $\alpha_{144}^{1425} = -1.9$ for both regions for the purposes of this calculation (estimated from our spectral index map and the ones given in van Weeren et al. 2011). Taking the average value of the derived magnetic field for both regions, we find that $B = 4.4\,\mu$G.

This equipartition value for the magnetic field needs to be corrected, taking into account a cutoff in the particle energy instead of a cutoff in the frequency of the radiation (Brunetti 2004). We have adopted the method proposed by Brunetti et al. (1997) (see also Beck & Krause 2005). The ratio of energy between protons and electrons is assumed be unity. Further, we have used spectral index values of -1 and -1.8 over the entire energy band as well as two different values for the low energy cutoff, expressed via the electron Lorentz factor γ. The derived magnetic field values are given in Table 4.3. Different parameter assumptions change the magnetic field by a factor of 3. We adopt a magnetic field value of $4\,\mu$G in our further analysis which is in agreement with what is found for similar sources (Murgia et al. 2011).

We have fitted the JP and KGJP models to our data for each area of the source using the following procedure. The free parameters of the model fit were the active and switched-off times as well as a flux scaling factor, while we have kept the magnetic field and injection spectral index fixed. To understand the injection spectral index dependence, we have taken 20 different values for the injection spectral index evenly distributed between -0.6 and -1.5 and performed the model fitting for each source area separately using different injection spectral index values.

We find that the best fit to the data is obtained for the models which use the JP assumption for the energy loss. Most of the source areas are best fit with a model which assumes an infinitesimally short duration particle acceleration phase and ageing (JP), while some are best fit with a model assuming a period of continuous injection and then ageing (KGJP). Our best fit parameter values are given in Table 4.4, and the derived

Table 4.3: Equipartition magnetic field $B_{\rm eq}$ and corresponding corrected values $B_{\rm eq}^{\rm cor}$.

α	$\gamma_{\rm min}$	$B_{\rm eq}[\mu{\rm G}]$	$B_{\rm eq}^{\rm cor}[\mu{\rm G}]$
-1[a]	100	2.18	3.86
-1[a]	700	2.18	2.37
-1.8	100	4.40	11.26
-1.8	700	4.40	3.925

[a] Injection spectral index. The IC equivalent magnetic field for the redshift of J1431.8+1331 is $B_{\rm IC} = 3.57\,\mu$G.
The minimum magnetic field (resulting in maximum radiative ages) is $B_{\rm min} = 2.52\,\mu$G.
The correction to the derived equipartition magnetic field value is performed according to Brunetti et al. (1997) and Beck & Krause (2005).

Table 4.4: Best fit $t_{\rm on}$, $t_{\rm off}$ and α_0 values for different source regions.

$N_{=}^{o}$	$t_{\rm on}$ [Myr]	$t_{\rm off}$ [Myr]	α_0	χ^2
3	20.4 ± 0.002	108.4 ± 2.8	$-0.88^{+0.28}_{-0.38}$	0.17
4	-	60.0 ± 3.5	-1.12 ± 0.38	0.72
6	22.9 ± 6.3	117.4 ± 0.002	$-0.74^{+0.14}_{-0.33}$	0.47
7	-	48.6 ± 5	$-1.50^{+0.47}$	0.23
8	-	91.3 ± 9.3	$-1.50^{+0.47}$	1.72
9	-	113.2 ± 3.5	$-1.03^{+0.38}_{-0.33}$	0.01
10	-	104.7 ± 2.7	$-0.93^{+0.33}_{-0.28}$	0.01
11	-	69.8 ± 10.9	$-1.50^{+0.43}$	2.72
12	-	97.2 ± 0.01	$-1.50^{+0.66}$	1.91
13	-	60.6 ± 13.9	$-1.50^{+0.81}$	1.25
14	-	121.4 ± 5.9	$-0.60_{-0.29}$	1.49
15	-	131.6 ± 13.5	$-0.60_{-0.66}$	0.51
16	7.8 ± 7	132.4 ± 2.8	-0.6	4.98
17	-	123.1 ± 7.5	$-0.6_{-0.14}$	2.34

The region age is: $t_{\rm s} = t_{\rm on} + t_{\rm off}$. For regions where $t_{\rm on}$ is not listed, the ageing only (JP) model provided the best fit, in which case $t_{\rm s} = t_{\rm off}$
We test the acceptance of the hypothesis that the data is consistent with the model using a significance level with a probability of 5%. The χ^2 threshold for the 95% confidence interval (Bevington & Robinson 2003) for two degrees of freedom is $\chi^2_{95\%} = 5.99$.

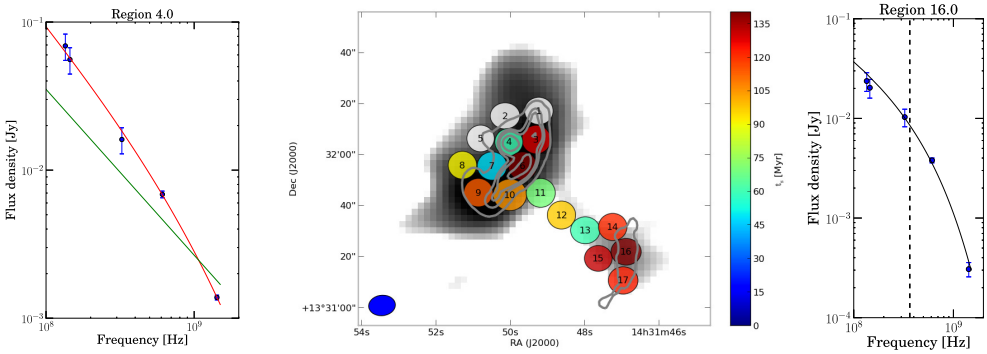

Figure 4.4: Derived total ages ($t_s = t_{on} + t_{off}$) for different areas using ageing model (JP and KGJP) fits to the data. The areas are marked with coloured ellipses overlaid on a LOFAR grayscale map of the target. Overlaid are also VLA 1425 MHz high resolution contours in gray (same as in Figure 4.2) indicating the position of the radio core in area 4. Areas for which all the model fits were rejected are marked in white. Model fits for areas 4 and 16 are shown in the left and right panels respectively. The green line in the plot for area 4 represents the (rejected) CI model fit. The break frequency for area 16 is marked with a dashed black vertical line. Detailed fit results are shown in Table 4.4.

ages for the various source areas are presented in Figure 4.4.

For regions 7, 8, 11, 12 and 13 the best fit injection index was the steepest in the range, and we could only place an upper limit on it, while for regions 14, 15 and 17 the inverse was true. For region 16, the only model fit which was not rejected was the one having an injection index of $\alpha_0 = -0.6$. Having all this in mind, judging from the regions for which we have constrained the injection index, we deduce that the youngest part of the source is located in region A,in the area around the faint radio core (region 4), while the oldest source region is region B. The derived ages range from 60 to 130 Myr. The models indicate that for region B the injection spectral index has a value of $\alpha_0 = -0.6$, while for region A the best fit models are those with the injection index of around $\alpha_0 = -1$. We further discuss the implications of these findings in Section 4.4.

Colour-colour representation and shift diagrams

The peculiar morphology of the source suggests that complex processes are shaping the emission regions and influencing their energy balance. We investigate whether the energy loss is predominantly due to synchrotron ageing and IC losses.

To do this, and to gain more insight into the plasma properties across the source, we have employed the colour-colour representation described by Katz-Stone et al. (1993). Such plots provide a simple overview of the measurements compared to different ageing models and allow for easier determination which theoretical models best describe the measurements. Also, the outlined shapes in this representation are conserved w.r.t. changes in the magnetic field and adiabatic compression / expansion.

We have constructed two spectral indices from our data, low and high. The low spectral index was obtained by fitting a first order polynomial through the 135, 145 and 325 MHz data points for each region, and the high frequency spectral index was obtained by a first order polynomial fit through the 325, 610 and 1425 MHz data points. The resulting colour-colour plots for a representative set of source regions are shown in Figure 4.5. This procedure is similar to the spectral curvature derivation described previously, with the curvature being the difference between the low and high spectral index. Plotting these two indices against each other is another way of distinguishing source regions with different properties which can give additional insight into the physical processes at work in the emission regions.

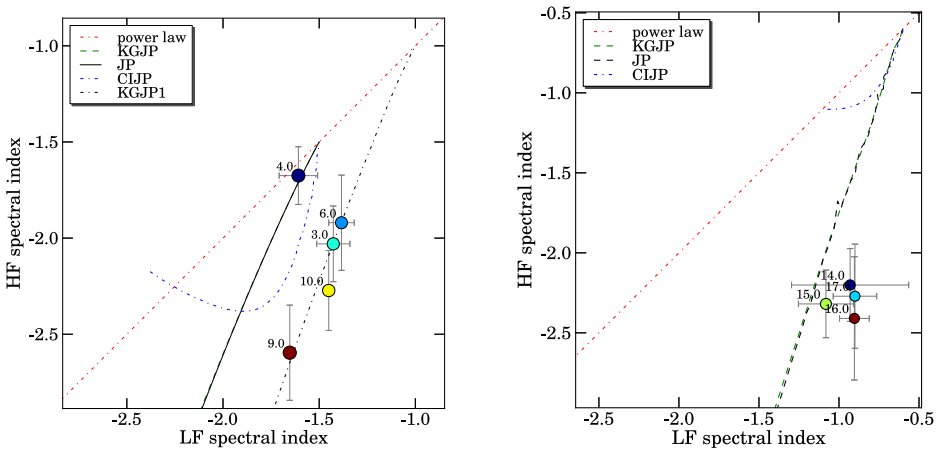

Figure 4.5: Colour-colour plots for different regions across the source. The red dashed-dot line marks the locus of points for a power-law spectrum. **Left:** The dashed green line and the solid black line (overlapping) represent the locus of points taken by KGJP and JP models respectively with injection index of $\alpha_0 = -1.5$. The dash-dot blue line represents a CIJP model with the same injection index. The dash-dot black line represents a KGJP model with injection index of $\alpha_0 = -1$. **Right:** The dashed green line and the dashed black line (overlapping) represent the locus of points taken by KGJP and JP models respectively with injection index of $\alpha_0 = -0.6$. The dash-dot blue line represents a CIJP model with the same injection index. Marker sizes are proportional to the low-frequency spectral indices for a given region and marker colours are proportional to the high-frequency spectral indices. Number labels mark the regions.

In the colour-colour plot for source region A we have taken into account only the measurement areas for which we have a good constraint on the injection index. We have not performed such a pre selection for the colour-colour plot for region B, since in that case we have a more limited number of measurement areas.

We can see that area 4 is close to a power law, but that it is best described by KGJP or JP models having a steep injection index (determined by the intersection point of the

ageing models and the power law line on the diagram) of $\alpha_0 = -1.5$. Measurement areas 3, 6, 9 and 10 are best described by a KGJP model with an injection index of $\alpha_0 = -1$. The areas in the source region B show larger scatter and are not well represented with a single ageing model; a KGJP or JP model with injection index of $\alpha_0 < -0.6$ is indicated by the measurements and supported by the derived injection indices and ages in Section 4.3.2.

Following the reasoning of Katz-Stone & Rudnick (1994), Rudnick et al. (1994); Rudnick (2001) and van Weeren et al. (2012a) we have performed a spectral shift analysis on regions 3, 6, 9 and 10 to gain further insight into our target and test the assumptions we have made during the spectral analysis. We have chosen these resions since they outline a single curve in the colour-colour space consistent with a particuler ageing model.

The idea behind the shift technique is as follows. Assuming that the energy loss of the particles is predominantly through synchrotron and IC mechanisms and that the magnetic field does not vary significantly across the source, then the spectra for all of the regions are self-similar, the only difference between them being the position of the break frequency. Further, all of the spectra should align by shifting them in the frequency-flux density plane if the dominant energy loss mechanism is synchrotron radiation and IC scattering and if our line of sight samples similar source regions. We have chosen region 9 as reference (it has the best model fit) and have shifted the spectra for regions 3, 6 and 10 so that their break frequencies matched that of region 9. The break frequencies for the KGJP model were determined using (Murgia et al. 2011):

$$\nu_{\rm b}^{\rm low} = \left(\frac{1590}{(B^2 + B_{\rm CMB}^2)t_{\rm s}}\right)^2 \cdot \frac{B}{(1+z)} \tag{4.1}$$

and

$$\nu_{\rm b}^{\rm high} = \nu_{\rm b}^{\rm low}\left(\frac{t_{\rm s}}{t_{\rm off}}\right)^2 \tag{4.2}$$

where $t_s = t_{on} + t_{off}$. For the JP model, we have set $t_{on} = 0$. The procedure has produced the shift diagram for these regions, shown in the left panel of Figure 4.6. It shows by how much the spectrum of each region was shifted in the $\log(\nu) - \log(S)$ plane. The data points for all of the regions after the shift, producing the global spectrum, are shown in the right panel of Figure 4.6. We have also fitted JP and KGJP models (Appendix B) through all of the shifted data points to show that indeed the shifted spectra are self-similar and taken together produce a spectrum which is consistent with radiative ageing and IC scattering being the dominant energy loss mechanism of the electrons.

The shifts made to the individual spectra to line them up can give us information about the physical parameters of the source (Katz-Stone & Rudnick 1994; van Weeren et al. 2012a). Specifically, shifts on the $log(\nu)$ axis relate to $\gamma^2 B$, while shifts along the $log(S)$ axis depend on $N_{\rm tot}B$, where $N_{\rm tot}$ is the total number of energetic particles in the source volume for a given beam size.

We can fit a straight line to the shifts in the $log(\nu) - log(S)$ plane (Figure 4.6) for the measurement areas belonging to source component A. This means that the spectra of individual regions are self-similar, meaning that there are no significant variations in either particle energy or magnetic field value from one area to another, and that the

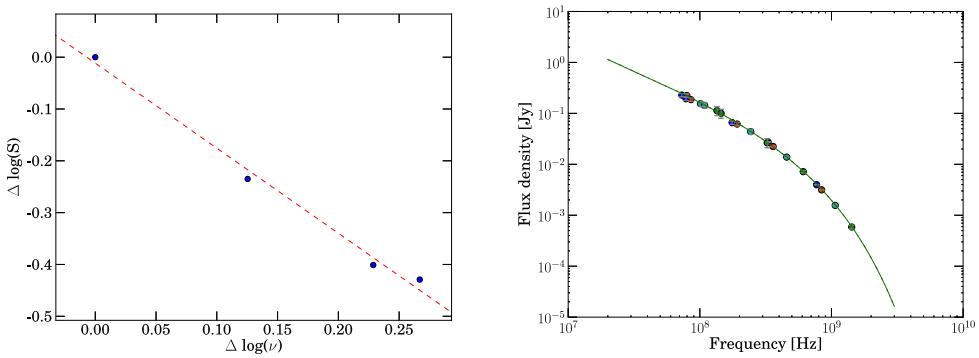

(a) The slope of the fit is −1.6. **(b)**

Figure 4.6: Spectral shifts in $\log(\nu) - \log(S)$ for regions 3, 6, 9 and 10 (4.6a). The red dashed line shows the best linear fit to the data points. Shifted data points giving the global spectrum are given in panel 4.6b. Different colours are used to mark the data points belonging to different regions. The best JP and KGJP model fits are plotted in red dashed-dot line and green lines respectively (overlaping, since there is essentially no difference between the models for these regions).

spectral shapes are the result of synchrotron ageing and IC losses. Further, the slope of the fit indicates the injection index.

The fact that the shifted data are fitted so well using radiative ageing models shows that, indeed, synchrotron ageing and IC scattering are the dominant energy loss mechanisms. The values we get for the injection index and the fact that they match what we had used for α_0 previously also serve to strengthen the inner consistency of our analysis.

The steepness of the injection index

The derived results on the ages of source region A are consistent with it being a relic from a past AGN activity episode; this claim is mainly supported by the derived age of area 4 compared to its surroundings and its identification with the faint radio core. There is a consistency throughout our model fits: for region A, the models with steeper injection index ($\alpha_0 \in [-0.9, -1.5]$) than what is usually accepted as standard value ($\alpha_0 \in [-0.6, -0.8]$) are the ones which best fit the data. We discuss the implications of the steep injection index further in Section 4.4.

Interestingly, Harwood et al. (2013) find larger than expected injection indices for their sample of FRII radio galaxies.

The integrated flux density spectrum

The integrated spectrum is slightly curved and steep. To see how spectral ageing in different regions of the source can affect the integrated spectrum, we have fitted a KGJP model to the integrated flux density measurements, and compared the results with the region fits done previously.

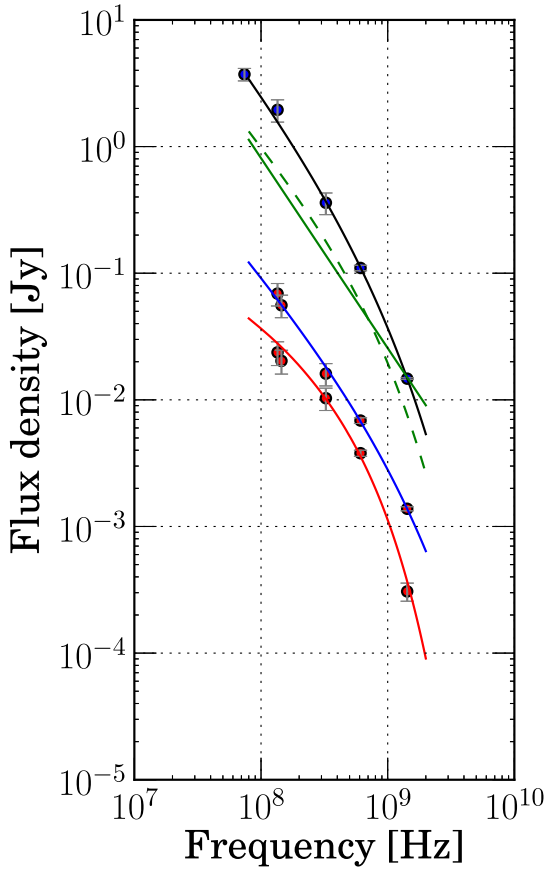

Figure 4.7: JP and KGJP model fits for regions 4 (blue) and 16 (red) are plotted along with the corresponding data points (LOFAR HBA, GMRT and VLA). The sum of the fits for all regions is represented by the green dashed line. The integrated flux density data points (VLSS, LOFAR HBA, GMRT and VLA) are best fitted by a KGJP model (black line) with an injection index of $\alpha_0 = -1.23 \pm 0.37$ and $t_{\rm on} = 0.1$ Myr, $t_{\rm off} = 77.7$ Myr. The measurement regions do not cover the source completely at lower frequencies, hence the sum of the fits does not precisely follow the integrated flux density. a CI model which is rejected by the integrated flux data is represented with a green line.

In Figure 4.7 we are showing the integrated flux density measurements of VLSS J1431.8+1331 from our LOFAR HBA, GMRT and VLA data sets as well as the VLSS catalog value. We can see that the integrated flux density follows the sum of the fitted flux densities for the different regions; the offset can be explained by the fact that our measurement regions do not perfectly cover the entire surface of the target. The spectra of different regions have breaks at different frequencies and have different curvatures. When they combine, the effect is that the integrated spectrum has smaller curvature. This demonstrates the fact that we should be careful when interpreting integrated spectral shapes of complex sources. The activity history, coupled with the detailed source morphology and the relative contribution of different source components can influence the shape of the integrated spectrum. We discuss the implications of this further in Section 4.4.

4.4 Discussion

The spectral index maps we have derived using LOFAR data, extending a factor two lower in frequency than previous studies of this object, confirm that there is a frequency break in the spectrum of source region B, while the larger, region A, still retains a steep spectral index at lower frequencies.

Our spectral mapping is in good agreement with the findings of van Weeren et al. (2011). It confirms that the spectral index of region B derived at lower (LOFAR HBA) frequencies continues to flatten out and reaches injection values. We are observing the particles which still have kept their energy from the last episode of acceleration. The data point to a spectral break in the spectrum of this region being at relatively low frequencies. This conclusion is supported by the spectral curvature map given in Figure 4.3.

Our synchrotron ageing models indicate that the youngest radio plasma in the target (around 60 Myr old) is located in the vicinity of the fading AGN core (region 4 in Figure 4.4). This is what would be expected if the AGN was diminishing in activity over time for a FRI like radio source morphology. The south-east regions of region A are older (around 100 Myr). The oldest part of the source is region B, with ages ranging from 120 Myr to 130 Myr. What we are seeing, then, could be a signature of an AGN hosted by the BCG of the cluster which was active around 120 Myr ago when it produced source region B and the outer part of region A. Then, the AGN switched to very low levels of activity around 60 Myr ago.

We can use morphological and kinematic arguments as an independent check of the timescales involved. The relative speed of maxBCG J217.95869+13.53470 w.r.t. the group of galaxies to the north-east (suspected to be a separate smaller cluster; one of its galaxies hosts a spectrally confirmed, currently active AGN) is around 3200 km s^{-1} (Ogrean et al. 2011). We assume that this value is equally distributed between the two clusters, and that the position of the BCG of maxBCG J217.95869+13.53470 at the beginning of the outburst was at the half-way point between regions A and B. Then, the activity began to decrease, as the BCG followed the cluster motion from south-west to north-east. The motion of the Intra Cluster Medium (ICM) halo gas (centered on the cluster core) has bent the radio emission, giving it its current appearance. In this scenario, the distance from the assumed position where the AGN host galaxy had the previous outburst of activity to its present position is 104 kpc. Moving at the previously

mentioned speed, it would take 32 Myr for the AGN host galaxy to arrive to its present position, which is around 4 times shorter than the estimated age of region B. Large uncertainties in the cluster velocity estimates propagate into the kinematic timescale, and we should keep this in mind.

What does the difference in the observed injection spectral indices between the two source regions mean? If we assume that region A was produced as a result of an AGN activity, the steeper injection spectral indices we infer for its plasma broadly agree with what was observed for several radio galaxies by Harwood et al. (2013) (the radio galaxies in their sample are FRIIs, while J1431.8+1331 was probably an FRI radio galaxy). Region B would be plasma released in a previous episode of AGN activity which has faded, losing its energy through radiation and expansion. Ogrean et al. (2011) estimate that it would take region B around 300 Myr to get to its present position rising as a buoyant bubble. It could have been compressed by a merger shock produced by the interaction of the two galaxy clusters (the BCG of one of which hosts J1431.8+1331). The shock compression would cause the plasma bubble to gain energy resulting in a boost in its radio emission. The compression of the plasma in region B would lead to a formation of a sheath-like radio emission region, which as time passes would evolve into a filamentary structure (Ensslin & Bruggen 2002). Looking at the radio morphology of region B, this is a possible scenario if we assume that we see it nearly edge on.

In relation to the compression shock scenario, another explanation of the source spectral properties presents itself. Its plausibility increases if we look at the injection spectral index values for the different measurement regions given in Table 4.4. The regions for which we have only upper limits to the injection index, and which have the steepest injection index are situated in region A and in between regions A and B. This may point to the possibility that what we are actually observing is the spectrum above the break frequency for region A, meaning that the ages we derive for it are lower limits to the true age. In this context, region B can be even older, and the shock compression could have not only revived its radio emission but also shifted its break frequency to higher values which we observe (Enßlin & Gopal-Krishna 2001).

We can estimate the maximum electron ages using equation (4.1) by taking the minimum value of the magnetic field of $B_{\rm min} = \frac{B_{\rm CMB}}{\sqrt{3}} = 2.52\,\mu$G. Assuming a value for the break frequency of 60 MHz, we get maximum ages of around 350 Myr, which make plausible the scenario mentioned above. Under the same assumptions, but using a magnetic field value of $10\,\mu$G we find an age of 160 Myr, more than a factor of two smaller. As can be expected, with everything else being equal, uncertainties in the magnetic field determination (Table 4.3) can affect the derived ages.

As we have shown in Section 4.4, the integrated flux density spectrum is steep and curved. This is caused by superposition of different source regions which have spectral breaks at different frequencies. It is similar to the spectra of cluster sources observed by Murgia et al. (2011). The integrated source spectrum contains information about the detailed spectral properties, depending on which source region is dominating the radio emission. In the case of J1431.8+1331, the steep spectrum, larger region is the dominant one, so the overall spectrum is very steep at higher frequencies showing characteristics of a fading radio source spectrum.

4.5 Conclusions

We have observed the steep spectrum radio source VLSS J1431.8+1331 using LOFAR, adding to an already existing data set taken with the GMRT and the VLA by van Weeren et al. (2011). Using the resulting broad band frequency coverage, and high resolution imaging we were able to study the spectral properties of different regions across the source.

Based on our analysis, we conclude that the AGN in region A has shut down around 60 Myr years ago.

We have found that different source regions have different spectral properties and ages. Our results are consistent with the results of Ogrean et al. (2011) who suggest that source region B might be a shock compressed plasma bubble.

The integrated flux density spectrum can be used as a classifying tool to identify (unresolved) sources in surveys which are comprised of multiple regions resulting from different stages of AGN activity.

Appendix 4.A Relic discovery in the field

We have discovered an extended diffuse emission in our combined LOFAR HBA image 6′ to the south-east of the point source J143405+140325. The discovery, J143411+135734, measures 4′ x 7′ across. Due to the close proximity to the brighter source, it is not so noticeable in the higher resolution LOFAR maps; we show a lower resolution LOFAR map in Figure 4.A1. At the same position, there is a 2σ NVSS source detection which seems to be related to the LOFAR structure.

The emission has two brightness peaks and it is unlikely to be produced by blended point sources. Near the western maximum, there is a galaxy (SDSS J143411.53+135744.6) for which we could not find a redshift reference. The source has a steep spectral index, $\alpha_{140}^{1400} = -1.92$, which indicates that it may be a radio relic (possibly connected with the brighter source to the north) or a redshifted, Ultra Steep Spectrum (USS) radio source.

Appendix 4.B Synchrotron emission models

The fundamentals of the formalism describing the synchrotron emission mechanisms were given by Ginzburg (1957) and later expanded by Kardashev (1962) in his seminal paper discussing various particle injection and energy loss processes, including synchrotron radiation. Pacholczyk (1970) and Jaffe & Perola (1973) further expanded their analysis.

Assuming that the radiating particles have energies described by a power law with a spectral index γ: $E^{-\gamma}$, they produce a radio spectrum which is also described by a power law with a spectral index $\alpha = -\frac{\gamma-1}{2}$. As time passes, these particles lose energy through synchrotron radiation and inverse Compton (IC) scattering off the Cosmic Microvave Background (CMB) photons. These losses can be represented by an energy loss term, depending on the model used. The Kardashev - Pacholczyk (KP) model assumes that the pitch angle of the radiating particles (the angle between the instantaneous velocity vector of the particle and the magnetic field lines) remains constant over time, giving a loss term:

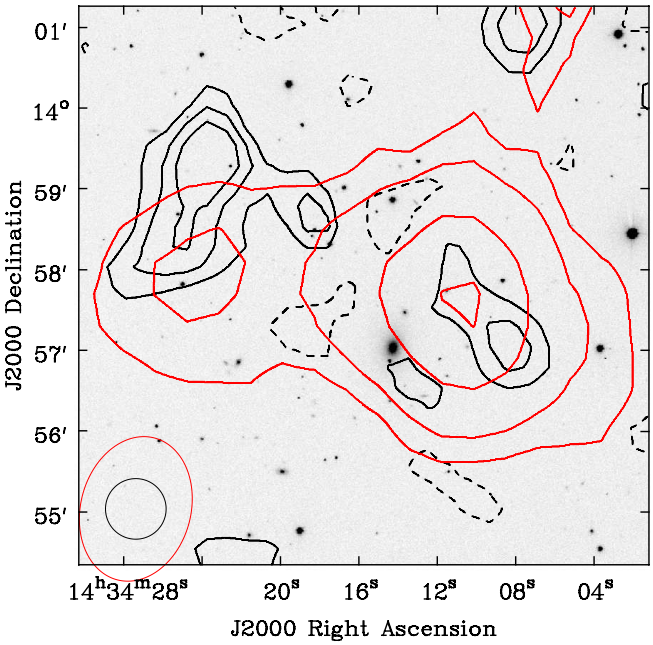

Figure 4.A1: Diffuse radio emission near J143405+140325. The background is an SDSSz image (inverted grayscale). Overlaid in red are LOFAR 144 MHz $(-3, 3, 5, 10, 15)\sigma$ contours. $\sigma = 5$ mJy beam^{-1}. The black contours are taken from an NVSS map at levels of $(-3, -2, 2, 3, 4, 6)\sigma$, $\sigma = 0.45$mJy beam^{-1}. The LOFAR (red) and NVSS beam sizes are given in the lower left corner.

$$b = c_2 B^2 \left[sin^2\theta + \left(\frac{B_{\rm IC}}{B} \right)^2 \right]$$

here, θ is the pitch angle, $B_{\rm IC} = \sqrt{\frac{2}{3}} B_{\rm CMB}$ is the effective IC magnetic field and $B_{\rm CMB} = 3.25(1+z)^2$ equivalent CMB magnetic field (Slee et al. 2001). $c_2 = 2.37 \cdot 10^{-3}$ (CGS units) is a constant defined in Pacholczyk (1971), and B is the magnetic field in the radiating region. In the Jaffe - Perola (JP) model, it is assumed that the pitch angle is isotropized on timescales much shorter than the radiation timescale, and the loss term becomes:

$$b = c_2 B^2 \left[\frac{2}{3} + \left(\frac{B_{\rm IC}}{B} \right)^2 \right]$$

For the particle energy we have: $E = c_1 \sqrt{\nu / x}$ where $c_1 = 4 \cdot 10^{-10} / \sqrt{B}$ (CGS units) is a constant, ν is the observing frequency, and $x = \nu / \nu_{\rm b}$ is the scaled frequency, depending on the $\nu_{\rm b}$, the frequency of the observed spectral break.

We need to find the particle distribution function, which depends on the energy of the particles. There are several separate cases we should consider. In the simplest case, there is a particle injection episode which lasts for an infinitesimally short time (the injection happens at $t = 0$), and afterwards the particles radiate away their energy (Kardashev 1962):

$$N(t_{\rm OFF}, b, \gamma, E) = \begin{cases} E^{-\gamma}(1 - bEt_{\rm OFF})^{\gamma-2} & \text{for} \quad E < \frac{1}{bt_{\rm OFF}} \\ \\ 0 & \text{for} \quad E \geqslant \frac{1}{bt_{\rm OFF}} \end{cases}$$

We label this model JP or KP depending on the treatment of the loss term, b, we adopt. $t_{\rm OFF}$ is the time elapsed since the injection, or in this case, the source age $t_s = t_{\rm OFF}$. When there is AGN activity (or shock particle acceleration) which is ongoing, then the distribution function becomes:

$$N(t_{\rm ON}, b, \gamma, E) = \begin{cases} E^{-\gamma} t_{\rm ON} & \text{for} \quad E < \frac{1}{bt_{\rm ON}} \\ \frac{E^{-(\gamma+1)}}{b(\gamma-1)} & \text{for} \quad E \geqslant \frac{1}{bt_{\rm ON}} \end{cases}$$

This is a continuous injection model and we label it CIJP or CIKP. In this case, the source age $t_s = t_{ON}$. Finally, if there is a period of injection of energetic particles followed by a cessation of the activity, we have (Komissarov & Gubanov 1994; van Weeren et al. 2009):

$$N(t_{\rm OFF}, t_{\rm ON}, b, \gamma, E) =$$

$$\begin{cases} \frac{E^{-(\gamma+1)}}{b(\gamma-1)((1-bE(t_{\rm OFF}-t_{\rm ON}))^{\gamma-1}-(1-bEt_{\rm OFF})^{\gamma-1})} & \text{for} \quad E < \frac{1}{bt_{\rm ON}} \\ \frac{E^{-(\gamma+1)}}{b(\gamma-1)(1-bE(t_{\rm OFF}-t_{\rm ON}))^{\gamma-1}} & \text{for} \quad \frac{1}{bt_{\rm OFF}} \leqslant E \leqslant \frac{1}{b(t_{\rm OFF}-t_{\rm ON})} \\ 0 & \text{for} \quad E > \frac{1}{b(t_{\rm OFF}-t_{\rm ON})} \end{cases}$$

This continuous injection model with a switch off we label KGJP or KGKP (van Weeren et al. 2009). Now, we can calculate the observed flux density as:

$$S(\nu) = S_0 \sqrt{\nu} \int F(x) x^{-1.5} N(x) dx$$

for the JP case, and:

$$S(\nu) = S_0 \sqrt{\nu} \int_0^{\pi} \sin^2\theta \int F(x) x^{-1.5} N(x, \theta) d\theta dx$$

in the KP case, where S_0 is a flux density scaling factor, and $F(x) = x \int_x^{\infty} K_{5/3}(z) dz$ with $K_{5/3}$ being the modified Bessel function.

Chapter 5

Age mapping of the AGN relic B2 0924+30: the LOFAR perspective

The first principle is that you must not fool yourself, and you are the easiest person to fool.

– Richard Feynman

Abstract

We have observed the steep spectrum radio source B2 0924+30 using the LOw Frequency ARray (LOFAR) telescope. Hosted by a z=0.026 elliptical galaxy, its extent of $30'$ allows us to make detailed studies of its structure and map its spectral index and age distribution.

We construct low frequency spectral index maps and use synchrotron aging models to derive source ages. We find that the derived integrated spectral index is consistent with results of earlier studies. Furthermore, our detailed spectral index mapping, while agreeing with earlier lower resolution studies, shows flattening of the spectral index towards the outer edges of the lobes. The spectral index of the lobes is $\alpha_{140}^{609} \sim -1$ and gradually steepens to $\alpha_{140}^{609} \sim -1.8$ moving towards the inner edges of the lobes.

Using radiative aging model fitting we show that the AGN activity has ceased around 100 Myr ago. We note that the inner regions of the lobes are younger (having ages around 20 Myr) which may be interpreted as signs of relic hotspots.

The spectral index properties as well as the derived ages of B2 0924+30 are consistent with it being an FRII AGN radio relic. LOFAR data are proving to be instrumental in extending our studies to the lowest radio frequencies and enabling analyses of the oldest source regions.

We also elaborate on the discovery of a double-double radio galaxy with relic outer lobes in the field (several other interesting sources), as well as the lowest frequency detection of a radio halo connected to the galaxy cluster Abell 781.

A. Shulevski, R. Morganti. P. D. Barthel et al.
to be submitted to *Astronomy & Astrophysics*

5.1 Introduction

Radio relics are the only observable tracer of a past accretion episode of an Active Galactic Nucleus (AGN). Once the acretion of matter onto its super massive black hole (SMBH) stops, the AGN ceases to emit jets of plasma that feed the regions around its host galaxy emitting the radio radiation. These radio relic regions then slowly fade away as time passes. Searches have uncovered relics with various spatial scales, from small (Stanghellini et al. 2005; Dwarakanath & Kale 2009) to large and in particular in galaxy clusters (Murgia et al. 2011). However, the question remains why there are so few AGN radio relics detected (a few dozen in total) relative to the number of active radio galaxies. Further, most of the radio relics observed so far are hosted by cluster galaxies. Questions arise whether the paucity of relics (especially in the field) is due to the fact that they fade out in a short time after the AGN ceases its activity. Does the cluster environment help preserve relics by confining the radio plasma and prolonging the relic lifetimes?

Here we study the B2 0924+30 relic radio source. Its host galaxy, IC 2476, belongs to a group of 8 galaxies (Jamrozy et al. 2004) located at a redshift[1] of $z = 0.026141$. Its Sloan Digital Sky Survey (SDSS; Aihara et al. 2011) spectrum does not show emission lines indicative of an optical AGN. The radio morphology (Figure 5.3) of B2 0924+30 suggests that it is an (FRII) radio relic. It has lobes reminiscent of those of active FRII radio galaxies which have maximum brightness regions at positions where hotspots would be located if this was an active source. It lacks a discernible radio core or jets. Spectral index studies (Cordey 1987; Jamrozy et al. 2004) show that the spectral index steepens going from the lobes to the inner regions, and the overall spectral index distribution is steeper ($\alpha \sim -1$) than what is observed in active FRII radio galaxies. All of these features point towards the conclusion that it is a radio relic of a shutdown FRII source.

We expand on previous research efforts by extending the spectral index studies to the lowest frequencies so far, using the LOw Frequency ARray (LOFAR, van Haarlem et al. 2013) with the highest spatial resolution to date, enabling us to characterize in detail the spectral properties of the relic lobes. Also, we derive radiative ages across the source extent.

The organization of this chapter is as follows. Section 5.2 describes the data used in this study and outlines the data reduction procedure. Section 5.3 outlines our results; in Section 5.3.1 we give the spectral analysis results and source ages. We discuss the implications of our study in Section 5.4.

5.2 Observations and data reduction

The target was observed with LOFAR in the night of March 13, 2014 for a total on source time with the high band antennas (HBA) of 7.5 hours. The HBA observation was done in interleaved mode, using the HBA_DUAL_INNER configuration. 3C 196 was observed as a flux calibrator source for two minutes, followed by a scan of the target of 30 minutes duration with a one minute gap between calibrator and target scans allowing for beam forming and target re-acquisition. 325 sub-bands (SBs) were recorded covering 64 MHz

[1] The adopted cosmology in this work is: $H_0 = 73$ km s^{-1}Mpc^{-1} , $\Omega_{matter} = 0.27$, $\Omega_{vacuum} = 0.73$. At the redshift of B2 0924+30, $1'' = 0.505$ kpc; its luminosity distance is 109.6 Mpc (Wright 2006).

Table 5.1: LOFAR HBA data properties

Central Frequency	150 MHz
Bandwidth	64 MHz
Integration time	2 s
Observation duration	7.5 h
Polarization	Full Stokes
UV coverage	$0.1\text{k}\lambda - 20\text{k}\lambda$

of bandwidth between 116 MHz and 180 MHz. Each SB has 64 frequency channels and a bandwidth of 200 kHz. The integration time was set to 2 seconds for both calibrator and target. Four polarizations were recorded. The HBA station field of view (FoV, primary beam) covers around 5 degrees full width at half maximum (FWHM) at 140 MHz. The station beams are complex valued, time, frequency and direction dependent, and are not the same for all of the stations.

The data were pre-processed by the observatory pipeline (Heald et al. 2010) as follows. Each SB was automatically flagged for RFI using the AOFlagger (Offringa et al. 2012), and then averaged in time to 10 seconds per sample and in frequency by a factor of 16, making the frequency resolution of the output data 4 channels / SB. The calibrator data were used to derive amplitude solutions for each (NL) station using the Black Board Self calibration - BBS (Pandey et al. 2009) tool which takes into account the time and frequency varying LOFAR station beams. The flux density scale of Scaife & Heald (2012) was used in the calibration model for 3C 196 ($S_{150} = 83$Jy).

The amplitudes of the target visibilities were corrected using the derived solutions. The target visibilities were then phase (self)calibrated incrementally, using progressively longer baselines to get to the final resolution (Vilchez et al. in preparation). The initial phase calibration model was derived from the VLSS[2] catalog covering the FoV out to the first null of the station, containing spectral index information for each source in the model. Before initializing the calibration, we have concatenated the data into 4 MHz (20 SB) groups previously averaging each SB to 1 frequency channel to reduce the data size. We have chosen this setup to maximize the S/N while maintaining frequency dependent ionospheric phase rotation to a manageable level. We have not performed any directional solving and did not perform further corrections to mitigate ionospheric effects.

The imaging was done using the LOFAR imager (Tasse et al. 2013), which incorporates the LOFAR beam and uses the A-projection (Chandra et al. 2004) algorithm to image the entire FoV. We have used Briggs (Briggs 1995) weights with the robustness parameter set to 0, and have imaged the field selecting baselines larger than 0.1 $k\lambda$. Ten self-calibration steps were performed, each using a sky model generated in the previous cycle and each subsequent one using larger baseline lengths. Once the imaging was completed, we obtained 10 images for each averaged SB group of 4 MHz. Out of these images, we have selected two sub-groups of images, a low resolution and a high resolution one. The low resolution images were chosen such as to ensure that we have the highest sensitivity to the diffuse emission of the target comparable to the integrated flux density measured in previous studies. The higher resolution images were chosen so that we have enough sensitivity to diffuse emission while being able to resolve finer details. Both sets

[2] VLSS is the VLA Low frequency Sky Survey carried out at 74 MHz (Cohen et al. 2007)

of images exclude the longest baselines which in general had poorer calibration solutions due in part to ionospheric phase errors. Finally, we have constructed our two final data sets by taking into account only the images from these two sub-groups with the lowest image noise and smallest source distortions. At the end of the selection, we were left with seven high resolution and seven low resolution LOFAR images.

Table 5.2: Image properties

ID	ν [MHz]	σ (low res. | high res.) [mJy beam^{-1}]	Beam size (low res. | high res.)
LOFAR[a]	113	8.3 | 4.5	$56.6'' \times 40.9''$ | $20.2'' \times 14.1''$
LOFAR[a]	124	6.3 | 3.6	$47.7'' \times 38.1''$ | $19.3'' \times 15.7''$
LOFAR[a]	132	4.3 | 3.1	$48'' \times 35.4''$ | $22'' \times 16.7''$
LOFAR[a]	136	4.3 | 3	$46.9'' \times 34.3''$ | $21.7'' \times 17.1''$
LOFAR[a]	160	2.3 | 1.9	$51.9'' \times 37.6''$ | $20'' \times 17.9''$
LOFAR[a]	163	2 | 1.8	$56.6'' \times 38.2''$ | $20.2'' \times 17.8''$
LOFAR[a]	167	1.8 | 1.7	$51.1'' \times 37.5''$ | $20.5'' \times 17.5''$
LOFAR[a e]	140	2.5 | 1.2	$60'' \times 43.5''$ | $22''$
WENSS[b]	325	3.6	$54'' \times 108''$
WSRT[c]	609	0.77	$29'' \times 56''$
NVSS[d]	1400	0.45	$45''$

[a] This work
[b] WENSS
[c] Jamrozy et al. (2004).
[d] NVSS
[e] Averaged images.

We have smoothed the high and low resolution LOFAR images to an identical restoring beam size and have averaged them to obtain two final images, each having a bandwidth of 28 MHz. We have used these images for studies of the target source, as well as investigating potential undiscovered relics in the LOFAR HBA FoV. The smoothed, non-averaged, images were used in our aging analysis. Table 5.2 lists the image properties for the LOFAR image set, as well as survey (WENSS[3] and NVSS[4]) images used in our subsequent analysis.

To check whether the station beam correction applied by the AW imager resulted in correct flux density scaling across the FoV, we have used PyBDSM (Ramanujam 2007) to extract sources from our averaged images and measure their flux densities. Then, we have matched the extracted sources with survey catalogs (VLSS, WENSS and NVSS using a $30''$ match radius) and determined the catalog flux density for each source by interpolating the flux densities from the catalog entries to the LOFAR frequency. Finally, we have divided the obtained catalog flux density at 140 MHz with the measured flux density from the LOFAR image. Assuming power law spectra, the ratio should be 1 if the station beam correction produces correct fluxes over the FoV. The results are given in Figure 5.1. We can see that for both of the HBA images the points cluster around 1, which shows that the flux correction over the FoV applied by the AW imager gives

[3] WENSS is the Westerbork Northern Sky Survey carried out at 325 MHz (Rengelink et al. 1997)
[4] NVSS stands for the NRAO VLA Sky Survey carried out at a frequency of 1.4 GHz (Condon et al. 1998)

reasonable flux density values. The scatter is around 20%. Most of the data points belong to point sources.

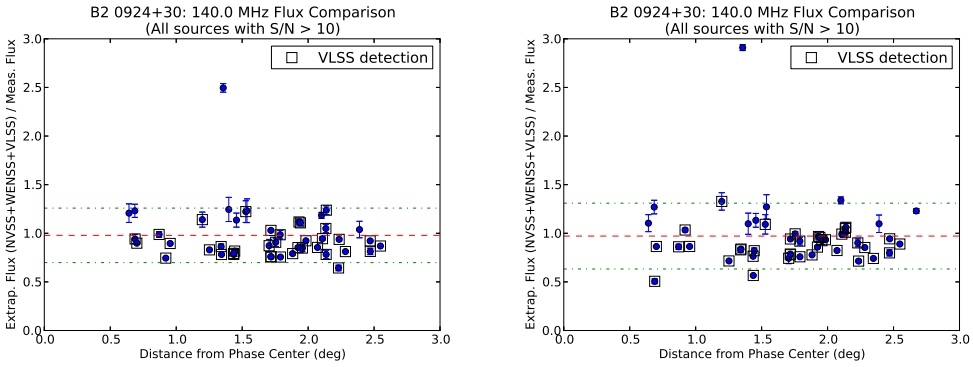

(a) HBA - Low resolution

(b) HBA - High resolution

Figure 5.1: Ratio of measured and catalog extrapolated fluxes for our high and low resolution averaged LOFAR images. The red dashed line denotes the median flux ratio, while the green dash dot lines give the 1σ limits.

5.3 Results

Figure 5.2 shows the averaged low resolution $5^\circ \times 5^\circ$ LOFAR image. It has a resolution of $60'' \times 43.5''$ and an r.m.s. noise level of 2.5mJy beam^{-1}.

Figure 5.3 shows the LOFAR view of the target in the high resolution averaged image (see Table 5.2). We can see that the extended lobes have the highest surface brightness, and that there is an enhancement of brightness at the position of the host elliptical galaxy UGC 5043 (IC 2476). There is no noticeable radio core. The source is enveloped in a low surface brightness radio cocoon. It is interesting to note that there are several localized increases in the surface brightness of the radio lobes. Two of them in the eastern lobe can be identified with background galaxies, possibly signifying that the enhancements are produced by radio emission connected to background galaxies. The highest surface brightness regions in the lobes are probably aged remnants of hotspots. There is an optical source at the highest radio surface brightness point in the western lobe, but this is probably a chance alignment. The cocoon has extensions at the lobe edges, causing the source to have an overall shape reminiscent of the letter Z. There is a bright point source off the edge of the western lobe which has been identified with a quasar (Ekers et al. 1981).

5.3.1 Spectral analysis

The morphology of B2 0924+30 and previous studies point to it being an AGN radio relic which is fading away after the AGN which has created it has shut down (i.e. a fader). Here, we elaborate on its spectral properties. The spectral shape encodes the

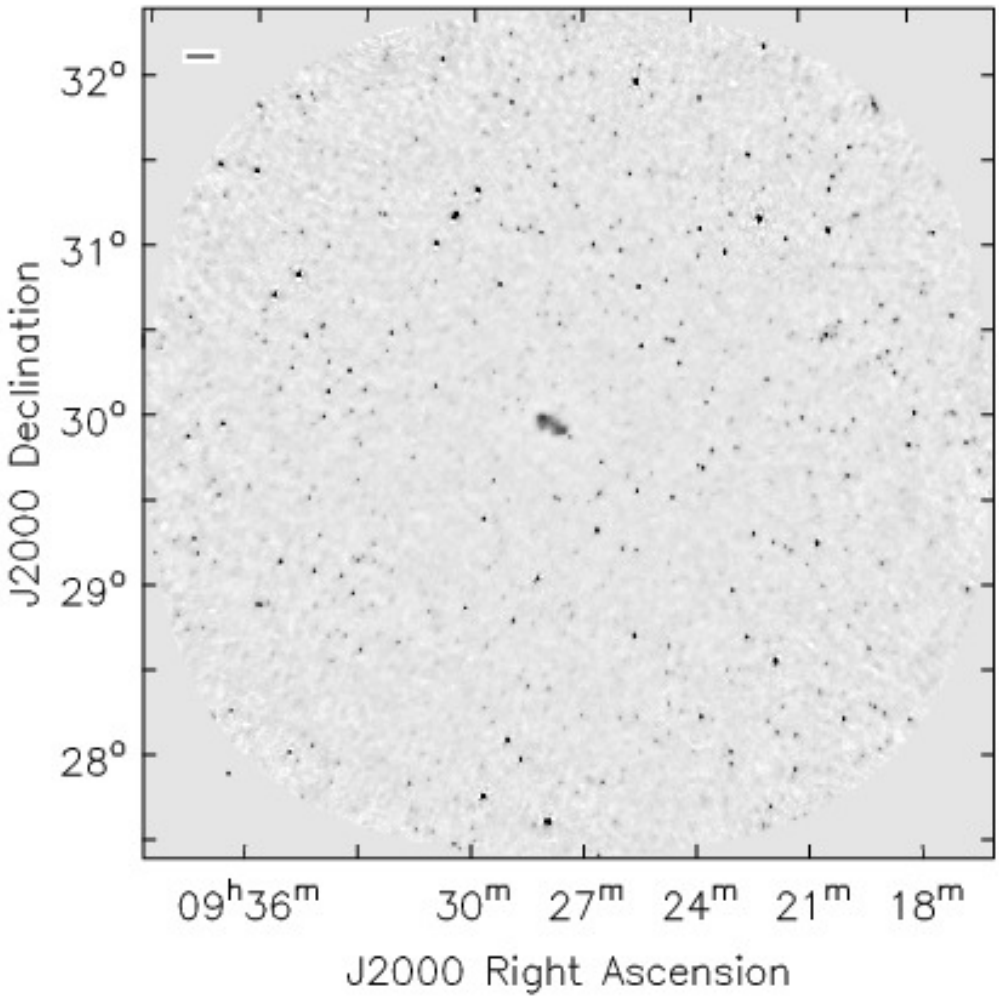

Figure 5.2: LOFAR FoV, averaged low resolution image (28 MHz bandwidth). Beam size: $60'' \times 43.5''$, $\sigma = 2.5$mJy beam^{-1}.

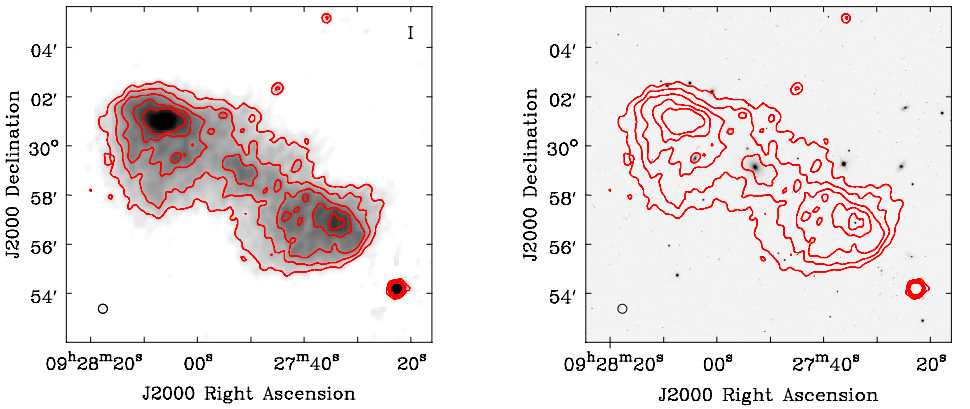

(a) B2 0924+30 LOFAR HBA

(b) B2 0924+30 LOFAR HBA contours overlaid on an SDSSr image.

Figure 5.3: B2 0924+30: LOFAR image obtained by averaging the higher resolution HBA images. Beam size: 22″ x 22″. Contour levels: $(-3, 3, 6, 9, 12, 15) \cdot 2\text{mJy beam}^{-1}$.

activity history of a fading radio source and can be a powerful tool in understanding the exact nature of the observed radio emission.

Integrated spectrum

Jamrozy et al. (2004) have fitted a synchrotron aging model to the data collected from the literature as well as their own observations. We have repeated the fitting procedure adding integrated flux densities measured from our LOFAR maps (all except the first two of the LOFAR images listed in Table 5.2; we have discarded them due to flux scaling issues; the measurements had systematically higher values). An overview of the measurements is given in Table 5.3.

We have performed the fit using a value for the magnetic field strength derived by assuming an equipartitition between the energy contained in the magnetic field and in relativistic particles according to Miley (1980). In our calculations, we have used a central frequency of 609 MHz, with a spectral index of $\alpha = -1.2$ (average over the source) and lobe extent of 4.8'. We have computed the magnetic field value for each lobe separately and then averaged the result. Our estimate gives a value of 1.35μG.

A Jaffe-Perola (JP, Jaffe & Perola 1973) model was fitted to the data, assuming an instantaneous particle injection phase (which is a reasonable assumption taking into account the nature of the target), and found best fit values for the overall source age (time elapsed since the particle injection has ceased) and injection index of $t_{off} = 60 \pm 8$ Myr and $\alpha_{inj} = -0.92 \pm 0.06$ respectively. The χ^2 value threshold for accepting the fit at a probability level of 5% was 14.1, and we had a value of $\chi^2 = 5.2$. Our best fit values are consistent with those reported by Jamrozy et al. (2004) within their error bars (54^{+12}_{-11} Myr). The best fit model is shown in Figure 5.4.

We notice the overall curvature of the integrated spectrum, an indication of the nature

Table 5.3: B2 0924+30 Flux density

ν [MHz]	S_ν [mJy]	Reference
132	6774 ± 1356	This work
136	6738 ± 1348	This work
151	4600 ± 360	Cordey (1987)
160	5214 ± 1043	This work
163	4751 ± 950	This work
167	4702 ± 940	This work
325	2425 ± 124	This work (WENSS)
609	1094 ± 56	This work (Jamrozy et al. 2004)
1400	420 ± 43	This work (NVSS)
4750	60 ± 7	Jamrozy et al. (2004)
10550	10 ± 4	Gregorini et al. (1992)

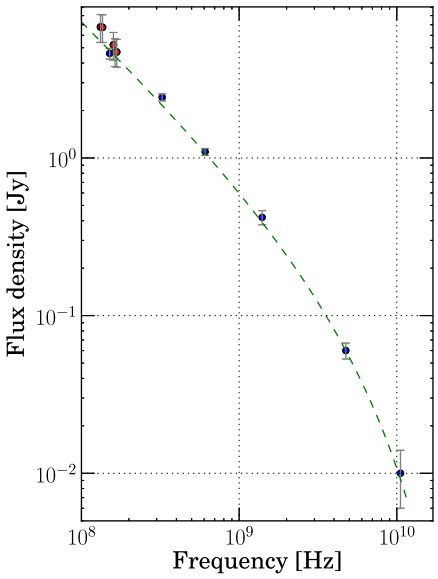

Figure 5.4: Best fit JP model to the integrated flux density measurements. LOFAR data are represented with red symbols.

of the target - a fader.

Spectral and curvature maps

To disentangle the plasma properties in the relic lobes, we have derived the highest resolution low frequency spectral index map of B2 0924+30 to date, using an average of our LOFAR observations and the 609 MHz WSRT image (kindly contributed by M. Jamrozy). The input images were matched in UV coverage and smoothed to a resolution of 60″. The spectral index map was derived by fitting a first order polynomial to the flux density values for each pixel above a 5σ level in the input images. We have also derived a spectral curvature map ($SPC = \alpha_{140}^{609} - \alpha_{609}^{1400}$). The resulting maps are shown in Figure 5.5.

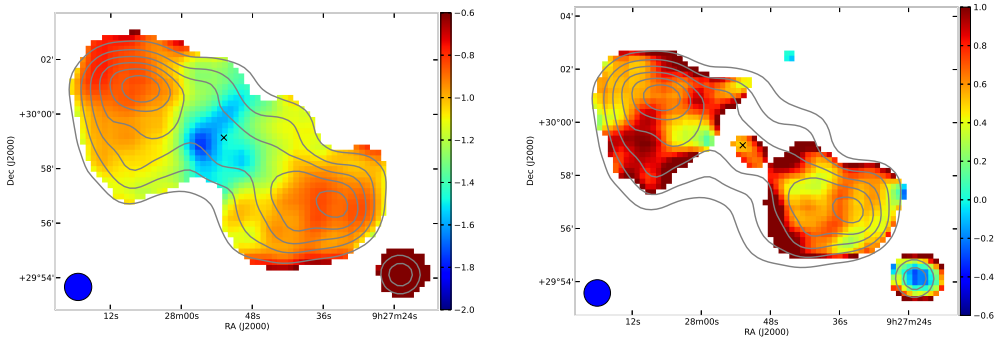

(a) α_{140}^{609} spectral index map. **(b)** $\alpha_{140}^{609} - \alpha_{609}^{1400}$ spectral curvature map.

Figure 5.5: Spectral index and spectral curvature maps for pixels with surface brightness greater than 5σ. We have used the averaged low resolution LOFAR image (Table 5.2). Overlaid are LOFAR contours with levels: $(-10, 10, 20, 30, 40, 50, 60)\cdot\sigma$, with $\sigma = 4$ mJy beam^{-1}. The black cross marks the position of the host galaxy.

In figure 5.5a we can see that the lobes show a relatively steep low frequency spectral index of $\alpha \sim -1$, in agreement with previous studies, and the derived injection spectral index we have obtained previously. The spectrum of the south-west lobe seems to be overall flatter compared to the north-eastern lobe ($\Delta\alpha \sim 0.1$), consistent with what was reported by Jamrozy et al. (2004).

Interestingly, this spectral index difference between the two lobes is exactly the same as the values reported by Liu & Pooley (1991); Garrington & Conway (1991); Garrington et al. (1991). They propose that in radio galaxies which have a one sided jet (possibly enhanced in brightness by doppler beaming), the jet side is closer to us than the counter-jet side and find that the counter-jet side is depolarized more w.r.t to the jet side (Laing-Garrington effect). Garrington & Conway (1991) find a correlation between the depolarization and the spectral index of the lobes; the lobe on the jet side has a flatter spectral index than the counter-jet lobe. In our case, this suggests that the south eastern lobe of B2 0924+30 is closer to us. Garrington & Conway (1991) suggest that in active sources the spectral index difference between the hotspots may be explained

by beaming effects, but that spectral index differences in the lobes are more difficult to explain. We do not observe jets in B2 0924+30, and the difference in spectral index between the lobes may be explained by different physical conditions of the lobes.

As was already mentioned, there is an alignment between the highest surface brightness region in the LOFAR image in this lobe and a background galaxy, which, if it is radio active may contribute to the surface brightness of that region of the lobe thus causing the spectral flattening.

Theoretical considerations (e.g. Komissarov & Gubanov 1994) indicate that what we observe are spectral index values typical for radio plasma not being replenished by AGN activity. Indeed, the observed low frequency spectral index is steeper than spectral indices in lobes and hotspots of active AGN, or acceleration regions (typical values are $-0.8 < \alpha < -0.6$); we observe at lower frequencies and expect to trace the injection spectral index. If so, we determine that the injection spectral index values are steeper than 0.8. Harwood et al. (2013) have also reported steeper injection spectral indices in lobes of active radio galaxies, in line with our observations.

Indeed, comparing our low frequency spectral index map with previous spectral index studies done at higher frequencies, we can see that LOFAR detects spectral index flattening in particular lobe regions which may signify that we detect the lowest energy particles which have energies comparable to the injection level values. This is prominent at the outer edges of the lobes.

The highest surface brightness regions are similar to hotspots which are no longer clearly outlined (since they are no longer replenished by the AGN), but we do not detect any structure in our spectral index maps which is on roughly the same spatial scale as the features in the intensity map. Consequently, we can not claim that we see spectral signatures of aged hotspots. We observe that the lobes have spectral index values of around -0.9 with spectral flattening on the outermost lobe edges, especially the north-eastern lobe. The spectral index steepens as we approach the host galaxy, consistent with what is typical of FRII sources.

In line with our previous discussion, the curvature map shown in Figure 5.5b is also very interesting. We observe a lot more structure in the relic lobes, with some areas showing large curvature up to $SPC = 1$. This suggests that different regions have spectral breaks at different frequencies, indicating different radiative ages.

Taken together, the spectral index map and the spectral curvature map of the relic core region suggest that it is the oldest part of the source. Its spectrum is the steepest at low frequencies and it steepens even more at higher frequencies. The appearance of the core regions with their steepest spectral index further support the claim that we are seeing a fading FRII source.

Radiative ages

To gain a better insight into the history of the radio source over its extent, we have taken five of our lower resolution LOFAR images (listed in Table 5.3) together with the 609 MHz WSRT image and an NVSS map and fitted a JP synchrotron aging model to the flux densities for measurement regions spanning the source. The JP model was chosen since B2 0924+30 is a relic source, with no signs of ongoing activity, thus a model with an infinitesimal duration of the injection phase of activity is more suitable. The injection index was not fitted for; its value was fixed to the one found during the integrated

spectrum modeling in Section 5.4.

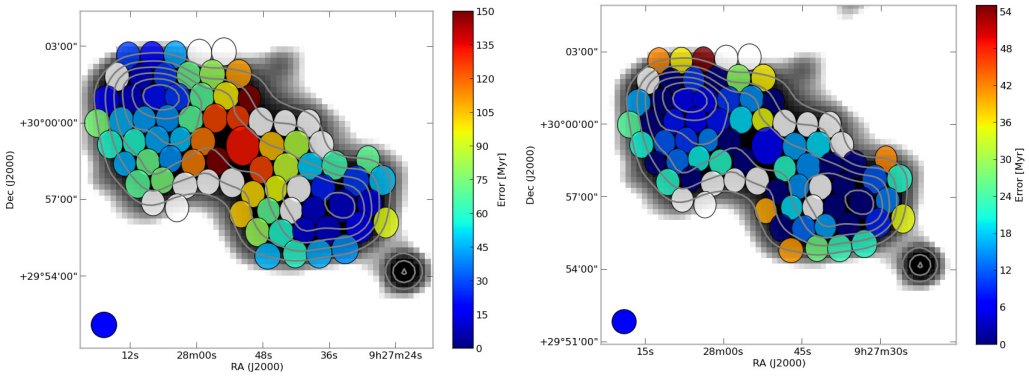

(a) Radiative ages **(b)** Fit errors

Figure 5.6: Fitted radiative ages and fit errors for a JP model. Contours like in Figure 5.5. Regions with unsatisfactory model fit are marked in white.

The results of the age analysis are shown in Figure 5.6. We note that the derived ages for the core and lobes follow a pattern which is in line with a fading FRII radio galaxy. The youngest ages (of around 20 Myr) are found towards the outer edges of the lobes, and the oldest are the regions towards the host galaxy. We have more limited spectral coverage (up to around 1400 MHz) than the integrated spectral index fit which we have presented earlier, but even so, the overall ages tend to average around the value arrived at during the integrated spectrum model fitting.

Our resulting ages show that (as expected) the age derived from a model fit to an integrated spectrum is only the average. Age mapping gives us more information; for example, we can see that the latest particle acceleration in the lobes ceased around 20 Myr ago, and that the AGN activity stopped at least 100 Myr before that (looking at the core regions). The ages derived for the core regions of B2 0924+30 are comparable to the oldest sources in e.g. the sample of Murgia et al. (2011).

Spectral shifts

Katz-Stone et al. (1993) have outlined a powerful tool for determining the energetic conditions in radio galaxies. A data set of imaging spread over at least three frequencies is needed to construct a "color-color" diagram of regions of interest.

Shifting the measured flux densities for each source region in the $log(S) - log(\nu)$ plane, we scale the spectrum of each region to a common break frequency. The amount of shift needed in the flux-frequency plane and the correlation between these shifts can point to the injection spectral index and give us a hint about the dominant energy loss mechanism. The technique has been implemented in a number of cases (van Weeren et al. 2012a, also see Chapter 4 of this thesis).

We have plotted our measurement regions in a color-color diagram and derived the corresponding shift diagrams for B2 0924+30. The results are given in Figure 5.7.

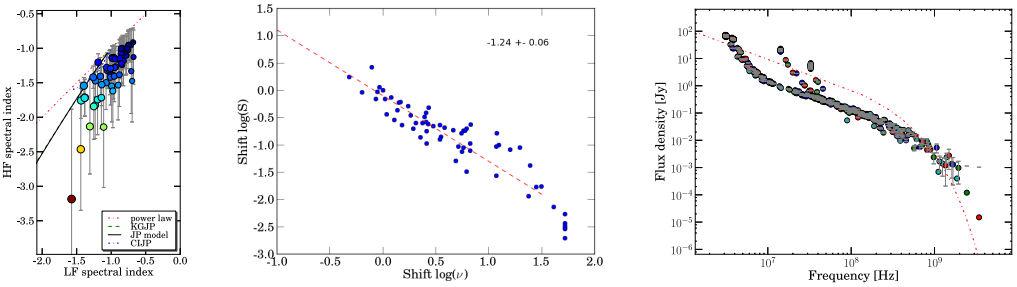

(a) Color-color plot.

(b) Shift diagram.

(c) Total set of shifted data and model fits for all of the regions. The slope of the fit in the shift diagram is -1.2 ± 0.06

Figure 5.7: Color-color plot and shift analysis results for the B2 0924+30 source regions.

The color-color plot (Figure 5.7a) of the source regions shows that the spectral shape for most of them is best fit by synchrotron radiation from an aged plasma.

There is a correlation between the shift in frequency and in flux (Figure 5.7b), meaning that the dominant energy loss are radiative synchrotron losses. Moreover, the fit to the shift data has a slope (-1.2) which has similar value as the injection spectral index we have found earlier from the integrated flux density fit.

5.4 Discussion

B2 0924+30 is an AGN radio relic, a leftover from the time when it was an active FRII radio galaxy. The relic radio lobes are very well outlined, which might may indicate confinement by the IGM (which is unusual, since it is not located in a dense environment). The lobes are younger roughly at the position where we observe an enhancement of the surface brightness in the LOFAR maps. Regions closer to the host galaxy are progressively older, and the diffuse radio emission at the position of the host galaxy (noticeable in the LOFAR image) is the oldest region of the source. There is no sign of a restarted AGN activity, which suggests that the AGN has been inactive for around 10^8 yrs.

In Section 5.3.1 we have argued that the dominant energy loss mechanism is synchrotron radiation. Jamrozy et al. (2004) mention a ROSAT detection identified with B2 0924+30 indicating the possibility that a hot gas halo is present around the source. Comparing the plasma ages that we have derived with those found by Murgia et al. (2011) for a sample of AGN relics located in galaxy clusters, we see that the overall age of B2 0924+30 corresponds to the total ages for 4 out of 7 sources in their sample. The ages derived for the lobes of B2 0924+30 are lower than the lowest total age for all of the sources in the sample of Murgia et al. (2011), while the ages of the central regions are comparable to the oldest sources found in their sample.

These arguments, and the fact that the relic lobes of B2 0924+30 are very well oulined seem to suggest that the radio emitting regions are sufficiently confined; at least comparable to radio sources found in some clusters of galaxies. A larger sample of AGN radio relics hosted by field galaxies is needed to infer whether B2 0924+30 is an outlier

in this sense.

5.5 Conclusions

We have used LOFAR to obtain images of B2 0924+39 at low frequencies with the highest resolution to date. This has enabled us to produce detailed spectral index maps and derive radiative ages over the extent of the source. We have confirmed previous inferences consistent with this source being a FRII relic. We have also shown that there is a continuum of ages increasing from the outer lobes (around 20 Myr) to the regions at the position of the host galaxy (around 100 Myr, the time elapsed since the AGN has shut down). Further studies on relics of the same type (when discovered) will be necessary to answer the question whether the derived timescales are typical for relics hosted by field galaxies.

Appendix 5.A Spectra of some field sources

There are two sources in the immediate vicinity of B2 0924+30 which show interesting spectral behavior (see Figure 5.A1).

The source to the north-east of the northern lobe has a steep low frequency spectrum ($\alpha_{140}^{609} \sim -1.2$), and surprisingly, shows signs of spectral flattening (SPC < 0) at higher frequencies. It is unresolved, and this might indicate that we are observing a restarted AGN where the active core dominates the emission at higher frequencies, with a flatter spectral index.

Another source, further to the north-east, shows a spectral index associated with active radio AGN ($\alpha_{140}^{609} \sim -0.6$) at low frequencies, but it also has a pronounced spectral curvature (SPC~ 1). It is suggestive of a source which we are observing very soon after its AGN has stopped being active.

These examples demonstrate the utility of wide field, low frequency observations and how we can use integrated spectral index properties to make preliminary inferences about the AGN activity history of multiple sources.

Appendix 5.B LOFAR Double-Double radio galaxy discovery

Most of the extended sources in our LOFAR image are radio galaxies. Based on their appearance (double lobes, sometimes with a visible radio core located in between them), most of them seem to be FRIIs. There are several others which resemble FRIs and some of irregular morphology. One of the former, J092743.8+293232, is a double-double source (DDRG; Schoenmakers et al. 2000), as can be noticed when we compare our LOFAR map with a FIRST image (Figure 5.B2). We can not resolve the inner pair of lobes, but the outer pair is noticeably fainter when looked at in an NVSS image. This fact points to the conclusion that the outer lobes are relic lobes. Indeed, their spectral index (Figure 5.B3) supports this conclusion.

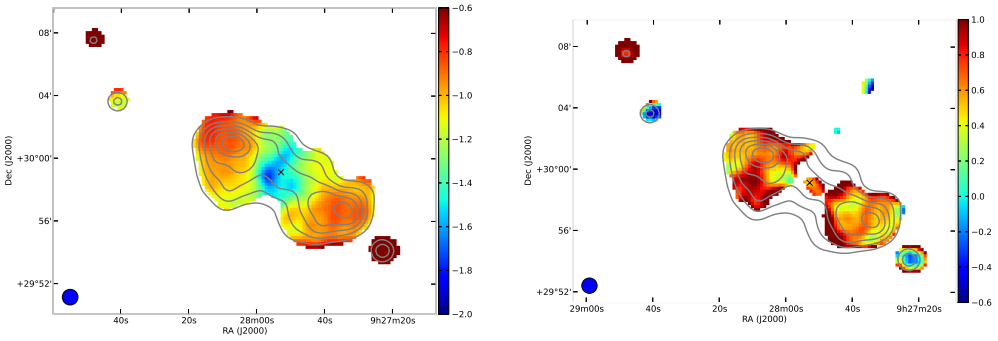

(a) α_{140}^{609} spectral index map. **(b)** $\alpha_{140}^{609} - \alpha_{609}^{1400}$ spectral curvature map.

Figure 5.A1: Spectral index and spectral curvature maps of sources located near B2 0924+30.

Appendix 5.C Abell 781

Another notable extended radio source in the LOFAR FoV is shown in Figure 5.C4; an extended radio emission connected to the galaxy cluster Abell 781. It has been studied in detail by Venturi et al. (2011) and Govoni et al. (2011), and classified to be a galaxy cluster radio halo. Our image is its lowest frequency detection so far. We also detect other sources in the vicinity which do not have a counterpart the NVSS survey maps, but appear in the higher sensitivity maps of Venturi et al. (2011) (labeled S3 and S5 with spectral indices $\alpha_{140}^{325} = -1.1$ and $\alpha_{140}^{325} = -0.3$ respectively). They may be components related to the galaxy cluster halo which is hosted by Abell 781.

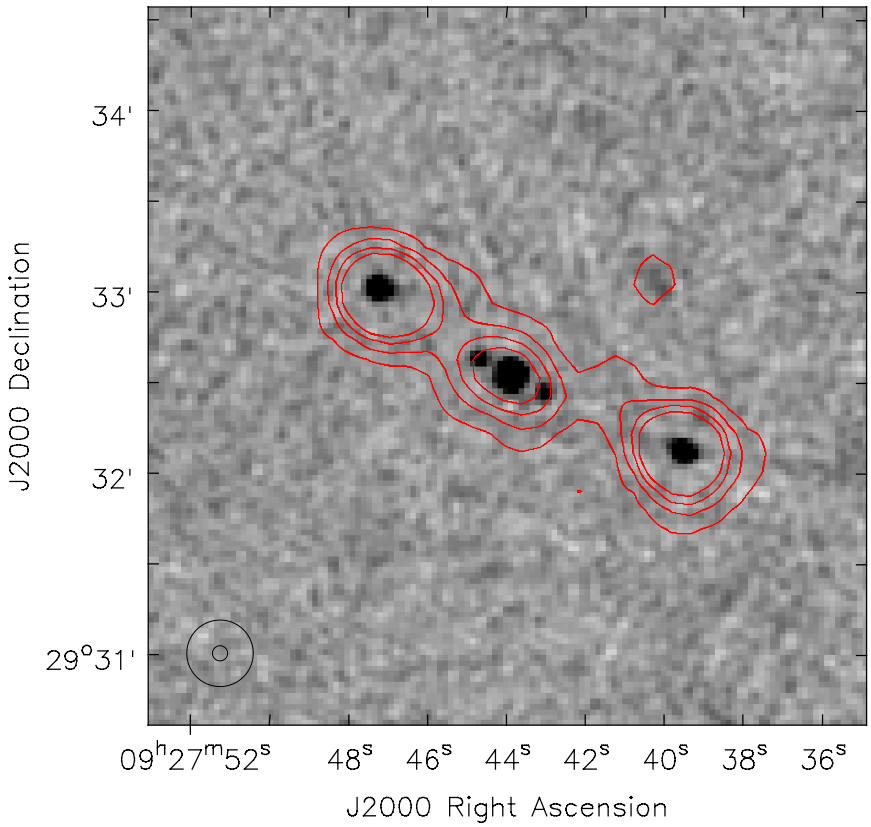

Figure 5.B2: LOFAR contours (red) superposed on a FIRST survey grayscale image of J092743.8+293232. Contour levels: $(-3, 3, 6, 9, 12)\sigma$. $\sigma = 2$ mJy beam^{-1}.

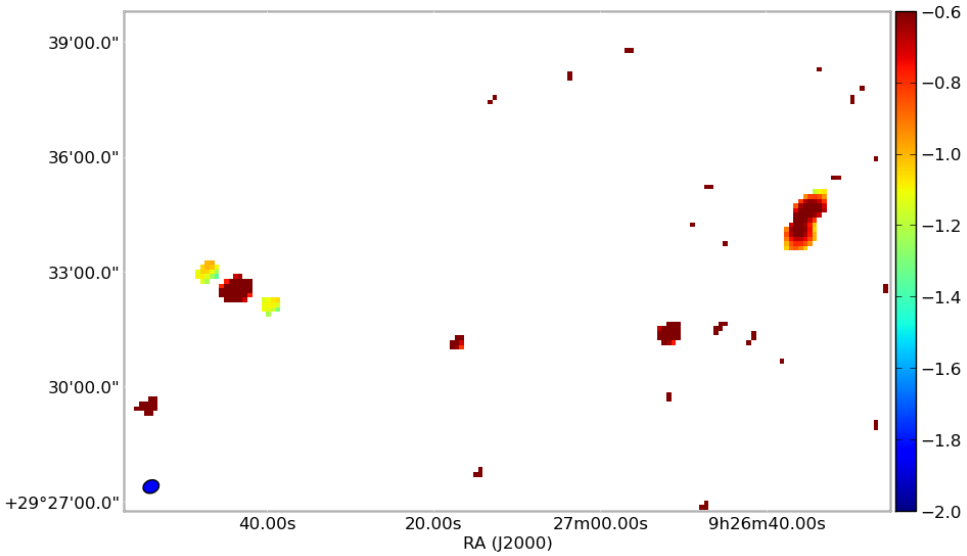

Figure 5.B3: α_{140}^{1400} spectral index map (made using our LOFAR image and an NVSS survey image) of the field double-double radio galaxy showing its steep spectrum relic outer lobes (left) compared to the active source 7C 0923+2947 (right).

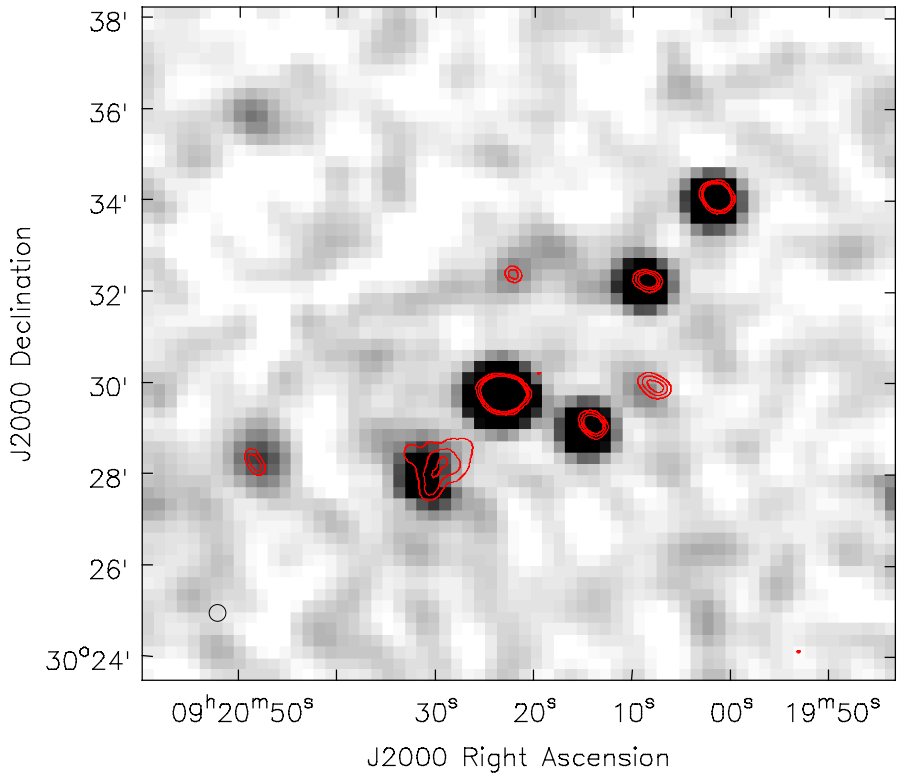

Figure 5.C4: LOFAR high resolution image contours (red) superposed on an NVSS survey grayscale image of Abell 781. Note that LOFAR detects the extended galaxy cluster halo, and that there are two LOFAR detections not having an NVSS counterpart. Contour levels: $(-3, 6, 9, 12)\sigma$. $\sigma = 2$ mJy beam^{-1}.

Chapter 6

A LOFAR search for AGN radio relics around young radio sources

If you gaze long enough into an abyss, the abyss will gaze back into you.

– Friedrich Nietzsche

Abstract

We know of a number of cases of radio relics around Compact Steep Spectrum (CSS) or Gigahertz Peaked Spectrum (GPS) sources. These active objects are considered to be young radio sources which are embedded in the ISM of their host galaxies. Studying the properties of the radio relics around them can help us to put firmer constraints on their Active Galactic Nuclei (AGN) duty cycle(s) and determine whether there are any intrinsic differences between AGN properties of CSS / GPS sources and larger radio galaxies.

We outline the results of a first systematic search for radio relics around CSS and GPS sources using the LOw Frequency ARray (LOFAR) telescope's Multifrequency Snapshot Sky Survey (MSSS). We are using several source samples: flux limited CSS and GPS source samples, and a volume limited GPS source sample.

For these samples, no relic detections were made down to the noise limit of the MSSS survey. This result may mean that radio relics around compact sources are fainter than what we can detect with the MSSS, but it may also point towards more fundamental reasons which are consistent with previous results that large scale AGN radio relics around compact sources are scarce.

A. Shulevski, P. D. Barthel, R. Morganti

6.1 Introduction

Compact Steep Spectrum (CSS) and Gigahertz Peak Spectrum (GPS) sources are thought to represent the initial observable stages of an Active Galactic Nucleus (AGN) radio phase (Fanti et al. 1990; O'Dea 1998). The sources are in the process of expanding through the Interstellar Medium (ISM) of their host galaxies and depending on their jet power, on the ISM properties (density) and on the duration of the AGN activity, may grow to become large radio galaxies.

Although the present active phase of radio activity has started recently in these objects ($< 10^5 - 10^6$yrs. ago), it may be the latest active episode in an ongoing duty cycle. Therefore, looking for diffuse emission around CSS / GPS sources may uncover relics of previous phase(s) of AGN activity, helping us to constrain the time scale of their duty cycle.

Remnants of past AGN activity episodes have been observed around GPS/CSS sources (Stanghellini et al. 2005; Shulevski et al. 2012), suggesting that a more systematic survey could uncover more similar structures. Existing surveys are relatively shallow; the VLSS has an image noise level of 100 mJy beam^{-1} at a resolution of $80''$ while the WENSS has a noise level of around 3 mJy beam^{-1} and a resolution of $54'' \times 54\,\mathrm{csc}(\delta)''$.

We have used the LOw Frequency ARray (LOFAR, van Haarlem et al. 2013) Multifrequency Snapshot Sky Survey (MSSS; Heald et al. 2014, submitted)[1] to search for diffuse emission around the sources in three samples described below. The MSSS is designed to cover the whole northern sky at the frequencies of the LOFAR low band and high band antennas (LBA and HBA). We have used the HBA part of the survey, centered on 140 MHz, having a bandwidth of 64 MHz. As discussed previously, AGN radio relics may be identified by a combination of their morphological characteristics and spectral properties. They have steep spectra[2] at higher frequencies ($\alpha < -1.5$, Murgia et al. 1999), which makes them brightest at low frequencies. Consequently, the MSSS is very well suited for the search we wish to perform.

6.2 MSSS data

The MSSS survey is using the core stations of the LOFAR telescope. Consequently, it has low spatial resolution of around $2.5'$ and a theoretical thermal noise level of around 1 mJy beam^{-1}, reached in 14 minutes of total observing time per field. The reported image noise measured in the MSSS verification field (MVF) is around 5mJy beam^{-1} (Heald et al. 2104, submitted), better than VLSS[3] and comparable to the noise of the WENSS[4]. The spatial resolution of MSSS is lower than that of either VLSS or WENSS.

We are searching for extended diffuse emission, so in principle we benefit from the coarser resolution which enables us to detect diffuse emission, although we do not know in advance the size of the relics we expect to find. The coarse resolution of the MSSS can blend possible relics with the CSS/GPS source to which they are associated. Some of the

1 http://msss.astron.nl/

2 $S \propto \nu^{\alpha}$

3 VLSS (Cohen et al. 2007) is the VLA Low frequency Sky Survey carried out at a frequency of 74 MHz

4 WENSS stands for the Westerbork Northern Sky Survey carried out at a frequency of 325 MHz (Rengelink et al. 1997)

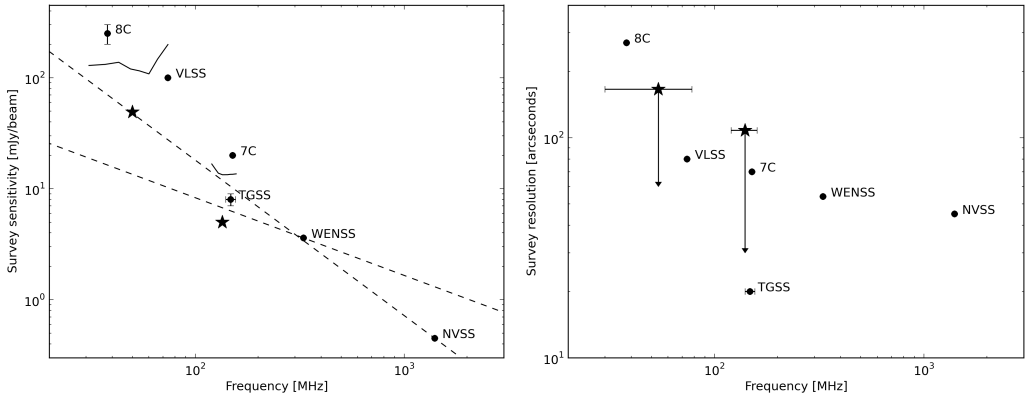

(a) MSSS sensitivity **(b)** MSSS resolution

Figure 6.1: Comparisons between MSSS sensitivities (left) and resolutions (right) with those of other existing radio surveys. In the left-hand panel, dashed lines indicate representative spectral indices $\alpha = -0.7$ and $\alpha = -1.4$. The solid black lines illustrate the frequency dependence of the sensitivity in the 8 bands in each of the LBA and HBA survey segments, while the black stars show the frequency-averaged sensitivity. In the righthand panel, the downward-pointing arrows indicate that the angular resolution of the initial MSSS catalog is limited with respect to the capabilities of the visibility data. Processing the full array will improve the survey performance. Reproduced from Heald et al. (2014, submitted).

sources under investigation are very bright compared to the expected surface brightness of the relic structures, so deconvolution artifacts introduced during the imaging could limit our sensitivity.

We have constructed two source samples:

- A flux limited sample ($S_{150} > 1$Jy) of CSS and GPS sources (Fanti et al. 2000)
- A volume limited GPS source sample with $z < 0.12$ taken from Labiano et al. (2007)

Adopting a cosmology with $H_0 = 73$ km s^{-1}Mpc^{-1}, $\Omega_M = 0.27$, $\Omega_\Lambda = 0.73$, and an average beam size of the MSSS to be $150''$ we can calculate (Wright 2006) the linear extent of the beam, giving the physical resolution we achieve. Several values are presented in Table 6.1. Any relics with a smaller size or separation from their CSS/GPS source will not be resolved.

We have performed a visual search around the source position in image mosaics produced from MSSS pointings covering the entire HBA band. In our study, we have measured the r.m.s. noise of the image in the vicinity of the target source, where we find noise values which are in general a factor of a few higher than what is reportedly measured in the MVF. The image noise is expected to improve in the final release of the MSSS. For each of the sources in our samples we have also calculated the MSSS - NVSS[5]

[5] NVSS is the NRAO VLA Sky Survey carried out at a frequency of 1.4 GHz (Condon et al. 1998)

Table 6.1: Dimensions of a 150″ beam

z	Scale [kpc]
0.01	30
0.05	141
0.1	266
0.2	477
0.5	887
1	1173

spectral index, α_{140}^{1400}. We show our results in Table 6.2.

Table 6.2: Sample matching results. The flux densities are given in Janskys. The beam size is the restoring beam of the MSSS mosaic image used for each entry.

ID	z	S_{140}	σ_{mos}	Beam	S_{1400}	α_{140}^{1400}	Det.
Flux limited sample							
			CSS				
3C 48	0.367	78.5	34.8	$150.4'' \times 149.9''$	16	-0.7	No
3C 67	0.310	13.5	18	$157.6'' \times 157''$	3	-0.6	No
3C 93.1	0.243	10.9	36.8	$153'' \times 152.5''$	2.4	-0.6	No
3C 138	0.759	29.8	107	$154.3'' \times 153.8''$	8.6	-0.5	No
3C 147	0.545	77.2	27.2	$147.7'' \times 147.2''$	22.9	-0.5	No
3C 213.1	0.190	8.1	13.4	$152.8'' \times 152.3''$	2	-0.6	No
3C 216	0.670	32.6	41.4	$152.9'' \times 152.4''$	4.2	-0.9	No
3C 236	0.1	23.2	32.6	$161.2'' \times 160.7''$	3.2	-0.9	Yes
3C 237	0.877	25	19.1	$162.3'' \times 161.8''$	6.5	-0.6	No
3C 268.3	0.371	16.6	26.3	$143.5'' \times 143''$	3.7	-0.6	No
3C 277.1[6]	0.319	14.6	24.2	$172'' \times 171.5''$	2.3	-0.8	No
3C 299	0.367	34	17.8	$275.5'' \times 275''$	3.1	-1	No
3C 286	0.849	21.8	30.4	$156.3'' \times 155.8''$	14.9	-0.2	No
3C 303.1[7]	0.267	14.6	39.3	$144.2'' \times 143.7''$	1.9	-0.9	No
3C 309.1	0.905	34.7	17.5	$149.3'' \times 148.8''$	7.5	-0.7	No
3C 343.1	0.750	14	23.6	$172.3'' \times 171.8''$	4.6	-0.5	No
3C 346	0.161	11.3	19.9	$154.8'' \times 154.3''$	3.7	-0.5	No
3C 380	0.692	84.1	41.8	$135'' \times 134.5''$	13.7	-0.8	No
3C 455	0.540	9.6	45.8	$173.9'' \times 173.4''$	2.7	-0.5	No
B2 0258+35	0.117	4.8	11.9	$151.8'' \times 151.3''$	1.8	-0.4	No
B3 1128+455	0.404	7.2	17.5	$142.4'' \times 141.9''$	2	-0.5	No
B3 1233+418	0.250	2.9	16.6	$154.9'' \times 154.4''$	0.7	-0.6	No
B3 1445+410[7]	0.195	1.4	38	$186.7'' \times 186.2''$	0.4	-0.5	No
B3 1201+394[7]	0.445	2	55.8	$157'' \times 156.5''$	0.5	-0.6	No
4C 30.19	0.091	2.4	21.7	$151.4'' \times 153.6''$	0.4	-0.8	No
4C 39.29	0.210	6.2	19.3	$143.6'' \times 143.1''$	1.4	-0.6	No
4C 39.32	0.361	3.4	13.9	$143.6'' \times 143.1''$	0.6	-0.7	No

[6] Confused
[7] Mosaic edge

Table 6.2: Continued

ID	z	S_{140}	σ_{mos}	Beam	S_{1400}	α_{140}^{1400}	Det.
			GPS				
4C 76.03	0.599	8	24.7	$144.5'' \times 144''$	5.6	-0.1	No
4C 14.41	0.362	1.5	31.9	$162.3'' \times 162''$	2.4	0.2	No
4C 32.44	0.368	4.5	18.8	$154.5'' \times 154''$	4.9	0	No
4C 12.5	0.121	3	20.5	$180.8'' \times 180.3''$	5.4	0.2	No
4C 62.22	0.429	1.6	14.9	$152.2'' \times 151.7''$	4.3	0.4	No
B2 2050+36	0.354	1.3	61.9	$163.4'' \times 162.9''$	5.1	0.6	No
PKS 0428+20	0.219	2.3	24.7	$157'' \times 156.5''$	3.7	0.2	No
DA 611	0.237	0.7	35.8	$160'' \times 159.5''$	2.3	0.5	No
7C 1031+5644	0.450	0.8	22	$152.3'' \times 151.8''$	1.8	0.3	No
PKS 1607+26	0.473	0.6	17.9	$147.8'' \times 129.8''$	4.9	0.9	No
J1245+676	0.107	0.6	20	$171.7'' \times 171.2''$	-	-	Yes
			Volume limited sample				
			GPS				
4C 31.04	0.06	2.6	38	$150.4'' \times 149.9''$	2.6	0	No
071509+452225[8]	0.042	-	10.5	$151.7'' \times 151.2''$	-	-	No
073328+560541[8]	0.104	-	164	$182.5'' \times 182''$	0.3	-	No
090615+463618[8]	0.085	-	19.5	$153.7'' \times 153.2''$	0.3	-	No
093609+331308[8]	0.076	-	14.8	$155.8'' \times 155.3''$	0.06	-	No
105731+405646	0.008	0.05	17.2	$155.5'' \times 155''$	0.04	-0.1	No
131739+411545	0.066	0.1	17.2	$149.8'' \times 149.3''$	0.3	0.5	No
132513+395552[8]	0.074	-	13.6	$149.8'' \times 149.3''$	0.06	-	No
134035+444817[8]	0.065	-	15.2	$148.2'' \times 147.7''$	0.08	-	No
OQ 208[8]	0.077	-	21.7	$150.3'' \times 149.8''$	0.8	-	No
194553+705550[8]	0.101	-	14.3	$147.2'' \times 146.7''$	0.9	-	No

6.3 Results and conclusions

We have detected two cases of extended emission in our sample (marked with a "Yes" entry in the last column of Table 6.2). Both of them are giant radio galaxies (GRGs), and are included in our flux limited samples.

The first detection are the outer lobes of 3C 236; we elaborate more on this source in Chapter 7 of this thesis. The integrated flux density of the north-west lobe measured by LOFAR is 5.5 Jy, and is detected well above the noise of the MSSS map. Due to its large size, the structure of 3C 236 is well resolved.

The other detection, J1245+676, spans $13.6'$ and its two outer lobes are well resolved by MSSS. It has a GPS core which is not detected by MSSS, probably because it has turned over and is too weak at 140 MHz. The core consists of an expanding compact double source, estimated to be several hundred years old (Marecki et al. 2003). The lobes have steep spectra: $\alpha_{140}^{1400} = -1.6$ and $\alpha_{140}^{1400} = -2$ for the north-eastern and south-

[8] Not detected

western lobe respectively, and are most probably relic radio lobes, remnants from a past epoch of AGN activity.

From the sources included in the sample of Stanghellini et al. (2005), J0108+388 has a size smaller than the MSSS beam size, and belongs to a GPS source too faint to be included in our samples. Their other relic candidate (J0941 − 080) is outside the MSSS sky coverage. 4C 12.50, which also has an extended emission on an arcminute scale, is not resolved by MSSS. The same holds for B3 1128+455.

Even though almost all of the sources in these samples were unresolved, the derived α_{140}^{1400} spectral index for some of them (3C 216, 3C 299, 3C 303.1) is steep enough ($\alpha_{140}^{1400} \sim -1$) that it may point to the possibility that their small scale extended emission has relic characteristics. The MSSS may be detecting additional emission (blended with the target source) which was possibly resolved out in earlier studies of these sources.

We have not detected any other relics in the vicinity of the CSS and GPS sources in our samples. How robust is this conclusion? Taking the case of B2 0258+35, it is a CSS source showing twin jets and relic lobes extending out beyond its host galaxy (see Chapter 2 of this thesis). The relic emission has a surface brightness of 0.5 mJy beam^{-1}. Assuming a relic spectral index of $\alpha = -1.5$ and extrapolating the surface brightness to the frequency of 140 MHz, we get a value of around 60 mJy beam^{-1} (accounting for the different beam sizes of the maps). This is a 5σ value w.r.t the noise measured in the corresponding MSSS map. The relic emission is large enough to be resolved by MSSS, but we have no detection. Its case represents one of the best MSSS maps (lowest noise) that we have. In Figure 6.2 we show the images of the detection in the case of J1245+676 and the non-detection for B2 0258+35.

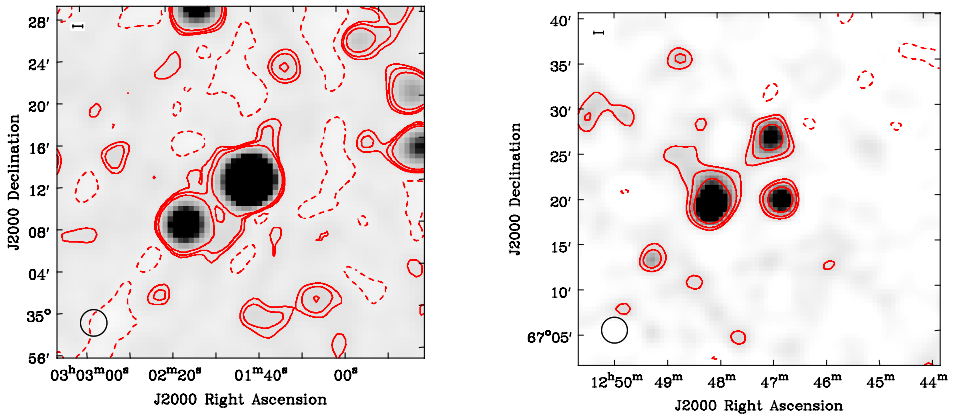

(a) B2 0258+35 **(b)** J1245+676

Figure 6.2: Comparison of the non-detection in the MSSS map of B2 0258+35 and the detection of the lobes of the GRG J1245+676. Contours in both images: $(-2, 2, 3, 5) \times \sigma$.

There are several reasons which may explain our results. If the relics have spectral breaks higher than the MSSS band (AGN activity stopped relatively recently), the assumed spectral index in the simple calculation for B2 0258+35 is too steep, and the

MSSS in this case is too shallow for a detection.

For the flux limited samples, our spatial resolution is on average 450 kpc. This means that we are sensitive to large structures - the GRGs, which we indeed detect (only a few cases, having extended emission with relatively high surface brightness, which MSSS picks up despite the not so steep spectral index).

The volume limited sample contains weaker GPS sources. In this case we have better spatial resolution, however Stanghellini et al. (2005) find that large scale emission associated with GPS sources is uncommon and that the time interval between subsequent active episodes is longer than the duration of the active episode.

On the other hand, the case study of Konar et al. (2013) on two double-double radio galaxies, finds that the dormant stage in radio AGN activity lasts a few percent of the time the AGN is active.

Having all of the above in mind, the lack of relic detections might mean that they fade fast (a few Myr), they have smaller sizes than we assume, or that the duty cycle of CSS and GPS sources is short.

The MSSS data may be re-processed to include all of the LOFAR Dutch stations. This would be a challenge, but the benefits are worthwhile. In that case, the resolution would be around $20''$, enough to put further constraints on our results (as would the Tier2 LOFAR survey which is the planning stage).

Acknowledgements We are very grateful to George Heald and the MSSS team who have allowed us to use MSSS data before the official survey release.

Chapter 7

LOFAR first look at the giant radio galaxies NGC 6251 and 3C 236

Curving back within myself, I create again and again.

– the Bhagavad Gita

Abstract

We have examinated the giant Mpc-class radio galaxies NGC 6251 and 3C 236 using LOFAR at 144 MHz. This represents the lowest frequency study of these objects to date at angular resolution comparable with observations done at higher frequencies. Our studies hence produced the highest resolution spectral index maps to date at low frequencies of these objects.

As for NGC 6251, we observe that the extent of the north-western lobe is larger at lower frequencies, and also find flatter spectral indices at low frequencies in its resolved jet and hotspots. We trace spectral index variations in the lobes. We also detect a counter-jet connecting the core to the south-eastern lobe. The jet/counter-jet brightness ratio is 60:1 at a distance of 240″ from the core and 27:1 at a distance of 340″ from the core.

The spectral index maps of 3C 236 show that the spectral steepening at the inner edges of the northern lobe is prominent at low frequencies. Our low frequency, high resolution spectral index map shows that the inner north-western lobe is broken up in multiple components, and that there is a pronounced spectral curvature of the lobe regions closer to the core, which is indicative of spectral aging.

A. Shulevski, P. D. Barthel, R. Morganti

7.1 Introduction

Giant radio galaxies (GRGs) are radio galaxies whose radio emitting regions (jets, lobes) extend over projected distances ≥ 1 Mpc (Willis et al. 1974; Schoenmakers et al. 1999, 2001; Machalski et al. 2008; Saripalli et al. 2012). Their morphology can be classified as belonging to either the FRI or FRII type, and there is no evidence to point to them being particularly more energetic than the general population of radio galaxies. The surrounding environment may be an important factor allowing their large sizes when compared to other radio sources. Mack et al. (1998) have indeed found that the surrounding medium for their sample of GRGs is an order of magnitude less dense than that around smaller radio sources. This may be the reason for their large sizes; they can expand freely, which in turn may imply that expansion losses are the dominant energy loss mechanism for the relativistic particle populations in their lobes.

Apart from their size, GRGs are not fundamentally different from other radio galaxies, and we expect them to be subject to the same processes that are present in smaller radio galaxies. The AGN that power them probably go through a cycle of active and inactive periods (e.g. Barthel et al. 1985). Consequently, we also expect to see morphological and spectral signatures of radiative aging in GRGs.

Images at lower frequencies trace the oldest particle populations, and using the LOw Frequency ARray (LOFAR; van Haarlem et al. 2013) telescope allows us to trace the oldest emission regions in radio galaxies. Its unprecedented resolution at low frequencies enables us to produce spectral index maps with the highest resolution at these frequencies and map the energetics of the jets and radio lobes.

We have observed two giant radio galaxies, NGC 6251 (e.g. Willis et al. 1978) and 3C 236 (e.g. Willis et al. 1974) as part of the studies of nearby AGN in the framework of the LOFAR Surveys Key Science Project (KSP). Our goal is to study the radio morphology of the jets and lobes at the lowest frequencies and derive the highest resolution low frequency spectral index maps of these sources to date.

The radio emission associated with the galaxy NGC 6251 ($z = 0.0247$) was discovered by Waggett et al. (1977) who describe it as a giant RG with an exceptionally outlined long jet. Readhead et al. (1978) discovered an inner radio jet and have shown that it is aligned to the larger scale one over spatial scales of six orders of magnitude.

For many years after its discovery in the late 1950s, 3C 236 was an unresolved source. It was cataloged as such in the first 3C catalog and kept its status up to and including the study of Pooley & Henbest (1974). However, using the Westerbork Synthesis Radio Telescope (WSRT), Willis et al. (1974) have discovered low surface brightness active radio lobes emanating from it and extending for 4 Mpc ($z = 0.1005$). For decades, it was the largest known radio galaxy (see Machalski et al. 2008). Hence, 3C 236 is listed as a GRG in radio survey catalogs. Strom et al. (1981) studied the spectral index variations across the lobes and found that the spectral index steepens going from the outward edges of the lobes towards the host galaxy, consistent with what is observed in FRII radio galaxies.

The Infrared Astronomy Satellite (IRAS) observations by Golombek et al. (1988) detected warm dust in the host galaxy probably connected to ongoing star formation (Hes et al. 1995). Barthel et al. (1985) performed investigations of the radio morphology at a variety of scales; the north-west lobe was shown to have a possible sign of an additional activity episode, with a middle lobe/ridge embedded in the larger scale emission. The compact core is a Compact Steep Spectrum (CSS) source showing structure down to pc

scales. The lobes show a ridge of emission along their axes which is observed to wiggle, independent of brightness contributions coming from background sources visible through the lobes. The ridge has flatter spectral index ($\alpha \sim 0.5$)

Hubble Space Telescope (HST) imaging (Martel et al. 1999; O'Dea et al. 2001; Tremblay et al. 2010) has revealed repeated bursts of star formation in the host galaxy and the possibility that the youngest starburst may be connected to the AGN reactivation which produced the currently active CSS radio source. Thus, 3C 236 may be a good example of a radio galaxy showing signs of multiple epochs (possibly three) of restarted radio activity.

The large scale lobes of 3C 236 are intriguing in the sense that the north-western one is shorter than the south-eastern one, and this relationship is inverse for the small scale emission of the CSS core; there the north-western extension is longer than the south-eastern as seen by Schilizzi et al. (2001). They also note that the dust lane imaged by the Hubble Space Telescope (HST) close to the core may be part of the material which shapes the radio emission. The south-eastern jet seems uninterrupted throughout its extent, while the appearance of the north-western lobe might indicate that the jet on that side is weaker or interrupted (this side is thought to be approaching us). The maps of the large scale emission lack sufficient resolution, so it is possible that short period disturbances may have gone unnoticed.

The organization of this chapter is as follows. Section 7.2 describes the data and the reduction procedure. In Section 7.3 we outline our results, we discuss them in Section 7.4 and conclude with Section 7.5.

7.2 Data

Both targets were observed with the LOFAR HBA antennas, using an interleaved approach, with 11 minutes of dwell time on the target and 2 minute scan of a calibrator (total on-source time of 4.4 hours). NGC 6251 was observed in the night of August 22, 2013, while 3C 236 was observed in the night of March 14, 2013. Details of the observation are given in Table 7.1.

Table 7.1: LOFAR observation configuration for both targets

Central Frequency [MHz]	144
Bandwidth [MHz]	64
Integration time	2 seconds
Observation duration	6 hours
Polarization	Full Stokes
UV range	$\leq 20k\lambda$

The data were initially calibrated by the observatory pipeline (Heald et al. 2010). The station gains were determined using the calibrator pointings and set to the (Scaife & Heald 2012) flux scale. The target data were corrected using the derived gains and then incrementally phase (self) calibrated with the LOFAR imaging pipeline (Vilchez et al. in prep.) using increasing baseline lengths for each calibration step. The imaging was performed using the LOFAR imager correcting for the station beam. Directional effects were not considered. For the starting model of the phase calibration, we have

used models extracted from a VLSS[1] image using a spectral index of $\alpha = -0.8$ for the model components.

In the case of NGC 6251, we have imaged the entire LOFAR HBA band; each image having a bandwidth of 4 MHz. After rejecting the edges of the band, and images which we judged to suffer from excessive artifacts, we were left with nine images which we have averaged to produce the final image (with 36 MHz total bandwidth) of the target and the surrounding field.

For 3C 236, the reduction procedure was the same, but we have imaged 12 MHz total bandwidth due to time constraints; the full-bandwidth images eventually will yield higher S/N.

K. H. Mack has kindly provided us with WSRT images of NGC 6251 at 325 MHz and 3C 236 at 609 MHz which we have used in our analysis. The image properties are summarized in Table 7.2.

Table 7.2: Image properties.

Target	Instrument	ν [MHz]	$\Delta\nu$ [MHz]	σ [mJy beam^{-1}]	Beam size
NGC 6251	LOFAR	144	36	4	$55''$
	WSRT[a]	325	15	2.3	$55''$
3C 236	LOFAR	144	12	7	$50'' \times 38.8''$
	WSRT[a]	609	-	0.7	$50'' \times 40''$
	WSRT[b]	1400	-	0.4	$45''$

[a] Image provided by K. H. Mack

[b] NVSS image (NVSS stands for the NRAO VLA Sky Survey carried out at a frequency of 1.4 GHz (Condon et al. 1998))

7.3 Results

7.3.1 NGC 6251

We present the image of the complete LOFAR HBA $5^\circ \times 5^\circ$ field of view (FoV) in Figure 7.1. There are no noticeable variations in the background noise levels and the remaining artifacts around brighter sources can be attributed to uncorrected phase errors over the FoV, most likely of ionospheric origin.

A detailed LOFAR view of NGC 6251 with a WSRT contour overlay is given in Figure 7.2.We have marked the significant regions with letters, in agreement with the labels used in the work of Willis et al. (1982). Background sources are visible through the lobes (one in the north-western lobe and another to the south of the region labeled B). Our image reveals interesting new features of the radio emission of NGC 6251. We detect an extension of the counter-jet (marked E in our image) which connects the core region (at the base of the prominent jet in the north-west lobe) to the south-east lobe. Taken together with the jet emission and the two lobes, it supports the FRI classification of NGC 6251 (its radio luminosity is $L_{1480} = 2.2 \times 10^{24}$ WHz^{-1} Perley et al. 1984). We also note that the extension of the north-western lobe goes on further to the west in

[1] VLSS (Cohen et al. 2007) is the VLA Low frequency Sky Survey carried out at a frequency of 74 MHz

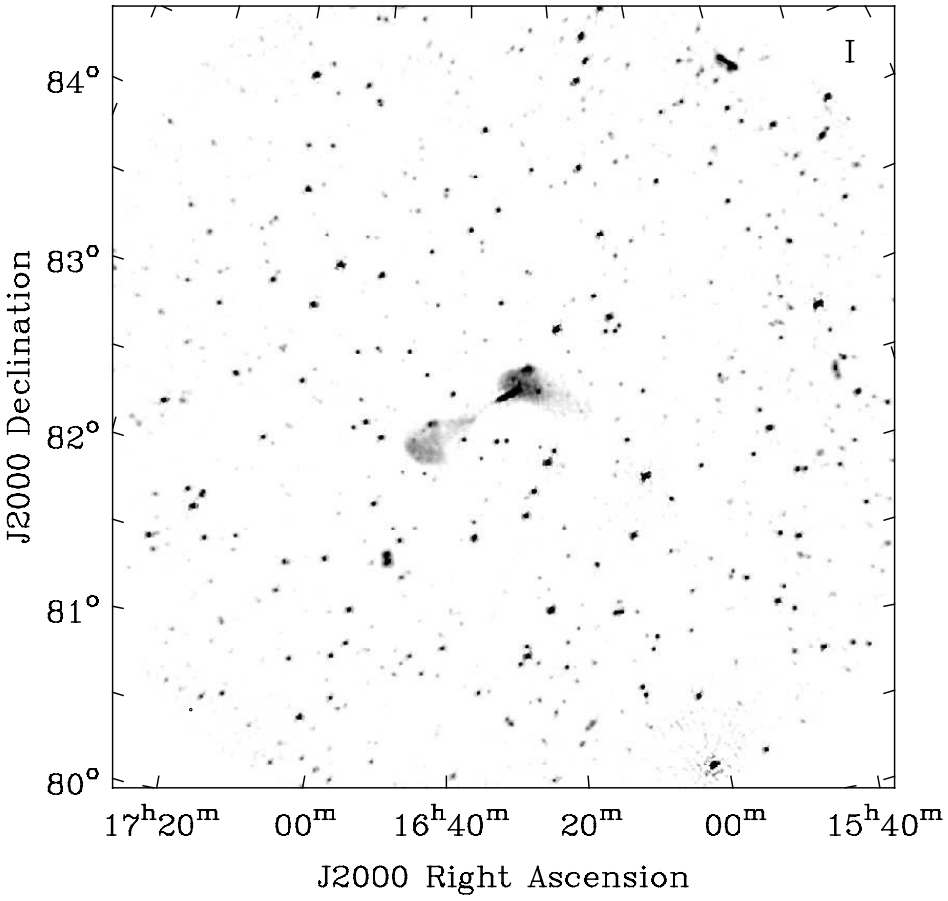

Figure 7.1: The HBA $5° \times 5°$ FoV with NGC 6251 in the center. Image properties are listed in Table 7.2.

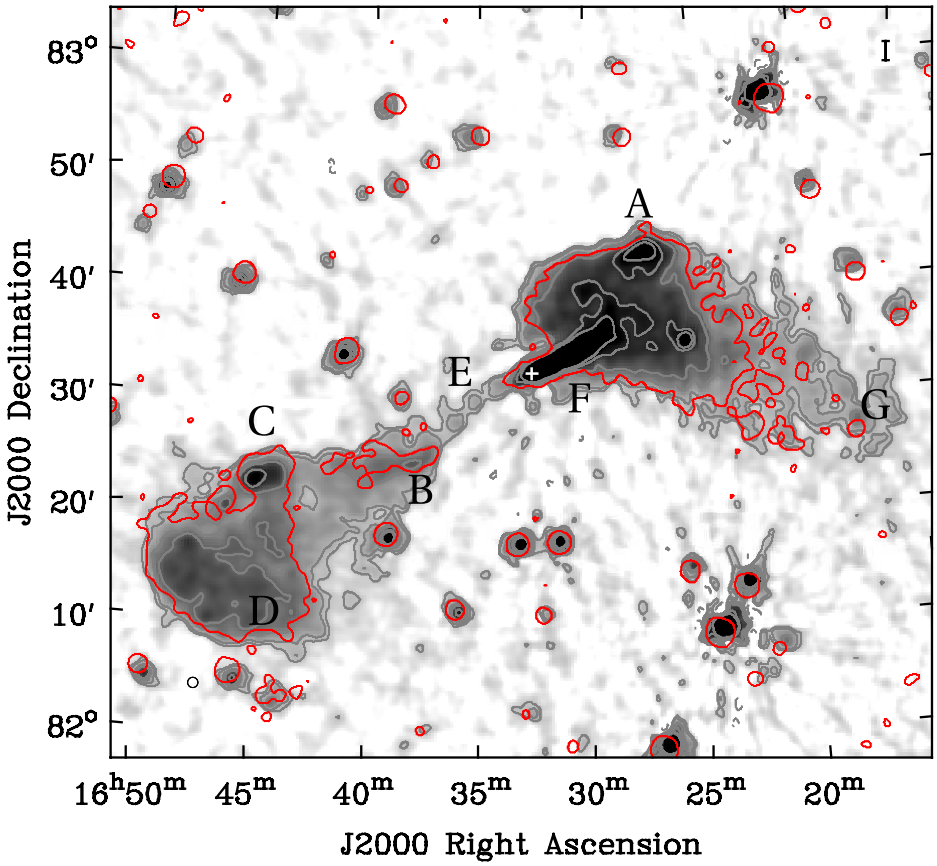

Figure 7.2: Grayscale LOFAR map of NGC 6251 at 140 MHz. Grey contours: $(-3, 2, 3, 6, 9, 18, 27)\sigma$. Shown in red is the 2σ contour level of the WSRT 325 MHz map. Map properties as listed in Table 7.2. The WSRT map is rotated around the phase center which induces increasing offset in the source positions as one moves away from it. Our conclusions are not significantly affected by the offset. The white cross indicates the position of the host galaxy.

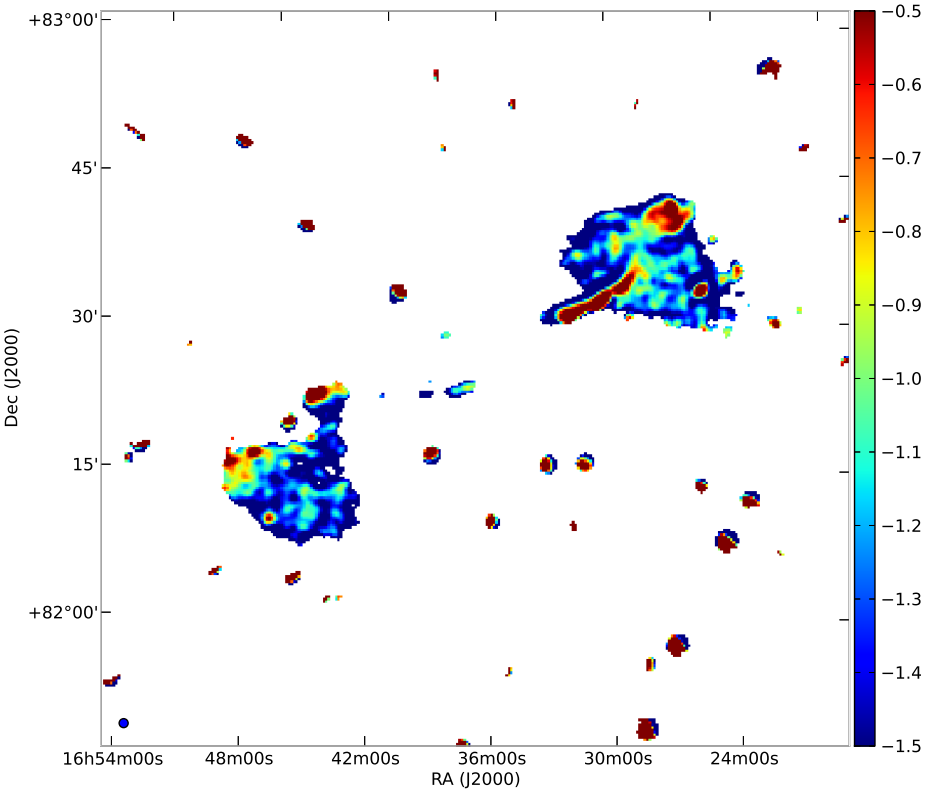

Figure 7.3: NGC 6251 α_{144}^{325} spectral index map.

the LOFAR image compared to the WSRT map (G). These are regions containing the lowest energy particles which radiate at lower frequencies and mark the oldest particle population in the lobes.

Connecting the hotspot in the north-western lobe (A) with the jet (F) and continuing through the core, the counter-jet (E), the brightness enhancement at the inner edge of the south-eastern lobe (B) and ending up at its hotspot (C), we trace a structure that resembles the stretched out letter "W". If we add the edges of the lobes (D and G) to it, we can think of the entire source as having a helical morphology, with the helix being smaller near the core, and the largest at the edges of the lobes. This is reminiscent of a structure created by jet precession, suggesting that the diffuse edges of both lobes may be farther away and in the background of the hotspots.

We show the α_{144}^{325} spectral index map in Figure 7.3. The spectral index map was made by fitting a first order polynomial to the flux density values vs. frequency in log-log space for each pixel of both the LOFAR and WSRT images. Only pixels with values above 3σ in the corresponding maps were taken into account. The spectral index map shows the

jet and hotspots to have the flattest spectrum; there is a gap between the jet and hotspot in the north-western lobe, which might indicate a flicker in the AGN activity. The lobes show a steep spectrum with small scale variations, indicative of localized differences in the energy of the particles, probably combined with magnetic field strength variations.

7.3.2 3C 236

The LOFAR image of 3C 236 suffers from overall higher noise levels when compared to the NGC 6251 image due in part to the fact that we have imaged a smaller bandwidth. Looking at the LOFAR image in Figure 7.4, we note the bright (restarted) CSS core. We can see ripple artifacts superposed over the lobes (most probably leftover sidelobes after the deconvolution caused by the very bright core). We also note that in our LOFAR maps we trace less lobe emission than what is seen in the literature; due to the limited bandwidth we have imaged we miss the fainter lobe regions towards the core.

Notably, we can see that the inner region of the north-western lobe is fragmented, meaning that we detect the middle lobe, a possible sign of a flicker in the past activity of the AGN (Barthel et al. 1985).

The low frequency spectral index map (Figure 7.5) shows that the mid regions of the lobes have a spectral index which is characteristic of a young particle population, identical to the spectral index of the recently restarted CSS core (Schilizzi et al. 2001). This might indicate that the lobes are still being replenished with plasma ejected by the AGN at the end of the previous active epoch, or that the particles are being re-accelerated in the lobes. We also can detect the middle lobe (fragmentation of the inner region of the north-western lobe). If the fragmentation is due to an interruption in AGN activity, the episode must have been very short.

We observe lobe edges having steep spectral index, with a sharp transition. Comparing with point sources in the field which show similar features, we note that the steep spectrum regions in the case of the target are slightly wider. At those positions there is enough source flux in both of the maps we use (above 5σ). We may be tracing the very low energetic particles outlining a radio cocoon enveloping the lobes.

Mack et al. (1998) estimate the age of 3C 236 to around 100 Myr, based on spectral aging arguments. There is a possibility that the lobe replenishment via the jets may have been interrupted on timescales of a few Myr due to jet collapse or encounter with intervening clumps of matter closer to the core. While not detected in the large scale maps, the intermittency might be causing the fragmentation which we see in the north-western lobe and spectral index maps.

7.4 Discussion

7.4.1 NGC 6251

Very Large Array (VLA) observations of the radio galaxy were performed by Perley et al. (1984) at frequencies ranging from 1370 MHz to 4885 MHz. They have discovered a $130''$ counter-jet. The jet/counter-jet brightness ratio ranges from 40:1 at $100''$ from the core (measured at 610 MHz) to more than 250:1 at $240''$ from the core (also at 610 MHz). In our LOFAR image we detect an extension to the already known inner counter-jet (also detected in lower resolution maps as an extension of the southern lobe by Waggett et al.

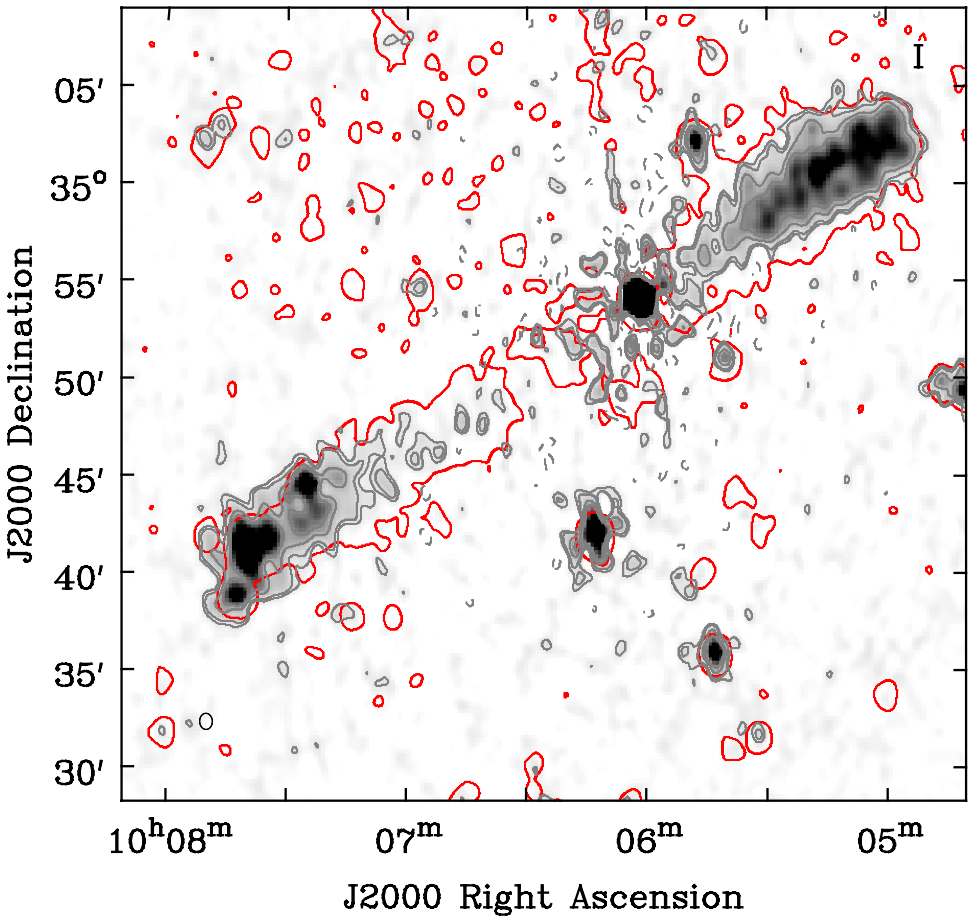

Figure 7.4: Grayscale LOFAR map of 3C 236 at 140 MHz. Gray contours: $(-3, 2, 3, 6, 9)\sigma$. Shown in red is the 2σ contour level of the WSRT 609 MHz map.

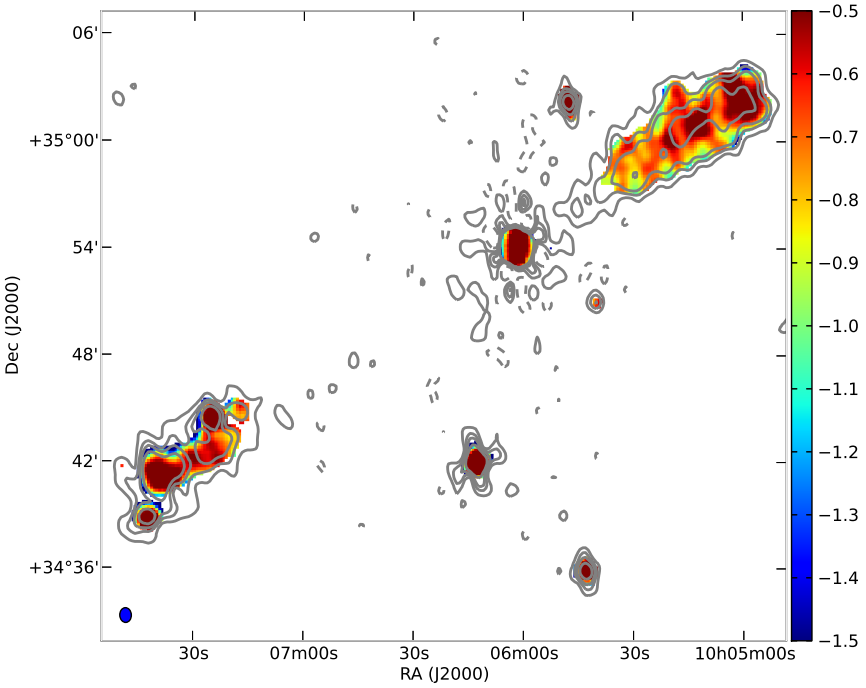

Figure 7.5: α_{144}^{609} spectral index map. Overlaid in gray are LOFAR contours with levels: $(-3, 3, 6, 9, 15)\sigma$

1977, but not seen by Mack et al. (1998)) which connects the south-eastern lobe to the core.

We compute the flux density ratio for the jet to the counter-jet at 144 MHz to be 60:1 at a distance of 240″ from the core and 27:1 at a distance of 340″ from the core.

Given its large (projected) size, the radio axis of NGC 6251 is likely to be close to the sky plane. Consequently, beaming and orientation effects are less important and there must be intrinsic differences between the east and west side of the source, possibly having to do with different radiative efficiencies between the jet/counter-jet.

The flux densities of the hotspots (A, C) and jet (F) at 140 MHz are: 1.3, 0.7 and 6.3 Jy respectively.

Comparing our spectral index map with ones made by Mack et al. (1998) at higher frequencies, we can see that our study is in agreement on the spectral index trends for the outermost edges of the lobes where spectral index values of $\alpha = -1.4$ are prevalent. Their coarser resolution prevents them from resolving the jet clearly, and they report different high frequency spectral index of the hotspots ($\alpha \sim -0.8$ for the north-western one and $\alpha \sim -1.2$ for the south-eastern one), while we see the jet and hotspots having a spectral index of about $\alpha \sim -0.6$ at low frequencies, a clear sign that we see older particle population, indicating that there are signs of spectral aging in the jet / hotspots.

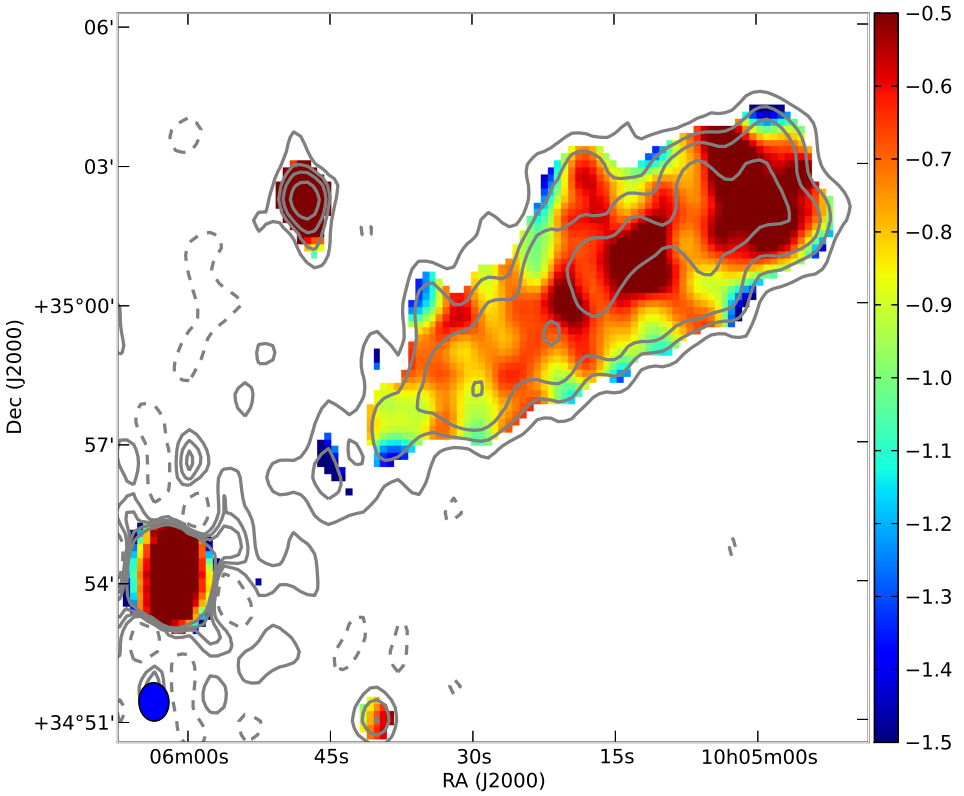

Figure 7.6: Zoom-in on the α_{144}^{609} spectral index map of the north-western lobe and core of 3C 236. Overlaid in gray are LOFAR contours with levels: $(-3, 3, 6, 9, 15)\sigma$

Minor jet misalignment was reported by Cohen & Readhead (1979), and a wiggle in the jet at a distance of 85 kpc from the core was discovered by Saunders et al. (1981). There may be a connection between it and the large scale morphology that we see. The spatial resolution of our map is too poor to directly compare the jet in our image with the deviations of the jet reported by Perley et al. (1984). We detect a noticeable bending of the counter-jet at a distance of around 240″ (150 kpc) from the core.

7.4.2 3C 236

Our low frequency spectral index studies match the conclusions drawn by Mack et al. (1998) from their higher frequency spectral index maps. We observe that the spectral index steepens from $\alpha = -0.5$ to $\alpha = -0.8$ going from the outer lobe edges towards the core, especially evident in the north-western lobe. We also note that the inner mid lobe regions have flatter spectral index and are fragmented (possible spectral index signature

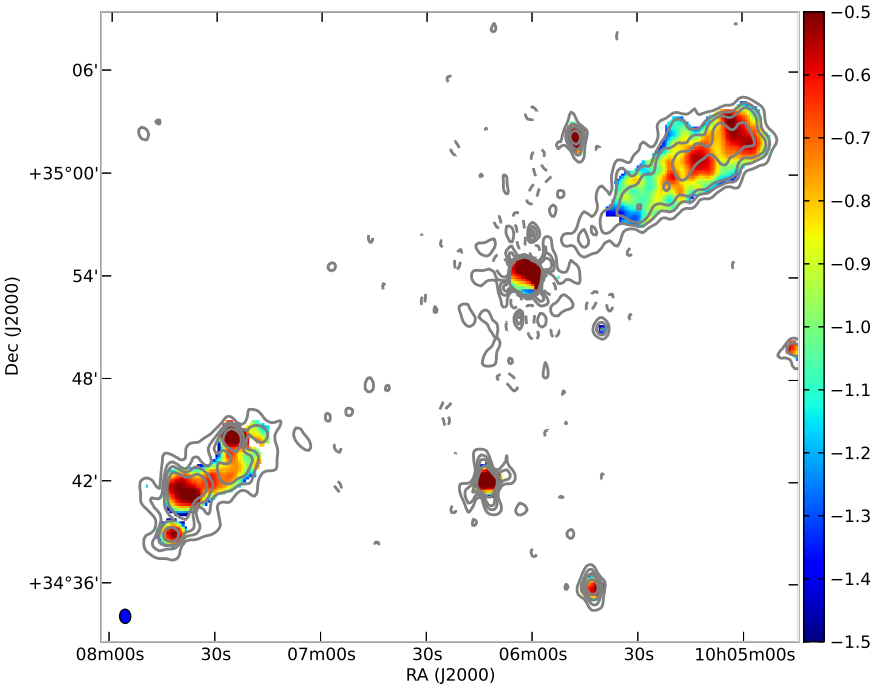

Figure 7.7: α_{144}^{1400} spectral index map of 3C 236. The contours are the same as shown in Figure 7.5.

of the middle lobe/ridge reported by Barthel et al. (1985); Figure 7.6). Mack et al. (1998) report that that lobe has an overall steeper spectral index compared to the south-eastern one. Our higher resolution spectral index mapping (Figure 7.5) shows that this may be due to beam effects averaging the spectral index in lower resolution maps.

A ridge of emission in the south-eastern lobe, mentioned previously, is observed in our spectral index maps (ex. Figure 7.5) and we see signs of the reported wiggle of the ridge.

Spectral index mapping at higher frequencies at the same spatial resolution (Figure 7.7) confirms these trends. The flatter spectral index regions in the north-western lobe is clearly outlined. The spectral curvature map shown in Figure 7.8 shows a spectral break at the inner edge of the north-western lobe, suggesting that it is a region of aged plasma. The northern edge of the south-eastern lobe shows no curvature, and steep low frequency spectrum, suggesting that it may be composed by the oldest particle population observed in 3C 236.

O'Dea et al. (2001) suggest (based on their HST studies of star formation in the nucleus of the host galaxy) an age of the large scale lobes in the range of 10^8 to 10^9 years and an off timescale of around 10^7 years. Assuming a total age (for the outer lobes) of $t_s = t_{ON} + t_{OFF} = 110$ Myr and a magnetic field strength in the lobes of 4μG, using the

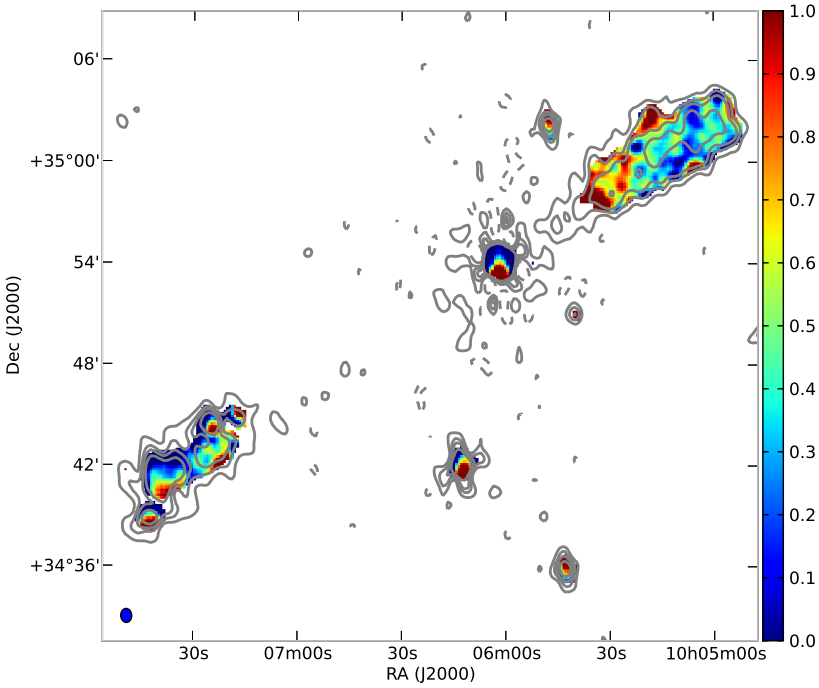

Figure 7.8: $\alpha_{144}^{609} - \alpha_{609}^{1400}$ spectral curvature map of 3C 236. The contours are the same as shown in Figure 7.5.

relations between the break frequency in the lobe spectrum and the age of the plasma given in Murgia et al. (2011), we estimate the break frequency to be $\nu_b = 1900$ MHz. From the spectral curvature map shown in Figure 7.8 we can see that the lobes show little curvature up to 1400 MHz, in line with the ages estimated in O'Dea et al. (2001). An exception to this argument is the inner north-western lobe which shows spectral curvature in the frequency range below 1400 MHz, pointing to its age being greater than 120 Myr under the above assumptions.

7.5 Conclusion

We have presented our LOFAR observations of two GRGs: NGC 6251 and 3C 236. We study these sources for the first time at a resolution of 50″ at such low frequencies. We elaborate the extent of low energy particle population in the lobes of NGC 6251, and describe a counter-jet cocoon. We confirm earlier work on the spectral properties of the lobes of 3C 236, and spatially resolve different particle populations.

The low frequency spectral index maps we have derived show previously undetected small scale variations (see Mack et al. 1998, for reference) in the surface brightness in the

lobes of NGC 6251 and a possible detection of a cocoon of low intensity radio emission enveloping the lobes of 3C 236. These results represent a first look and can be improved upon by utilizing the full LOFAR bandwidth, especially in the case of 3C 236.

LOFAR represents a very valuable instrument for these kind of studies. As we have demonstrated in this chapter, its sensitivity combined with its potential for high resolution imaging at low frequencies offers an unprecedented detailed view at the oldest diffuse emission regions. Using LOFAR will prove instrumental in the future in revealing new features in known objects as well as enabling new discoveries.

Chapter 8

Summary and future prospects

The Great Way is gateless,
approached in a thousand ways.
Once past this checkpoint, you
stride through the universe.

– Wu-wen kuan

In this work we have shown the variety of relic structures formed as a consequence of AGN activity. We have demonstrated the use of multi-wavelength data to put constraints on aging models and derive radiative ages of relics. Also, we have shown that new facilities like the LOw Frequency ARray (LOFAR; van Haarlem et al. 2013) which operate at the lowest frequency end of the radio spectrum can be very useful in both discovering new relics and tracing out the oldest particle populations in known relics and helping to constrain our modeling.

Below we give a systematic overview of AGN properties and their relation to AGN radio relics. We conclude with our findings and outline a path for future studies, having in mind the availability of novel facilities such as LOFAR.

8.1 The AGN - relic connection

AGN radio relic properties obviously depend on the specifics of the past active phase of the radio source. The most obvious morphological division of radio sources is the Fanaroff & Riley (1974) classification scheme, dividing radio sources into two categories: FRI and FRII. FRI sources are characterized by a bright radio core, flaring jets, no hotspots, they tend to be brighter toward the location of the AGN and have spectral indices which are steeper going outward from the host galaxy. The FRII sources have sometimes a noticeable radio core, tightly collimated relativistic jets, clearly delineated hotspots where the jets end and plasma lobes surrounding the jets/hotspots. Typically, the surface

brightness of these sources peaks at the hotspots located symmetrically w.r.t the host galaxy. The specific radio luminosity which divides these two classes is $L_{1400MHz} \sim 10^{24} - 10^{25}\mathrm{WHz}^{-1}$, although this division is not sharp. Best (2009) has shown that more massive galaxies are more likely to host a radio source, but that the luminosity of a radio source is largely unrelated to the mass of the host galaxy.

The spectral properties of optical AGN and their relation to the radio phenomenology is also ambiguous. The fraction of galaxies hosting an AGN as identified from their optical spectra (emission line AGN) shows no dependence on the mass of the host galaxy (Kauffmann et al. 2003). Best et al. (2005) show that the probability of an AGN being radio loud is independent on whether it is classified as an emission line AGN or not.

With respect to radio power, low luminosity radio sources are predominantly powered by radiatively inefficient (low excitation, advection dominated accretion, jet mode accretion) AGN. Conversely, high luminosity radio sources are predominantly powered by radiatively efficient (emission line, high excitation, radiative mode accretion) AGN. The radiatively inefficient accretion probably arises by (relatively small amounts of) hot gas acreting onto a Super Massive Black Hole (SMBH), while the radiatively efficient accretion is though to arise from higher accretion rates of (cold) gas onto a SMBH.

Relative to the radio morphology, most of the FRII radio galaxies are powered by radiatively efficient (emission line, high excitation, radiative mode accretion) AGN, while most of the FRI radio galaxies are powered by radiatively inefficient (low excitation, advection dominated accretion, jet mode accretion) AGN. The radiatively inefficient AGN show no sign of a quasar (visible or hidden) at optical, infrared or X-ray wavelengths (Hardcastle et al. 2007), but some FRIs have quasar nuclei. Best & Heckman (2012) show that FRIIs occur in somewhat less massive and somewhat bluer host galaxies than FRIs.

Hence, the initial accretion (and AGN triggering) mechanism is probably unrelated to the large scale radio morphology. Best (2009) finds that, in his sample, FRII sources are in general smaller than FRIs. He suggests that all radio sources start their life as young (CSS, GPS) FRIIs. In some cases, their relativistic radio jets are later disrupted (decollimated) by the host galaxy ISM and they become FRIs with lower radio luminosity. The fact that CSS source morphologies do show symmetric structure reminiscent of FRIIs seems to support this suggestion.

The nature of the AGN accretion and triggering mechanisms is related to the expected morphology of relic structures, whether the radio source (and relic) morphological type changes between activity episodes and to the specifics of the AGN duty cycle. In relation to what was discussed above, based on the radio source morphology, we can summarize the relic-related radio source properties as follows:

- FRI radio sources have lower radio luminosities and their AGN are predominantly hosted by massive elliptical galaxies which are members of galaxy clusters. There are no known instances of FRI radio relic faders. Several instances of restarted FRIs are known, one of which is 4C 35.06, studied in Chapter 3 of this thesis.

- FRII radio sources have higher radio luminosities and their AGN are generally hosted by less massive field galaxies. So far, we know of just one well studied case of an FRII relic fader in the field (B2 0924+30, studied in Chapter 5 of this thesis). In some cases (steeper spectral index of the outer pair of radio lobes w.r.t the inner ones) the double-double radio galaxies (DDRGs) could be thought of as restarted FRIIs.

Statistical studies of the luminosity of radio sources (Best et al. 2005; Shabala et al. 2008) demonstrate that FRII radio galaxies are switched off for one to few Gyr, while FRIs seem to have a duty cycle of $t_{off} < 3t_{on}$. These observations might provide a clue for the scarcity of (FRII) radio relics in the field. We would only be able to detect them in the short time before they fade from view.

Studies by Dwarakanath & Kale (2009) and Best et al. (2005) show that we should be able to observe many more AGN radio relics than we do now. However, AGN radio relics are scarce, and the reasons behind this are still a mystery. If adiabatic energy losses are responsible for the very fast fading of relics, it may explain their scarcity, but there is no clear evidence that the a substantially larger number of relics is observed in cluster environments vs. the field, even though there are hints in surveys pointing in this direction. A possibility exists that our current radio surveys (even the low frequency ones) are not sensitive enough.

Radiative aging studies performed on radio relic faders were carried out by Parma et al. (2007) on six faders and three restarted relics. The duration of the active phase was estimated to be in the range of 10^7 - 10^8yrs. with the duration of the inactive period an order of magnitude shorter. No clear dependence was observed w.r.t environment (cluster vs. field).

Murgia et al. (2011) find that in their sample of five radio relics hosted by galaxies belonging to clusters, three have a duration of their inactive periods which is longer than the active radio phase, and for the rest the inactive period lasted a third of the active period. Compared to the field sources studied by Parma et al. (2007) it seems that radio relics in clusters tend to have longer lifetimes, maybe because of radio plasma confinement mitigating the energy losses. Morphologically, the sources WNB 1734+6407 and B2 1610+29 in the sample of Murgia et al. (2011) resemble FRII relics; B2 1610+29 has also a spectral index profile consistent with it being a FRII relic. The other sources show morphological and spectral characteristics of FRI relics (possibly with restarted cores). Murgia et al. (2011) have also merged the statistics of their sample and the Colla et al. (1972) complete B2 bright sample and have found that the probability of a radio relic fader being located in a cluster is around 80%. This might indicate that the hot cluster gas is confining the plasma and decreasing or stopping its expansion, thus extending the radiative lifetime. Another possibility is that radio sources hosted by cluster galaxies have shorter duty cycles, so at any given time they will present an observable AGN radio relic emission.

Giacintucci et al. (2007) have studied seven radio relics (faders and restarted) hosted by cD galaxies in clusters. Their results in general agree with those of Murgia et al. (2011) in that the derived relic ages are larger than those observed in field galaxies. Most of the fader sources in the sample show characteristic spectral index profiles suggesting that these relics can be thought of as being remnants of FRI radio galaxies.

How do all these pieces of radio morphology, size, triggering mechanisms, environment and distance fit in the AGN radio relic puzzle? Notwithstanding the inter-dependencies between these factors, one possible overview would be the following.

- **Morphology.** Assuming that all radio sources start as FRIIs, a fraction of them whose jets are de-collimated will grow to be FRIs, with the rest having a large scale FRII morphology. It may be that jet de-collimation is more likely in massive cluster galaxies, which would explain the association of FRI radio galaxies (and their relics) with massive cluster galaxies.

Studies of Murgia et al. (2011) and Giacintucci et al. (2007), the radio morphology of the 4C 35.06 source (Chapter 3) as well as that of 3C 388 are relevant cases in this point, showing aged radio sources in clusters, sometimes restarted, which tend to be older than sources in the field. The notion that FRI radio galaxies have duty cycles characterized by short inactive epochs and activate more frequently may explain why there is a tendency to find relics of radio loud galaxies (possibly of FRI type) on average slightly more often in clusters than in the field.

As we have noted before, FRII radio relics are sparse. This may be because FRII radio galaxies tend to be found more in the field (as mentioned previously) where any radio relics quickly fade away. Based on the recent work of Eilek (2014), the maximum electron radiative lifetime assuming a reasonable value of the magnetic field would be between 150 and 200 Myr. After that, the relics would fade away and be undetectable. In our study of the AGN radio relic B2 0924+30 we have shown that the outer lobes are as young as 20 Myr. Even though in this case it seems that radiative and Inverse Compton (IC) energy losses are dominant, it may be that in the future expansion losses will take on the dominant role and this relic will disappear fast (as may already have been the case with others similar relics). A duty cycle characterized with longer inactive periods will contribute to these sources being more difficult to observe at any given epoch; they will only be visible for a short time after the end of the active phase. If the (cold gas) fueling of FRIIs is connected to galaxy mergers, the period between two consecutive activity epochs would be on the order of a Gyr (as mentioned previously).

As a side note, the large scale, low surface brightness relic discovery which we have discussed in Chapter 2 of this work is associated with a CSS source, B2 0258+35, which has an FRI morphology. If the proposition of Best (2009) holds, it follows that its jet de-colimation has happened very close to the AGN.

- **Size.** A fraction of the AGN would shut down after a short period of activity due to lack of fuel, and possibly restart again. We would expect to see the radio relics from this brief active phase as relics around young, CSS or GPS sources. Previous studies have shown that small-scale relics around compact sources are scarce; this may be due to the fact that in majority of cases the AGN active timescale is not so short, or it may be a selection effect - looking for small-scale AGN radio relics around currently active compact sources (and being able to see them) would require that the AGNs stop their previous active phase in a relatively short time and restart again before the relic fades away. This would naturally limit the number of relics observed. Our low frequency search for large radio relics around young compact sources (elaborated in Chapter 6) has not uncovered new relics, although this result is probably biased by our sample selection and the limited sensitivity and spatial resolution of the MSSS survey we have used.

- **Triggering.** It is not very clear what is the relation of cold gas and in particular H I to the AGN duty cycle. We have discussed the large reservoir of cold gas found around the host galaxy and in the vicinity of the CSS source B2 0258+35 in Chapter 2. Also, the H I absorption profile found in the host galaxy of 4C 35.06 was discussed in Chapter 3. The kinematics of the gas in these cases suggests no connection with previous AGN activity or AGN re-start. The presence of cold gas

hints at a supply which may fuel the AGN activity, even though the gas transport mechanisms to the AGN are less clear and remain an open issue at the moment. However, several studies suggest that the occurrence of H I in the central regions of restarted radio sources is higher than in other radio sources (Saikia & Jamrozy 2009; Chandola et al. 2010; Geréb et al. 2013).

Konar et al. (2013) have found that the inactive phase of two DDRGs they have studied (hosted by field galaxies) lasted only a few percent of the active phase, which is in stark contrast to the duty cycles discussed above. The reasons why these field radio galaxies are so different in this respect, and whether they are just outliers will need more study to be ascertained with any certainty. It is certainly possible that within broad subgroups or relic/re-started radio sources finer variations exist which blur the clear demarcation lines that we are discussing.

- **Environment.** Independent of other variables, denser cluster environments may prolong the fading timescale. This may be a contributing factor why we are seeing more large scale relics in cluster environments and why field galaxy hosted relics are scarce. However, much more studies are needed (and especially large relic samples) before we can claim any conclusive results.

- **Distance.** Tasse et al. (2008) have shown that lower luminosity, FRI radio galaxies are connected to galaxy overdensities at $z = 0.5$, consistent with what we observe locally. However, the recent work of Hatch et al. (2014) and Wylezalek et al. (2013) notes radio galaxies consistent with observed $L_{500MHz} = 10^{27.5} - 10^{29}\mathrm{WHz}^{-1}$ specific luminosities associated with galaxy clusters at $1.3 < z < 3.2$. These luminosities correspond to FRII radio galaxy luminosities. This result suggests (barring any selection effects) that at higher redshifts in cluster environments FRII radio galaxies are (at least) equally abundant as FRIs, indicating evolution with redshift of the radio galaxy population in cluster environments. The implications of this result on AGN radio relics would be that FRII relics dominate high redshift clusters of galaxies, as opposed to FRI type relics locally.

8.2 Results and future work

We have given an overview of and summarized the most important AGN properties as they relate to AGN radio relics, and have gone over the interdependencies of various astrophysical properties which influence the AGN duty cycle and relic properties. In this thesis, we have studied various types of AGN radio relics to constrain their properties and quantify the AGN duty cycle and any environmental influence on the relic properties.

- In **Chapter 2** we have investigated a very low surface brightness relic discovered around the young Compact Steep Spectrum (CSS) source B2 0258+35. It is a very interesting relic, since it is relatively large for relics typically reported around CSS sources. It also shows a distinct lobed appearance, suggestive that it may still be connected to the central source and re-fueled at a very low level of activity. Under the assumption that it is a rising relic bubble, we have been able to derive its dynamical age and estimate the accretion rate of the CSS source, both estimates agreeing with literature values.

Assessment of the radiative ages should follow using follow-up observations, preferably at low frequencies. The relic structure has been detected at 150 MHz using LOFAR (Marisa Brienza, private communication). More relics may be discovered around compact sources, this may be just an example of why we have not been able to detect them so far, they may be too faint at high frequencies and present observational difficulties since they are located in the vicinity of a bright source.

- **Chapter 3** discusses a serendipitous discovery of extended steep spectrum emission connected to the radio galaxy 4C 35.06. The observations were performed in the LOFAR LBA band around 60 MHz as part of the commissioning activities and have actually been centered on the target discussed in Chapter 2. This demonstrates the added value of the large LOFAR field of view; we present an analysis of the radio source properties in this field in Appendix A.

  We were able do determine that the source has an unusual helical morphology and that it is a restarted FRI source. We have shown that its outer regions have extremely curved spectra and were able to quantify the contribution of various source regions to the integrated source spectrum. Such insight can prove useful when searching for relics or restarted radio sources; the integrated spectrum properties (steepness as it relates to curvature) can be a useful tool in such a search. Benchmarking these tools on resolved sources which we can study in detail is a necessary step which we have performed in our study.

- **Chapter 4** showcases a targeted study of an AGN relic (J1431.8+1331) located in a cluster of galaxies. We have extended previous studies of this intriguing object to the lowest frequencies to date (around 150 MHz, using the LOFAR HBA band) and have derived low frequency spectral index, spectral curvature and spectral aging maps. We have showed that radiative aging is the dominant energy loss mechanism, possibly a sign that the hot gas in the cluster is constraining the radio plasma expansion. Our results are in line with fading timescales derived for cluster relics. For this particular source, we have been able to show that two distinct source regions have different radio emission origin: AGN relic and a shock wave compressed plasma bubble, underlining the value of spatially resolved low frequency observations.

- **Chapter 5** studies a very rare AGN relic type, B2 0924+30, which shows an aged FRII morphology. It is the only known relic of this type. Our spatially resolved LOFAR HBA data were again instrumental to demonstrate its FRII origin and to constrain the time of cessation of AGN activity to around 150 Myr ago. We have been able to derive the highest resolution spectral index and age maps at low frequencies. Interestingly, we have shown that for this field relic the dominant energy loss mechanisms are still radiative losses.

- **Chapter 6** outlines our use of the preliminary LOFAR Multi-frequency Snapshot Sky Survey (MSSS) maps to search for AGN radio relics around young (CSS and GPS) radio sources. We have been able to detect several known giant radio galaxies, but due to the limited sensitivity and resolution we have not discovered any new relics near compact sources. Even so, we have placed constraints in that a moderate surface brightness relic population does not seem to exist around the neraest compact sources, which supports the results of Chapter 2.

- In **Chapter 7** we have performed the first of its kind low frequency (150 MHz, LOFAR) high resolution study of two giant radio galaxies, 3C 236 and NGC 6251. We have studied the spectral index and discovered a counterjet connecting the core region of NGC 6251 to its south-eastern lobe as well as mapping extended emission on the outskirts of its lobes. We have also mapped the curved spectrum of the region close to the core in the north-western lobe of 3C 236, and have confirmed that the inner lobe region has injection index spectral indices ($\alpha \propto -0.6$) at low frequencies.

These results demonstrate the usefulness of LOFAR as a relic survey instrument thanks to its unprecedented sensitivity at low frequencies, as well as the high imaging resolution. Our discoveries showcase its abilities. We have discovered unknown steep spectrum sources in almost every LOFAR pointing, maybe a hint of an unknown low surface brightness relic population.

In the future we would like to address the still unanswered questions pertaining to the AGN radio relics and also contribute towards gaining more insight into their properties. In summary:

- What are the ON and OFF timescales for the AGN activity (the AGN duty cycle)?
- Does the duty cycle depend on the AGN environment (AGNs in clusters vs. AGNs in the field)?
- For resolved sources, what is the age of the radio plasma across the source?
- How do the properties of the integrated radio spectrum change over the lifetime of the AGN, and can these properties be used as a diagnostic tool to infer the ages of source components for unresolved / high redshift radio sources?

Such questions require much larger AGN radio relic sample sizes to be answered conclusively. Due to the nature of the non-thermal emission, the AGN radio relics are more likely to be found at lower frequencies. As we have demonstrated, the LOFAR telescope is providing science-worthy data and should provide the sample sizes we need, as a precursor for the SKA which will really open up the skies for these studies.

The MSSS survey (Heald et al. 2014, submitted) has proven that LOFAR is ready for such surveys. However, we may need better sensitivity to really uncover the relic population. This means that the LOFAR tier 1 and 2 surveys should begin the proper characterization of the AGN radio relic population. A hint of this is already apparent; our dedicated high sensitivity LOFAR observations have already uncovered several new relic candidates. We will also need multi-frequency follow-up of any relic discoveries if we wish to model the radiative aging process or disentangle between the predictions of different models.

In general, there is a trend for the re-starting of AGN to happen more often for AGN hosted by galaxies in clusters. This may be even more so for AGN hosted by multi-core cD galaxies in clusters. A systematic LOFAR observation of all of these objects should allow us to check this hypothesis and lead to better understanding of AGN activity triggering/feedback in these systems.

Following up on our studies of relics around compact sources is essential to put constraints on the duty cycle of these sources, and to explain the relative relic scarcity around

them. High resolution, high dynamic range imaging is a prerequisite. Ways ahead include re-processing of the MSSS data including longer baselines, or using deeper observations. The large LOFAR FoV makes these deep pointings a rich hunting ground for relics as we have shown in this thesis.

In addition, the way in which the various source components, i.e. substructure in the AGN radio relics influence the integrated flux density spectrum of these sources and the derived ages were discussed in Chapters 4 and 5. These considerations help us to avoid mistakes when using spectral shapes to classify sources and point to a technique of quickly picking up relics from future surveys. Enlarging our samples of relics would allow us to further refine this technique.

The selection techniques used for finding new relics are an important issue. Our results show that having access to high frequency complementary data sets (in sensitivity and spatial resolution) is essential. Morphological selection of relics can be unreliable. The integrated flux density spectrum can be a good tracer not only of relic sources, but give valuable insight into their current activity.

In an era when radio astronomy is using novel instruments like LOFAR, opening the low frequency curtain to the universe and gearing up for the Square Kilometre Array (SKA), there is plenty of science to be done, and the challenges which the AGN radio relics present are worthy of the capabilities of these powerful new facilities.

Appendices

We have included as appendices analyses connected to the content presented in this writing.

The first appendix analyses the source properties in the field around the CSS source B2 0258+35 which we have studied in Chapter 2.

The second appendix lays out the clock/TEC fitting procedure performed on the data set taken for Chapter 4. The procedure was performed as part of the LOFAR commissioning efforts.

The third and final appendix outlines a recent case of mis-identifying a radio source structure as a consequence of not taking instrumental effects into account when interpreting interferometric images.

Appendix A

Radio sources in the LOFAR field centered on B2 0258+35

We shall not cease from exploration, and the end of all our exploring will be to arrive where we started and know the place for the first time.

– T. S. Eliot

A.1 Motivation

The large instantaneous field of view of the LOw Frequency ARray (LOFAR; van Haarlem et al. 2013) telescope (around $4° \times 4°$ at 60 MHz in the LBA band) encompasses many sources in the vicinity of the target of a particular pointing. Such a large FoV can almost be considered a "mini-survey", since it covers an area of the sky much larger than other facilities at comparable spatial resolution.

We have performed spectral index studies on the sources found in the area around the B2 0258+35 Compact Steep Spectrum (CSS) source. This source was observed with LOFAR as part of follow-up studies related to the study elaborated in Chapter 2 in this thesis. The details of the LOFAR observation and data reduction are given in Chapter 3 of this thesis. We have observed in the LOFAR LBA band, around 60 MHz.

A.2 Results

The central part of the resulting LOFAR image is presented in Figure A.1.

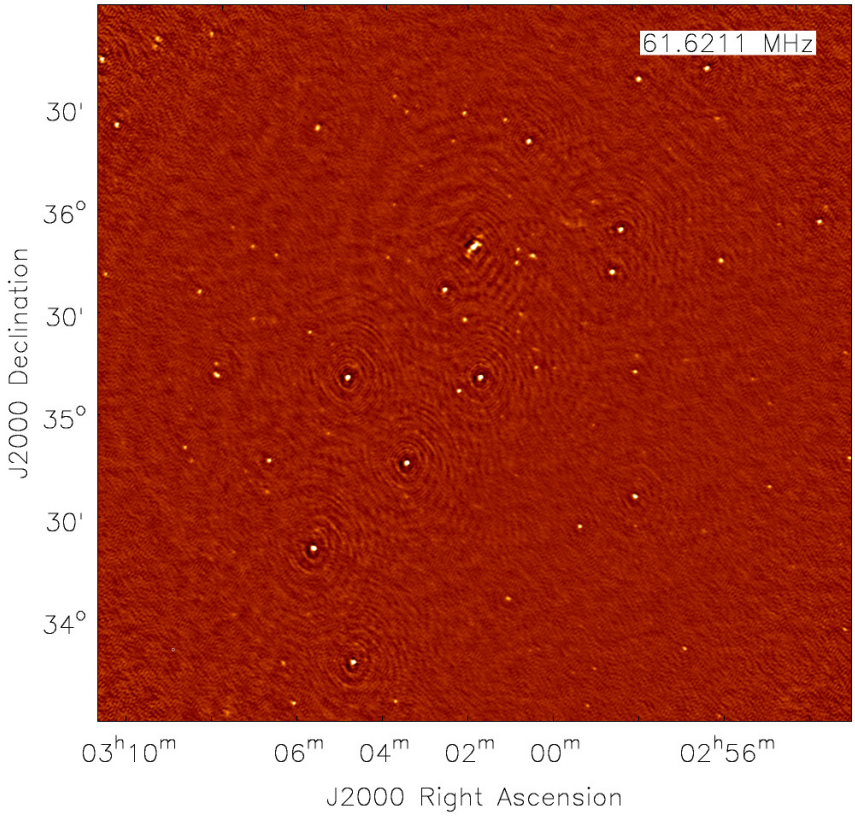

Figure A.1: Final LOFAR image. B2 0258+35 is in the phase center.

We have compared the LOFAR image to VLSS[1] and NVSS[2] survey maps and a 1400 MHz deep Westerbork Synthesis Radio Telescope (WSRT) image centered on the target, described in Chapter 2 of this thesis. We have performed our studies on a $3.5° \times 3.5°$ region around the phase center. The properties of the images we have used are summarized in Table A.1:

A.2.1 Source extraction

The PyBDSM package (Ramanujam 2007) was used to extract sources from our images; the source counts are presented in Table A.1. We have matched the positions of the sources in the source catalogs by using a $80''$ match radius around each source position. Out of the 40 sources detected in the VLSS image, we find 35 matches between LOFAR

[1] VLSS (Cohen et al. 2007) is the VLA Low frequency Sky Survey carried out at a frequency of 74 MHz

[2] NVSS stands for the NRAO VLA Sky Survey carried out at a frequency of 1.4 GHz (Condon et al. 1998)

Table A.1: Comparison of the data sets

ID	ν[MHz]	$\Delta\nu$[MHz]	Beam size	σ[mJy/b]	Source count
LOFAR	61	6	$48.2'' \times 43''$	30 (img. avg.)	98
VLSS	74	-	$80'' \times 80''$	100	40
NVSS	1400	-	$45'' \times 45''$	0.4	479
WENSS	325	-	$96'' \times 54''$	3.6	147
WSRT	1400	20	$38.8'' \times 33.1''$	0.2	-

and VLSS. Taking possible mis-matches into account, we can say that all of the sources which were part of the initial VLSS calibration skymodel were recovered in the LOFAR image.

A.2.2 Position accuracy

We have compared the sky positions of the sources detected using PyBDSM between our LOFAR and NVSS catalogs, as well as between the NVSS and WENSS[3] catalogs. The results are shown in Figure A.2. It can be noted that there are source position differences on the order of a few arcseconds. There is, however, a trend in the LOFAR/NVSS comparison that the sources are shifted in declination on average by $2''$. Ionospheric distortions might explain some positional differences, but the systematic shift is surprising.

A.2.3 Spectra

We have calculated the α_{62}^{1400} (LOFAR/NVSS) spectral index[4] for the matched catalog sources. The results are given in Figure A.3.

Using a 5σ detection threshold, we have found 10 sources with $\alpha_{61}^{1400} < -1$. Table A.2 summarizes their properties.

By plotting α_{61}^{325} vs. α_{325}^{1400}, we get a "color-color" plot (Figure A.4) for all of the sources which were identified (as matches based on their sky position) in the LOFAR image, and extracted from WENSS and NVSS catalogue images.

Not all of the sources which are marked as steep spectrum ones in Figure A.4 are listed in Table A.2 and vice versa. The reason for this is that some sources were excluded from a combined match across all of the catalogs.

Figure A.5 shows the α_{61}^{1400} spectral index vs. the LOFAR flux for sources detected as matches both in the LOFAR image and the NVSS catalog. We detect a slight spectral flattening towards lower flux levels (in line with the findings of Intema et al. 2011, however we should be careful of over interpreting our initial results).

In Figure A.6 we have matched the LOFAR steep spectrum sources listed in Table A.2 with DSS/Sloan Digital Sky Syrvey (SDSS, Aihara et al. 2011) DR8 imaging. J030328+343738 and J030325+354620 have particularly interesting optical counterparts.

[3] WENSS stands for the Westerbork Northern Sky Survey carried out at a frequency of 325 MHz (Rengelink et al. 1997)

[4] defined as: $S \propto \nu^{\alpha}$

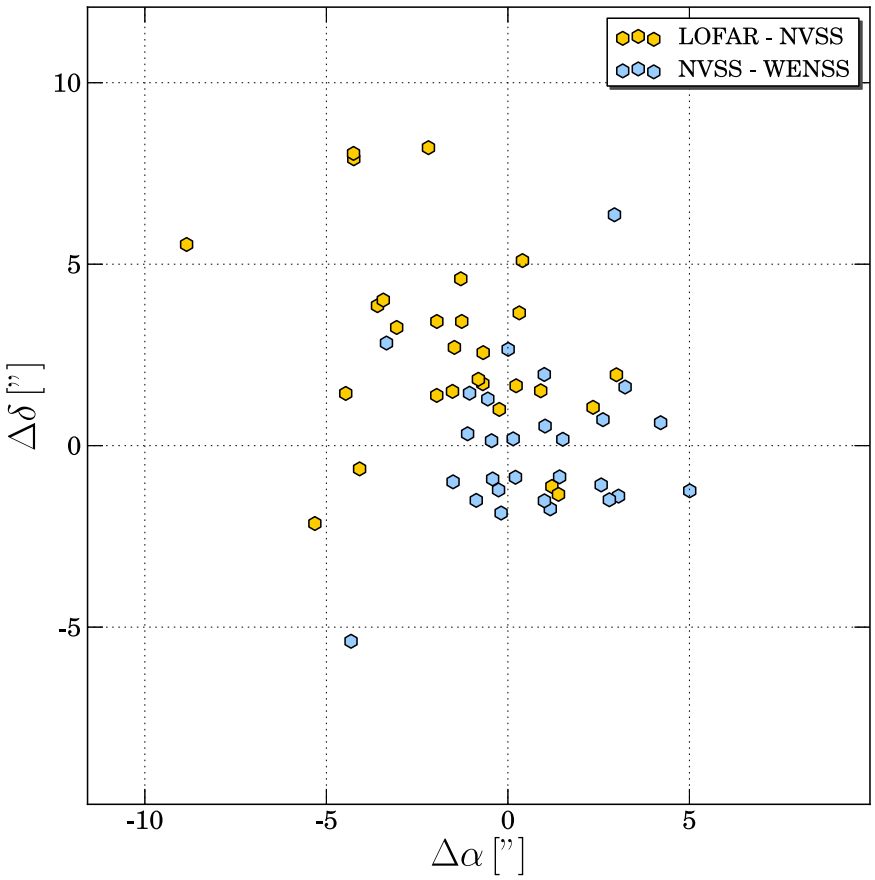

Figure A.2: Position errors in $\alpha[''']$ and $\delta[''']$ between the LOFAR, NVSS and WENSS source catalogs.

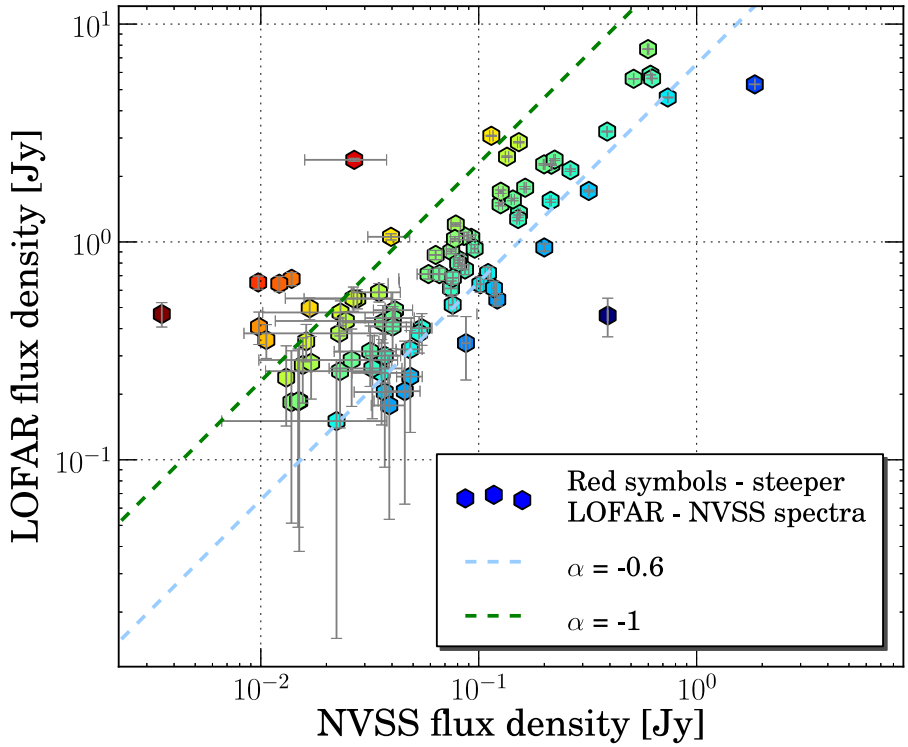

Figure A.3: NVSS - LOFAR Flux Comparison for source detection thresholds of 5σ.

Table A.2: Steep spectrum sources

ID	α_{J2000} [h:m:s]	δ_{J2000} [°:′:″]	S_{61} [Jy]	S_{325} [Jy]	α_{61}^{1400}	α_{325}^{1400}
J031054+364401[1]	03:10:55	36:44:08	2.38	0.163	-1.43	-1.70[2]
J030710+355006	03:07:11	35:50:12	0.65	0.038	-1.34	-0.94
J030604+333630	03:06:05	33:36:40	1.05	0.149	-1.05	-0.9
J030547+352513[13]	03:05:47	35:25:17	0.67	0.069	-1.24	-1.33[2]
J030328+343728	03:03:28	34:37:24	0.46	0.043	-1.56	-1.7
J030329+362956	03:03:30	36:30:02	0.49	-	-1.08	-
J030325+354620[4]	03:00:42	35:26:25	0.34	-	-1.11	-
J030100+360511	03:01:00	36:05:20	0.35	0.029	-1.12	-0.68
J030048+354946[4]	03:00:48	35:49:47	0.64	-	-1.26	-
J025819+355526	02:58:20	35:55:26	3.06	0.376	-1.05	-0.81

[1] Ultra Steep Spectrum (USS) source according to de Breuck et al. (2000)
[2] Taken from de Breuck et al. (2000)
[3] Quasi Stellar Object (QSO), z = 3
[4] Associated with the galaxy cluster Abell 407, z=0.0462

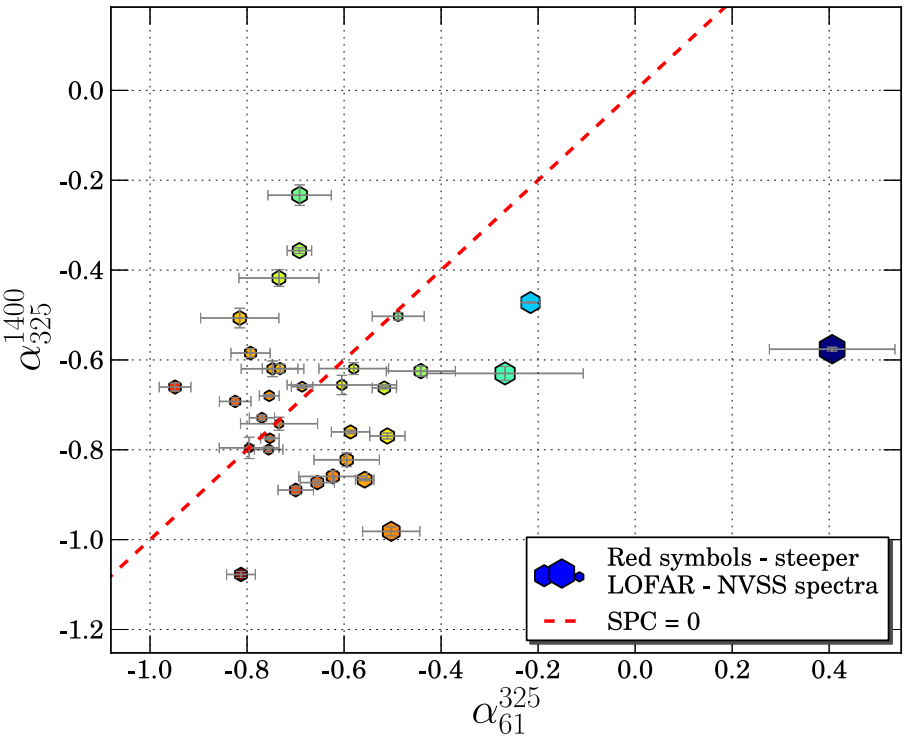

Figure A.4: Color - color plot of α_{61}^{325} vs. α_{325}^{1400} spectral indices for matching sources in the LOFAR, WENSS and NVSS source catalogs for the field studied. The source detection level is 5σ; the error bars for the spectral indices are obtained by propagating the errors of the flux measurements. The red dashed line represents zero spectral curvature ($SPC = \alpha_{61}^{325} - \alpha_{325}^{1400}$).

A.2.4 NVSS Dropouts

We mark as "NVSS dropouts" those sources which are found in the LOFAR image catalog, but absent in the NVSS survey catalog.

For a 5σ detection threshold and a match radius of $50''$we have identified two sources as NVSS dropouts. Their properties are given in Table A.3.

Table A.3: NVSS Dropouts

ID	α[h:m:s]	$\delta[^\circ:':'']$	S_{61} [Jy]
J030104+365824[1]	03:01:04	36:58:24	0.11
J030050+351832[2]	03:00:50	35:18:32	0.24

[1] $m_u = 22$ SDSS galaxy at z=0.2
[2] Close to a bright source

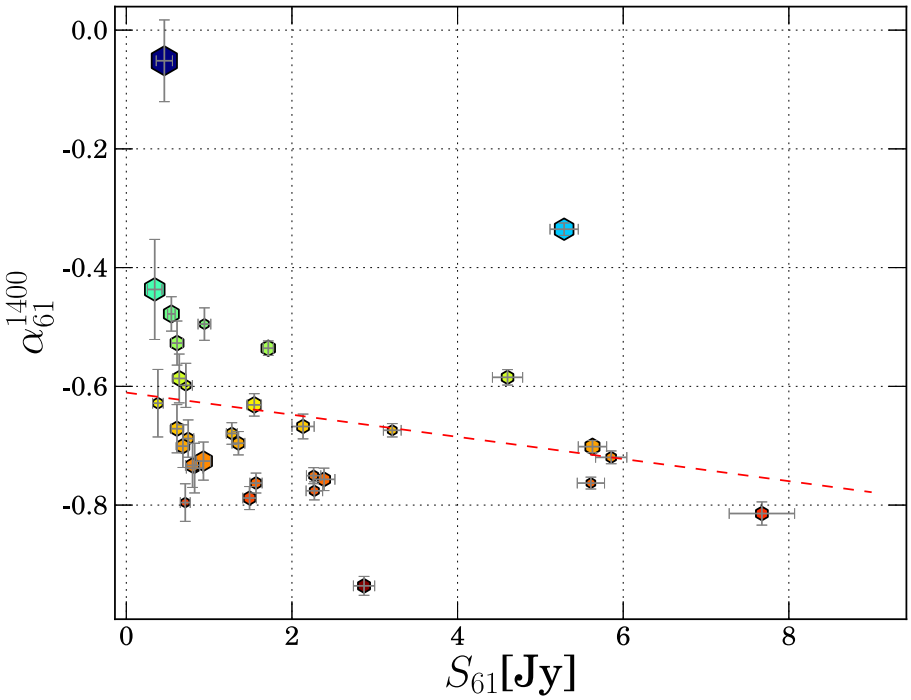

Figure A.5: α_{61}^{1400} vs. LOFAR flux. The red dashed line represents a linear regression to the data.

They are possible ultra steep spectrum sources $\alpha_{61}^{1400} < -1.5$. Figure A.7 shows optical cutouts (DSS/SDSS DR8) centered at the corresponding source position.

A.3 Diffuse extended sources

Apart from the diffuse extended emission source 4C 35.06 which we have studied in detail in Chapter 3 of this thesis, we detect another four extended emission sources in the LOFAR image.

Three of these, NVSS J025291+3556, J030027+354754 and J030653+352747, are shown in Figure A.8.

The last extended source, J030026+352036, is detected as a slightly resolved source by the WSRT but extended by LOFAR, which suggests that LOFAR is detecting an extended, possibly relic emission. An overlay of WSRT (red) and LOFAR (black) contours on a SDSSr optical image is shown in Figure A.9. The integrated spectral index is $\alpha_{61}^{1400} = -0.87$.

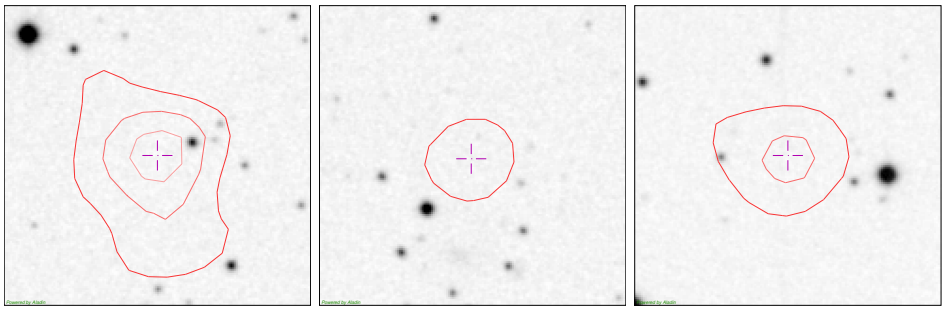

J031054+364401 J030710+355006 J030604+333630

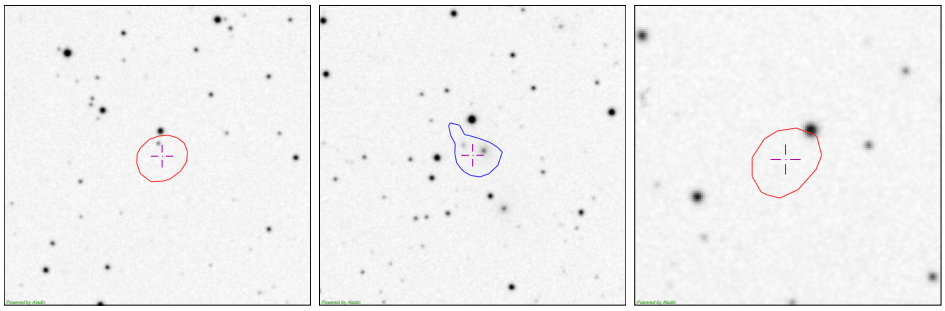

J030547+352513 J030328+343728 J030329+362956

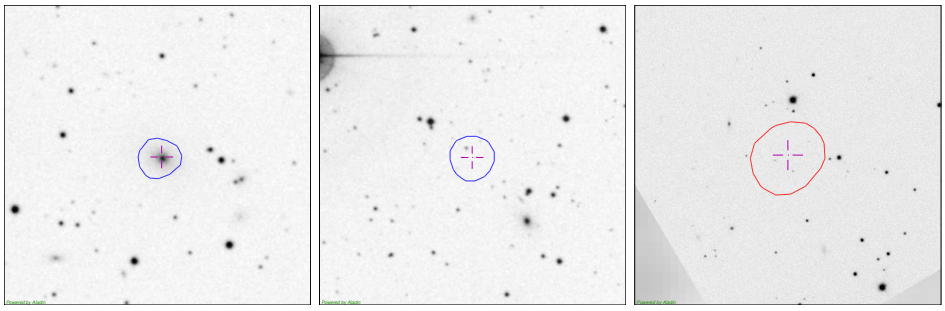

J030325+354620 J030100+360511 J030048+354946

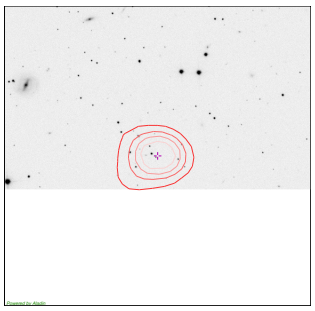

J025819+355526

Figure A.6: Optical thumbnails at the position of the steep spectrum sources listed in Table A.2.

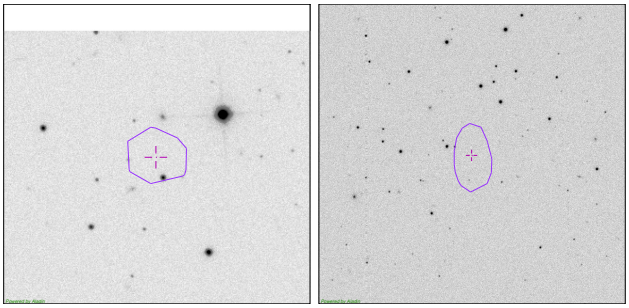

J030104+365824 J030050+351832

Figure A.7: DSS/SDSS DR8 optical images of the NVSS dropouts.

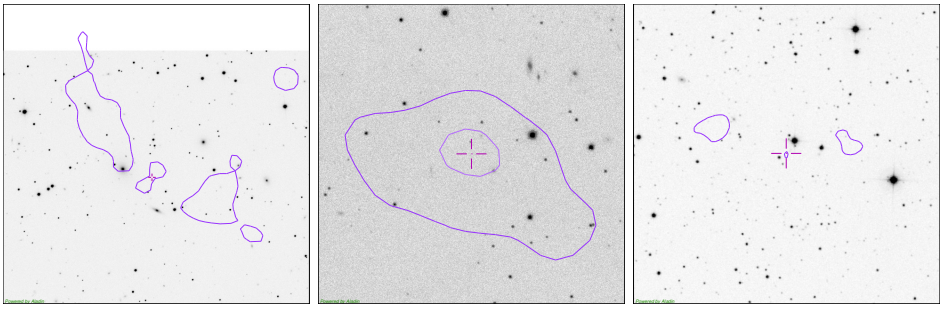

NVSS J025921+355635 J030027+354754 J030653+352747

Figure A.8: DSS/SDSS DR8 optical images of the extended sources.

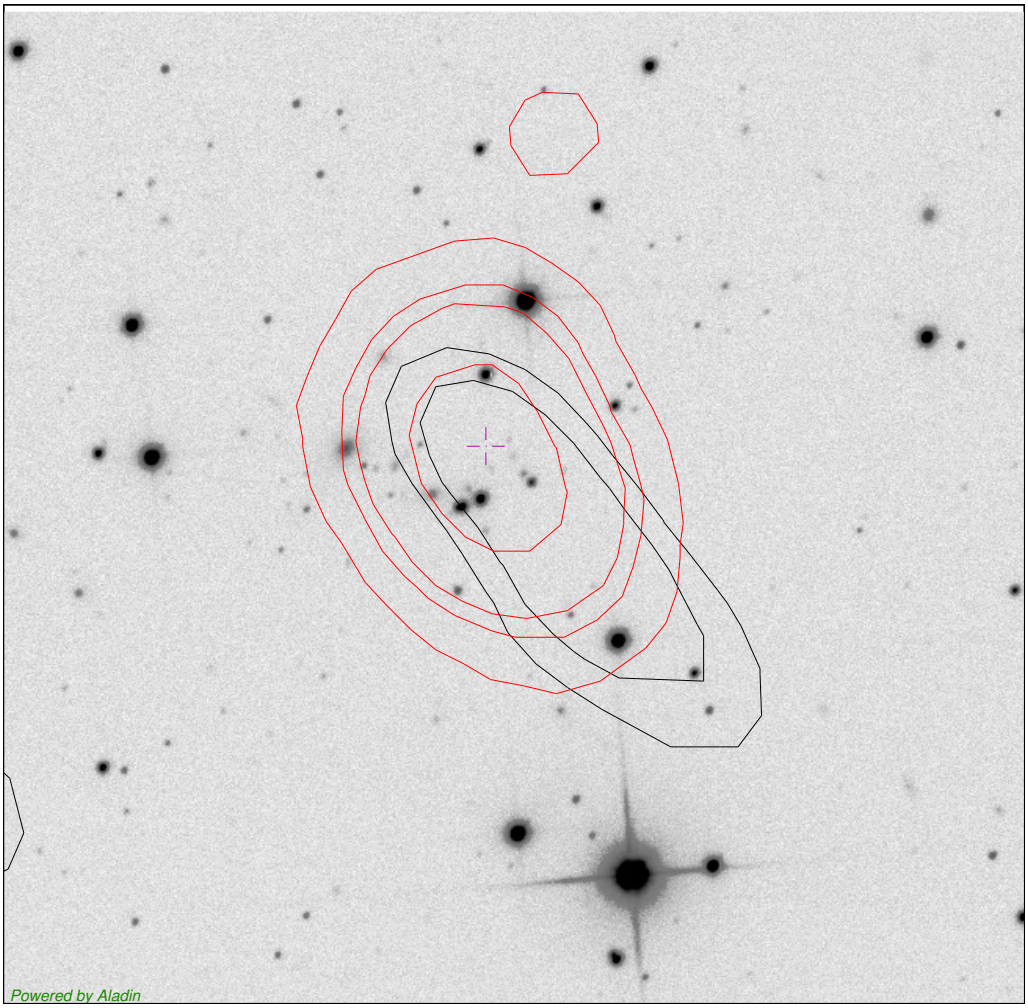

Figure A.9: Comparison of a marginally resolved WSRT detection (red) with an extended LOFAR detection (black) of the J030026+352036 source overlaid on a SDSSr image of its vicinity.

Appendix B

Clock/TEC fit on an interleaved LOFAR HBA observation

I believe a leaf of grass is no less than the journey-work of the stars.

– Walt Whitman

A. Shulevski and M. Mevius
presented at the 18-th LOFAR Busy Week
17 - 21 June 2013, ASTRON

B.1 Introduction

The ionosphere, a layer of plasma at a height of around 200 km above the surface of our planet acts as a refracting medium for the incoming electromagnetic waves from cosmic sources. This makes observations over wide fields of view with low frequency radio telescopes (such as LOFAR) especially challenging. The degree of ionization of the ionosphere is expressed in a measure called the Totel Electron Content (TEC). Discerning the ionospheric influence (and that of the clock signals sent to each LOFAR station) on the phase calibration procedure for the array will enable their removal during calibration and provide optimal imaging results.

The contribution of the ionosphere to the phase of the incoming radiation is a frequency dependent phase term (TEC/ν). It is useful to know that for a given frequency range, in order to avoid phase wrapping, the TEC contribution to the phase should be less than 180°:

$$\Delta TEC \cdot 8.4479745 \cdot 10^9 \cdot \left(\frac{1}{\nu_2} - \frac{1}{\nu_1}\right) \leq \pi$$

here, ν_1 amd ν_2 (in MHz) mark the edges of the band, and the TEC of the ionosphere is expressed in TEC units (TECU).

The goal of this test is to see whether we can perform an efficient clock and TEC fit over the entire frequency band of an interleaved (2 min on calibrator, 15 on target) LOFAR HBA observation. The details of the observation are outlined in Chapter 3 of this thesis. The target is VLSS J1431.8+1331 and 3C 295 was used as a calibrator.

B.2 Clock - TEC fitting

We have solved for amplitude and phase for the calibrator pointing using a two component model for 3C 295. We have split the frequency band in segments containing 20 channels each (obtained by concatenating 20 0.2 kHz sub-bands) and lasting one calibrator "visit" which in our case was 15 minutes. The solution interval was set to 10 seconds. We have obtained solutions per time chunk and per 20 sub-bands (SBs). Further, we have concatenated the solutions in time, and have obtained a solution set for the entire observing time on the calibrator. Then, we have concatenated in frequency these 20 SB solution segments and have obtained a solution set spanning the entire frequency band and observing time. Using it, we have performed a clock/TEC fit and have separated the TEC and clock contributions over the HBA band. For the fitting function we have used:

$$f(\nu) = \frac{\Delta TEC}{\nu} + clk \cdot \nu$$

We show the results of the fits in Figure B.1.

CS031HBA(0,1) is bad as can be plainly seen from the fits and should be removed from further consideration (this was already known from the observing logs).

What we can see is that the fitting works in the case of an interleaved observing mode with sufficient confidence. However, we can still see that the fit suffers from jumps (around 3 ns for the clock and 0.05 TECU for the TEC in the case of the core stations), since it uses the previous solution interval as a starting point for the next solution, but both the clock and the ionosphere contribute to the phase drift.

To see whether we can improve upon the result, we did a modified fit, fitting each calibrator scan independently. We present the results in Figure B.2.

We can see that we get very slight improvement in the solution discontinuities between calibrator scans. The fit generally finds the correct value, but intermittently there are phase "wraps". The phase wraps are solutions of $f(\nu)$ on $\phi + 2\pi$, resulting in clock offsets of 3 ns and TEC offsets of 0.05 TECU for the HBA band on the core stations. The independent fit shows us that most of the core stations for most of the time have good clock values recovered, and the phase wraps for some of the time.

However, the plot where the clock (TEC) is determined by taking the solution value from the previous calibrator scan as a starting point shows more consistent behavior, and we can identify phase wrapping (core) stations by the offset (0.05 TECU). Remote stations are more complicated, as is to be expected, since they don't share the same ionospheric patch.

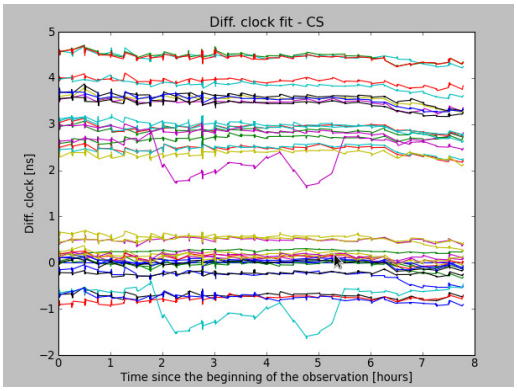

(a) Clock, core stations

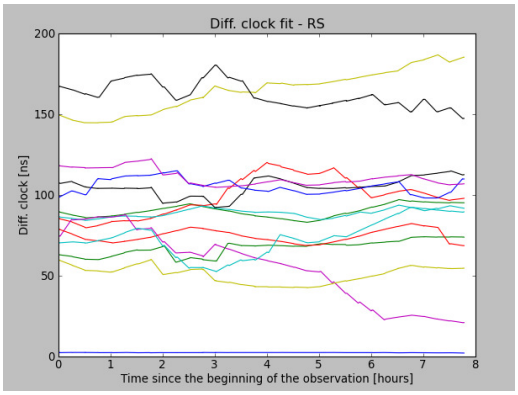

(b) Clock, remote stations

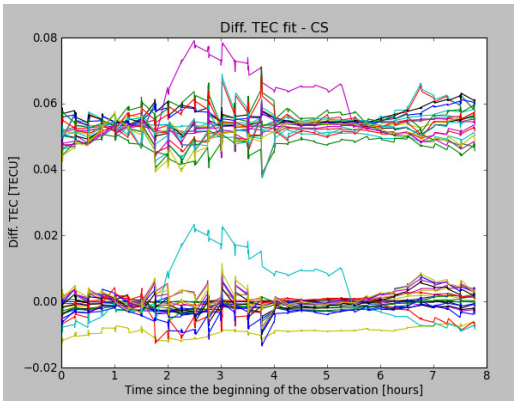

(c) TEC, core stations

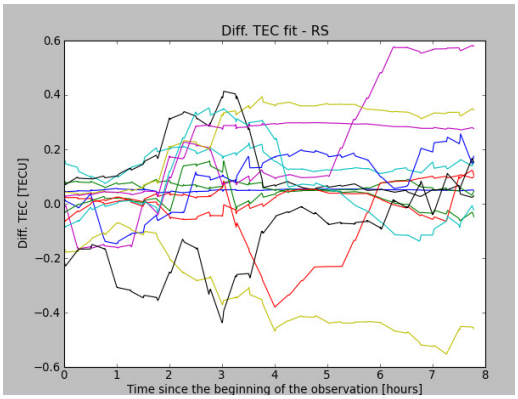

(d) TEC, remote stations

Figure B.1: Differential clock and TEC fits.

B.3 Solution stability

We have performed a test to determine whether the transfer of the calibrator (amplitude) calibration solutions affects the flux density levels of the target in the final image. The transfer was done in three modes:

- 1:1, meaning that each target scan used its previous calibrator scan solutions to correct the amplitudes of the data.
- 2:1, where calibrator solutions were applied to two subsequent target scans (ignoring one calibrator scan after the one being transferred).
- 4:1, where 4 target scans had the same calibrator solutions applied.

The duration of a calibrator scan is 110 seconds and of a target scan 650 seconds with a gap of 70 seconds in between. So, in the 1:1 scenario, we test the stability of the

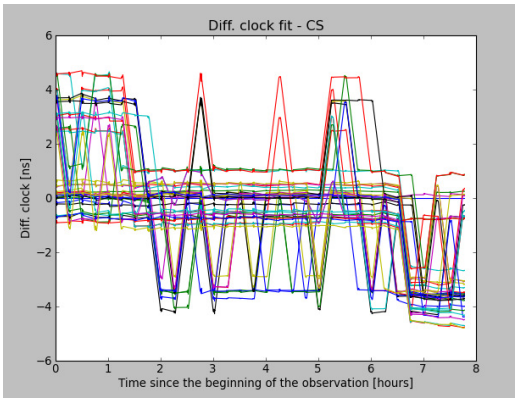

(a) Clock, core stations

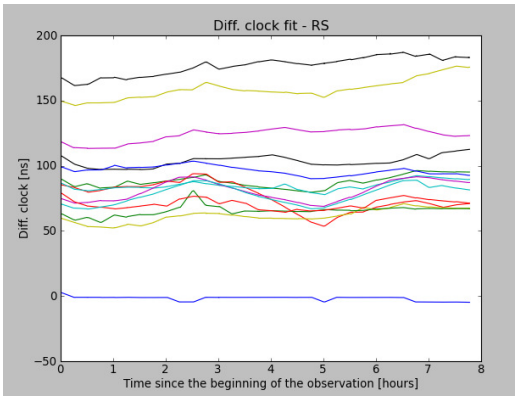

(b) Clock, remote stations

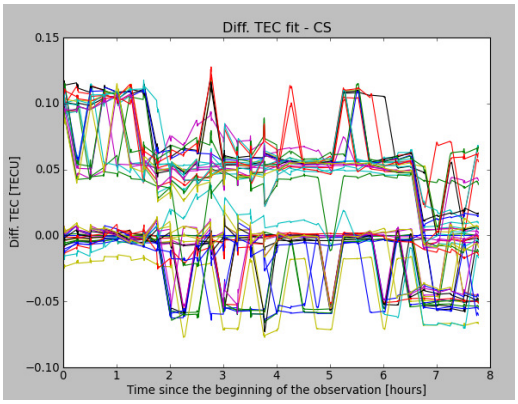

(c) TEC, core stations

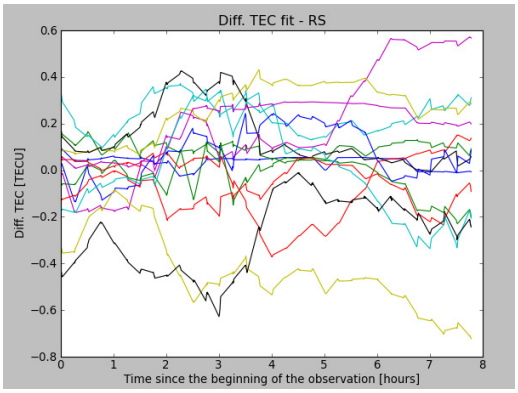

(d) TEC, remote stations

Figure B.2: Independent differential clock and TEC fits.

solutions on timescales of about a minute, in the 2:1 case the stability timescale is about 25 minutes, and in the 4:1 scenario about an hour.

The test was done on a data set covering 1 MHz (5 SBs) in frequency and spanning 8 hours of combined calibrator and target scans with durations as noted above. The results are given in Figure B.3.

The green contours in each image are plotted at a level of $(-3, 6, 12)\sigma$ and the magenta contour indicates the region used to measure the target flux density. We have measured flux densities of 3.17, 2.98 and 3.01 Jy for the one minute, 25 minutes and one hour timescales respectively, which indicates that the stability of the ionosphere was good at the time of the observation. This suggests that we can observe a calibrator once per hour, and maybe even less frequently (further testing is needed to demonstrate this).

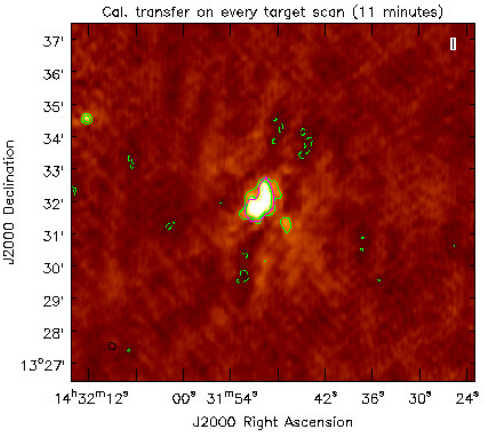

(a) Image noise, $\sigma = 11.24\text{mJy beam}^{-1}$

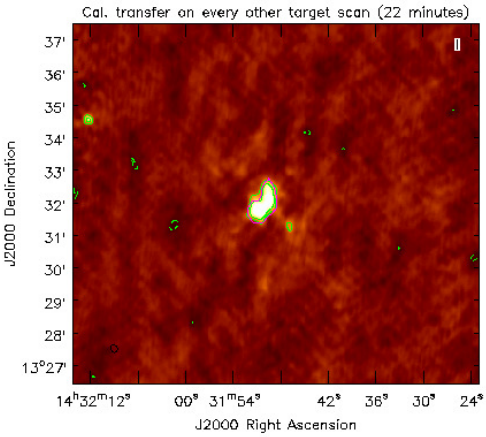

(b) Image noise, $\sigma = 14.20\text{mJy beam}^{-1}$

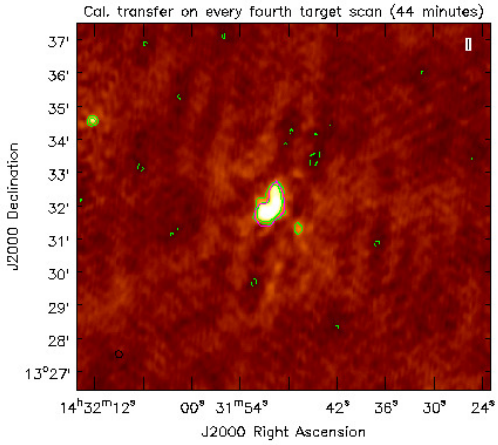

(c) Image noise, $\sigma = 12.28\text{mJy beam}^{-1}$

Figure B.3: Solution stability effects on imaging.

B.4 Conclusions and outlook

We have demonstrated that we can fit for the clock in the case of interleaved HBA observations. The next step is to remove it from the target fields (correct for it during calibration), as a step towards constructing a TEC screen.

Also, the solution stability seems good over (at least) a one hour period, which suggests that we can gain better time coverage of the target by doing less frequent calibrator scans.

Appendix C

The ghostly outer lobes of 4C 34.47

There are things known and there are things unknown, and in between are the doors of perception.

– Aldous Huxley

C.1 Introduction

In what what follows, we elaborate on the reported discovery (Marecki & Rusinek 2014) of an outer pair of relic lobes connected to the quasar 4C 34.47. The linear extent of these lobes is reported to be around 1.8 Mpc, which would make this a giant radio quasar.

C.2 Discussion

Marecki & Rusinek (2014) were conducting a search for foreshortened Giant Radio Galaxies (GRGs). To do this, they have conducted a study of radio loud quasars with Mpc sized radio morphologies. To do that, they have extracted a $10' \times 10'$ cutout from the FIRST[1] and NVSS[2] surveys. In the case of 4C 34.47 they have noticed an additional pair of what seemed to be radio lobes oriented at an almost 45° angle w.r.t the known lobes of the radio galaxy.

[1] FIRST is the Faint Images of the Radio Sky at Twenty centimeters radio survey performed by the VLA.

[2] NVSS stands for the NRAO VLA Sky Survey carried out at a frequency of 1.4 GHz (Condon et al. 1998)

4C 34.47 was studied a lot over the years; a detailed study of its polarization and orientation (as it pertains to the unification scheme for quasars and radio galaxies) was done by Hocuk & Barthel (2010). They have concluded that its size and orientation fit within the unification framework.

We present the comparison between one of the VLA images (1471 MHz, $\sigma = 0.08$mJy beam^{-1}, $4.6'' \times 3.8''$ resolution) of 4C 34.47 taken from Hocuk & Barthel (2010) and the FIRST image taken from Marecki & Rusinek (2014) in Figure C.1.

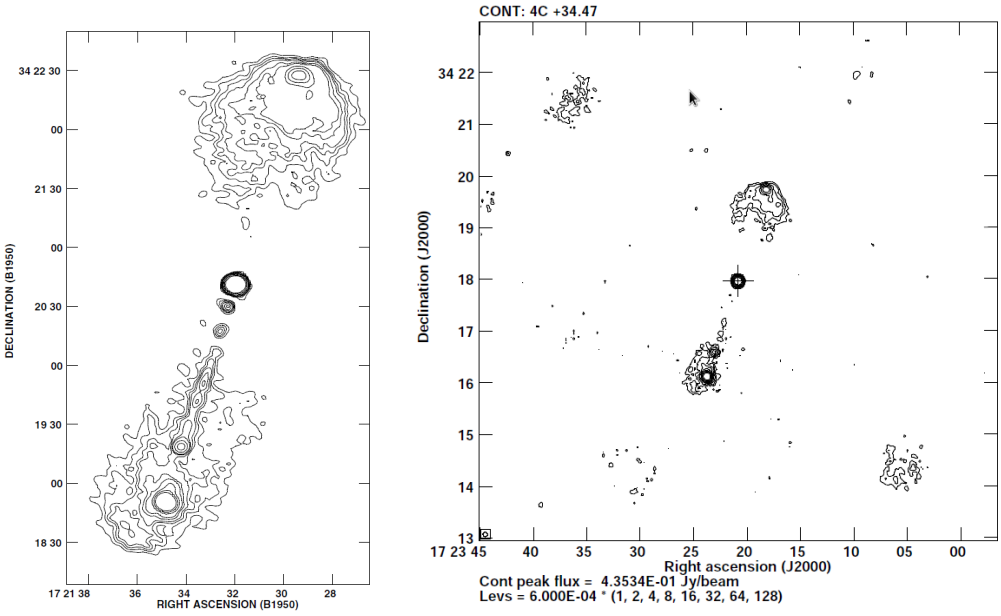

(a) Taken from Hocuk & Barthel (2010) **(b)** Taken from Marecki & Rusinek (2014)

Figure C.1: 4C 34.47 image comparison.

The map of Hocuk & Barthel (2010) has sufficient dynamic range to detect the lobes seen by Marecki & Rusinek (2014); the frequencies of the observations match, as well as the resolution. Marecki suggest that Hocuk & Barthel (2010) miss the outer lobes because of the (RA) extent of their maps.

We were intrigued by this discovery, so we have performed a visual inspection of images made using the LOw Fequency ARray (LOFAR; van Haarlem et al. 2013) at 150 MHz as part of the Multifrequency Snapshot Sky Survey (MSSS; Heald et al. 2014, submitted). We could see that the MSSS detects the previously known radio lobes of 4C 34.47 (Figure C.2), but the outer lobes reported by Marecki & Rusinek (2014) were not detected. If they were steep spectrum relic lobes, MSSS should have been able to detect them.

Another feature in the image of Marecki & Rusinek (2014) caught our attention; there is a hint of another faint pair of lobes at the same distance from the radio core, but aligned with the main lobes. This fact prompted us to inspect the FIRST survey image of 4C 34.47, using a larger spatial slice. We show this image in Figure C.3.

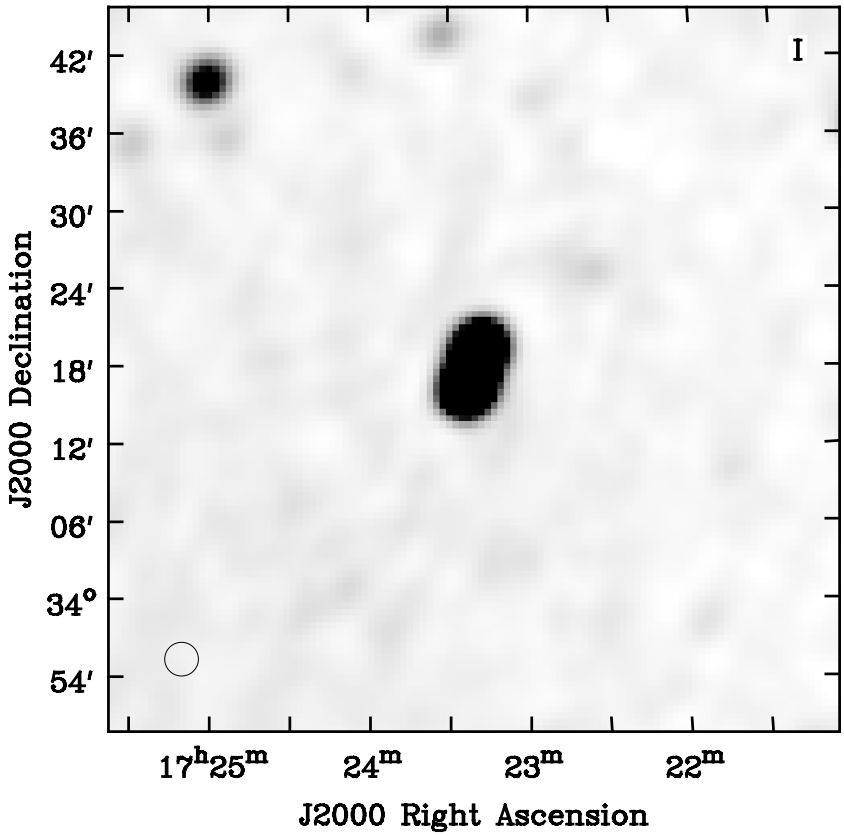

Figure C.2: 4C 34.47 field MSSS image.

We can see that the "lobes" are in fact image artifacts caused by the UV coverage of the FIRST survey, and there are in fact more of them. Had the FIRST image cutout of Marecki & Rusinek (2014) been larger, they would have noticed them. Following our communication of these facts to the authors, they have retracted their paper.

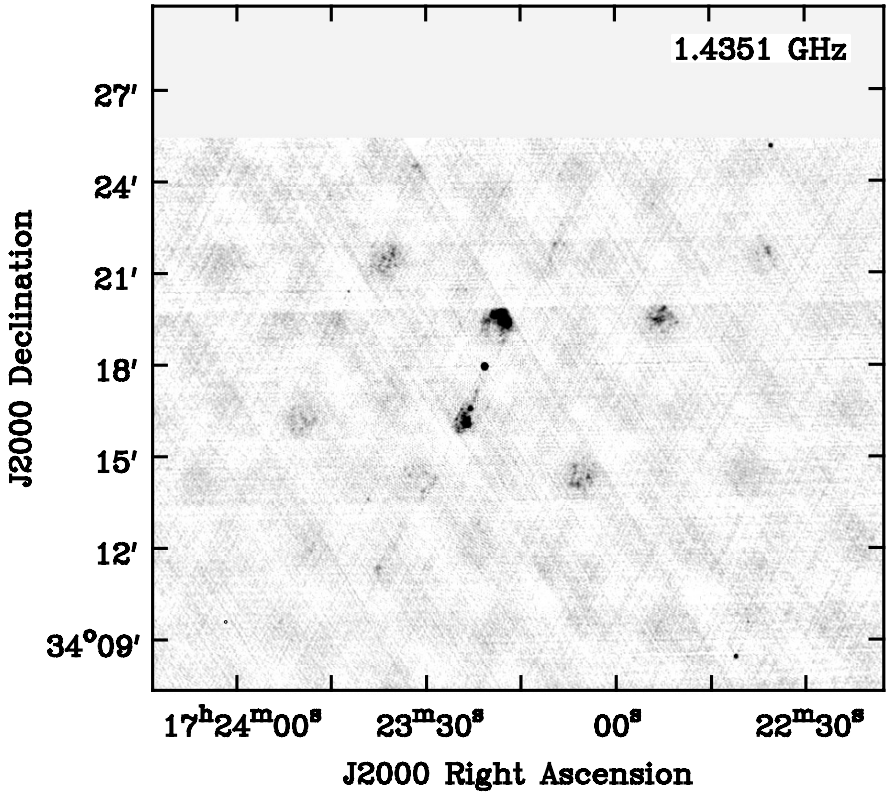

Figure C.3: 4C 34.47 field FIRST image.

Bibliography

Aihara, H., et al. 2011, ApJS, 193, 29

Akylas, A., & Georgantopoulos, I. 2009, A&A, 500, 999

Alatalo, K., et al. 2011, AJ, 735, 88

Allen, S. W., Dunn, R. J. H., Fabian, A. C., Taylor, G. B., & Reynolds, C. S. 2006, MNRAS, 372, 21

Baade, W., & Minkowski, R. 1954, ApJ, 119, 206

Baars, J. W. M., Genzel, R., Paulinytoth, I. I. K., & Witzel, A. 1977, A&A, 61, 99

Balmaverde, B., Baldi, R. D., & Capetti, A. 2008, A&A, 486, 119

Barthel, P. D., Schilizzi, R. T., Miley, G. K., Jagers, W. J., & Strom, R. G. 1985, A&A, 148, 243

Beck, R., & Krause, M. 2005, Astronomische Nachrichten, 326, 414

Best, P. N. 2009, Astronomische Nachrichten, 330, 184

Best, P. N., & Heckman, T. M. 2012, MNRAS, 421, 1569

Best, P. N., Kauffmann, G., Heckman, T. M., Brinchmann, J., Charlot, S., Ivezic, Z., & White, S. D. M. 2005, MNRAS, 362, 25

Bevington, P. R., & Robinson, D. K. 2003, Data reduction and error analysis for the physical sciences

Bhatnagar, S., Rau, U., & Golap, K. 2013, The Astrophysical Journal, 770, 91

Binney, J., Nipoti, C., & Fraternali, F. 2009, MNRAS, 397, 1804

Blundell, K. M., & Fabian, A. C. 2011, MNRAS, 412, 705

Bondi, M., Gregorini, L., Padrielli, L., & Parma, P. 1993, A&AS, 101

Bower, R. G., Benson, A. J., Malbon, R., Helly, J. C., Frenk, C. S., Baugh, C. M., Cole, S., & Lacey, C. G. 2006, MNRAS, 370, 645

Bridle, A. H., Kesteven, M. J. L., & Brandie, G. W. 1977, AJ, 82, 21

Briggs, D. S. 1995

Brunetti, G. 2004, in The Role of VLBI in Astrophysics, Astrometry and Geodesy, ed. F. Mantovani & A. Kus, 29

Brunetti, G., Setti, G., & Comastri, A. 1997, A&A, 325, 898

Burbidge, G. R., Burbidge, E. M., S, & age, A. R. 1963, Reviews of Modern Physics, 35, 947

Burns, J. O., Schwendeman, E., & White, R. A. 1983, The Astrophysical Journal, 271, 575

Buttiglione, S., Capetti, A., Celotti, A., Axon, D. J., Chiaberge, M., Macchetto, F. D., & Sparks, W. B. 2010, A&A, 509

Chandola, Y., Saikia, D. J., & Gupta, N. 2010, MNRAS, 403, 269

Chandola, Y., Sirothia, S. K., & Saikia, D. J. 2011, MNRAS, 418, 1787

Chandra, P., Ray, A., & Bhatnagar, S. 2004, ApJ, 612, 974

Chen, J., Huchra, J. P., McNamara, B., & Mader, J. 1998, BAAS, 30

Cheung, C. C., Healey, S. E., L, t, H., Kleijn, G. V., & Jordán, A. 2009, ApJS, 181, 548

Churazov, E., Bruggen, M., Kaiser, C. R., Bohringer, H., & Forman, W. 2001, ApJ, 554, 261

Ciotti, L., Ostriker, J. P., & Proga, D. 2010, ApJ, 717

Cisternas, M., Jahnke, K., & Collaboration, C. 2013, in Astronomical Society of the Pacific Conference Series, Vol. 477, Astronomical Society of the Pacific Conference Series, ed. W. H. Sun, C. K. Xu, N. Z. Scoville, S, & D. B. ers, 173

Cohen, A. S., Lane, W. M., Cotton, W. D., Kassim, N. E., Lazio, T. J. W., Perley, R. A., Condon, J. J., & Erickson, W. C. 2007, AJ, 134, 1245

Cohen, M. H., & Readhead, A. C. S. 1979, ApJ, 233, 101

Colla, G., et al. 1973, A&AS, 11, 291

—. 1972, A&AS, 7, 1

Condon, J. J., Cotton, W. D., Greisen, E. W., Yin, Q. F., Perley, R. A., Taylor, G. B., & Broderick, J. J. 1998, AJ, 115, 1693

Conway, J. E. 2002, New A Rev., 46, 263

Cordey, R. A. 1987, MNRAS, 227, 695

Cornwell, T. J. 2008, Ieee Journal of Selected Topics in Signal Processing, 2, 793

Crawford, C. S., Allen, S. W., Ebeling, H., Edge, A. C., & Fabian, A. C. 1999, MNRAS, 306, 857

Croton, D. J., et al. 2006, MNRAS, 365, 11

Czerny, B., Siemiginowska, A., Janiuk, A., Nikiel-Wroczynski, B., & Stawarz, L. 2009, ApJ, 698, 840

de Breuck, C., van Breugel, W., Röttgering, H. J. A., & Miley, G. 2000, A&AS, 143, 303

de Gasperin, F., et al. 2012, A&A, 547, 56

de Vries, N. 2009, The Evolution of Radio-Loud Active Galactic Nuclei

de Vries, N., Snellen, I. A. G., Schilizzi, R. T., Mack, K. H., & Kaiser, C. R. 2009, A&A, 498, 641

Dwarakanath, K. S., & Kale, R. 2009, ApJ, 698, L163

Edge, A. C. 2001, MNRAS, 328, 762

Eilek, J. A. 2014, New Journal of Physics, 16, 045001

Ekers, R. D., Fanti, R., Lari, C., & Parma, P. 1981, A&A, 101, 194

Emonts, B. 2006, Nearby radio galaxies: the interplay of gas, star formation and active nucleus

Emonts, B. H. C., Morganti, R., Tadhunter, C. N., Holt, J., Oosterloo, T. A., van der Hulst, J. M., & Wills, K. A. 2006, A&A, 454, 125

Ensslin, T. A., & Bruggen, M. 2002, MNRAS, 331, 1011

Enßlin, T. A., & Gopal-Krishna. 2001, A&A, 366, 26

Fanaroff, B. L., & Riley, J. M. 1974, MNRAS, 167, P31

Fanti, C. 2009, Astronomische Nachrichten, 330, 120

Fanti, C., et al. 2000, A&A, 358, 499

Fanti, R., Fanti, C., Schilizzi, R. T., Spencer, R. E., Rendong, N., Parma, P., Vanbreugel, W. J. M., & Venturi, T. 1990, A&A, 231, 333

Feretti, L., Giovannini, G., Govoni, F., & Murgia, M. 2012, Astronomy and Astrophysics Review, 20, 54

Ferrarese, L., & Merritt, D. 2000, ApJ, 539, 9

Garrington, S. T., & Conway, R. G. 1991, MNRAS, 250, 198

Garrington, S. T., Conway, R. G., & Leahy, J. P. 1991, MNRAS, 250, 171

Gaspari, M., Ruszkowski, M., & Oh, S. P. 2013, MNRAS, 432, 3401

Gaspari, M., Ruszkowski, M., & Sharma, P. 2012, ApJ, 746, 94

Ge, J., & Owen, F. N. 1994, AJ, 108, 1523

Gereb, K., Morganti, R., & Oosterloo, T. 2014, Probing the gas content of radio galaxies through HI absorption stacking, accepted to A&A

Geréb, K., Morganti, R., & Oosterloo, T. A. 2014, A&A, 569, A35

Geréb, K., Morganti, R., Oosterloo, T. A., Guglielmino, G., Pr, & oni, I. 2013, A&A, 558, A54

Giacintucci, S., Venturi, T., Murgia, M., Dallacasa, D., Athreya, R., Bardelli, S., Mazzotta, P., & Saikia, D. J. 2007, A&A, 476, 99

Ginzburg, V. L. 1957, Uspekhi Fizicheskii Nauk, 62, 37

Giroletti, M., Giovannini, G., & Taylor, G. B. 2005, A&A, 441, 89

Golombek, D., Miley, G. K., & Neugebauer, G. 1988, AJ, 95, 26

Govoni, F., Murgia, M., Giovannini, G., Vacca, V., & Bonafede, A. 2011, A&A, 529, A69

Gregorini, L., Klein, U., Parma, P., Schlickeiser, R., & Wielebinski, R. 1992, A&AS, 94, 13

Gregorini, L., Padrielli, L., Parma, P., & Gilmore, G. 1988, A&AS, 74

Gregory, P. C., & Condon, J. J. 1991, ApJS, 75, 1011

Hardcastle, M. J., Cheung, C. C., Feain, I. J., & Stawarz, L. 2009, MNRAS, 393, 1041

Hardcastle, M. J., Evans, D. A., & Croston, J. H. 2007, MNRAS, 376, 1849

Harwood, J. J., Hardcastle, M. J., Croston, J. H., & Goodger, J. L. 2013, MNRAS, 435, 3353

Hatch, N. A., et al. 2014, MNRAS, 445, 280

Heald, G., et al. 2010, ArXiv e-prints, 1008.4693

Heitsch, F., & Putman, M. E. 2009, AJ, 698, 1485

Helmboldt, J. F., Kassim, N. E., Cohen, A. S., Lane, W. M., & Lazio, T. J. 2008, Astrophysical Journal Supplement Series, 174, 313

Hes, R., Barthel, P. D., & Hoekstra, H. 1995, A&A, 303, 8

Hocuk, S., & Barthel, P. D. 2010, A&A, 523, A9

Hota, A., & Saikia, D. J. 2006, MNRAS, 371, 945

Intema, H. T., van Weeren, R. J., Röttgering, H. J. A., & Lal, D. V. 2011, A&A, 535, A38

Jaffe, W. J., & Perola, G. C. 1973, A&A, 26, 423

Jamrozy, M., Klein, U., Mack, K. H., Gregorini, L., & Parma, P. 2004, A&A, 427, 79

Jamrozy, M., Saikia, D. J., & Konar, C. 2009, MNRAS, 399, 141

Jansky, K. G. 1933, Popular Astronomy, 41, 548

Joshi, S. A., N, i, S., Saikia, D. J., Ishwara-Ch, ra, C. H., & Konar, C. 2011, Journal of Astrophysics and Astronomy, 32, 487

Kaiser, C. R. 2009, Astronomische Nachrichten, 330, 270

Kardashev, N. S. 1962, Astronomicheskii Zhurnal, 39, 393

Katz-Stone, D. M., & Rudnick, L. 1994, ApJ, 426, 116

Katz-Stone, D. M., Rudnick, L., & Anderson, M. C. 1993, ApJ, 407, 549

Kauffmann, G., & Haehnelt, M. 2000, MNRAS, 311, 576

Kauffmann, G., et al. 2003, MNRAS, 346, 1055

Klein, U., & Emerson, D. T. 1981, A&A, 94, 29

Koester, B. P., et al. 2007, ApJ, 660, 239

Komissarov, S. S., & Gubanov, A. G. 1994, A&A, 285, 27

Konar, C., Hardcastle, M. J., Jamrozy, M., & Croston, J. H. 2013, MNRAS, 430, 2137

Kunert-Bajraszewska, M., Gawronski, M. P., Labiano, A., & Siemiginowska, A. 2010a, MNRAS, 408, 2261

Kunert-Bajraszewska, M., Janiuk, A., Gawronski, M. P., & Siemiginowska, A. 2010b, ApJ, 718, 1345

Kunert-Bajraszewska, M., Marecki, A., & Thomasson, P. 2006, A&A, 450, 945

Labiano, A., Barthel, P. D., O'Dea, C. P., de Vries, W. H., Pérez, I., & Baum, S. A. 2007, A&A, 463, 97

Leahy, J. P., & Perley, R. A. 1991, AJ, 102, 537

Liu, R., & Pooley, G. 1991, MNRAS, 249, 343

Liuzzo, E., Giovannini, G., Giroletti, M., & Taylor, G. B. 2010, A&A, 516, A1

Lynden-Bell, D., & Rees, M. J. 1971, MNRAS, 152, 461

Machalski, J., Kozieł-Wierzbowska, D., Jamrozy, M., & Saikia, D. J. 2008, ApJ, 679, 149

Mack, K. H., Klein, U., O'Dea, C. P., Willis, A. G., & Saripalli, L. 1998, A&A, 329, 431

Marasco, A., Fraternali, F., & Binney, J. J. 2012, MNRAS, 419, 1107

Marecki, A., Barthel, P. D., Polatidis, A., & Owsianik, I. 2003, PASA, 20, 16

Marecki, A., & Rusinek, K. 2014, arXiv

Marecki, A., & Szablewski, M. 2009, A&A, 506, 33

Martel, A. R., et al. 1999, ApJS, 122, 81

Matteo, T. D., Springel, V., & Hernquist, L. 2005, 433, 607

McKernan, B., Maller, A., & Ford, K. E. S. 2010, ApJ, 718, L83

McMullin, J. P., Waters, B., Schiebel, D., Young, W., & Golap, K. 2007, in XVI (ASP Conf. Ser. 376) (San Francisco, CA: R. A. Shaw, F. Hill, & D. J. Bell), 127

McNamara, B. R., & Nulsen, P. E. J. 2007, ARA&A, 45, 117

McNamara, B. R., et al. 2014, The Astrophysical Journal, 785, 44

—. 2000, The Astrophysical Journal Letters, 534, L135

McNamara, B. R., Wise, M. W., & Murray, S. S. 2004, The Astrophysical Journal, 601, 173

Miley, G. 1980, Annual Review of Astronomy and Astrophysics, 18, 165

Morganti, R., Fogasy, J., Paragi, Z., Oosterloo, T., & Orienti, M. 2013, Science, 341, 1082

Morganti, R., Holt, J., Tadhunter, C., Almeida, C. R., Dicken, D., Inskip, K., Oosterloo, T., & Tzioumis, T. 2011, A&A, 535, A97, 1109.0630

Morganti, R., Killeen, N. E. B., Ekers, R. D., & Oosterloo, T. A. 1999, 307, 750

Morganti, R., Oosterloo, T. A., Tadhunter, C. N., van Moorsel, G., & Emonts, B. 2005, A&A, 439, 521

Morganti, R., Peck, A. B., Oosterloo, T. A., van Moorsel, G., Capetti, A., Fanti, R., Parma, P., & de Ruiter, H. R. 2009, A&A, 505, 559

Murgia, M., Fanti, C., Fanti, R., Gregorini, L., Klein, U., Mack, K. H., & Vigotti, M. 1999, A&A, 345, 769

Murgia, M., et al. 2011, A&A, 526, A148

Noordermeer, E., van der Hulst, J. M., Sancisi, R., Swaters, R. A., & van Albada, T. S. 2005, A&A, 442, 137

O'Dea, C. P. 1998, Publications of the Astronomical Society of the Pacific, 110, 493

—. 2002, New Astronomy Reviews, 46, 41

O'Dea, C. P., & Baum, S. A. 1997, AJ, 113, 148

O'Dea, C. P., Baum, S. A., & Gallimore, J. F. 1994, The Astrophysical Journal, 436, 669

O'Dea, C. P., Koekemoer, A. M., Baum, S. A., Sparks, W. B., Martel, A. R., Allen, M. G., Macchetto, F. D., & Miley, G. K. 2001, AJ, 121, 1915

Offringa, A. R., van de Gronde, J. J., & Roerdink, J. B. T. M. 2012, A&A, 539, A95

Ogrean, G. A., Brueggen, M., van Weeren, R., Simionescu, A., Roettgering, H., & Croston, J. H. 2011, MNRAS, 414, 1175

Oosterloo, T., et al. 2010, MNRAS, 409, 500

Pacholczyk, A. G. 1970, Radio Astrophysics

Pandey, V. N., van Zwieten, J. E., de Bruyn, A. G., & Nijboer, R. 2009, in Astronomical Society of the Pacific Conference Series, Vol. 407, The Low-Frequency Radio Universe, ed. D. J. Saikia, D. A. Green, Y. Gupta, & T. Venturi, 384

Parma, P., Murgia, M., de Ruiter, H. R., Fanti, R., Mack, K. H., & Govoni, F. 2007, A&A, 470, 875

Parma, P., Murgia, M., Morganti, R., Capetti, A., de Ruiter, H. R., & Fanti, R. 1999, A&A, 344, 7

Perley, R. A., Bridle, A. H., & Willis, A. G. 1984, ApJS, 54, 291

Pilkington, J. D. H., & Scott, J. F. 1965, MmRAS, 69, 183

Pooley, G. G., & Henbest, S. N. 1974, MNRAS, 169, 477

Ramanujam, N. M. 2007, Anaamika v 2.1

Randall, S. W., et al. 2011, ApJ, 726

Readhead, A. C., & Hewish, A. 1974, MNRAS, 167, 663

Readhead, A. C. S., Cohen, M. H., Bl, & ford, R. D. 1978, Nature, 272, 131

Reber, G. 1944, ApJ, 100, 279

Rengelink, R. B., Tang, Y., deBruyn, A. G., Miley, G. K., Bremer, M. N., Rottgering, H. J. A., & Bremer, M. A. R. 1997, A&AS, 124, 259

Roettiger, K., Burns, J. O., Clarke, D. A., & Christiansen, W. A. 1994, ApJ, 421, 23

Rottgering, H. J. A. 2010, in ISKAF2010 Science Meeting

Rudnick, L. 2001, in Astronomical Society of the Pacific Conference Series, Vol. 250, Particles and Fields in Radio Galaxies Conference, ed. R. A. Laing & K. M. Blundell, 372

Rudnick, L., Katz-Stone, D. M., & Anderson, M. C. 1994, Astrophysical Journal Supplement Series, 90, 955

Saikia, D. J., Gupta, N., & Konar, C. 2007, MNRAS, 375, L31

Saikia, D. J., & Jamrozy, M. 2009, Bulletin of the Astronomical Society of India, 37, 63

Salomé, P., & Combes, F. 2003, A&A, 412, 657

Saripalli, L., Subrahmanyan, R., Thorat, K., Ekers, R. D., Hunstead, R. W., Johnston, H. M., & Sadler, E. M. 2012, ApJS, 199, 27

Sault, R. J., Teuben, P. J., & Wright, M. C. H. 1995, Astronomical Society of the Pacific Conference Series, 77

Saunders, R., Baldwin, J. E., Pooley, G. G., & Warner, P. J. 1981, MNRAS, 197, 287

Saxton, C. J., Sutherland, R. S., & Bicknell, G. V. 2001, ApJ, 563, 103

Scaife, A. M. M., & Heald, G. H. 2012, MNRAS, 423, 30

Scheuer, P. A. G. 1974, MNRAS, 166, 513

Schilizzi, R. T., et al. 2001, A&A, 368, 398

Schneider, D. P., & Gunn, J. E. 1982, ApJ, 263

Schoenmakers, A. P., de Bruyn, A. G., Rottgering, H. J. A., & van der Laan, H. 1999, A&A, 341, 44

Schoenmakers, A. P., de Bruyn, A. G., Röttgering, H. J. A., & van der Laan, H. 2001, A&A, 374, 861

Schoenmakers, A. P., de Bruyn, A. G., Rottgering, H. J. A., van der Laan, H., & Kaiser, C. R. 2000, MNRAS, 315, 371

Serra, P., et al. 2012, MNRAS, no

Shabala, S. S., Ash, S., Alexander, P., & Riley, J. M. 2008, MNRAS, 388, 625

Shulevski, A., Morganti, R., Oosterloo, T., & Struve, C. 2012, A&A, 545, A91

Slee, O. B., Roy, A. L., Murgia, M., Andernach, H., & Ehle, M. 2001, AJ, 122, 1172

Stanghellini, C., O'Dea, C. P., Dallacasa, D., Cassaro, P., Baum, S. A., Fanti, R., & Fanti, C. 2005, A&A, 443, 891

Strom, R. G., Baker, J. R., & Willis, A. G. 1981, A&A, 100, 220

Struve, C. 2010, The Role of Neutral Hydrogen in the Evolution of Nearby Radio Galaxies

Struve, C., & Conway, J. E. 2010, A&A, 513, 10

Struve, C., Oosterloo, T., Sancisi, R., Morganti, R., & Emonts, B. H. C. 2010a, A&A, 523

Struve, C., Oosterloo, T. A., Morganti, R., & Saripalli, L. 2010b, A&A, 515, A67

Tasse, C., Best, P. N., Röttgering, H., & Borgne, D. L. 2008, A&A, 490, 893

Tasse, C., van der Tol, S., van Zwieten, J., van Diepen, G., & Bhatnagar, S. 2013, A&A, 553, A105

Taylor, G. B. 1996, ApJ, 470, 394

Taylor, G. B., O'Dea, C. P., Peck, A. B., & Koekemoer, A. M. 1999, ApJ, 512, L27

Terlouw, J. P., & Vogelaar, M. G. R. 2012, Kapteyn Package, version 2.2 (Kapteyn Astronomical Institute)

Tremblay, G. R., O'Dea, C. P., Baum, S. A., Koekemoer, A. M., Sparks, W. B., de Bruyn, G., & Schoenmakers, A. P. 2010, AJ, 715, 172

Tribble, P. C. 1993, MNRAS, 261, 57

van Bemmel, I. M., Morganti, R., Oosterloo, T., & van Moorsel, G. 2012, A&A, 548, 93

van Haarlem, M. P., et al. 2013, A&A, 556, 2

van Weeren, R. J., Rottgering, H. J. A., & Brueggen, M. 2011, A&A, 527, A114

van Weeren, R. J., Rottgering, H. J. A., Brueggen, M., & Cohen, A. 2009, A&A, 508, 75

van Weeren, R. J., Rottgering, H. J. A., Intema, H. T., Rudnick, L., Brueggen, M., Hoeft, M., & Oonk, J. B. R. 2012a, A&A, 546, A124

van Weeren, R. J., et al. 2012b, A&A, 543, 43

Veilleux, S., Teng, S. H., Rupke, D. S. N., Maiolino, R., & Sturm, E. 2014, ApJ, 790, 116

Venturi, T., Dallacasa, D., & Stefanachi, F. 2004, A&A, 422, 515

Venturi, T., Giacintucci, G., Dallacasa, D., Brunetti, G., Cassano, R., Macario, G., & Athreya, R. 2011, MNRAS, 414, 65

Verkhodanov, O. V., Trushkin, S. A., Andernach, H., & Cherenkov, V. N. 2009, A&AS, 58, 118

Viner, M. R., & Erickson, W. C. 1975, AJ, 80, 931

Waggett, P. C., Warner, P. J., & Baldwin, J. E. 1977, MNRAS, 181, 465

Wagner, A. Y., & Bicknell, G. V. 2011, ApJ, 728, 29

Wagner, A. Y., Bicknell, G. V., & Umemura, M. 2012, ApJ, 757, 136

Wild, V., Heckman, T., & Charlot, S. 2010, MNRAS, 405, 933

Willis, A. G., Strom, R. G., Perley, R. A., & Bridle, A. H. 1982, in IAU Symposium, Vol. 97, Extragalactic Radio Sources, ed. D. S. Heeschen & C. M. Wade, 141–144

Willis, A. G., Strom, R. G., & Wilson, A. S. 1974, Nature, 250, 625

Willis, A. G., Wilson, A. S., & Strom, R. G. 1978, A&A, 66, 1

Wright, E. L. 2006, Publications of the Astronomical Society of the Pacific, 118, 1711

Wylezalek, D., et al. 2013, ApJ, 769, 79

Yatawatta, S. 2007

Young, L. M., et al. 2011, MNRAS, 414, 940

Zhang, X., Zheng, Y., Chen, H., Wang, S., Cao, A., Peng, B., & Nan, R. 1997, A&AS, 121, 59

Resume

So high above, so deep below.

– Macedonian proverb

AGN and their radio relics

The first celestial radio emission was registered by Karl Jansky, an engineer working for the Bell Labaratories (owned by AT&T) in the fourth decade of the last century. He noticed that the source of a persistent noise affecting wireless communications was the center of the Galaxy (Figure 1). About a decade later, Grote Reber made maps of the Galaxy and some other radio sources on the sky using a radio telescope that he built himself. Radio astronomy was born.

Over the decades that followed, radio astronomy has made huge advancements, uncovering a whole new range of phenomena which became observable only at radio frequencies.

Gigantic lobes of radio radiation were observed at either side of elliptical galaxies. As the resolving power of radio telescopes increased, these were found to be sometimes connected to the cores of their host galaxies by thin jets of radio emission.

Later, a different class of intriguing sources were found - bright quasi stellar objects displaying very unusual optical spectra having unknown emission and absorption lines. In the 60's, in a flash of insight, astronomer Maarten Schmidt has deduced that the spectra were pointing to the fact that these objects were very, very distant, on average being billions of light years away. The fact that they are so bright and star-like (they were named quasi stellar objects, QSOs or quasars in short) means that the large amounts of energy they radiate originate in a relatively small volume.

After considering a few theoretical mechanisms which could account for such energetic processes, over time an understanding has emerged that the only candidate process is accretion of matter onto a compact object. The observed physical parameters pointed towards a super massive black hole (SMBH) being the central object, with a mass in

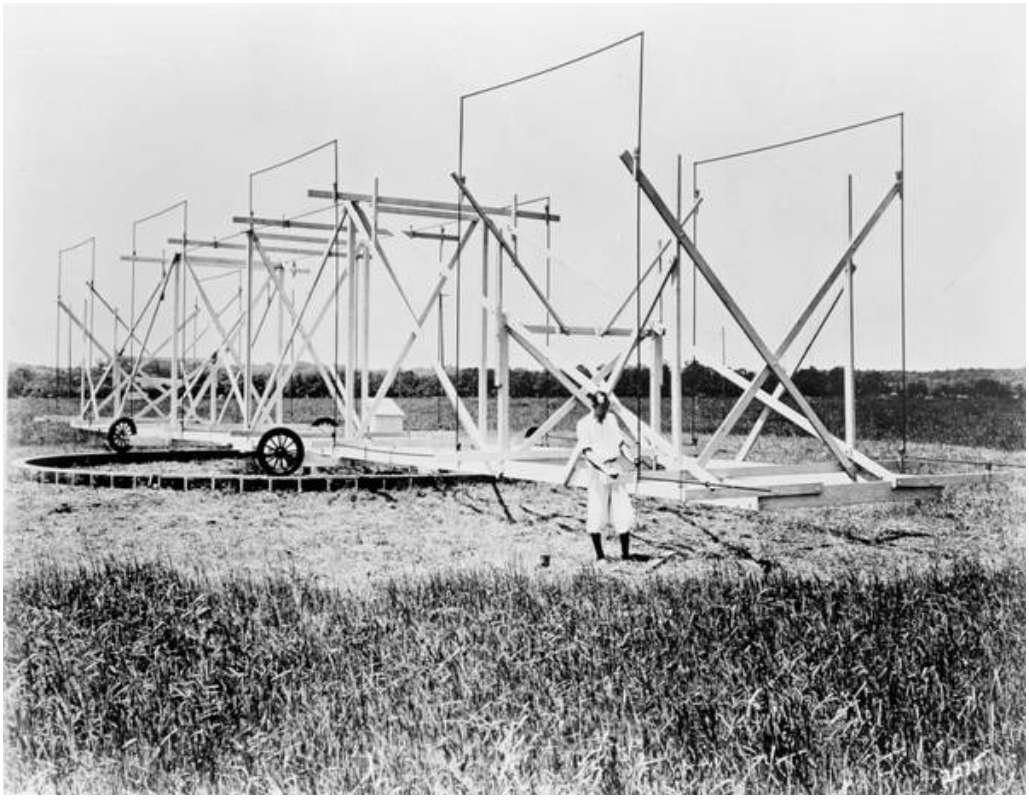

Figure 1: Karl Jansky and the antenna he used for his studies of static (© Bell Telephone Labaratories).

the range of millions to billions of solar masses. Infalling matter forms an accretion disk which radiates over all of the electromagnetic (EM) spectrum. Further out, the disk may expand into a torus; at right angles to the disk, the magnetic fields present in the SMBH / disk may collimate a jet of highly relativistic particles which radiate non-thermal, synchrotron radiation. These jets remain coherent for huge distances, pushing through the interstellar medium (ISM) of the host galaxy and producing the radio emission regions observed (see Figure 2 for an image of the radio galaxy HerA). This phenomenon is one of the most spectacular manifestations of an Active Galactic Nucleus (AGN).

Soon (in the 80's) it was realized that AGN could be the phenomenon behind radio galaxies, quasars and other similar sources. AGN come in many flavors; this diversity is mostly due to orientation effects and unification schemes were proposed to explain how what we observe relates to the AGN concept. When our line of sight views an AGN down the rotation axis of the SMBH or with a slight offset we observe a point-like optical source. If the AGN does not produce radio emission, we can observe an optical QSO, or a type 1 or 2 (if looking almost at right angles to the rotation axis) Seyfert galaxy. In the case where the AGN is also a radio source, we observe a quasar accompanied with strong (highly relativistically beamed) radio emission mostly coming from the radio jet when we view the AGN almost in the direction of the rotation axis. If we look at the

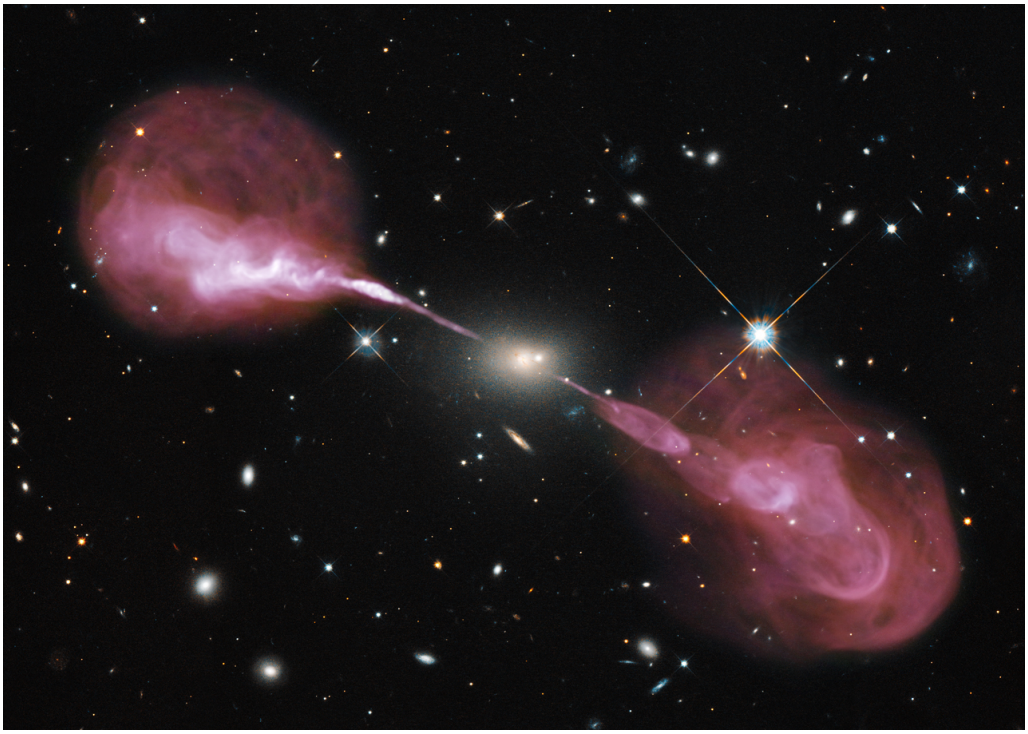

Figure 2: A composite image of the brightest radio source in the constellation of Hercules. HST's Wide Field Camera 3 provides the optical image, while the radio map (purple) is obtained by the Karl Jansky VLA radio telescope. We can see the radio jets emanating from the AGN hosted by the elliptical galaxy which is a 1000 times more massive than our milky way galaxy. The radio jets feed the radio emitting lobes; we can see flickers in the AGN activity reflected in multiple bubbles of plasma in the right side jet, while the opposite jet shows a helical structure. (© NASA, ESA, S. Baum and C. O'Dea (RIT), R. Perley and W. Cotton (NRAO/AUI/NSF), and the Hubble Heritage Team (STScI/AURA))

AGN at a high angle to the rotation axis, the central engine is hidden from view, and the radio emission is the most prominent feature - we observe a radio galaxy. Imaging the host galaxies of some quasars (especially since the launch of the Hubble Space Telescope; HST) contributed towards strengthening this point of view.

Studying AGN is an entire sub-field in astronomy. Much has been ascertained in the past few decades about their energetics, spectral properties and their interaction with the surroundings. At the same time, much remains a mystery. AGN radiate over the entirety of the EM spectrum and span a staggering range of spatial scales; their SMBH engine is comparable to the extent of our solar system, yet their jets and radio lobes can span millions of light years. Consequently, studying them requires observations with a variety of instruments and requires an understanding of processes involving quantum theory, general relativity, galaxy evolution and even cosmology, basically the entirety of modern astronomy.

In the present study we concern ourselves with studying AGN in the radio part of the EM spectrum. AGN in the radio can be variable objects, showing fluctuations in brightness at timescales from days to years. Using radio interferometry (connecting multiple telescopes and thus obtaining an instrument with larger sensitivity and resolving power) we can study AGN emission on varying spatial scales. Variability is most noticeable in the radio cores of AGN. The larger scale morphology of radio galaxies, the radio lobes, record the variability of AGN activity on much longer time scales.

The SMBH can exhaust its supply of accreting matter and once that happens, the AGN shuts down and becomes inactive. The optical emission stops, the radio jets vanish. Consequently, after a time delay long enough for the information of the shutdown to be transmitted to the extended lobes, the supply of accelerated particles to the radio lobes ceases. The lobes start to fade, i.e. their radio brightness diminishes. However, the magnitude by which the radio lobe brightness decreases is different at different radio wavelengths. Thus, observing the fading radio lobes across the radio spectrum is a necessary step in inferring the activity history of an AGN.

The theoretical basis for describing non-thermal (synchrotron) radio emission was given in the 60's by Vitaly Ginzburg and Nikolai Kardashev. Later, it was expanded upon by many other astrophysicists. Comparing theoretical models of radio source spectra to observations can help us estimate the period of time an AGN has spent in an active phase and the time interval that has passed since its shutdown. Radio relics thus become very important; they are the only observational tracer of past AGN activity episodes.

These relic structures are brightest at low radio frequencies. We have a powerful new tool to aid us in their discovery and characterization. The LOw Frequency ARray (LOFAR) telescope (Figure 3) is a radio interferometer working in the frequency ranges of 20 MHz - 80 MHz and 120 MHz - 240 MHz. Its antennas are clustered in groups called stations. Most of these stations are spread across the northern parts of the Netherlands, with some extending out to Germany, the UK, Poland and Sweden. In a single exposure, LOFAR can image a patch of the sky 5° across (as large as 10 full Moons arranged side by side) which facilitates discovery.

This thesis

We have studied various AGN relics and for some of them we have determined their spectral properties, leading to an estimate of the age of the AGN that have powered them.

Chapter 2 describes the properties of a relic we have discovered observing at a frequency of 1400 MHz using the Westerbork Synthesis Array Telescope (WSRT) located in northern Netherlands. The region of relic emission is located around a currently active AGN which is classified as a compact steep spectrum (CSS) radio source. The surface brightness of the relic is very low. Spectral index and ageing studies will enable us to determine the duty cycle of the host AGN. The host elliptical galaxy is rich in cold gas (there is a vast ring of neutral hydrogen gas around it) which may provide the fuel for the AGN activity.

AGNs can be hosted by galaxies in more complex environments, such as galaxy clusters. In Chapter 3 we have studied a relic produced by such an AGN. Its morphology and age are defined by its environment. We have studied in detail its radio radiation at different frequencies, spanning from 61 MHz (LOFAR, see Figure 4) to 4800 MHz (using

Figure 3: The six stations comprising the very core of the LOFAR telescope, the so called super-terp imaged on May 23, 2010 (© Top-Foto, Assen).

the Very Large Array - VLA interferometer located near Socorro, New Mexico - USA). We have found that the radio source (catalogued as 4C 35.06) is a combination of an old relic and a re-started phase of AGN activity. We have also used the WSRT to search for cold gas (traced by H I) and found cold gas connected to the host galaxy of the AGN.

Another AGN relic in a galaxy cluster was studied in Chapter 4, located at a larger distance (z = 0.159). Using LOFAR data as well as VLA imaging and images from the Giant Meterwave Radio Telescope (GMRT, located near Pune in India) we have determined that the AGN which created the now relic emission has shut down around 60 million years ago. In the same source, we have detected another radio component which is most likely an older plasma bubble compressed by a shock wave generated by the merger of two galaxy clusters (the brightest galaxy in one of them is the host galaxy of our AGN).

AGN relics are also found in galaxies which are not part of a cluster. We have analyzed such a relic in Chapter 5, and we have found that the AGN has stopped its activity more than 100 million years ago. However, sections of the radio lobes which were replenished by the radio jet are just 20 million years old.

In this thesis, we have shown the usefulness of LOFAR to detect relic emission at low frequencies, at a spatial resolution comparable to that obtained at much higher frequencies. This has enabled us to do matched comparisons of multi-frequency maps.

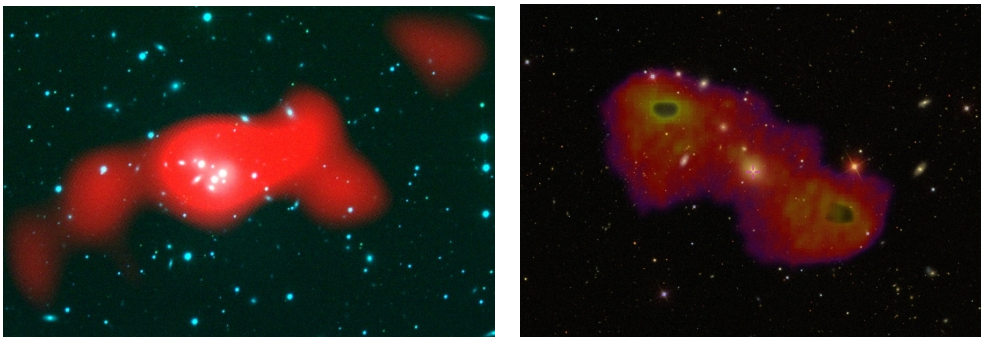

Figure 4: Left: LOFAR 61 MHz radio image (red) overlaid onto an optical image of the AGN host galaxy of the radio source 4C 35.06. **Right:** LOFAR 140 MHz image (red, yellow) overlaid onto an optical image of the AGN host galaxy of the B2 0924+30 radio source.

The usefulness of LOFAR as a survey instrument is showcased in Chapter 6 where we have performed a search for AGN radio relics in the first LOFAR sky survey, the Multi-frequency Snapshot Sky Survey (MSSS). While having a limited resolution and sensitivity, it is a valuable proof of concept. We have been able to put limits on the prevalence of relics around compact radio sources.

In Chapter 7, we have studied in detail the low frequency properties of two giant radio galaxies (3C 236 and NGC 6251). This was done for the first time at the relatively high resolution of about $1'$ at around 140 MHz. We have been able to image previously undetected radio emission regions in the radio lobes of NGC 6251 (Figure 5).

Our research shows the potential of LOFAR and is the first attempt at using LOFAR observations in the studies of AGN radio relics. We have found that low frequency observations are necessary to provide constraints to models and are essential for proper interpretation of the obtained results. We have also uncovered new potential relic sources, thus demonstrating the survey capabilities of LOFAR. The future is bright at low frequencies.

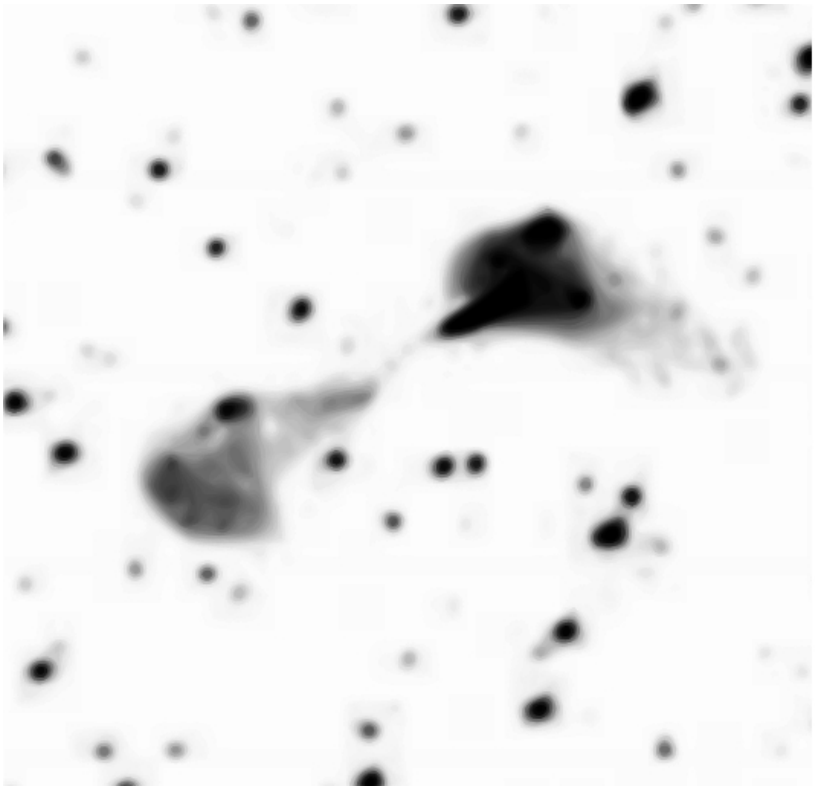

Figure 5: LOFAR image of the giant radio galaxy NGC 6251 at 140 MHz.

Samenvatting

Zo hoog naar boven, zo diep naar beneden.

– Macedonische gezegde

Aktieve sterrenstelsels en hun radiorestanten

De eerste die kosmische radiostraling detecteerde was Karl Jansky, een ingenieur die werkte voor de Bell laboratoria (van AT&T). Hij ontdekte dat de bron van een constante storing in het draadloze communicatieverkeer van buitenaardse oorsprong was: het centrum van de Melkweg (figuur 1). Ruwweg tien jaar later maakte Grote Reber kaarten van de radiostraling van de Melkweg en van enkele andere radiobronnen aan de hemel, gebruikmakend van een telescoop die hij zelf in zijn tuin bouwde. Radiosterrenkunde was geboren.

Gedurende de volgende decennia maakte die radiosterrenkunde een enorme bloei door, en openbaarde tot dan toe volslagen onbekende astrofysische processen die louter bij radiogolflengten "zichtbaar" zijn.

Gigantische wolken van radiostraling werden waargenomen aan weerszijden van bepaalde elliptische sterrenstelsels. Dankzij de ontwikkeling van de radio-interferometrie werd een grotere beeldscherpte mogelijk waardoor men kon zien dat dunne straalstromen de radiowolken met de kernen van de sterrenstelsels verbonden.

Weer later openbaarde zich een andere soort intrigerende bronnen: heldere quasistellaire objecten waarvan de raadselachtige optische spectra onbekende emissie- en absorptielijnen vertoonden. In de jaren zestig begreep astronoom Maarten Schmidt plotseling dat die spectra begrepen konden worden als de objecten op enorme afstanden staan: miljarden lichtjaren van de aarde. Het feit dat ze erg helder zijn en klein (quasistellair - ze werden dus quasistellaire objecten, QSO, of quasar genoemd) impliceert dat een enorme energieproduktie moet plaatsvinden in een relatief klein volume.

Hoewel verschillende fysische mechanismen voor die energieproductie werden voorgesteld bleek er in de loop van de tijd maar een levensvatbaar: de accretie van materie

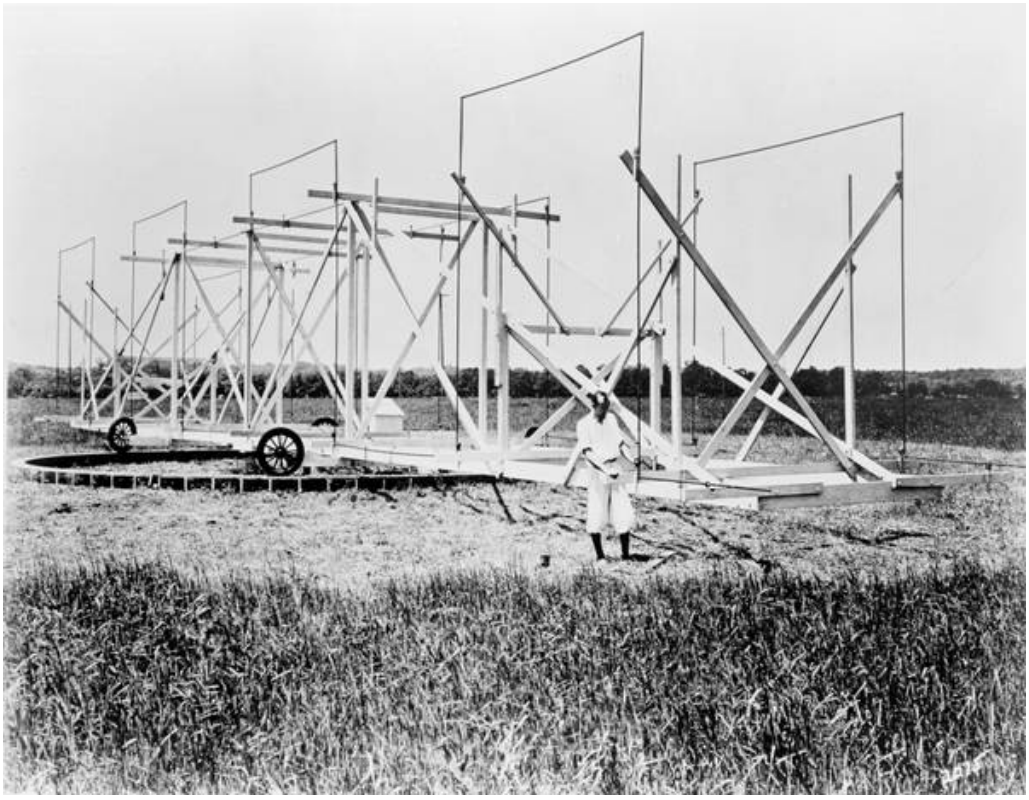

Figuur 1: Karl Jansky bij diens antenne voor zijn onderzoek naar de herkomst van radiostoringen (© Bell Telephone Labaratories).

door een zwaar compact object. Uit de waarnemingen volgde dat een zwart gat dat compacte object moet zijn, met een massa van de orde van miljoenen tot een paar miljard maal de massa van de zon. Materie die naar dat zwarte gat wordt getrokken vormt een hete accretieschijf; deze straalt in alle golflengten van het elektromagnetische spectrum. Buiten die schijf kan zich een ring (torus) van gas en stof vormen, en loodrecht erop, langs de rotatie-as van het zwarte gat, kunnen zich dunne bundels (straalstromen) vormen, die relativistische deeltjes over grote afstanden naar buiten transporteren. Deze straalstromen, of jets, produceren niet-thermische straling, zgn. synchrotronstraling. Ze blijven coherent over grote afstanden, tot ver buiten de sterrenstelsels waarin ze ontstaan, en zijn uiteindelijk verantwoordelijk voor de uitgestrekte radiowolken (figuur 2 toont radiosterrenstelsel Hercules A). Zo'n radiostelsel is een van de meest spectaculaire verschijningsvormen van een aktief sterrenstelsel, een sterrenstelsel met een aktieve kern, AGN.

In de jaren 80 werd het steeds duidelijker dat die aktieve kernen de energiebronnen zijn, niet alleen in radiostelsels maar ook in quasars en andere soorten objecten. Aktieve stelsels komen in allerlei soorten en maten voor; deze diversiteit wordt voor een deel veroorzaakt door orientatie-effecten. Zogenaamde unificatiemodellen werden voorgesteld om schijnbaar verschillende soorten aktieve stelsels toch onder een noemer te brengen.

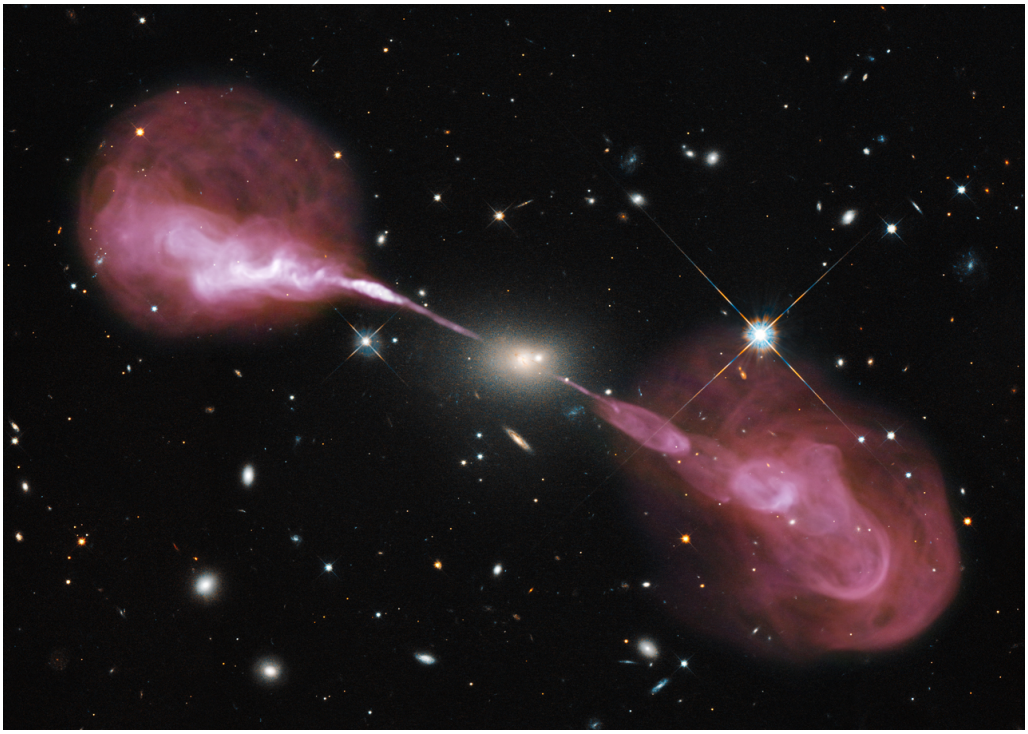

Figuur 2: Een samengestelde afbeelding van de helderste radiobron in het sterrenbeeld Hercules, Her A. De optische afbeelding werd gemaakt door de Hubble telescoop, de radio-afbeelding (paarse kleuren) door de Jansky Very Large Array radio telescoop. De straalstromen uit de aktieve kern van het elliptische stelsel voeden de gigantische radiowolken aan weerszijden ervan. Het sterrenstelsel is wel duizend keer zwaarder dan ons sterrenstelsel, de Melkweg. De radiostructuur rechts toont duidelijk dat het object verschillende episoden van activiteit heeft gehad; links is een kurketrekkerachtige structuur te zien (© NASA, ESA, S.Baum & C.O'Dea (RIT), R.Perley en W.Cotton (NRAO/AUI/NSF), en het Hubble Heritage Team (STScI/AURA)).

Zien we een AGN van boven of onderen, dat wil zeggen, langs de rotatie-as van het zwarte gat en min of meer loodrecht op de torus daaromheen, dan zien we een heldere, centrale pit. Is er geen radiostraling dan kan het een QSO of type-1 Seyfert zijn. Is er wel radiostraling dan is het een quasar die we ongeveer langs de straalstroom waarnemen. Zien we datzelfde object van opzij, onder een grote hoek ten opzichte van de straalstroom dan is de centrale pit verduisterd door de torus en zien we een radiosterrenstelsel. Afbeeldingen van de moederstelsels van sommige quasars (in het bijzonder met de Hubble ruimtetelescoop) bevestigde dat beeld.

Aktieve sterrenstelsels en AGN vormen een groot en belangrijk onderzoeksterrein in de sterrenkunde. Gedurende de afgelopen decennia is veel duidelijk geworden met betrekking tot hun energie-opwekking, spectrale eigenschappen, en de interactie met hun omgeving. Tegelijkertijd zijn er ook nog grote raadsels. Deze objecten zenden alle soorten van elektromagnetische straling uit over een enorm bereik aan dimensies; hun centrale

"motor" beslaat een gebied ter grote van ons zonnestelsel, maar hun straalstromen en radiowolken zijn soms wel miljoenen lichtjaren in afmeting. Studie van deze objecten vereist dus waarnemingen met een scala van instrumenten. Het begrijpen van de onderliggende fenomenen vereist kennis van kwantum- en relativiteitstheorie, van sterrenstelsels en hun evolutie, en van kosmologie, in feite de complete moderne astronomie.

In dit proefschrift wordt verslag gedaan van radiostudies van aktieve sterrenstelsels. Bij radiogolflengten kunnen de stelsels en hun aktieve kernen variabel zijn, op tijdschalen van dagen tot vele jaren. Gebruikmakend van radio-interferometrie, waarbij verschillende telescopen digitaal gekoppeld worden zodat een instrument van grote gevoeligheid en beeldscherpte ontstaat, kunnen de objecten op verschillende ruimtelijke schalen worden bestudeerd. De eerder genoemde variabiliteit is het sterkst op de kleinste schaal, in de radio-kernen van de objecten. Op veel grotere schaal, zoals in de radiowolken, kan de variabiliteit op veel grotere tijdschaal waarneembaar zijn (zie Fig. 2).

Het centrale zwarte gat kan zijn brandstofvoorraad opmaken. Wanneer dat gebeurt stopt de accretie en dus de AGN: het object is niet meer aktief. De optische emissie stopt en de straalstromen ook. Na verloop van tijd zal het bericht van het stoppen van de aktiviteit ook de radiowolken bereiken: de aanvoer van nieuwe geladen deeltjes staakt, de radio-straling van de wolken sterft geleidelijk uit. Echter, het tempo waarin die straling uitdooft is golflengte-afhankelijk. Met andere woorden: metingen bij verschillende golflengten vertellen iets over de levensgeschiedenis van uitstervende radiowolken.

De theorie van niet-thermische (synchrotron) radiostraling is in de jaren 60 ontwikkeld door de astrofysici Vitaly Ginzburg en Nicolai Kardashev. Later is deze theorie door vele anderen uitgebreid. Door theoretische modellen te vergelijken met de waarnemingen van aktieve radiowolken en zogenaamde radiorestanten kunnen we iets zeggen over de aktieve episode van een AGN en over het tijdsverloop sinds het stoppen van de aktiviteit. Die radiorestanten zij dus heel belangrijk want ze stellen ons in staat om terug te kijken in het aktieve verleden van sterrenstelsels.

Radiorestanten zijn het helderst bij lange golflengten. Er staat ons sinds enkele jaren een nieuw instrument ter beschikking om die restanten te ontdekken en te karakteriseren. De LOFAR (Low Frequency Array) telescoop (Figuur 3) is een nieuw concept radio-interferometer die werkt in de frequentiegebieden 20 - 80 MHz en 120 - 240 MHz. De LOFAR antenne's zijn gegroepeerd in zgn. stations. De meeste van die stations staan verspreid in Noord-Nederland, maar er zijn ook LOFAR stations in Duitsland, Engeland, Polen en Zweden. LOFAR kan instantaan een stuk hemel van vijf graden in diameter (tien volle manen naast elkaar) afbeelden. Dat is een groot gebied waardoor LOFAR ook een grote potentie heeft voor onverwachte ontdekkingen.

Dit proefschrift

We hebben verschillende radiorestanten bestudeerd en voor enkele daarvan ook de spectrale eigenschappen vastgesteld, en daarmee een schatting kunnen geven van de leeftijd van de bijbehorende AGN.

Hoofdstuk 2 beschrijft de eigenschappen van een restant dat we met de Westerbork Synthese Radio Telescoop (WSRT) in Nederland hebben ontdekt op een frequentie van 1400 MHz. Het stralingsgebied van dit restant bevindt zich naast een AGN die nog steeds actief is. Deze erg zwakke AGN is geklassificeerd als een compacte bron met een stijl spectrum (CSS). Met het bestuderen van de spectrale eigenschappen van dit

Figuur 3: De zes stations die samen de binnenste kern vormen van LOFAR, beter bekent als de Superterp. d.d. 23 Mei, 2010 (© Top-Foto, Assen).

restant kunnen we vaststellen met welke regelmaat de bijbehorende AGN in het verleden activiteit heeft vertoont. Deze AGN bevindt zich in een elliptisch sterrenstelsel met een grote hoeveelheid aan koud gas (het stelsel wordt omgeven door een uitgestrekte ring van neutraal waterstofgas) dat tot brandstof kan dienen voor de AGN.

De omgeving van een AGN kan een grote complexiteit vertonen. Zo worden AGN ook in clusters van sterrenstelsels gevonden. In Hoofdstuk 3 bestuderen we een radiorestant van zo'n AGN. De morfologie en leeftijd van dit restant zijn een resultaat van zijn omgeving. We hebben de radiostraling van dit object nauwkeurig bestudeerd op verschillende frequentiegebieden, lopende van 61 MHz (LOFAR, figuur 4) tot 4800 MHz (gebruikmakende van de Very Large Array (VLA) bij Socorro, New Mexico - VS). Onze bevindingen zijn dat de radiobron (bekend als 4C 35.06) een combinatie is van een oud restant en een herstartte jongere fase van AGN activiteit. We hebben hierbij ook gekeken naar neutraal waterstofgas met de WSRT en een brug gevonden van koud gas die de AGN en haar bijbehorende sterrenstelsel verbindt.

In Hoofdstuk 4 bestuderen we een ander radiorestant in een cluster. Deze AGN bevindt zich op grote afstand ($z = 0.159$). Aan de hand van zowel LOFAR data als afbeeldingen gemaakt met VLA en de Giant Meterwave Radio Telescope (GMRT, nabij Pune in India) hebben we vast kunnen stellen dat de AGN, die verantwoordelijk is voor het restant, ongeveer 60 miljoen jaar geleden haar activiteit heeft gestaakt. In dezelfde

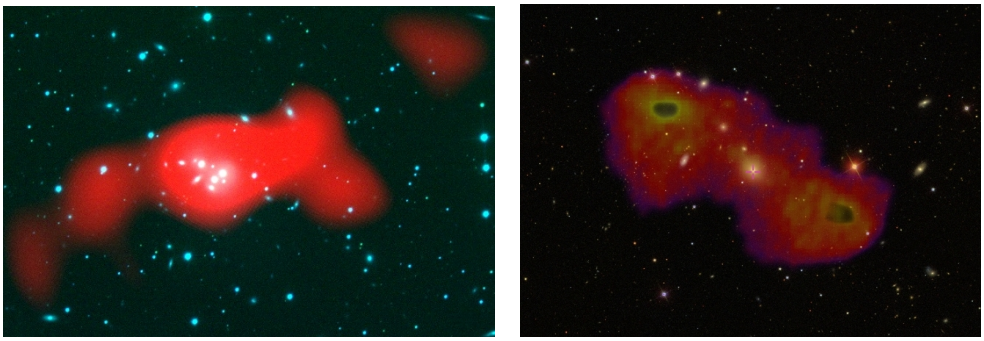

Figuur 4: Links: LOFAR 61 MHz radio intensiteit (rood) afgebeeld over een optische waarneming van hetzelfde stelsel, 4C 35.06, welke een AGN huisvest. **Rechts:** LOFAR 140 MHz radio intensiteit (rood, geel) afgebeeld over een optische waarneming van het sterrenstelsel waarin zich de radiobron B2 0924+30 bevindt.

radiobron hebben we een component gevonden van een mogelijkerwijs veel oudere plasmabel die in elkaar wordt gedrukt door een schokgolf afkomstig van de versmelting van twee clusters (het helderste sterrenstelsel in één van deze clusters is de thuishaven van onze AGN).

Radiorestanten worden ook gevonden in sterrenstelsels die niet tot een cluster behoren. We analyseren zo'n restant in Hoofdstuk 5. Hierbij hebben we vastgesteld dat de AGN in kwestie al meer dan 100 miljoen jaar geleden haar activiteit heeft gestaakt. Sommige delen van de radiowolken in het restant zijn echter opnieuw gevoed door de jet en zijn slechts 20 miljoen jaar oud.

In dit proefschrift hebben we aangetoond dat LOFAR een uitermate geschikt instrument is om de straling van radiorestanten te detecteren in de lagere frequentiebereiken; dit met een resolutie die weinig onderdoet voor resultaten die andere instrumenten behalen met veel hogere frequenties. Hierdoor hebben we afbeeldingen kunnen vergelijken op een breed scala aan frequentiebereiken.

De bruikbaarheid van LOFAR als survey-instrument wordt tentoongespreid in Hoofdstuk 6, waarbij we systematisch hebben gezocht naar radiorestantent van AGN in de eerste LOFAR survey, de Multi-frequency Snapshot Sky Survey (MSSS). Hoewel deze survey slechts een beperkte resolutie alsook gevoeligheid heeft, is het een belangrijke lakmoesproef. We konden goed vaststellen hoe vaak een compacte radiobron wordt vergezeld van een radiorestant.

In Hoofdstuk 7 hebben we van twee reusachtige radiosterrenstelsels de stralingseigenschappen in lage frequenties kunnen bestuderen. In de combinatie van een relatief hoge resolutie van ongeveer $1'$ en lage frequentie van 140 MHz, was dit de eerste keer dat zulke waarnemingen gedaan zijn. We hebben hierbij radiowolken in kaart gebracht die tot dusver niet gedetecteerd werden (figuur 5).

Ons onderzoek toont het grote potentieel van LOFAR als instrument om radiorestanten van AGN waar te nemen, en is daarin een eerste poging. Een van onze bevindingen is dat deze studies in het lage frequentiegebied essentiëel zijn om de waarnemingen in

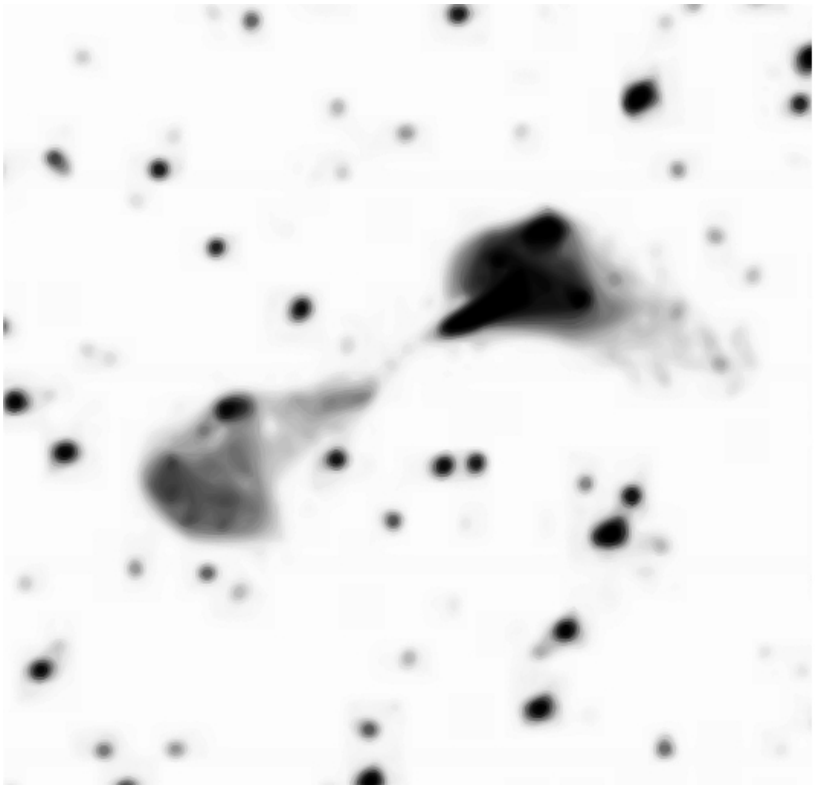

Figuur 5: LOFAR afbeelding van het reuze radiosterrenstelsel NGC 6251 op een frequentie van 140 MHz.

andere golflengtes goed te interpreteren. Ook hebben we een aantal kandidaten voor radiorestanten ontdekt en daarmee de kwaliteiten van LOFAR als survey-instrument laten zien. Lage frequenties hebben een heldere toekomst!

Резиме

Угоре високо, удолу длабоко.

– народна поговорка

АГЈ и нивните радио остатоци

Првите радиобранови од небото биле набљудувани од Карл Јански, инженер кој работел за Бел лабораториите (кои биле во сопственост на компанијата AT&T) во 30. години од минатиот век. Тој забележал дека центарот на нашата Галаксија е извор на постојан шум кој им пречи на радио врските (Слика 1). Речиси една деценија подоцна, Гроте Рибер создал карти на Галаксијата и неколку други посилни извори на радио зрачење на небото користејќи радио телескоп кој го направил самиот. Така настанала радио астрономијата.

Во текот на наредните децении, радио астрономијата многу напредуваше. Се откри цел еден опсег на нови природни феномени кои може да се набљудуваат само со помош на радио бранови.

Џиновски региони на радио зрачење беа откриени од обете страни на некои елиптични галаксии. Со зголемувањето на раздвојната моќ на радио телескопите, беше откриено дека понекогаш тенки млазеви на радио зрачење ги поврзуваат овие региони со јадрата на нивните матични галаксии.

Подоцна беше пронајдена и друга категорија на мистериозни небесни извори на зрачење - сјајни објекти кои наликуваат на ѕвезди, со многу невообичаени оптички спектри во кои се забележани непознати емисиони и апсорпциони спектрални линии. Во 60. години, во момент на инспирација, астрономот Мартен Шмит заклучи дека спектрите на овие објекти можат да се објаснат ако се претпостави дека тие се наоѓаат на огромни растојанија од нас, во просек милијарди светлосни години далеку. Поради тоа што се многу сјајни и наликуваат на ѕвезди (беа наречени ѕвездолики објекти или популарно квазари), големите количества на енергија кои тие ја зрачат мора да потекнуваат од релативно мал регион во вселената.

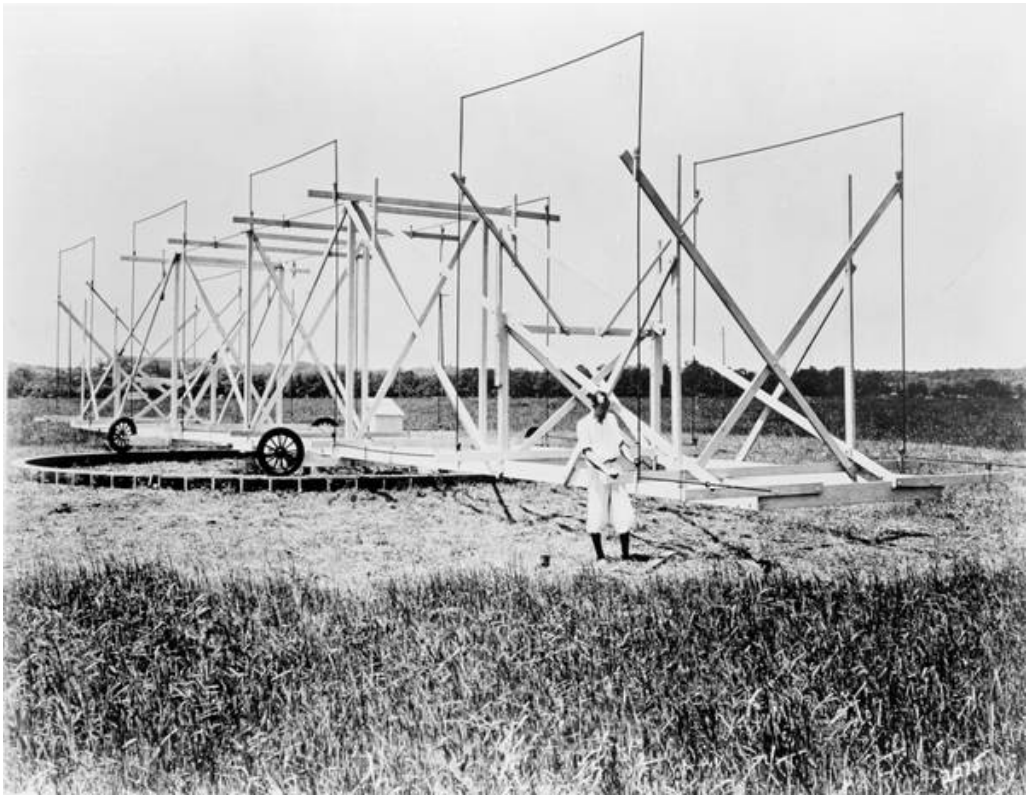

Слика 1: Карл Јански и антената која ја користел во неговите изучувања на вселенскиот шум (© Bell Telephone Labaratories).

Разгледувајќи неколку физички процеси кои можат да произведат толку голема енергија, постепено се дојде до сознанието дека единствениот процес кој што може да ги објасни набљудувањата е акреција на материја врз компактен објект. Податоците водеа кон заклучокот дека централниот објект е супермасивна црна дупка (СЏД) со маса во опсег од милиони до милијарди сонца. Материјата која што паѓа во СЏД формира акрециски диск околу неа кој зрачи преку целиот електромагнетен (ЕМ) спектар. Подалеку од СЏД, дискот може да се рашири и формира торус; магнетните полиња кои се наоѓаат во СЏД и акрецискиот диск можат да формираат и насочат млаз на високо релативистички честички под прав агол во однос на рамнината во која се наоѓа дискот. Овие честички зрачат нетоплотно, синхротронско зрачење. Млазевите остануваат тенки и насочени преку огромни растојанија, пробивајќи се низ меѓувсезденатa средина на матичнатагалаксијата и произведувајќи ги регионите кои емитуваат радио бранови кои ние ги набљудуваме (видете ја Слика 2 на која е прикажана слика на радио галаксијата HerA). Овој феномен е најимпресивните манифестации на активно галактичко јадро (АГЈ).

Наскоро (во 80. години) се дојде до сознанието дека АГЈ може да бидат феноменот кој е одговорен за специфичните својства на радио галаксиите, квазарите и други слични извори на зрачење. АГЈ може да се најдат во многу различни верзии; оваа

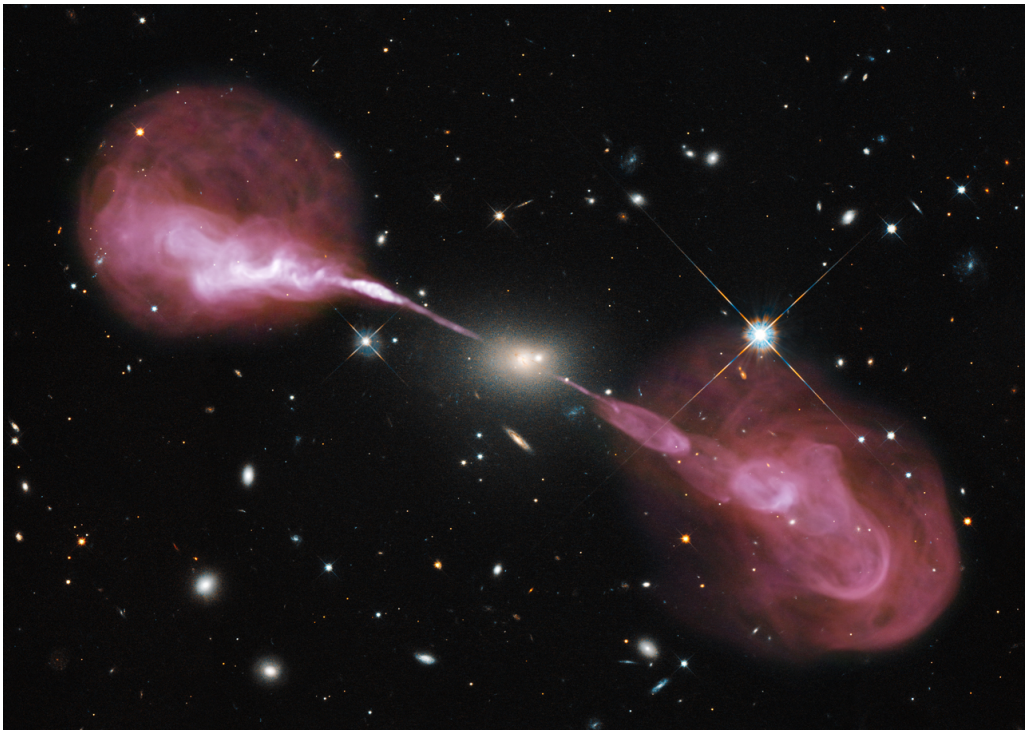

Слика 2: Повеќеслојна слика на најсјајниот радио извор во созвездието Херкул. Оптичката слика е снимена со широкоаголната камера 3 на Хабловиот вселенски телескоп, додека радио сликата (розево) е снимена со радио телескопот наречен големата низа на Карл Јански (VLA). Можеме да ги забележиме млазовите на радио зрачење кои извираат од АГЈ кое се наоѓа во центарот на елиптичната галаксија која е илјада пати помасивна од нашата галаксија - Млечен Пат. Радио млазевите завршуваат во големи региони кои емитуваат радио бранови; можеме да забележиме промени во активноста на АГЈ кои се одразени во неколкуте меурчиња плазма видливи во млазот на десната страна, додека млазот од другата страна има спирална структура. (© NASA, ESA, С. Баум и К. О'Деј (RIT), Р. Перли и В. Котон (NRAO/AUI/NSF), и екипата која се грижи за архивите на Хабловиот вселенски телескоп (STScI/AURA))

разновидност се должи најмногу на тоа како се ориентирани во просторот. Различни обединувачки класификации беа предложени за да се даде објаснување на соодносот помеѓу она што го набљудуваме и феноменот на АГЈ. Кога правецот на набљудување се совпаѓа со оската на ротација на СЏД или помеѓу нив има сосема мал агол, тогаш набљудуваме sвездолик извор на зрачење. Ако АГЈ не емитува (или емитува занемарливо малку) радио бранови, набљудуваме оптички квазар или таканаречена Сејфертова галаксија од тип 1 или 2 (ако правецот на набљудување е под речиси прав агол во однос на оската на ротација на СЏД). Во случајот кога АГЈ е исто така извор на радио зрачење, набљудуваме квазар заедно со силно (релативистички засилено) радио зрачење кое доаѓа најповеќе од радио млазот кога го набљудуваме АГЈ речиси паралелно со неговата оска на ротација. Ако пак го набљудуваме АГЈ под релативно големи агли во однос на оската на ротација, централниот регион е сокриен и радио зрачењето е она кое што е најзабележливо - тогаш набљудуваме радио галаксија. Фотографирањето на матичните галаксии на некои квазари (посебно по лансирањето на Хабловиот вселенски телескоп) придонесе кон зацврстувањето на овие гледишта.

Изучувањето на АГЈ е цела под-област на истражување во радио астрономијата. Во текот на изминатите децении дознавме многу околу нивните енергетски процеси, спектрални својства и односот помеѓу нив и нивната околина. Истовремено, има многу нешта кои остануваат непознати. АГЈ зрачат низ целиот ЕМ спектар и се простираат низ зачудувачки голем опсег на растојанија; СЏД која е во центарот на АГЈ не е поголема од нашиот сончев систем, додека нивните млазеви и региони на радио зрачење можат да се опфаќаат растојанија од милиони светлосни години. Според тоа, нивното проучување бара набљудувања со најразлични инструменти и познавање на процеси кои вклучуваат квантна теорија, општа и специјална теорија на релаивност, еволуција на галаксиите, па дури и космологија, всушност познавање на севкупната модерна астрономија.

Во овој труд се фокусираме на изучување на АГЈ во радио делот на ЕМ спектар. Во радио доменот АГЈ може да бидат со променлив сјај кој може да варира со период од денови или години. Радио интерферометријата (поврзување на повеќе радио телескопи за да се добие инструмент со поголема осетливост и раздвојна моќ) ни овозможува подобро да ги истражуваме АГЈ и зависноста на нивните својства од резолуцијата со која набљудуваме. Променливоста на зрачењето на АГЈ е најзабележлива во нивните (радио) јадра. На поголеми размери, регионите на радио зрачење кои се далеку од јадрото ја забележуваат променливата во активност на АГЈ во текот на подолги временски интервали.

СЏД може да ги исцрпи своите залихи на акрециска материја. Штом тоа се случи, АГЈ престанува со активност. Зрачењето во оптичкиот дел на спектарот исчезнува, исто како и радио млазевите. Со задоцнување кое е соодветно на времето потребно за информацијата за престанокот на активноста да стаса до оддалечените региони на радио зрачење, снабдувањето на тие региони со релативистички честички престанува. Тогаш, овие региони започнуваат да исчезнуваат, т.е. нивниот радио сјај се намалува. Меѓутоа, вредностите на намалувањето на радио сјајот се различни во зависност од фреквенцијата на зрачењето. Потребно е набљудување на овие радио структури преку целиот радио спектар за да се дознае повеќе за активноста на АГЈ во минатото.

Теориските основи за опишување на не-топлотното (синхротронско) зрачење ги поставија Виталиј Гинзбург и Николај Кардашев во 60. години на минатиот век.

Подоцна, тие беа продлабочени од страна на повеќе астрофизичари. Преку споредба на теориски модели на спектри на радио извори со мерења добиени од набљудувања можеме да го определиме времетраењето на активност на АГЈ, како и тоа колку време протекло од моментот кога АГЈ престанало да биде активно. Затоа, радио остатоците од изгаснати АГЈ се многу важни; тие се единствена трага од минатата активност на АГЈ.

Радио остатоците се најсјајни кога се набљудуваат на ниски радио фреквенции. Моќна алатка во нивното изучување е новиот нискофреквентен радио телескоп - ниско фреквентната низа (НФН/LOFAR, прикажан на Слика 3). Тоа е радио интерферометар кој работи во фреквенцискиот опсег од 20 MHz до 80 MHz и од 120 MHz до 240 MHz. Се состои од двојни диполни антени кои се групирани во т.н. станици. Повеќето од овие станици се распоредени во северниот дел на Холандија, а некои се наоѓаат и во Германија, Обединетото кралство, Полска и Шведска. Во текот на едно набљудување LOFAR може да произведе слика на радио небото со дијаметар од 5° (што е еквивалентно на 10 полни месечини наредени една до друга), овозможувајќи полесно истражување на целото небо и откривање на нови извори на радио зрачење.

Слика 3: Шесте станици кои го сочинуваат центарот на НФН телескопот, таканаречениот супер-терп, сликано на 23 Мај 2010 година (© Top-Foto, Assen).

Нашето истражување

Во овој труд изучувавме повеќе радио остатоци од АГЈ, а за некои од нив ги определивме и нивните радио спектри, што ни овозможи да ја процениме староста на АГЈ од кои тие настанале.

Глава 2 ги опишува својствата на радио остаток кој што го откривме набљудувајќи на фреквенција од 1400 MHz со користење на радио телескопот WSRT кој се наоѓа во северна Холандија. Радио остатокот се наоѓа околу АГЈ кое што е моментално активно, класифицирано како компактно АГЈ со стрмен радио спектар. Радио сјајот на остатокот е многу мал. Проучувањето на неговиот спектрален индекс и старост ќе ни овозможат да го утврдиме времетраењето на активноста на АГЈ како и интервалот на време кој поминал помеѓу две последователни епизоди на активност. Елиптичната галаксија која е дом на ова АГЈ е богата со гас (постои огромен прстен на водород околу неа) кој може да ја поттикнува активноста на АГЈ.

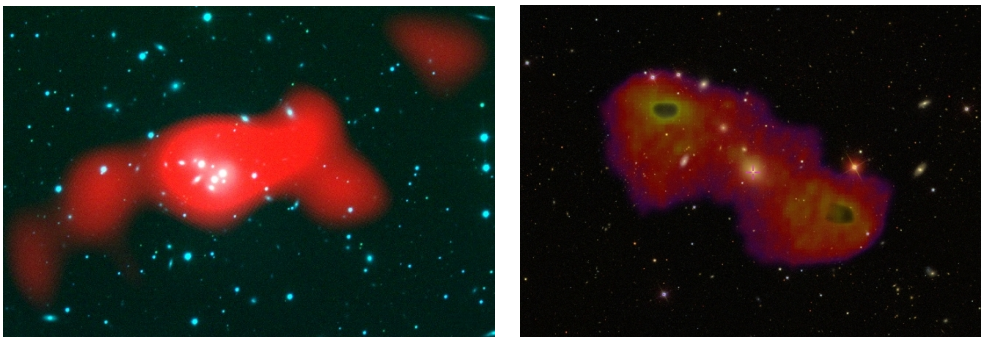

Слика 4: Лево: Радио слика направена со LOFAR телескопот на фреквенција од 61 MHz (црвено) поставена врз оптичка слика на галаксијата-домаќин на АГЈ кое го создало изворот на радио зрачење 4C 35.06. Десно: Радио слика направена со LOFAR телескопот на фреквенција од 140 MHz (црвено, жолто) поставена врз оптичка слика на галаксијата-домаќин на АГЈ кое го создало радио изворот B2 0924+30.

АГЈ може да се наоѓаат и во галаксии кои се дел од галактички јата. Во глава 3 изучувавме радио остаток од такво АГЈ. Неговиот изглед и старост се определени од галактичката околина во која тој се наоѓа. Го измеривме неговото радио зрачење на повеќе различни фреквенции, од 61 MHz (со LOFAR, види ја Слика 4) до 4800 MHz (користејќи ја VLA, радио интерферометар кој се наоѓа во Сокоро, Ново Мексико, САД). Откривме дека радио изворот 4C 35.06 е комбинација на стар радио остаток и АГЈ кое е повторно активно. Повторно го искористивме WSRT за да провериме дали во близината на АГЈ има гас, и навистина, најдовме водород во близина на галаксијата која е домаќин на ова АГЈ.

Уште еден радио остаток од АГЈ кој што се наоѓа во подалечно ($z = 0.159$) галактичко јато беше тема на изучување во глава 4. Користејќи податоци добиени со помош на радио телескопите LOFAR и VLA, како и слики направени со помош на радио телескопот GMRT (кој се наоѓа во близина на Пуне во Индија), утврдивме

дека АГЈ кое го создало овој радио остаток се угасило пред околу 60 милиони години. Во рамките на истиот радио извор забележавме и втора компонента на радио зрачење која најверојатно претставува регион на постара плазма која била компримирана од бран на материја создаден при спојувањето на две галактички јата (најсјајната галаксија во едно од нив е галаксијата-домаќин на АГЈ кое го изучувавме).

АГЈ радио остатоци се наоѓаат и во галаксии кои не се дел од галактички јата. Изучувањето на таков остаток е тема на глава 5, каде што утврдивме дека активноста на АГЈ престанала пред повеќе од 100 милиони години. Меѓутоа, делови од регионите кои емитуваат радио зрачење и кои биле снабдувани со релативистички честички и по престанувањето на активноста на АГЈ (преку радио млазот кој сеуште бил активен) се со старост од само 20 милиони години.

Во овој труд демонстриравме колку LOFAR е корисен при детектирањето на радио зрачење од радио остатоци на ниски фреквенции со резолуција слична на онаа која може да се добие со користење на инструменти кои работат на повисоки фреквенции. Поради тоа што поседуваме радио слики со приближно иста резолуција на различни фреквенции, бевме во можност да правиме споредби помеѓу нив.

Можностите на LOFAR како инструмент за истражување ги демонстриравме во глава 6 каде што извршивме потрага по радио остатоци од АГЈ користејќи радио слики направени како дел од првото систематско истражување на небото на ниски фреквенции изведено со LOFAR, мулти-фреквенциското истражување на небото во кратки интервали (MSSS). Иако со ограничена осетливост и резолуција, истражувањето е вредно како претставување на можностите на LOFAR за откривање на радио остатоци. Бевме во можност да поставиме граници на тоа колку често радио остатоците се присутни околу компактни радио извори.

Во глава 7 извршивме детално изучување на радио зрачењето на две џиновски радио галаксии (3C 236 и NGC 6251). Нашиот труд претставува прво истражување на овие галаксии со резолуција од околу $1'$ на фреквенција од 140 MHz. Откривме региони на радио зрачење во галаксијата NGC 6251 кои не беа забележани досега (Слика 5).

Во овој труд го опишавме големиот истражувачки потенцијал на LOFAR. Тој претставува прв обид за користење на LOFAR во изучувањето на радио остатоци на АГЈ. Утврдивме дека нискофреквентните радио набљудувања се неопходни за поставување на граници на теоретските модели и се неопходни при толкувањето на добиените резултати. Исто така, откривме радио извори за кои постои можност дека се радио остатоци, и со тоа ги демонстриравме можностите кои LOFAR ги нуди како инструмент за истражувања на небото. Иднината е светла на ниски радио фреквенции.

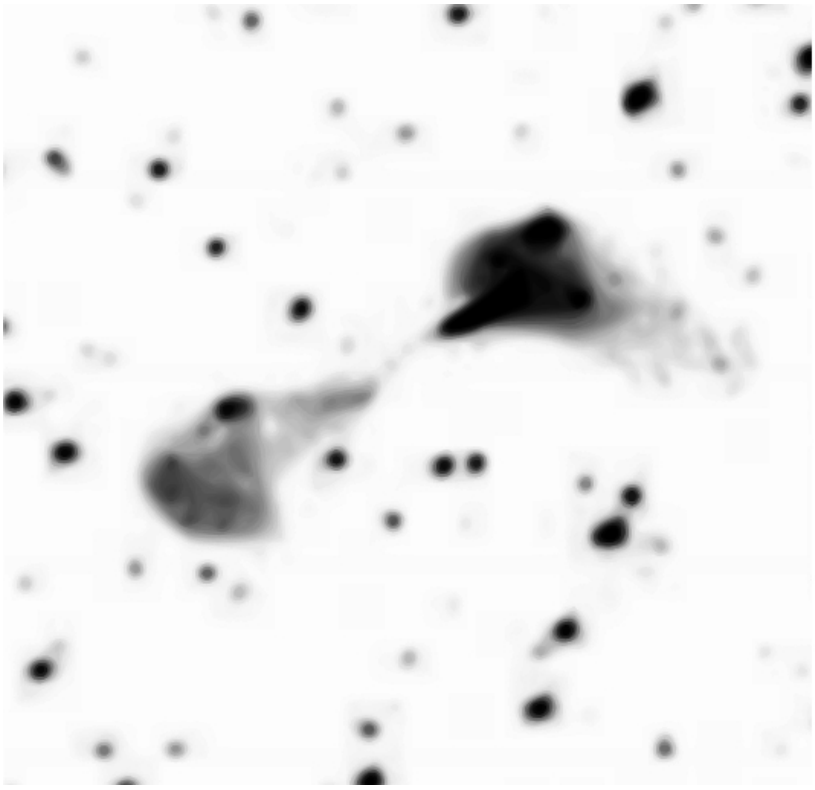

Слика 5: Радио слика на џиновската радио галаксија NGC 6251 направена со LOFAR на фреквенција од 140 MHz.

Acknowledgements

What is to give light must endure burning.

– Viktor E. Frankl

It is finished. This thesis marks a culmination of my doctoral research, but it is also so much more. It encapsulates the work I have done at the Kapteyn instituut and at ASTRON, tracing my growth as a scientist. In between its pages the reader can find the science results of my project, but above that the writer finds memories, experiences and growth which have marked the past four years.

Embarking on the path of a career in astronomy was not an easy feat; apart from my resolve, I have had a lot of help getting where I am now, and my thanks is due to all who have guided me along. My high school physics teacher, Danica, has her share in molding a young mind and directing me into taking up physics, apart from astronomy which I became interested in it seems even before I could walk. All of my math and physics teachers and the faculty of electrical engineering in Skopje, Macedonia, as well as the friends over at the faculty of natural sciences who have engaged in fruitful discussions and who have done heroic efforts to advance astronomy in times of hardship. Mijat, you are remembered and missed. My dear friends from the community of amateur astronomers who have kept the ember of interest in astronomy in Macedonia alive in the pre-internet times deserve a special mention. Gordana, Olja, Zoran, and lots of others have contributed in many ways in those early days.

Rudolf, you are among those who have helped in my transition to Leiden and to the Netherlands at a crucial point in my life, when I was about to give up on following up on my long held intention to delve into astronomy on a professional level. The observatory in Leiden will always have a special significance for me. It has opened my eyes to the world and exposed me to so many different cultures. It provided its share of challenges too, and I am better for it. Daniel, thanks for all the thought-provoking discussions. Huub, Yuri, you have been wonderful at focusing my attention to the problems at hand. Ali, Giles, and many others who are still there or spread across the globe, you have made

my first encounter with the Netherlands a memorable one.

A field trip was responsible for my first look at ASTRON, and an invited talk to our radio astronomy class has led to me meeting Raffaella, who was to be my PhD supervisor. I remember coming to Groningen and to the institute for the interviews and immediately feeling its particularly pleasent character. My PhD has been another, but this time inflationary period of personal and professional growth. Almost immediately after starting my appointment I was at the defense of the outgoing PhD student of Raffaella, Christian, who has written in his thesis that the number of emails exchanged with her was around 10^4 over 4 years. I think I have matched that number, if not exceeded it, and all for a reason. Raffaella, thank you. You have provided me with a primer of perseverance and traced a path for me through the tribulations of dealing with LOFAR data, a feat which had its share of difficulties. But, you never failed to be always there and remain positive. You have helped me mature and learn a lot of what it takes to be a scientist. Peter, I feel that I have been extremely lucky in that I had two supervisors during my tenure at Kapteyn/ASTRON, since I never felt that you are co-supervising. You were always there, and proved invaluable on many occasions when I needed advice, and not just a scientific one. Your enthusiasm, love for outreach, encyclopedic knowledge and wisdom leave me in debt. Years ago, when I was not an astronomer I read about the AGN unification scheme and thought how awesome it would be to meet the guy who thought of it. In the past four years I have worked together with you. Life is indeed mysterious. Thank you for your teaching through kindness.

Kapteyn is the kapteyners. Boris, thanks for helping me move into my first apartment. Thomas, Stefan, you have been great old office mates. You have endured my endless rants. Stefano, Francesco, and Saikat you too have proven to be worthy of the 192 legacy. Katinka, thanks for keeping up with my HI questions. Johan, all the dinners, sci-fi and music will be fondly remembered. Since we took our cats from the asiel on the same day, that makes us family... I guess. Marisa, I leave the relics in your care. Marius, Filipo, Burcu, Harish, Ajinkya, Saleem, Thijs, Maarten, Hugo, Stephanie, Eugenia, Rosina, Pece... I could go on and on, and I will most probably miss to thank someone who has marked these four years and has made them just a bit more special. Everyone, thank you. For the scientific discussion, pranks, help, for everything.

Special thanks of course goes to the secretaries. Jackie, Christa, the research goes on smoothly because you are present. Hennie, who retired at the same time I am leaving, the fact that we are a widely known bunch is also due to your tireless work. Thank you.

Eite, Wim, and Maarten, thank you for the computing support, for being there to deal with the consequences of our badly implemented hacks, and for helping me with the Kapteyn package. Your scientific legacy continues.

My colleagues at ASTRON/LOFAR, thanks for putting up with me during the commissioning efforts. Roberto, Manu, Fra, Adriaan, George, Ger, John, Elizabeth, Ashish, Cyril, Reinout, Jeremy, Nicolas et al., you were indispensable and have always been there for me. ASTRON is a thriving nexus of expertise because of you.

My family deserves a special mention for their support. It was not easy putting up with my headstrong ways. Goce, my brother, thank you for your faith. Violeta, as an older sister you have guided me through life and always kept my corner. Mom, you have been always there for me. Father, I think that you would have liked this work. Thank you for the stars.

Jasmina, my dear wife, you have endured having a PhD husband. That says a lot.

Thank you for your infinite love. Filip, my son, you have been a precious discovery. I think that all of us are going to write some wonderful new chapters in the book of life.

Aleksandar Shulevski
January 2015, Groningen